HIGH-RESOLUTION PALEOCEANOGRAPHY OF THE GULF OF ALASKA, SUBARCTIC NORTHEAST PACIFIC OCEAN, SINCE THE LAST GLACIAL MAXIMUM: INSIGHTS INTO A DYNAMIC ATMOSPHERE-OCEAN-ECOSYSTEM LINKAGE AT DECADAL TO MILLENNIAL TIMESCALES

A

DISSERTATION

Presented to the Faculty

of the University of Alaska Fairbanks

in Partial Fulfillment of the Requirements

for the Degree of

DOCTOR OF PHILOSOPHY

By

Jason A. Addison, B.S.

Fairbanks, Alaska

December 2009

HIGH-RESOLUTION PALEOCEANOGRAPHY OF THE GULF OF ALASKA,

SUBARCTIC NORTHEAST PACIFIC OCEAN, SINCE THE LAST GLACIAL

MAXIMUM: INSIGHTS INTO A DYNAMIC ATMOSPHERE-OCEAN-

ECOSYSTEM LINKAGE AT DECADAL TO MILLENIAL TIMESCALES
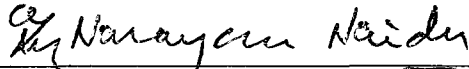
By

Jason A. Addison

RECOMMENDED:

Dr. Nancy H. Bigelow

Dr. A. Sathy Naidu

Dr. Dean A. Stockwell

Dr. Matthew J. Wooller

Dr. Bruce P. Finney, Advisory Committee Chair

Dr. James E. Begét, Advisory Committee Co-Chair

Dr. Michael T. Whalen,
Chair, Department of Geology and Geophysics
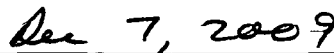
APPROVED:

Dr. Paul W. Layer,
Dean, College of Natural Science and Mathematics

Dr. Lawrence K. Duffy,
Dean of the Graduate School

Dec 7, 2009

Date

Abstract

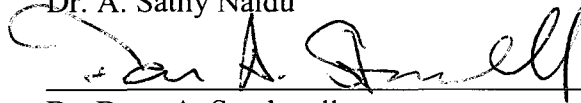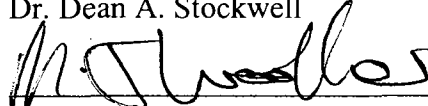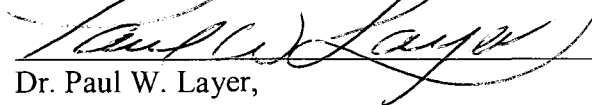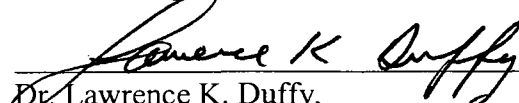Environmental conditions in the Subarctic Northeast Pacific Ocean are an important component of North American climate patterns, as well as a potential driver of Northern Hemisphere climate variability. The North Pacific Ocean is also the terminus of modern global thermohaline circulation, suggesting that paleoceanographic records from this region have the potential to preserve evidence of both climate forcing and response on regional and global scales. A suite of high-resolution marine sediment cores collected from the Gulf of Alaska margin in 2004 provide new paleoceanographic records at decadal and centennial timescales from fjord and continental slope environments. Key findings include: (i) decadal oscillations in marine productivity correlate with previously identified terrestrial records, indicative of forcing by the Aleutian Low pressure cell; (ii) the standard binary model of the modern Pacific Decadal Oscillation (PDO) as the major pattern of ocean-atmosphere variability is insufficient to describe the full range of Holocene paleoenvironmental fluctuations observed in Gulf of Alaska records of marine productivity, freshwater discharge, and bottom-water anoxia; (iii) the North Pacific ecosystem is a sensitive recorder of abrupt climate events observed in global records; and (iv) the fjords of Southeast Alaska contain a detailed record of volcanic activity and fall-out events useful for developing composite chronological models of sedimentation that correlate with other regionally important stratigraphic records. Collectively, the results presented here will potentially redefine current theoretical models of atmosphere-ocean-ecosystem variability in the North Pacific Ocean, as well as contribute to a growing body of high-resolution paleoenvironmental time-series datasets from the high latitudes.

Table of Contents

Page

List of Figures

List of Tables

List of Appendices

Acknowledgements

The first and by far the most important person involved in this work is my wonderful wife Jennifer; her dedication and patience are worthy of song and poem. My family and friends were also important, but most notably my mother whom fostered an early love of science in me. I am indebted to my advisors Bruce Finney and Jim Begét. Their guidance over the last five years has been instrumental in my professional development. I also thank my graduate advisory committee members: Nancy Bigelow, Mat Wooller, Sathy Naidu, and Dean Stockwell. In the laboratory, I have benefitted greatly from discussions with Andy Krumhardt, Nicole Misarti, and Mark Shapley, as well as the dedication of Tara Borland, Jamie Coon and Lisa Baraff. Ken Severin, Tom Trainor, Karen Spaleta, and Thomas Kircher at the UAF Advanced Instrumentation Laboratory, and Tim Howe and Norma Haubenstock at the Alaska Stable Isotope Facility provided the high-technology toys I have now become addicted to using for good. I am also appreciative of Shelly Baumann at the UAF Graduate School for assistance with formatting of this dissertation.

Over the course of this project, I have also been honored to work with a number of colleagues all over the United States: John Jaeger and Gillian Rosen at the University of Florida; Joe Stoner, Alan Mix, Fred Prahl, and Maureen Davies at Oregon State University; Tom Ager, John Barron, and Walt Dean at the US Geological Survey; Ellen Cowan at Appalachian State University; Ross Powell at Northern Illinois University; Sean Gulick at the University of Texas at Austin; Larry Mayer at the University of New Hampshire; and Sally Zellers at the University of Central Missouri. At one time or another, all of these investigators have had to deal with a dumb question from an Alaskan graduate student – their patience during this process has been greatly appreciated.

Chapter 1 Introduction

Earth's climate history is complex, and a comprehensive description of its past variability is essential for future prediction. The geological sciences have contributed much to the science of paleoclimatology at timescales ranging from millions of years to seasonal variations, yet the spatial coverage of high-quality records remains sparse. This scarcity complicates climate modeling efforts, as do parameters that are not preserved in the sedimentary record. Nevertheless, these complex models are the only tools capable of predicting future climate change and are thus a necessity for preparing human society for these changing conditions (Randall et al., 2007). Yet general circulation models are only capable of describing the datasets that they incorporate, thus as a shared necessity, it is imperative the scientific community increases the spatial and temporal resolution of high-quality paleoclimatology datasets (Lohmann, 2008).

The Gulf of Alaska is a dynamic region for studying past climate histories. This basin dominates the Subarctic Northeast Pacific Ocean, an important component of Northern Hemisphere climate patterns with atmospheric teleconnections reaching as far east as the US Atlantic Coast (Trenberth and Hurrell, 1994), and as far south as the Sonoran Desert in northern Mexico (Latif and Barnett, 1994). The Gulf of Alaska is also the terminus of modern global thermohaline circulation (Broecker, 1991) which suggests any perturbation in the North Atlantic, Southern, or Indian Ocean deep waters will invariably manifest itself in the North Pacific as well. Modeling studies have also suggested that perturbations originating in the Subarctic Northeast Pacific Ocean can also drive abrupt climate events on global scales (Peteet et al., 1997; Kiefer et al., 2002).

Despite the obvious role the Gulf of Alaska plays in modern climate, and by inference past climates, the Gulf remains one of the most poorly studied regions in the world ocean, second perhaps only to the sea-ice covered Arctic Ocean. Several important high-resolution paleoclimate datasets have been recovered from the terrestrial margin of the Gulf of Alaska, including ice cores (Moore et al., 2002; Rupper et al., 2004; Fisher et al., 2008), paleovegetation records (Peteet, 1991; Mann and Peteet, 1994; Peteet and Mann, 1994), and lacustrine sediments (Finney et al., 2000; Finney et al., 2002; Anderson

et al., 2005), yet none of these data directly preserve ocean conditions in this region. Those paleoceanographic records that have been recovered from the region suffer either from poor core recovery (DSDP Site 178; Kulm et al., 1973), low temporal resolution (ODP Site 887; Rea et al., 1995), or insufficient length to resolve periods greater than a few millennia (Boughan, 2008).

Some of the same processes that manifest themselves as important drivers of hemispheric climate also make the Gulf of Alaska and its margin a region of extreme conditions. Collisional tectonics over the relatively short time interval of the last 10 million years have generated the massive Kenai-Chugach-St. Elias mountain complex adjacent to the Gulf of Alaska with many peaks exceeding 5000 m in elevation within 25 km of sea level (Gulick and Jaeger, 2003). These mountains have strong orographic effects on precipitation with local maxima of 700 cm·yr^{-1}, making this one of the highest precipitation rates in the world. In turn, this precipitation drives a highly effective glacial erosion system with denudation rates exceeding 10 mm·yr^{-1} with minimal terrestrial sediment storage (Hallet et al., 1996). Marine sediment accumulation rates are correspondingly high, ranging from 0.02 – >100 cm·yr^{-1} (Jaeger et al., 1998; Walinsky et al., 2009). Furthermore, oceanographic conditions in the Gulf of Alaska support a diverse marine ecosystem with high seasonal primary productivity and several economically valuable commercial fisheries (Mueter and Norcross, 2002; Childers et al., 2005). Taken as a whole, these environmental and ecological conditions are ideal for preserving a highly detailed sedimentary record of paleoclimatic change from the Gulf of Alaska.

The data presented in this dissertation are some of the first results from cruise EW0408, a comprehensive geophysical and sediment coring survey conducted along the southern coast of Alaska during the summer of 2004 by the R/V *Maurice Ewing*. Sediment cores were collected between 55°N to 60°N latitude, spanning many of the unique environments that dot the Alaskan continental shelf, including tidewater glacier bays, ice-free temperate fjords, deep-sea submarine fans, and the continental slope and shelf. This cruise was undertaken as an assessment for coordinating a future Integrated

Ocean Drilling Program cruise, and included extensive high-resolution multibeam bathymetry mapping, seismic imaging, water column sampling, and benthic multicore and jumbo piston coring operations. Collaborations with workers at Oregon Statue University, University of Florida, Appalachian State University, Northern Illinois University, University of New Hampshire, University of Texas at Austin, and the United States Geological Survey have all contributed vital elements of the work presented here.

This dissertation focuses on results from the sediment coring portion of the multi-disciplinary EW0408 cruise. The contributions presented here can be divided broadly into two categories: (i) establishing chronological constraints for the regional Late Quaternary sedimentary record, and (ii) developing high-resolution datasets of paleoproductivity and paleoenvironmental change to reconstruct ocean, atmosphere, and ecosystem variability in the Gulf of Alaska since the Last Glacial Maximum around 18,000 years ago. Chapter 2 describes the Late Quaternary history of marine volcanic ash deposition (tephrochronology) along the Alexander Archipelago in southeast Alaska, and uses the stratigraphy of these deposits to establish a chronological framework for linking depositional records from marine and terrestrial environments along the Gulf of Alaska margin. The remaining chapters are focused exclusively on paleoceanographic reconstructions, including: a decadal-scale record of productivity and sedimentary isotope accumulation trends for the last 8,000 years from a fjord on Baranof Island that reflects high-frequency climate changes driven by the Pacific Decadal Oscillation (PDO) and the Aleutian Low pressure cell (Chapter 3); a transect of high-resolution fjord records that span the last 18,000 years and exhibit coherent patterns in productivity and biogeochemical proxies that reflect both decadal-scale PDO changes, and previously unknown millennial-scale regime shifts (Chapter 4); and a record from the continental shelf of the northern Gulf of Alaska that reflects basin-wide North Pacific Ocean changes and Cordilleran Ice Sheet dynamics since the Last Glacial Maximum (Chapter 5). This compilation is then summarized in Chapter 6 with a comprehensive outline of major outcomes from this body of research.

Recurring themes between all of these dissertation chapters include: use of radiometric techniques as geochronologic constraints; the effect of relative sea-level change along this tectonically-active margin; changes in sedimentation regimes due to retreat of the Cordilleran Ice Sheet and associated climate change; high spatial and temporal variability in sedimentology and organic matter composition between different depocenters along the Gulf of Alaska margin; and the tightly coupled atmosphere-ocean-ecosystem structure that exists in the Subarctic Northeast Pacific Ocean. It is this last component that is the primary focus of the paleoceanographic work, namely that use of records that preserve variations in export productivity and other parameters can be used to reconstruct both high-frequency climate oscillations and abrupt climate events.

Each of Chapters 2-5 have been prepared as a series of manuscripts intended for future publication. Chapter 2 has been written for the journal *Quaternary Research*, and has been accepted by the journal editorial board. Chapter 3 is a short article intended for submission to *Science*, while Chapters 4 and 5 have both been prepared for the journals *Continental Shelf Research* and *Paleoceanography*, respectively.

1.1   References

Anderson, L., Abbott, M. B., Finney, B. P., and Burns, S. J. (2005). Regional atmospheric circulation change in the North Pacific during the Holocene inferred from lacustrine carbonate oxygen isotopes, Yukon Territory, Canada. *Quaternary Research* **64,** 21-35.

Boughan, M. M. (2008). "Paleoceanographic shifts in the Gulf of Alaska over the past 2000 years: a multi-proxy perspective." University of Alaska Fairbanks.

Broecker, W. S. (1991). The great ocean conveyor. *Oceanography* **4,** 79-90.

Childers, A. R., Whitledge, T. E., and Stockwell, D. A. (2005). Seasonal and interannual variability in the distribution of nutrients and chlorophyll a across the Gulf of Alaska shelf: 1998-2000. *Deep-Sea Research Part II-Topical Studies in Oceanography* **52,** 193-216.

Finney, B. P., Gregory-Eaves, I., Douglas, M. S. V., and Smol, J. P. (2002). Fisheries productivity in the northeastern Pacific Ocean over the past 2,200 years. *Nature* **416,** 729-733.

Finney, B. P., Gregory-Eaves, I., Sweetman, J., Douglas, M. S. V., and Smol, J. P. (2000). Impacts of climatic change and fishing on Pacific salmon abundance over the past 300 years. *Science* **290,** 795-799.

Fisher, D., Osterberg, E., Dyke, A., Dahl-Jensen, D., Demuth, M., Zdanowicz, C., Bourgeois, J., Koerner, R. M., Mayewski, P., Wake, C., Kreutz, K., Steig, E., Zheng, J., Yalcin, K., Goto-Azuma, K., Luckman, B., and Rupper, S. (2008). The Mt Logan Holocene-late Wisconsinan isotope record: Tropical Pacific-Yukon connections. *Holocene* **18,** 667-677.

Gulick, S., and Jaeger, J. (2003). The interplay of collisional tectonics and Late Cenozoic glacial climate in Alaska and the Northeastern Pacific Ocean, pp. 79. Continental Dynamics Program, Earth Sciences Division, National Science Foundation and Joint Oceanographic Institutions/U.S. Science Support Program, Austin, Texas.

Hallet, B., Hunter, L., and Bogen, J. (1996). Rates of erosion and sediment evacuation by glaciers: A review of field data and their implications. *Global and Planetary Change* **12,** 213-235.

Jaeger, J. M., Nittrouer, C. A., Scott, N. D., and Milliman, J. D. (1998). Sediment accumulation along a glacially impacted mountainous coastline: north-east Gulf of Alaska. *Basin Research* **10,** pp. 155-173.

Kiefer, T., Lorenz, S., Schulz, M., Lohmann, G., Sarnthein, M., and Elderfield, H. (2002). Response of precipitation over Greenland and the adjacent ocean to North Pacific warm spells during Dansgaard-Oeschger stadials. *Terra Nova* **14,** 295-300.

Kulm, L. D., von Huene, R., Duncan, J. R., Ingle, J. C., Kling, S. A., Piper, D. J. W., Pratt, R. M., Scharder, H.-J., Wise, S. W., and Musich, L. F. (1973). Introduction. *In* "Initial reports of the Deep Sea Drilling Project, Leg 18." (L. F. Musich, and O. E. Weser, Eds.), pp. 5-8. US Government Printing Office, Washington D.C.

Latif, M., and Barnett, T. P. (1994). Causes of Decadal Climate Variability over the North Pacific and North-America. *Science* **266,** 634-637.

Lohmann, G. (2008). Linking data and models. *PAGES News* **16,** 4-5.

Mann, D. H., and Peteet, D. M. (1994). Extent and Timing of the Last Glacial Maximum in Southwestern Alaska. *Quaternary Research* **42,** 136-148.

Moore, G. W. K., Holdsworth, G., and Alverson, K. (2002). Climate change in the North Pacific region over the past three centuries. *Nature* **420,** 401-403.

Mueter, F. J., and Norcross, B. L. (2002). Spatial and temporal patterns in the demersal fish community on the shelf and upper slope regions of the Gulf of Alaska. *Fishery Bulletin* **100**, 559-581.

Peteet, D. M. (1991). Postglacial migration history of lodgepole pine near Yakutat, Alaska. *Canadian Journal of Botany-Revue Canadienne De Botanique* **69**, 786-796.

Peteet, D. M., Del Genio, A., and Lo, K. K. W. (1997). Sensitivity of northern hemisphere air temperatures and snow expansion to North Pacific sea surface temperatures in the Goddard Institute for Space Studies general circulation model. *Journal of Geophysical Research-Atmospheres* **102**, 23781-23791.

Peteet, D. M., and Mann, D. H. (1994). Late-glacial vegetational, tephra, and climatic history of southwestern Kodiak Island, Alaska. *Ecoscience* **1**, 255-267.

Randall, D. A., Wood, R. A., Bony, S., Colman, R., Fichefet, T., Fyfe, J., Kattsov, V., Pitman, A., Shukla, J., Srinivasan, J., Stouffer, R. J., Sumi, A., and Taylor, K. E. (2007). Climate models and their evaluation. *In* "Climate Change 2007: The physical science basis. Contribution of Working Group 1 to the Fourth Assessment Report of the Intergovernmental Panel on Climate Change." (S. Solomon, D. Qin, M. Manning, Z. Chen, M. Marquis, K. B. Averyt, M. Tignor, and H. L. Miller, Eds.), pp. 589-662. Cambridge University Press, Cambridge, United Kingdom and New York, NY, USA.

Rea, D. K., Basov, I. A., and Krissek, L. A. (1995). Scientific results of drilling the North Pacific Transect. *In* "Proceedings of the Ocean Drilling Program, Scientific Results, Vol. 145." (D. K. Rea, I. A. Basov, D. W. Scholl, and J. F. Allan, Eds.), pp. 577-596.

Rupper, S., Steig, E. J., and Roe, G. (2004). The relationship between snow accumulation at Mt. Logan, Yukon, Canada, and climate variability in the North Pacific. *Journal of Climate* **17**, 4724-4739.

Trenberth, K. E., and Hurrell, J. W. (1994). Decadal atmosphere-ocean variations in the Pacific. *Climate Dynamics* **9**, 303-319.

Walinsky, S. E., Prahl, F. G., Mix, A. C., Finney, B. P., Jaeger, J. M., and Rosen, G. P. (2009). Distribution and composition of organic matter in surface sediments of coastal southeast Alaska. *Continental Shelf Research*.

Chapter 2 Marine tephrochronology of the Mt. Edgecumbe Volcanic Field, Southeast Alaska, USA[1]

2.1 Abstract

The Mt. Edgecumbe Volcanic Field (MEVF), located on Kruzof Island near Sitka Sound in southeast Alaska, experienced a large multiple-stage eruption during the Last Glacial Maximum (LGM) – Holocene transition that generated a regionally extensive series of compositionally similar rhyolite tephra horizons, and a single well-dated dacite (MEd) tephra. Marine sediment cores collected from adjacent basins to the MEVF contain both tephra-fall and pyroclastic flow deposits that consist primarily of rhyolitic tephra and a minor dacitic tephra unit. The recovered dacite tephra correlates with the MEd tephra, whereas many of the rhyolitic tephras correlate with published MEVF rhyolites. Correlations were based on age constraints and major oxide compositions of glass shards. In addition to LGM-Holocene macroscopic tephra units, four marine cryptotephras were also identified. Three of these units appear to be derived from mid-Holocene MEVF activity, while the youngest cryptotephra corresponds well with the White River Ash eruption at ~1147 cal yr BP. Furthermore, the sedimentology of the Sitka Sound marine core EW0408-40JC, as well as high-resolution SWATH bathymetry, both suggest that extensive pyroclastic flow deposits associated with the activity that generated the MEd tephra underlie Sitka Sound, and that any future MEVF activity may pose significant risk to local population centers.

2.2 Introduction

Tephrochronology has long been recognized as an important tool for establishing regional correlations and constraining chronostratigraphic units in terrestrial areas that have extensive historic and prehistoric volcanism. Recent studies have also begun to utilize tephrochronology to correlate between terrestrial and marine sedimentary records in an effort to develop more complete and comprehensive chronologies of regional geologic change (Stoner et al., 2007; Hillenbrand et al., 2008). Tephra correlations can provide precise tie points between widely separated terrestrial and marine proxy climate records, and can also be used to determine the reservoir age-correction factor for marine radiocarbon samples, thus providing an additional tool to constrain marine sediment core chronologies for calculating age-depth models (Sikes et al., 2000). The recognition of cryptotephra deposits has added further value to tephrochronological studies because of the prevalence of these units in several types of marine and terrestrial sedimentary sequences (Turney et al., 1997; Davies et al., 2005), with cryptotephras typically comprised of fine volcanic glass shards (<100 μm diameter) sparsely preserved and/or invisible within peat, lacustrine, marine, or ice core archives (Lowe, 2008).

This study reports on the marine tephrochronologic record of southeastern Alaska using a suite of sediment piston cores recovered by the *R/V Maurice Ewing* in 2004. Tephra samples were geochemically analyzed to chronologically constrain these sediment cores, as well as develop marine-terrestrial correlations for these fallout deposits. This paper is the first study of coastal marine-terrestrial tephra correlations in the Subarctic Northeast Pacific Ocean.

2.2.1 Geologic Setting

Quaternary volcanism in southeast Alaska is dominated by the regionally-extensive volcaniclastic deposits of the Mt. Edgecumbe Volcanic Field (MEVF), located on the southern end of Kruzof Island near Sitka Sound (Fig. 2.1; Grewingk, 1850). The MEVF is composed of two eruptive centers arranged along a northeast-southwest axis, and has had intermittent activity since 611 ± 74 ka (Riehle et al., 1989) with its most

recent eruption between 4260 – 4820 calibrated years before present (cal yr BP; Riehle and Brew, 1984). Bathymetric surveys of the adjacent Kruzof Island shelf have also revealed an additional extensive submarine volcanic field that was exposed during the sea level lowstand associated with the Last Glacial Maximum (LGM) and perhaps other glacial stadia (Greene et al., 2007).

Volcaniclastic deposits from the MEVF range in composition from basalt to rhyolite (Fig. 2.2) and reflect a stratified magma chamber source (Riehle et al., 1992a). Early eruptive products were dominated by basalt, basaltic andesite, and andesite; activity then transitioned to more silicic material that resulted in several extensive Latest Pleistocene and early Holocene tephra-fall deposits (Riehle et al., 1992b; Beget and Motyka, 1998). Of these silicic deposits, a single dacite unit MEd has been correlated regionally and well-dated to between 13,050 – 13,250 cal yrs BP (Beget and Motyka, 1998).

The southeast Alaska margin has also experienced limited volcanism unrelated to the MEVF. Several small vents have generated small effusive basalt flows, but no major intermediate or silicic eruptive units unrelated to activity at MEVF have been observed (Eberlein and Churkin, 1970). A recent survey of terrestrial peat bogs near the Juneau area found several cryptotephra deposits (Payne and Blackford, 2004; Payne et al., 2008), though surprisingly none of these tephras share a geochemical affinity with published data on MEVF deposits. Payne et al. (2008) recognized a consistent 'Lena tephra' common amongst the five peat cores they analyzed. Although this Lena tephra was geochemically correlative with the White River Ash (WRA) deposit (Downes, 1985; Beget et al., 1992; Richter et al., 1995), two accelerator mass spectrometry (AMS) radiocarbon dates underlying the deposit in one peat core gave an age range of 280 – 460 cal yr BP (equivalent to AD 1670 – 1490), making the Lena tephra five hundred years younger than the extensive and well-documented WRA. In addition, Payne et al. (2008) also discovered evidence of (i) a single tephra layer at 1260 – 1375 cal yr BP, identical to the WRA as dated by Clague et al. (1995); (ii) a previously-unidentified Aniakchak

eruption that occurred between 5030 – 5300 cal yr BP; and (iii) a second WRA-like tephra at ~6330 cal yr BP.

2.3   Methods

The R/V *Maurice Ewing* collected a suite of short multicores, trigger cores, and jumbo piston cores (10-cm diameter and up to 18 m length) along the continental shelf of southeast and south-central Alaska in 2004. A suite of geophysical measurements was performed on each core using a ship-borne GEOTEK Multi-Sensor Core Logger, including continuous one-centimeter-resolution measurements of both gamma-ray wet bulk density and volume magnetic susceptibility. Following geophysical analysis, each core was subsequently split, the sedimentary lithologies were described, and high-resolution linescan images were recorded.

Nine tephras were visually identified in core EW0408-40JC (Fig. 2.3A), as well as an additional macroscopic tephra in EW0408-25MC3. While tephras tend to have both higher density and magnetic susceptibility values relative to biogenic-rich sediments (Beget et al., 1994; Haberle and Lumley, 1998; Lowe, 2008), several of the EW0408-40JC tephras do not exhibit such geophysical properties, possibly as a result of either low iron concentrations or inaccuracies due to the bulk whole-core measurements. Nevertheless, the volcanic nature of these identified units was confirmed by optical smear slide analysis and subsequent geochemical analysis as described below. Combined volume magnetic susceptibility measurements and smear slide analysis also revealed the presence of two additional cryptotephras in EW0408-33JC, and one cryptotephra each in cores EW0408-22JC and -47JC (Fig 3B).

Approximately 20 cm^3 of material was collected from each tephra sample. The four cryptotephra samples were concentrated using the sodium polytungstate density separation technique outlined by Blockley et al. (2005), with minor modifications including the use of a weaker 5% HCl acid wash and targeted sieving for tephra-rich size fractions in bulk sediment splits. Samples were dried at 50°C for several days to drive off moisture, and thin sections were prepared for each sample. Tephra grains were set in a matrix of Petro-Poxy© and the surface was polished to a smoothness of <1 μm.

Following the application of a 300-Å-thick carbon coating, samples were analyzed for major elemental compositions using grain-specific electron probe microanalysis (EPMA) on a Cameca SX-50 microprobe with four wavelength-dispersive spectrometers at the University of Alaska Advanced Instrumentation Laboratory. Beam conditions were set to an accelerating voltage of 15 keV at 10 nA current with a beam diameter of 10 μm. A minimum of forty glass grains per sample were analyzed to minimize intra-sample variations. Replicate samples of the well-characterized Old Crow tephra (Beget and Keskinen, 2003) were also analyzed to monitor inter-run accuracy and instrument drift during EPMA analysis. Inaccurate grain analyses were removed from each sample dataset based on the following qualifiers: (i) obvious non-tephra geochemistry (e.g. feldspar, quartz, olivine, etc.); (ii) calculated H_2O content >10 wt% (Pollard et al., 2006; Pearce et al., 2008); (iii) any elemental concentration below EPMA detection limits; and (iv) single outliers in discernible grain populations. While discarding single grains may inadvertently remove subpopulations from the larger sample dataset, these single grains may represent magma heterogeneities (Downes, 1985; Riehle et al., 2008; Shane et al., 2008), volatilization of mobile elements during EPMA analysis (Goldstein et al., 2003), or alternatively potential contamination by reworked tephra from earlier eruptive activity. Given that tephra glass is an ubiquitous background component of Gulf of Alaska sediment (Shipboard Science Party, 1993) and the large number of explosive eruption events along the Alaskan coastline throughout the Quaternary Period (e.g. Miller and Smith, 1987; Riehle et al., 1999; Fierstein, 2007), this conservative approach seems appropriate to distinguish primary tephra-fall events from post-eruptive sedimentary mixing.

Tephra-derived glass samples were classified according to the International Union of Geological Sciences total alkali-silica classifications of Le Bas et al. (1986) after normalizing analytical totals to 100 wt% on a volatile-free basis. Correlations to published MEVF tephra glass deposits were made using the datasets of Riehle and Brew (1984), Riehle et al. (1992a), Riehle et al. (1992b), Begét and Motyka (1998), and unpublished datasets provided by J. Riehle and J. Westgate. Correlation coefficients

between samples were calculated using the standard-deviation-weighted multivariate SIMAN analysis of (Borchardt et al., 1972; Borchardt, 1974). This statistical approach derives a similarity coefficient d between tephra sets A and B such that

$$d_{(A,B)} = \frac{\sum_{i=1}^{n} R_i g_i}{\sum_{i=1}^{n} g_i} \qquad \text{[Eqn 1.1]}$$

where R is the ratio between a mean oxide concentration ($\overline{X}$) from A and B where

$$R_i = \frac{\overline{X}_{iA}}{\overline{X}_{iB}} \text{ if } \overline{X}_{iB} > \overline{X}_{iA} \quad \text{or} \quad R_i = \frac{\overline{X}_{iB}}{\overline{X}_{iA}} \text{ if } \overline{X}_{iA} > \overline{X}_{iB} \qquad \text{[Eqn 1.2]}$$

Eqn 1.1 also includes a weighting term g that is derived from the relationship between the standard deviation (σ) and mean of an oxide analysis by means of the relative analytical deviation function RD

$$g_i = 1 - \frac{RD_i}{ERLEV} \qquad \text{[Eqn 1.3]}$$

$$RD_i = \sqrt{\left(\frac{\sigma_{iA}}{\overline{X}_{iA}}\right)^2 + \left(\frac{\sigma_{iB}}{\overline{X}_{iB}}\right)^2} \qquad \text{[Eqn 1.4]}$$

The ERLEV function is the relative analytical deviation corresponding to the instrumental detection limits, and is assigned a value between 0 and 1 by the investigator. It has the practical effect of minimizing the weighting of a particular oxide that may have a large uncertainty associated with its measurement as determined by the standard deviation from the mean. This weighted SIMAN approach differs from its traditional application in tephra similarity analyses (e.g. Beget et al., 1992; Payne et al., 2008). In this paper, ERLEV was intentionally minimized on a sample-by-sample basis such that the oxides with the largest standard deviations were excluded from the similarity calculations. For a mean ERLEV value of 0.85, this approach usually removed TiO_2, and occasionally Cl, from the similarity calculations. The accuracy of the SIMAN analysis was verified using oxide bivariate and ternary plots.

2.3.1   Geochronology

A core chronology was developed for EW0408-40JC using AMS radiocarbon dates on five marine bivalves (Table 2.1; Fig. 2.4). Calibrations to calendar years BP were calculated according to the INTCAL04 curve (Reimer et al., 2004), using the CALIB 5.01 software of Stuiver and Reimer (1993), assuming a carbon reservoir effect of 732 years, based on the mean ^{14}C date discrepancy between paired marine bivalve and terrestrial wood samples from three different EW0408 coastal marine sediment cores. A linear interpolated depth/age model (r^2 = 0.98) was then used to convert depths in EW0408-40JC into ages.

The EW0408-22JC cryptotephra at 1.63 meters below seafloor (mbsf) is constrained by two AMS-radiocarbon-dated wood fragments, while an additional AMS sample at 0.98 mbsf was rejected due to an apparent age reversal (Table 2.1). The stratigraphic order and lack of overlap between the uncalibrated ^{14}C dates of the two accepted AMS samples argue against deposition of reworked organic material. The 2σ INTCAL04 calibration ranges of the two AMS samples overlap, indicating a period of rapid sediment accumulation during this interval. Applying a linear interpolation between these two samples and assuming steady-state sediment accumulation gives an age for the EW0408-22JC cryptotephra of ~1200 cal yr BP. An ^{137}Cs- and excess ^{210}Pb-supported chronology developed for the corresponding gravity core EW0408-21GC yields a maximum apparent sedimentation rate of between 3 and 4 mm/yr (Jaeger, J.M. and Rosen, G.P., personal communication, 2007), in broad agreement with the interpolated calibrated ^{14}C age. Given the limited geochronological constraints in this interpolation, the age of deposition of the cryptotephra should be considered a first-order approximation.

Four AMS ^{14}C dated wood fossils constrain the two cryptotephas within core EW0408-33JC (Table 2.1). These four samples are part of a larger AMS dataset that chronologically constrains the full length of EW0408-33JC (Fig. 2.4); the full description of these data is beyond the scope of this current work. The full model yields a linear

interpolated age for the upper tephra at 12.78 mbsf of ~5300 cal yr BP, whereas the lower cryptotephra at 16.18 mbsf is calculated to be ~6750 cal yr BP.

The cryptotephra deposit at 6.46 mbsf recovered in core EW0408-47JC lies above three AMS ^{14}C samples of terrestrial wood fragments (Fig. 2.4). The closest radiocarbon date to the tephra is between 7501 – 7608 cal yr BP at 7.28 mbsf (Table 2.1). A linear depth-age model constructed using this AMS sample and the two lower samples deeper in core EW0408-47JC give an extrapolated age for the tephra of ~7300 cal yr BP.

Because of the prevalence of bioturbation along the Gulf of Alaska continental slope, the visible macroscopic tephra in core EW0408-25MC3 at 0.21 mbsf remains undated at this time. It lies below the 11-cm-thick surface mixed layer, as evidenced by the maximum depth of excess ^{210}Pb, so it is a minimum of 100 years old (Rosen et al., 2005; Walinsky et al., 2009). Rosen et al. hypothesize the relatively high levels of bioturbation in this core are a consequence of a reduced continental shelf accumulation rate due to sediment entrapment by adjacent nearshore embayments.

2.4   Results

Fourteen tephras were geochemically analyzed by EPMA (Table 2.2). Two coherent subpopulations were also found in samples 9.08 mbsf and 6.46 mbsf in cores EW0408-40JC and -47JC, respectively. These subpopulations were identified on the basis of (i) distinctive differences in geochemistry from the primary population and (ii) several glass particles shared this same composition. For the purposes of discussion in this text, the primary populations are indicated by the (I) designation, while the secondary populations are marked by a (II) label. According to the Le Bas et al. (1986) classification, all samples are rhyolitic except for the dacitic secondary population in the EW0408-47JC sample at 6.46 mbsf (Fig. 2.5A). All geochemical analyses are included in the online data repository.

The multivariate SIMAN similarity analysis indicates four distinct rhyolitic groupings of these data (Table 2.3). With the exception of samples EW0408-40JC at 9.08 mbsf (II) and EW0408-22JC at 1.63 mbsf designated as Units C and D, respectively, all studied tephras fall into two general categories. Unit A tephras generally contain

lower concentrations of SiO_2 and total alkali, and higher Fe_2O_3 contents, than Unit B tephras. Both total-alkali-silica (TAS) and $CaO-K_2O$ variation plots agree with these generalized geochemical classifications (Fig. 2.5).

2.5 Discussion

2.5.1 Correlations: MEVF suite

The chronological and geochemical characteristics of the marine tephras described here are similar to those of several terrestrial tephras known to be part of the MEVF eruptive sequence. Applying the same SIMAN similarity analysis to previous MEVF tephra analyses yielded strong correlations (>0.95) between the Unit A tephras and several high-Si rhyolitic tephras described by Riehle et al. (1992a, b), and with an unpublished high-Si rhyolite tephra described by Westgate (Table 2.4). The Unit B tephras also bear some resemblance to the Riehle high-Si rhyolite (Table 2.4); however, the compositions appear to be distinctly different in several oxides (Fig. 2.6), suggesting that Unit B may be unique to this study. It is important to note that, despite the geochemical differences between Units A and B, the presence of both units in fine- and coarse-grained lithologies in core EW0408-40JC suggests the same volcanic source (e.g. the MEVF).

Unit C is composed solely of a secondary population (n=7) identified in a tephra sample in core EW0408-40JC at 9.08 mbsf (II) (Tables 1 and 2). The SIMAN analysis of Unit C indicates strong affinities to several potential deposits (Table 2.4). However, it is the only EW0408 tephra recovered that has a relatively high similarity coefficient (>0.93) with the MEd dacite tephra of Beget and Motyka (1998). A $CaO-K_2O$ variation plot (Fig. 2.6) shows considerable compositional overlap between EW0408 Unit C, the MEd dacite, and the low-Si rhyolite of Riehle et al. (1992a, b). The MEd tephra is constrained by five radiocarbon dates that, when calibrated according to the method described above, places the time of deposition of the MEd deposit between 13,050 – 13,250 cal yrs BP (Beget and Motyka, 1998), suggesting that Unit C is broadly equivalent in age to the MEd tephra. The late Pleistocene MEVF eruptions produced both tephra-fall and pyroclastic flow

deposits with very diverse geochemical characteristics (Fig. 2.2; Riehle et al., 1989; Riehle et al., 1992a, b), consistent with the somewhat heterogeneous nature of sample 9.08 mbsf (II) (Fig. 2.6).

Terrestrial-marine relationships with the MEVF suite

The stratigraphy of the tephra sequence in marine core EW0408-40JC resembles that of a lacustrine core (Fig. 2.7) recovered from an unnamed lake on Baranof Island 29 km NNE of the MEVF (Fig. 2.1) by Riehle et al. (1992b). The lake core (herein referred to as the Riehle lake core) contains >0.7 m of volcanic material within lacustrine silts, which in turn overlie a glacial till. The volcaniclastic deposits (listed in order of increasing core depth) consist of a rhyolitic tephra, a dacitic tephra, a second rhyolitic tephra, an andesitic tephra, a mixed rhyolitic/andesitic tephra, and a basal basaltic-andesitic tephra (Fig. 2.7). The thickness of the volcanic units in the Riehle lake core are comparable to the total thickness of volcanic material contained within EW0408-40JC after correcting for the presence of autochthonous diatom-rich muds.

The uppermost rhyolite and dacite tephra units in the Riehle lake core are likely correlative with the primary and secondary populations of rhyolitic tephra found in the 9.08 mbsf sample from EW0408-40JC (Fig. 2.7). The 9.08 mbsf samples are associated with a coarse sand that underlies a massive lithogenic mud; this fining-upwards sequence suggests deposition by a fallout event into the marine environment, interrupting the deposition of *in-situ* diatomaceous organic matter. The lack of autochthonous organic matter in the Riehle lake core underlying the dacite may reflect (i) an erosional unconformity or hiatus between the dacite and upper rhyolite or (ii) much lower sedimentation rates, relative to the extremely high rates evident in EW0408-40JC.

The lower rhyolitic tephra in the Riehle lake core is composed of lapilli-size clasts (Riehle et al., 1992b), and is correlative with the upper poorly-sorted lithogenic mud and gravel in EW0408-40JC (Fig. 2.7). EPMA analysis of volcanic glass from EW0408-40JC tephra samples 9.80 and 10.00 mbsf confirms a rhyolitic composition for this unit.

The andesitic tephra in the Riehle lake core does not appear in the EW0408-40JC core (Fig. 2.7). Given that the two cores are equidistant from the MEVF (Fig. 2.1), this

absence suggests that the andesite deposition may have been more heavily influenced by wind direction or other processes that resulted in non-deposition.

The andesitic tephra is underlain by a mixed rhyolite/andesite unit in the Riehle lake core (Fig. 2.7). Although a definitive andesite population was not recognized within any of the EW0408-40JC tephra deposits, the post-EPMA data treatment of the rhyolite sample at 10.29 mbsf eliminated several glass shards. These shards represented a widely heterogeneous grouping that did not warrant classification as a separate population due to the calculated means and standard deviations for these shards (ex. SiO_2 = 65.23 ± 4.07 wt%; n=4). Nevertheless, the low SiO_2 content suggests a possible andesitic deposit within the EW0408-40JC core; further analysis is required to confirm this possibility.

The lowermost volcaniclastic unit in the Riehle lake core, a basaltic andesite, does not occur in EW0408-40JC, nor do the basal rhyolitic volcaniclastic units from EW0408-40JC appear in the Riehle lake core (Fig. 2.7). The divergence in sedimentology between the two cores most likely represents differences in topography related to the two coring locations. Given that Lower Sitka Sound is directly downslope from the MEVF, while a topographic high separates the Riehle lake core site from the MEVF, it follows that only fallout volcanic deposits should accumulate at the Riehle lake core location whereas both fallout and gravity-driven deposition will accumulate at the EW0408-40JC site. Thus, it seems likely that EW0408-40JC did not penetrate deep enough into the seafloor to recover the basaltic andesite observed in the Riehle lake core.

2.5.2   Correlations: EW0408 tephras and non-MEVF contemporaneous deposits

EW0408-22JC

The estimated age of the cryptotephra at 1.63 mbsf in core EW0408-22JC places this event at ~1200 cal yr BP. The deposition of this tephra is thus contemporaneous with the regionally-extensive White River Ash deposited at ~1147 cal yr BP (Downes, 1985; Richter et al., 1995). Recent work by Robinson (2001) extends the eastern lobe of this Plinian eruption from its source near Mt. Churchill in east-central Alaska to the Great Slave Lake in Canada, with an estimated eruptive volume of approximately 47 km^3

(Lerbekmo, 2008). Furthermore, electrical conductivity spikes tied to an accumulation age model in the Prospector Ridge Col ice core from Mt. Logan are attributed to deposition of volcanic sulfate from the White River Ash eruption (Fisher et al., 2004). However, some doubt has been cast upon Mt. Churchill as the source of the White River Ash because of the lack of an appropriately-aged deposit within an ice core collected from the col between Mts. Churchill and Bona (Mashiotta et al., 2004).

Payne et al. (2008) recovered a cryptotephra sample (LNA 100) from a peat bog near Juneau, Alaska, that is convincingly derived from the White River Ash. Payne et al. showed that their LNA 100 sample has a high geochemical similarity coefficient (>0.93), agreeing closely with previous published analyses of the White River Ash. The LNA 100 cryptotephra is also directly underlain by two fragments of *Sphagnum* moss that were AMS radiocarbon dated to 1260 – 1360 and 1290 – 1375 cal yr BP, respectively.

Applying the SIMAN similarity analysis to the published geochemistry of the White River Ash and the cryptotephra in EW0408-22JC shows that the two deposits have a similarity coefficient of 0.90 for published distal deposits and 0.89 for ash deposits recovered from the summit of Mt. Churchill proper (Table 2.5). However, the SIMAN analyses of both EW0408-22JC and LNA 100 of Payne et al. (2008) show a strong relationship with a similarity coefficient of 0.93. The oxide compositions of the EW0408-22JC cryptotephra and LNA 100 show a high degree of overlap (Fig. 2.8A). The relatively low degree of similarity calculated by the SIMAN analysis for the EW0408-22JC sample and the Mt. Churchill samples may reflect differences associated with statistical analysis (e.g. normalizations, Fe calculated as FeO or Fe_2O_3, etc.). Nevertheless, the available dates and geochemical analyses of the EW0408-22JC cryptotephra agree very well with those of the LNA 100 sample of Payne et al. (2008). Furthermore, a SIMAN analysis conducted between the EW0408-22JC deposit and distal White River Ash deposits collected from eastern central Alaska (Beget et al., 1992) have a calculated similarity coefficient of 0.94, clearly indicating the presence of the White River Ash within EW0408-22JC.

EW0408-33JC at 12.78 mbsf

The SIMAN analyses of the full EW0408 tephra dataset presented in this paper classified the two cryptotephras from EW0408-33JC at 12.78 and 16.18 mbsf, and the sample at 6.46 mbsf (I) in EW0408-47JC, all as Unit A (Table 2.3). As described earlier, Unit A has a very high similarity coefficient with rhyolites from the MEVF (>0.96; Table 2.4). Other mid-Holocene eruptions do not appear to share similarly high values (Table 2.5). Of the tephra deposits examined in this paper, the strongest non-MEVF relationship for all three of the mid-Holocene EW0408 samples is with ECR 162 of Payne et al. (2008), which is chronologically constrained by an underlying *Sphagnum* moss fragment radiocarbon dated by AMS to between 5030 – 5300 cal yr BP. Despite a similar age with an eruption at Black Peak on the Alaska Peninsula (Miller and Smith, 1987), Payne et al. found little geochemical similarity between ECR 162 and the Black Peak tephra (Riehle et al., 1999); likewise, a low similarity coefficient is calculated for the potentially contemporaneous EW0408-33JC cryptotephra at 12.78 mbsf (Table 2.5). Payne et al. instead attributed ECR 162 to a previously unidentified Aniakchak eruption that is significantly older than the large caldera-forming eruption at 3400 cal yr BP (Beget et al., 1992).

The chronology of core EW0408-33JC places the date of deposition of the 12.18 mbsf cryptotephra at ~5300 cal yr BP, which is equivalent to the age associated with ECR 162 of Payne et al. (2008). The geochemical composition of these two cryptotephra units bear some overlap (Fig. 2.8B). However, the 12.18 mbsf tephra in EW0408-33JC appears more closely related to the rhyolitic activity from the MEVF than either ECR 162 or its purported source at Aniakchak on the Alaska Peninsula. Nevertheless, Aniakchak is known to have had at least 40 Holocene eruptions, with at least half of these occurring between 3,500 and 10,000 years ago (Riehle et al., 1999; Neal et al., 2001). It is difficult to disregard Aniakchak as a distal source particularly since it plots in the region of overlap between the EW0408-33JC 12.78 mbsf tephra and ECR 162 in a ternary K_2O-CaO-Fe_2O_3 diagram (Fig. 2.8B). Conversely, the strong geochemical relationship between the MEVF and the -33JC tephra suggest the likelihood of a mid-Holocene

eruption of Mt. Edgecumbe. This observation is supported by independent age dating of bulk peat deposits by Riehle and Brew (1984) that bracket a rhyolitic tephra horizon between 4000-4300 ^{14}C yr BP (4800 – 5300 cal yr BP; Fig. 2.2) recovered on the western slope of Mt. Edgecumbe proper.

EW0408-33JC at 16.18 mbsf and EW0408-47JC at 6.46 mbsf (I)

The cryptotephras in cores EW0408-47JC and EW0408-33JC at 6.46 mbsf (I) and 16.18 mbsf, respectively [referred to as the -47JC and -33JC tephras for brevity in the following section], show several equivalent characteristics. The -33JC tephra is well-constrained chronologically by a wood macrofossil only 18 cm above the tephra that was AMS radiocarbon dated to between 6659 – 6743 cal yr BP (Fig. 2.4). Although the -47JC tephra has no upper bounding date, it is underlain by a wood fragment between 7501 – 7608 cal yr BP that is 82 cm below the tephra. The interpolated dates for both tephras using the age models plotted in Fig. 2.4 place the -33JC tephra at ~6800 cal yr BP, and the -47JC tephra at ~7300 cal yr BP, a difference of only 500 years which may be sufficiently explained by errors in the age models of the two different cores (Telford et al., 2004).

The geochemical characteristics of both the -33JC and -47JC tephras are also comparable. Oxide variation diagrams show both tephra populations overlapping (Fig. 2.8C). The multivariate SIMAN analysis calculated a similarity coefficient of 0.99 (Table 2.3), indicating that the two tephras are virtually identical, and belong to the Unit A designation for the EW0408 tephra suite.

As stated earlier, Unit A is most likely derived from MEVF rhyolitic activity, and potential alternative sources for the -33JC and -47JC tephras appear unlikely (Table 2.5). The Oshetna tephra, dated to 6700 – 7000 cal yr BP, and observed in south-central Alaska (Dixon and Smith, 1990; Child et al., 1998), bears little similarity to either the -33JC or -47JC tephras (Table 2.5; Fig. 2.8C). Surprisingly, the best similarity coefficient for -47JC is observed with ECR 162 of Payne et al. (2008), but the -47JC geochemical data suffer from the same problems as noted above for the 12.18 mbsf tephra in EW0408-33JC, in that while ECR 162 is attributed to an undocumented

Aniakchak eruption (Payne et al., 2008), the geochemical composition of the -47JC tephra correlates better with an MEVF source (Fig. 2.8C).

The potential for an MEVF source for both the -33JC and -47JC tephras is further supported by a dated rhyolitic horizon contained within a single dated peat sample of 6400 – 6700 cal yr BP on the southwest coast of Kruzof Island (Riehle and Brew, 1984). This terrestrial peat date is consistent with the interpolated chronology for the -33JC tephra, but is slightly too young for a chronological correlation to the -47JC tephra. If the interpolated age of -47JC is correct, then the occurrence of two explosive MEVF eruptions of identical composition occurring within 500 years of one another may be a potential alternative explanation.

EW0408-25MC3

The poor age control associated with the EW0408-25MC3 core is problematic for understanding its role in the accumulation of MEVF pyroclastic material. The 35-cm-long core is composed of: (i) an upper 19 cm of olive-green diatomaceous silty clay; (ii) a macroscopic 3-cm-thick sandy rhyolitic tephra (Table 2.2); and (iii) a lower mottled dark-gray silty clay for the remaining 13 cm of the core. In other EW0408 cores from the Gulf of Alaska continental shelf, the upper contact of the dark-gray silty clay unit occurs approximately 12,000 cal yr BP, with the silty clay unit likely reflecting increased glaciomarine sedimentation during deglaciation (Barron et al., 2009). If the overlying diatomaceous clay is a continuous autochthonous record of Holocene biogenic sedimentation, then the EW0408-25MC3 tephra may be contemporaneous with the Latest Pleistocene eruptions of the MEVF. Indeed, the geochemistry of the EW0408-25MC3 tephra supports an MEVF source because of its high similarity to other MEVF-derived EW0408 tephras described here (Table 2.3; Fig. 2.5). Until a comprehensive chronology is developed, the conservative interpretation of the EW0408-25MC3 tephra is that it is derived from MEVF activity that is older than 100 years BP based on interpretation of excess ^{210}Pb data (Rosen et al., 2005; Walinsky et al., 2009).

EW0408-40JC

Whereas the close proximity of the MEVF to the EW0408-40JC core location makes the MEVF seem the likely source of the pyroclastic material contained within - 40JC, other large Late Pleistocene eruptions may have potentially contributed tephra. The Lethe tephra represents one of the most explosive eruptions from the Valley of Ten Thousand Smokes in Katmai National Park, Alaska, and occurred at least 14,300 – 15,200 cal yrs BP (Pinney and Beget, 1991; Fierstein, 2007). Further dating by Reger et al. (2007) on the Kenai Peninsula also constrains several periods of explosive activity to between 16,300 – 19,200 cal yr BP. Lethe tephra deposits have been identified in several locations throughout the Kenai and Alaska Peninsulas with some compositional heterogeneity (Pinney, 1993; Riehle et al., 2008), and because of the possibility of deposition in southeast Alaska, the geochemistry of the 'average' Lethe tephra (Pinney and Beget, 1991) was compared against the EW0408 tephra geochemistries. Of the three EW0408 tephra geochemistries, Unit C is the most similar to the Lethe deposit but only with a similarity coefficient of 0.91 (Table 2.5). This result suggests little similarity between any of the EW0408 tephras and the Lethe tephra. Therefore, it seems most likely the tephras recovered from core EW0408-40JC are all derived from the MEVF and not from distal volcanic activity along the Alaska Peninsula.

2.5.3 Implications and volcanic hazards

The complicated stratigraphy of core EW0408-40JC makes interpretation of these tephra units difficult (Fig. 2.7). With the exception of the sample from 9.08 mbsf, the Unit A samples consistently underlie poorly sorted lithogenic muds and gravels that fine upwards into diatomaceous silty clays. These latter deposits presumably represent the autochthonous biogenic sedimentation regime present in Lower Sitka Sound, whereas the sedimentology of the former deposits suggests emplacement by episodic subaqueous pyroclastic flows (Fisher, 1979). Proximal deposits from turbulent subaerial pyroclastic density currents that enter large water bodies and mix with water may transition into aqueous density currents (Orton, 1996), which are known to include a lowermost massive poorly-sorted unit with a sharp basal contact that fines upwards (Cole and DeCelles,

1991). Both of these characteristics are present in the deposits contained within EW0408-40JC, as well as several fine-grained upper units that may represent the atmospheric fallout of volcanic ash. Recent high-resolution bathymetric mapping of Sitka Sound (Fig. 2.9; National Ocean Service Hydrographic Database) shows a low-angle submarine slope extending from the southeast coastline of Kruzof Island towards the site of EW0408-40JC. Previous mapping by Riehle et al. (1989) indicates subaerial pyroclastic flow deposits adjacent to this submarine slope, suggesting that the low-angle slope may be the submarine expression of the subaerial pyroclastic flow deposits (Fig. 2.9).

The land-sea configuration of Kruzof Island and Sitka Sound prior to deposition of the MEd tephra is complicated by deglacial changes in both eustatic and relative sea level. The LGM lowstand likely exposed a large subaerial region of the shallow margin of Kruzof Island and portions of Sitka Sound. Radiocarbon constraints on the MEd tephra correspond to a eustatic sea level at least 70 m lower than that of today (Fairbanks, 1989). Modern Sitka Sound bathymetric features include an outer sill at approximately 130 m water depth, and the EW0408-40JC core was recovered from an inner basin at 216 m water depth. The presence of freshwater lacustrine diatoms within the laminated siliceous muds (Starratt, S.W., personal communication, 2009) intercalated between the tephra deposits below 9 mbsf in EW0408-40JC (Fig. 2.3A) argues for the closing of Sitka Sound from the open Gulf of Alaska sometime during the LGM/Holocene deglacial transition. The lack of submerged well-defined cut marine terraces within Sitka Sound (Fig. 2.9) imply that the major topographic barrier to the Gulf of Alaska was likely the outer sill, and would thus require some amount of vertical adjustment to isolate Sitka Sound. These constraints suggest the pre-MEd pyroclastic flows from the MEVF crossed the then-exposed margin of Kruzof Island and were deposited within "paleolake" Sitka Sound, which was then subsequently inundated by marine waters. Additional AMS ^{14}C dating and diatom biostratigraphy of EW0408-40JC is underway to better constrain the timing of this inundation.

The tephra stratigraphy of EW0408-40JC is complicated by the consistent presence of the Unit B tephras within, or directly overlying, the poorly-sorted mud and gravel units. If these poorly-sorted units are preserved portions of two different pyroclastic flow deposits, then possibly the Unit A tephras represent the early-stage eruptive products, whereas the Unit B tephras occurred later in the eruption sequence. This explanation is consistent with the MEVF originating from a stratified magma chamber (Riehle et al., 1992a).

Subaqueous emplacement of large subaerial pyroclastic flows represent a significant risk in terms of tsunami generation. Although direct displacement of water by the entrance of a pyroclastic flow into the sea is known to generate tsunami waves (e.g. Beget et al., 2008), experimental evidence has also shown that flows at >250°C that encounter bodies of water are also able to generate tsumani via steam explosions (Freundt, 2003). Regardless of the mechanism, tsunamis generated by pyroclastic flows have caused massive loss of life in many regions, including the AD 1883 Krakatau eruption (Carey et al., 2000; Carey et al., 2001) and the Late Bronze Age eruption of Thera on Santorini (McCoy and Heiken, 2000a, b). The close proximity of the city of Sitka to both Kruzof Island and Sitka Sound, combined with the observation that the MEVF has been active several times throughout the Holocene (Riehle and Brew, 1984; Riehle et al., 1992b; this study), suggests that this active volcanic center poses potential future risk to inhabitants and warrants further evaluation for safety considerations.

2.6   Conclusions

The marine record of volcanic activity preserved along the Gulf of Alaska margin will prove to be an important component of future Holocene and Late Pleistocene stratigraphic correlations between terrestrial and marine environments in this region. Two examples of such correlations were presented in this paper: (i) a Latest Pleistocene MEVF eruption sequence correlation between EW0408-40JC and a nearby lake core from Baranof Island; and (ii) the regionally-extensive ~1147 cal yr BP White River Ash deposit. In the case of the White River Ash, this unit has been mapped previously from the Wrangell Volcanic Field eastward into the Canadian Yukon Territory as far as the

Great Slave Lake. The discovery of White River Ash in core EW0408-22JC makes this the most southerly Pacific Coast location yet described, and implies a much more widespread eruption than previously thought. Corroborating evidence for this southerly dispersal is the presence of White River Ash contained within peat deposits near Juneau, Alaska (Payne et al., 2008).

The MEVF itself has also proven an important source of regional stratigraphic horizons. The MEd dacitic tephra (Engstrom et al., 1990; Beget and Motyka, 1998; Riehle et al., 1992b) already provides a useful regional chronostratigraphic marker, but pyroclastic flow deposits in EW0408-40JC show evidence of at least two major eruptions prior to the deposition of MEd (Fig. 2.9), agreeing with previous terrestrial survey work (Riehle et al., 1992a, b). The identification of three mid-Holocene MEVF cryptotephras in cores EW0408-33JC and -47JC argue for the presence of additional stratigraphic markers in the adjacent terrestrial environment. It is important to note, however, that the limited range of MEVF rhyolitic major-element compositions will not make stratigraphic correlations between sites easy and straightforward, particularly if no chronological information is available.

2.8 References

Barron, J. A., Bukry, D., Dean, W. E., Addison, J. A., and Finney, B. P. (2009). Paleoceanography of the Gulf of Alaska during the past 15,000 years: results from diatoms, silicoflagellates, and geochemistry. *Marine Micropaleontology* **72**, 176-195.

Beget, J., Gardner, C., and Davis, K. (2008). Volcanic tsunamis and prehistoric cultural transitions in Cook Inlet, Alaska. *Journal of Volcanology and Geothermal Research* **176**, 377-386.

Beget, J. E., and Keskinen, M. J. (2003). Trace-element geochemistry of individual glass shards of the Old Crow tephra and the age of the Delta glaciation, central Alaska. *Quaternary Research* **60**, 63-69.

Beget, J. E., Mason, O., and Anderson, P. (1992). Age, extent and climatic significance of the c. 3400 BP Aniakchak tephra, western Alaska, USA. *Holocene* **2**, 51-56.

Beget, J. E., and Motyka, R. J. (1998). New dates on late Pleistocene dacitic tephra from the Mount Edgecumbe volcanic field, southeastern Alaska. *Quaternary Research* **49**, 123-125.

Beget, J. E., Stihler, S. D., and Stone, D. B. (1994). A 500-Year-Long Record of Tephra Falls from Redoubt Volcano and Other Volcanos in Upper Cook Inlet, Alaska. *Journal of Volcanology and Geothermal Research* **62**, 55-67.

Blockley, S. P. E., Pyne-O'Donnell, S. D. F., Lowe, J. J., Matthews, I. P., Stone, A., Pollard, A. M., Turney, C. S. M., and Molyneux, E. G. (2005). A new and less destructive laboratory procedure for the physical separation of distal glass tephra shards from sediments. *Quaternary Science Reviews* **24**, 1952-1960.

Borchardt, G. A. (1974). The SIMAN coefficient for similarity analysis. *Classification Society Bulletin* **3**, 2-8.

Borchardt, G. A., Aruscavage, P. J., and Millard, H. T., Jr. (1972). Correlation of the Bishop Ash, a Pleistocene marker bed, using instrumental neutron activation analysis. *Journal of Sedimentary Petrology* **42**, 301-306.

Carey, S., Morelli, D., Sigurdsson, H., and Bronto, S. (2001). Tsunami deposits from major explosive eruptions: An example from the 1883 eruption of Krakatau. *Geology* **29**, 347-350.

Carey, S., Sigurdsson, H., Mandeville, C. W., and Bronto, S. (2000). Volcanic hazards from pyroclastic flow discharge into the sea: examples from the 1883 eruption of Krakatau, Indonesia. *In* "Volcanic Hazards and Disasters in Human Antiquity." (F. W. McCoy, and G. Heiken, Eds.), pp. 1-14. Geological Society of America, Boulder, CO.

Child, J. K., Beget, J. E., and Werner, A. (1998). Three Holocene tephras identified in lacustrine sediment cores from the Wonder Lake area, Denali National Park and Preserve, Alaska, USA. *Arctic and Alpine Research* **30**, 89-95.

Clague, J. J., Evans, S. G., Rampton, V. N., and Woodsworth, G. J. (1995). Improved age estimates for the White River and Bridge River tephras, western Canada. *Canadian Journal of Earth Sciences* **32**, 1172-1179.

Cole, R. B., and DeCelles, P. G. (1991). Subaerial to submarine transitions in early Miocene pyroclastic flow deposits, southern San Joaquin basin, California. *Geological Society of America Bulletin* **103**, 221-235.

Davies, S. M., Hoek, W. Z., Bohncke, S. J. P., Lowe, J. J., O'Donnell, S. P., and Turney, C. S. M. (2005). Detection of Lateglacial distal tephra layers in the Netherlands. *Boreas* **34**, 123-135.

Dixon, E. J., and Smith, G. S. (1990). A regional application of tephrochronology in Alaska. *In* "Archaeological Geology of North America." (N. P. Lasca, and J. Donahue, Eds.), pp. 383-398. Geological Society of America, Boulder, CO.

Downes, H. (1985). Evidence for magma heterogeneity in the White River Ash (Yukon Territory). *Canadian Journal of Earth Sciences* **22**, 929-934.

Eberlein, G. D., and Churkin, M., Jr. (1970). Tlevak Basalt, west coast of Prince of Wales Island, southeastern Alaska. *In* "Changes in stratigraphic nomenclature by the U.S. Geological Survey, 1968." (G. V. Cohee, R. G. Bates, and W. B. Wright, Eds.), pp. 25-55. Geological Survey Bulletin 1294-A. United States Government Printing Office, Washington D.C.

Engstrom, D. R., Hansen, B. C. S., and Wright, H. E. (1990). A possible Younger Dryas record in southeastern Alaska. *Science* **250**, 1383-1385.

Fairbanks, R. G. (1989). A 17,000-year glacio-eustatic sea-level record - influence of glacial melting rates on the Younger Dryas event and deep-ocean circulation. *Nature* **342**, 637-642.

Fierstein, J. (2007). Explosive eruptive record in the Katmai region, Alaska Peninsula: an overview. *Bulletin of Volcanology* **69**, 469-509.

Fisher, D. A., Wake, C. P., Kreutz, K., Yalcin, K., Steig, E. J., Mayewski, P. A., Anderson, L., Zheng, J., Rupper, S., Zdanowicz, C., Demuth, M., Waszkiewicz, M., Dahl-Jensen, D., Goto-Azuma, K., Bourgeois, J. B., Koerner, R., Sekerka, J., Osterberg, E. C., Abbott, M. B., Finney, B., and Burns, S. J. (2004). Stable isotope records from Mt. Logan, Eclipse ice cores and nearby Jellybean Lake; water cycle of the North Pacific over 2000 years and over five vertical kilometers; sudden shifts and tropical connections. *Geographie Physique et Quaternaire* **58**, 337-352.

Fisher, R. V. (1979). Models for pyroclastic surges and pyroclastic flows. *Journal of Volcanology and Geothermal Research* **6**, 305-318.

Freundt, A. (2003). Entrance of hot pyroclastic flows into the sea: experimental observations. *Bulletin of Volcanology* **65**, 144-164.

Goldstein, J., Newbury, D. E., Joy, D. C., Lyman, C. E., Echlin, P., Lifshin, E., Sawyer, L. C., and Michael, J. R. (2003). "Scanning electron microscopy and X-ray microanalysis." Springer Science + Business Media, Inc., New York.

Greene, H. G., O'Connell, V. M., Wakefield, W. W., and Brylinsky, C. K. (2007). The offshore Edgecumbe lava field, southeast Alaska: geologic and habitat characterization of a commercial fishing ground. *In* "Mapping the Seafloor for Habitat Characterization." (B. J. Todd, and H. G. Greene, Eds.), pp. 277-295. Geological Association of Canada.

Grewingk, C. (1850). "Geology of Alaska and the Northwest Coast of America." The University of Alaska Press, Fairbanks, AK.

Haberle, S. G., and Lumley, S. H. (1998). Age and origin of tephras recorded in postglacial lake sediments to the west of the southern Andes, 44°S to 47°S. *Journal of Volcanology and Geothermal Research* **84**, 239-256.

Hillenbrand, C. D., Moreton, S. G., Caburlotto, A., Pudsey, C. J., Lucchi, R. G., Smellie, J. L., Benetti, S., Grobe, H., Hunt, J. B., and Larter, R. D. (2008). Volcanic time-markers for Marine Isotopic Stages 6 and 5 in Southern Ocean sediments and Antarctic ice cores: implications for tephra correlations between palaeoclimatic records. *Quaternary Science Reviews* **27**, 518-540.

Le Bas, M. J., Lemaitre, R. W., Streckeisen, A., and Zanettin, B. (1986). A chemical classification of volcanic rocks based on the total alkali silica diagram. *Journal of Petrology* **27**, 745-750.

Lerbekmo, J. F. (2008). The White River Ash: largest Holocene Plinian tephra. *Canadian Journal of Earth Sciences* **45**, 693-700.

Lowe, D. J. (2008). Globalization of tephrochronology: new views from Australasia. *Progress in Physical Geography* **32,** 311-336.

Mashiotta, T. A., Thompson, L. G., and Davis, M. E. (2004). The White River Ash: new evidence from the Bona-Churchill ice core record. *Eos Trans. AGU* **85,** Fall Meet. Suppl., Abstract PP21A-1369.

McCoy, F. W., and Heiken, G. (2000a). The Late-Bronze Age explosive eruption of Thera (Santorini), Greece: regional and local effects. *In* "Volcanic Hazards and Disasters in Human Antiquity." (F. W. McCoy, and G. Heiken, Eds.), pp. 43-70. Geological Society of America, Boulder, CO.

McCoy, F. W., and Heiken, G. (2000b). Tsunami generated by the Late Bronze Age eruption of Thera (Santorini), Greece. *Pure and Applied Geophysics* **157,** 1227-1256.

Miller, T. P., and Smith, R. L. (1987). Late Quaternary caldera-forming eruptions in the eastern Aleutian arc, Alaska. *Geology* **15,** 434-438.

Neal, C. A., McGimsey, R. G., Miller, T. P., Riehle, J. R., and Waythomas, C. F. (2001). Preliminary volcano-hazard assessment for Aniakchak Volcano, Alaska. *In* "Open-File Report 00-519." (US Geological Survey, Ed.), pp. 42. Alaska Volcano Observatory, Anchorage, Alaska.

Orton, G. J. (1996). Volcanic environments. *In* "Sedimentary environments: processes, facies, and stratigraphy." (H. G. Reading, Ed.), pp. 485-567. Blackwell Science, Oxford.

Payne, R., and Blackford, J. (2004). Distal tephra deposits in southeast Alaskan peatlands. *In* "Yukon Exploration and Geology 2003." (D. Emond, and L. Lewis, Eds.), pp. 191-197. Yukon Geological Survey, Whitehorse, Canada.

Payne, R., Blackford, J., and van der Plicht, J. (2008). Using cryptotephras to extend regional tephrochronologies: An example from southeast Alaska and implications for hazard assessment. *Quaternary Research* **69,** 42-55.

Pearce, N. J. G., Bendall, C. A., and Westgate, J. A. (2008). Comment on "Some numerical considerations in the geochemical analysis of distal microtephra" by A.M. Pollard, S.P.E. Blockley and C.S. Lane. *Applied Geochemistry* **23,** 1353-1364.

Pinney, D. S. (1993). "Late Quaternary glacial and volcanic stratigraphy near Windy Creek, Katmai National Park, Alaska." Unpublished M.S. thesis, University of Alaska Fairbanks.

Pinney, D. S., and Beget, J. E. (1991). Late Pleistocene volcanic deposits near the Valley of Ten Thousand Smokes, Katmai National Park, Alaska. *In* "Short Notes on Alaskan Geology 1991." (R. D. Reger, Ed.), pp. 45-54. State of Alaska, Division of Geological and Geophysical Surveys.

Pollard, A. M., Blockley, S. P. E., and Lane, C. S. (2006). Some numerical considerations in the geochemical analysis of distal microtephra. *Applied Geochemistry* **21**, 1692-1714.

Reger, R. D., Sturmann, A. G., Berg, E. E., and Burns, P. A. C. (2007). A guide to the Late Quaternary history of northern and western Kenai Peninsula, Alaska, pp. 120. State of Alaska Dept. of Natural Resources, Division of Geological and Geophysical Surveys, Fairbanks, Alaska.

Reimer, P. J., Baillie, M. G. L., Bard, E., Bayliss, A., Beck, J. W., Bertrand, C. J. H., Blackwell, P. G., Buck, C. E., Burr, G. S., Cutler, K. B., Damon, P. E., Edwards, R. L., Fairbanks, R. G., Friedrich, M., Guilderson, T. P., Hogg, A. G., Hughen, K. A., Kromer, B., McCormac, G., Manning, S., Ramsey, C. B., Reimer, R. W., Remmele, S., Southon, J. R., Stuiver, M., Talamo, S., Taylor, F. W., van der Plicht, J., and Weyhenmeyer, C. E. (2004). IntCal04 terrestrial radiocarbon age calibration, 0-26 cal kyr BP. *Radiocarbon* **46**, 1029-1058.

Richter, D. H., Preece, S. J., McGimsey, R. G., and Westgate, J. A. (1995). Mount Churchill, Alaska: Source of the late Holocene White River Ash. *Canadian Journal of Earth Sciences* **32**, 741-748.

Riehle, J. R., Ager, T. A., Reger, R. D., Pinney, D. S., and Kaufman, D. S. (2008). Stratigraphic and compositional complexities of the late Quaternary Lethe tephra in South-central Alaska. *Quaternary International* **178**, 210-228.

Riehle, J. R., and Brew, D. A. (1984). Explosive latest Pleistocene(?) and Holocene activity of the Mount Edgecumbe volcanic field, Alaska. *In* "The United States Geological Survey in Alaska: accomplishments during 1982." (K. M. Reed, and S. Bartsch-Winkler, Eds.), pp. 111-115.

Riehle, J. R., Brew, D. A., and Lanphere, M. A. (1989). Geologic map of the Mount Edgecumbe volcanic field, Kruzof Island, southeastern Alaska. *In* "Miscellaneous Investigations Series Map I 1983." U.S. Geological Survey.

Riehle, J. R., Champion, D. E., Brew, D. A., and Lanphere, M. A. (1992a). Pyroclastic deposits of the Mount Edgecumbe volcanic field, southeast Alaska: eruptions of a stratified magma chamber. *Journal of Volcanology and Geothermal Research* **53**, 117-143.

Riehle, J. R., Mann, D. H., Peteet, D. M., Engstrom, D. R., Brew, D. A., and Meyer, C. E. (1992b). The Mount Edgecumbe tephra deposits, a marker horizon in southeastern Alaska near the Pleistocene Holocene boundary. *Quaternary Research* **37**, 183-202.

Riehle, J. R., Meyer, C. E., and Miyaoka, R. T. (1999). Data on Holocene tephra (volcanic ash) deposits in the Alaska Peninsula and lower Cook Inlet region of the Aleutian volcanic arc, Alaska. USGS Open-File Report 99-135.

Robinson, S. D. (2001). Extending the late Holocene White River ash distribution, northwestern Canada. *Arctic* **54**, 157-161.

Rosen, G. P., Jaeger, J. M., Stoner, J. S., and Channell, J. E. T. (2005). Establishing the temporal resolution of high-latitude paleoclimatic and paleomagnetic signals in bioturbated Gulf of Alaska continental margin sediments. *Eos Trans. AGU* **86**, abstract H51G-0446.

Shane, P., Nairn, I. A., Martin, S. B., and Smith, V. C. (2008). Compositional heterogeneity in tephra deposits resulting from the eruption of multiple magma bodies: Implications for tephrochronology. *Quaternary International* **178**, 44-53.

Shipboard Science Party. (1993). Site 887. *In* "Proceedings of the Ocean Drilling Program, Initial Reports." (D. K. Rea, I. A. Basov, T. R. Janecek, A. Palmer-Julson, and e. al., Eds.), pp. 335-391. Ocean Drilling Program, College Station, TX.

Sikes, E. L., Samson, C. R., Guilderson, T. P., and Howard, W. R. (2000). Old radiocarbon ages in the southwest Pacific Ocean during the last glacial period and deglaciation. *Nature* **405**, 555-559.

Stoner, J. S., Jennings, A., Kristjansdottir, G. B., Dunhill, G., Andrews, J. T., and Hardardottir, J. (2007). A paleomagnetic approach toward refining Holocene radiocarbon-based chronologies: Paleoceanographic records from the north Iceland (MD99-2269) and east Greenland (MD99-2322) margins. *Paleoceanography* **22**, doi:10.1029/2006PA001285.

Stuiver, M., and Reimer, P. J. (1993). Extended ^{14}C data base and revised CALIB 3.0 radiocarbon age calibration program. *Radiocarbon* **35**, 137-189.

Telford, R. J., Heegaard, E., and Birks, H. J. B. (2004). All age-depth models are wrong: but how badly? *Quaternary Science Reviews* **23**, 1-5.

Turney, C. S. M., Harkness, D. D., and Lowe, J. J. (1997). The use of microtephra horizons to correlate Late-glacial lake sediment successions in Scotland. *Journal of Quaternary Science* **12**, 525-531.

Walinsky, S. E., Prahl, F. G., Mix, A. C., Finney, B. P., Jaeger, J. M., and Rosen, G. P. (2009). Distribution and composition of organic matter in surface sediments of coastal southeast Alaska. *Continental Shelf Research* **29,** 1565-1579.

Table 2.1: AMS ^{14}C dates constraining EW0408 tephras.

Core depth (mbsf)	Material	Reported ^{14}C age (yrs BP)	Corrected ^{14}C age (yrs BP)[a]	2σ calibrated range (yrs BP)	AMS ^{14}C Laboratory[b]	Sample ID
EW0408-22JC						
0.82	terrestrial organics	1240 ± 20		1083 - 1263	Keck - UCI	65503
0.98	terrestrial organics*	1505 ± 20		1336 - 1480	Keck - UCI	50810
2.17	wood fragment	1335 ± 20		1185 - 1300	Keck - UCI	50811
EW0408-33JC						
10.99	terrestrial organics	3980 ± 20		4416 - 4517	Keck - UCI	50818
13.94	wood fragment	4985 ± 30		5619 - 5878	CAMS - LLNL	127768
16.00	terrestrial organics	5880 ± 20		6659 - 6743	Keck - UCI	50819
17.03	wood fragment	6485 ± 20		7327 - 7434	Keck - UCI	50820
EW0408-40JC						
0.96	bivalve	10881 ± 61	10149 ± 61	11408 - 12054	NSF - AAMS	WW5472
1.89	bivalve	10952 ± 55	10220 ± 55	11713 - 12142	NSF - AAMS	WW5473
3.75	bivalve	10987 ± 56	10255 ± 56	11759 - 12348	NSF - AAMS	WW5474
5.94	bivalve	11126 ± 59	10394 ± 59	12055 - 12605	NSF - AAMS	WW5475
8.61	bivalve	11522 ± 58	10790 ± 58	12725 - 12885	NSF - AAMS	WW5476
EW0408-47JC						
7.28	wood	6685 ± 30		7501 - 7608	NSF - AAMS	WW6079
11.28	wood	7660 ± 30		8398 - 8538	NSF - AAMS	WW6080
17.80	wood	8865 ± 50		9744 - 10176	NSF - AAMS	WW6104

* Sample rejected from age model; see text for details.

a: Marine reservoir correction of 732 yrs subtracted from carbonate samples.

b: Keck - UCI = Keck Carbon Cycle AMS facility, University of California - Irvine; CAMS - LLNL = Center for Accelerator Mass Spectrometry, Lawrence Livermore National Lab; NSF - AAMS = National Science Foundation - Arizona AMS facility, Tucson

Table 2.2 Mean glass EPMA analyses of EW0408 tephra samples. n = total number of glass shards analyzed for each tephra sample. Mean and estimated error to one standard deviation shown for each sample. Analyses normalized to 100 wt% on a water-free basis. Water content calculated by difference from analytical total. Total iron oxide concentration expressed as Fe_2O_3. Individual glass shard analyses contained in online supplemental material.

	n	Na_2O	MgO	Al_2O_3	SiO_2	Cl	K_2O	CaO	TiO_2	Fe_tO_3	H_2O
Old Crow Tephra											
internal standard	194	3.80 ± 0.30	0.30 ± 0.03	13.24 ± 0.20	75.05 ± 0.38	0.29 ± 0.06	3.72 ± 0.23	1.45 ± 0.10	0.30 ± 0.17	1.85 ± 0.15	5.10 ± 2.07
EW0408-22JC: Crawfish inlet											
1.63 mbsf	11	4.17 ± 0.36	0.32 ± 0.09	14.63 ± 0.08	73.28 ± 0.33	0.19 ± 0.15	2.93 ± 0.41	1.89 ± 0.10	0.28 ± 0.14	2.32 ± 0.51	4.41 ± 2.48
EW0408-25MC3: Sitka Slope											
0.21 mbsf	20	4.49 ± 0.16	0.31 ± 0.04	14.05 ± 0.35	73.34 ± 0.50	0.15 ± 0.10	2.61 ± 0.09	1.86 ± 0.17	0.26 ± 0.16	2.92 ± 0.15	1.36 ± 2.23
EW0408-33JC: Katlian Bay											
12.78 mbsf	13	4.58 ± 0.13	0.29 ± 0.05	14.72 ± 0.35	72.95 ± 0.40	0.09 ± 0.03	2.58 ± 0.15	1.89 ± 0.17	0.17 ± 0.09	2.74 ± 0.17	2.77 ± 1.57
16.18 mbsf	19	5.02 ± 0.19	0.28 ± 0.06	14.35 ± 0.38	72.97 ± 0.58	0.09 ± 0.03	2.52 ± 0.19	1.64 ± 0.25	0.33 ± 0.12	2.81 ± 0.21	3.80 ± 2.71
EW0408-40JC: Lower Sitka Sound											
9.08 mbsf (I)	21	5.01 ± 0.33	0.31 ± 0.13	14.58 ± 0.28	72.50 ± 0.55	0.08 ± 0.03	2.56 ± 0.15	1.73 ± 0.12	0.33 ± 0.10	2.90 ± 0.30	4.55 ± 1.30
9.08 mbsf (II)	7	5.03 ± 0.37	0.58 ± 0.43	14.77 ± 0.78	71.27 ± 0.52	0.09 ± 0.01	2.36 ± 0.19	1.95 ± 0.22	0.57 ± 0.21	3.37 ± 0.91	3.35 ± 1.50
9.80 mbsf	14	5.36 ± 0.61	0.28 ± 0.04	14.53 ± 0.17	72.93 ± 0.50	0.08 ± 0.03	2.20 ± 0.13	1.45 ± 0.19	0.31 ± 0.12	2.85 ± 0.18	1.71 ± 1.59
10.00 mbsf	10	5.82 ± 0.35	0.29 ± 0.05	14.34 ± 0.30	72.88 ± 0.65	0.09 ± 0.03	2.28 ± 0.23	1.48 ± 0.23	0.22 ± 0.18	2.60 ± 0.16	4.61 ± 0.91
10.29 mbsf	58	4.75 ± 0.39	0.28 ± 0.05	14.65 ± 0.48	72.72 ± 0.57	0.09 ± 0.03	2.66 ± 0.18	1.76 ± 0.20	0.31 ± 0.15	2.79 ± 0.25	2.66 ± 2.05
10.49 mbsf	20	5.37 ± 0.38	0.29 ± 0.07	14.56 ± 0.38	73.01 ± 0.62	0.09 ± 0.03	2.16 ± 0.18	1.43 ± 0.20	0.30 ± 0.13	2.80 ± 0.35	1.93 ± 1.57
10.82 mbsf	27	5.43 ± 0.37	0.26 ± 0.04	14.59 ± 0.44	72.97 ± 0.74	0.08 ± 0.02	2.21 ± 0.19	1.47 ± 0.30	0.22 ± 0.17	2.76 ± 0.29	1.81 ± 1.60
11.08 mbsf	19	5.08 ± 0.18	0.30 ± 0.06	14.44 ± 0.25	72.80 ± 0.45	0.09 ± 0.04	2.48 ± 0.09	1.56 ± 0.15	0.33 ± 0.08	2.92 ± 0.21	3.27 ± 2.23
11.10 mbsf	29	5.46 ± 0.41	0.26 ± 0.06	14.53 ± 0.39	72.93 ± 0.55	0.09 ± 0.03	2.36 ± 0.17	1.44 ± 0.26	0.28 ± 0.19	2.66 ± 0.29	1.79 ± 1.14
11.20 mbsf	21	5.09 ± 0.40	0.32 ± 0.08	14.57 ± 0.29	72.37 ± 0.67	0.09 ± 0.03	2.58 ± 0.12	1.74 ± 0.17	0.32 ± 0.11	2.91 ± 0.19	4.43 ± 1.46
EW0408-47JC: Slocum Arm											
6.46 mbsf (I)	14	5.06 ± 0.25	0.30 ± 0.07	14.26 ± 0.29	72.78 ± 0.42	0.10 ± 0.04	2.57 ± 0.11	1.68 ± 0.09	0.30 ± 0.08	2.96 ± 0.23	1.74 ± 1.62
6.46 mbsf (II)	10	5.28 ± 0.17	0.70 ± 0.06	15.28 ± 0.18	69.44 ± 0.50	0.07 ± 0.04	2.04 ± 0.07	2.72 ± 0.14	0.51 ± 0.14	3.97 ± 0.21	3.77 ± 3.39
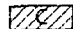
Table 2.3 EW0408 tephra SIMAN similarity coefficients.

EW0408 Core	Sample depth (mbsf)	25MC3 0.21	33JC 12.78	33JC 16.18	40JC 9.08 (I)	40JC 9.08 (II)	40JC 9.80	40JC 10.00	40JC 10.29	40JC 10.49	40JC 10.82	40JC 11.08	40JC 11.10	40JC 11.20	47JC 6.46 (I)	47JC 6.46 (II)
22JC	*1.63*	0.94	0.93	0.89	0.91	0.87	0.86	0.87	0.93	0.86	0.86	0.89	0.86	0.91	0.90	0.77
25MC3	0.21	-	0.96	0.94	0.96	0.92	0.90	0.89	0.95	0.90	0.89	0.94	0.89	0.96	0.96	0.76
33JC	12.78	-	-	0.97	0.95	0.93	0.91	0.91	0.97	0.92	0.92	0.94	0.91	0.95	0.95	0.78
33JC	16.18	-	-	-	0.98	0.91	0.95	0.96	0.97	0.95	0.94	0.98	0.94	0.97	0.98	0.79
40JC	9.08 (I)	-	-	-	-	0.91	0.94	0.92	0.97	0.93	0.93	0.97	0.93	0.99	0.99	0.81
40JC	*9.08 (II)*	-	-	-	-	-	0.89	0.90	0.92	0.89	0.89	0.91	0.91	0.93	0.89	0.88
40JC	9.80	-	-	-	-	-	-	0.96	0.94	0.98	0.98	0.95	0.97	0.93	0.94	0.79
40JC	10.00	-	-	-	-	-	-	-	0.91	0.96	0.96	0.94	0.97	0.92	0.92	0.77
40JC	10.29	-	-	-	-	-	-	-	-	0.93	0.93	0.95	0.93	0.97	0.96	0.78
40JC	10.49	-	-	-	-	-	-	-	-	-	0.98	0.95	0.96	0.97	0.93	0.81
40JC	10.82	-	-	-	-	-	-	-	-	-	-	0.94	0.99	0.92	0.92	0.79
40JC	11.08	-	-	-	-	-	-	-	-	-	-	-	0.94	0.97	0.98	0.78
40JC	11.10	-	-	-	-	-	-	-	-	-	-	-	-	0.92	0.92	0.79
40JC	11.20	-	-	-	-	-	-	-	-	-	-	-	-	-	0.98	0.80
47JC	6.46 (I)	-	-	-	-	-	-	-	-	-	-	-	-	-	-	0.78

Unit	EW0408 tephra horizons (mbsf)
A	25MC3 - 0.21; 33JC - 12.78 & 16.18; 40JC - 9.08 (I), 10.29, 11.08, 11.20; 47JC - 6.46 (I)
B	40JC - 9.80, 10.00, 10.49, 10.82, & 11.10
▨	40JC - 9.08 (II)
▨	22JC - 1.63

Table 2.4 Marine EW0408 - terrestrial MEVF correlations.

EW0408 geochemistry Representative sample	Unit A 40JC - 10.29 mbsf	Unit B 40JC - 9.80 mbsf	Unit C* 40JC - 9.08 (II) mbsf	Unit D 22JC - 1.63 mbsf
Riehle high-Si dacite	0.78	0.78	0.87	0.79
Riehle low-Si rhyolite	0.87	0.87	**0.94**	0.85
Riehle high-Si rhyolite	**0.98**	**0.94**	0.94	0.92
Beget dacite	0.81	0.81	**0.93**	0.80
Westgate low-Si rhyolite	0.81	0.79	0.90	0.78
Westgate high-Si rhyolite	**0.96**	0.91	0.95	0.90

* SIMAN analysis did not use MgO data due to high standard deviation.

Table 2.5 Correlations between EW0408 marine tephras and contemporaneous deposits.

		Mt. Katmai Novarupta[a] AD 1912		Lena tephra[b] 280-320	? ~480	White River Ash 1147		? 1260-1375
Approximate age (cal yrs BP)		Dacite	Andesite	ECR 32	CHP 184[b]	Mt. Churchill summit[c]	Distal[d]	LNA 100[b]
EW0408-25MC3								
0.21 mbsf	>50	0.83	0.87	0.84	0.81	0.83	0.84	0.86
EW0408-22JC							0.90[d]	
Unit D(1.63 mbsf)	~900	0.88	0.86	0.90	0.86	0.89	**0.94**[g]	**0.93**

		Bridge River tephra[e] ~2600 Otter Creek Bog[f]	Aniakchak[g] ~3400	Jarvis Creek ash[h] ~3600	Black Peak[i] 4600-5600[3]	? 5030-5300 ECR 162[b]	Oshetna tephra[j] ~6000	? ~6300 MTR 146[k]
Approximate age (cal yrs BP)								
EW0408-33JC								
12.78 mbsf	~5300	0.83	0.87	0.79	0.81	**0.90**	0.89	0.83
16.18 mbsf	~6700	0.83	0.89	0.77	0.80	0.89	0.85	0.83
EW0408-47JC								
6.46 mbsf (I)	~7300	0.83	0.88	0.78	0.80	**0.90**	0.83	0.85
6.46 mbsf (II)		0.69	0.82	0.76	0.69	0.79	0.82	0.70

		Lethe tephra[k] ~12600
Approximate age (cal yrs BP)		
EW0408-40JC		
Unit A(10.29 mbsf)	>12800	0.81
Unit B(9.80 mbsf)	>12800	0.80
Unit C(9.08 mbsf II)[1]	13154±100[2]	0.91

1: SIMAN analysis did not use MgO data due to high standard deviation
2: Calibrated from AMS dates on MEd data presented in Beget & Motyka (1998)
3: Calibrated from AMS date presented in Payne et al., 2008

Data sources
a: Fierstein & Hildreth, 1992
b: Payne et al., 2008
c: Richter et al., 1995
d: Downes, 1985
e: Zoltai, 1988

f: Westgate, 1977
g: Beget et al., 1992
h: Beget et al., 1991
i: Riehle et al., 1999
j: Child et al., 1998
k: Pinney & Beget, 1991

2.10 Figures
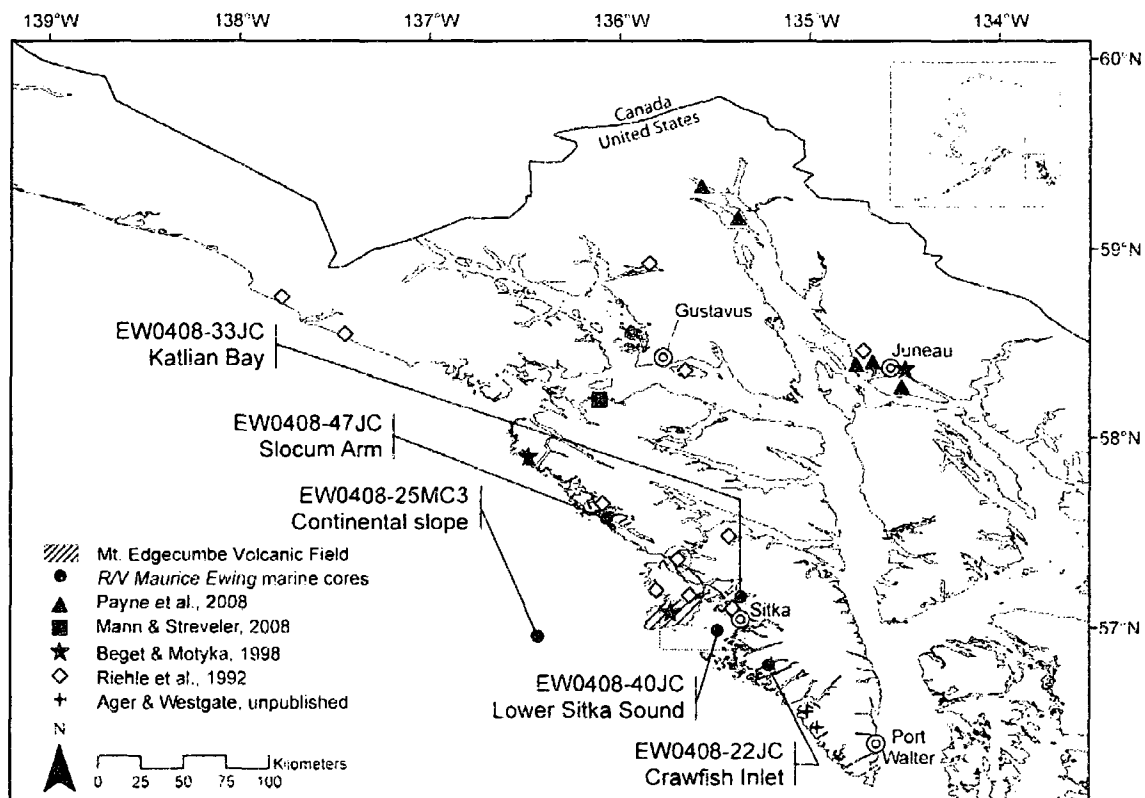
Figure 2.1: Location map of R/V *Maurice Ewing* marine sediment cores discussed in this study, as well as outcrops of MEVF-derived tephras previously described. Circled diamond indicates location of lake core described in text (Riehle et al., 1992b). Dashed inset represents extent of Figure 9.
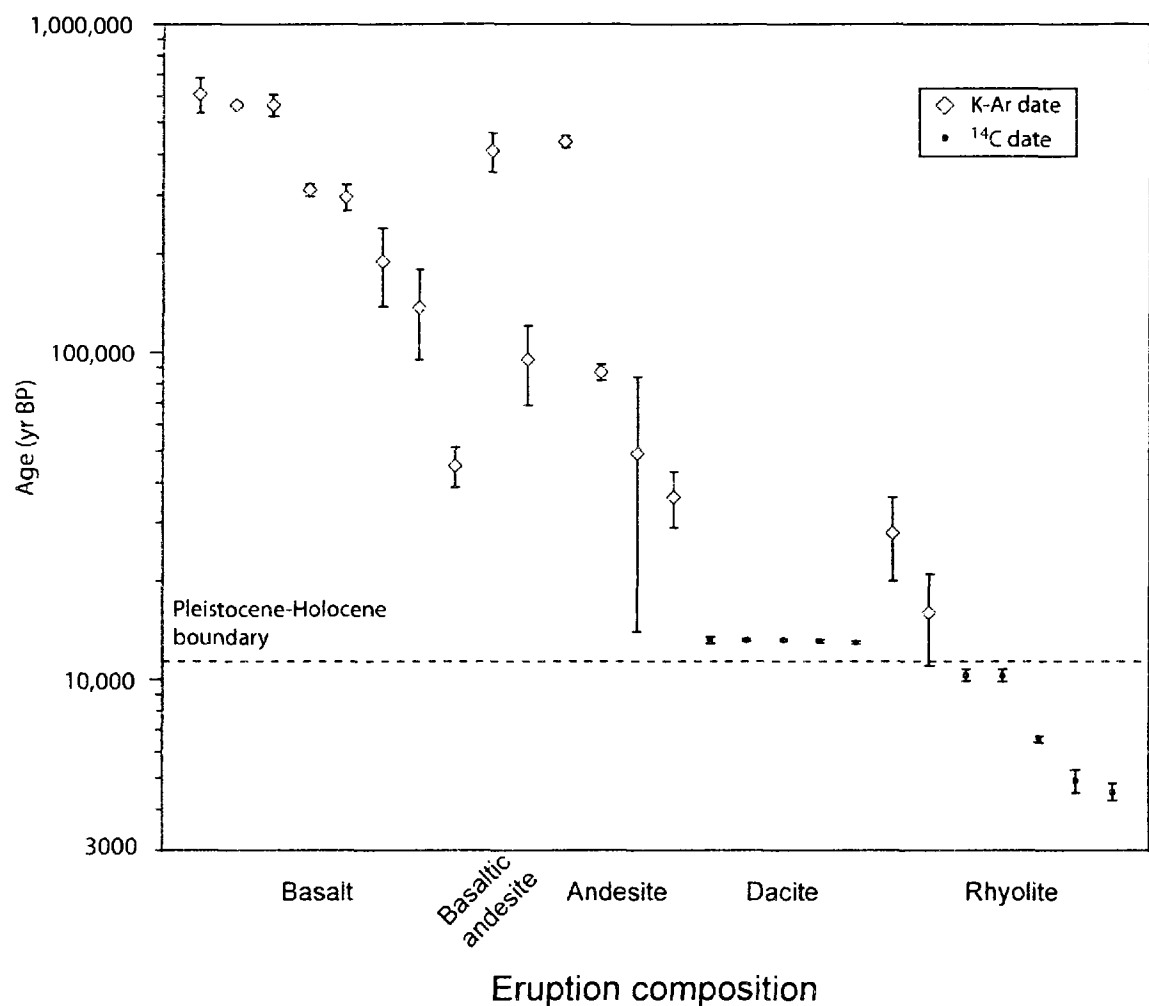
Figure 2.2: Quaternary history of terrestrial volcanic tephra deposits from the MEVF. Dates and geochemical compositions based on data compiled from Riehle and Brew (1984), Riehle et al. (1992a), Riehle et al. (1992b), and Begét and Motyka (1998). All ^{14}C dates have been calibrated to calendar years BP using the CALIB 5.01 program (Stuvier and Reimer, 1993) and the INTCAL04 curve (Reimer et al., 2004).
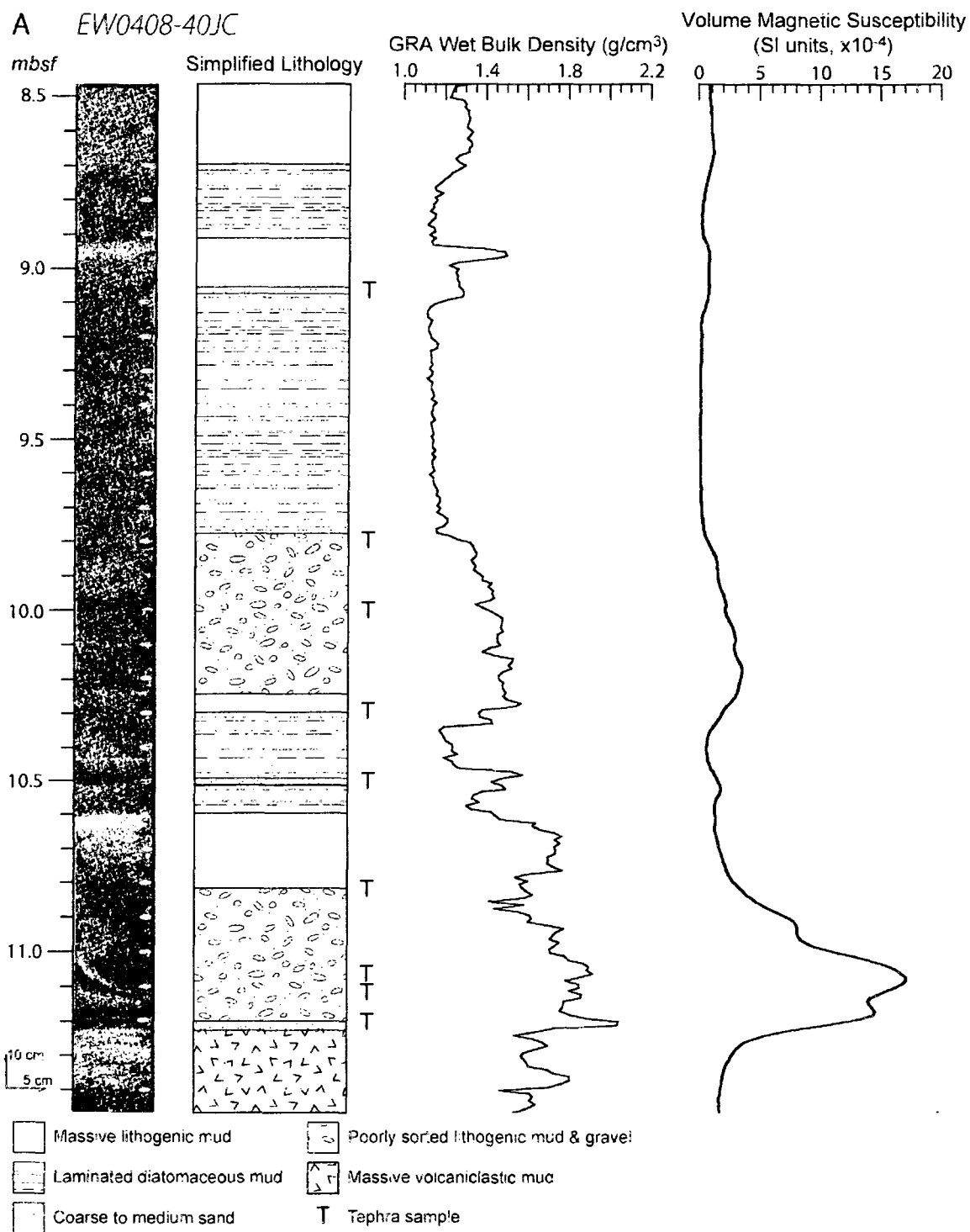
A *EW0408-40JC*

Figure 2.3: (A) High-resolution linescan imagery, simplified lithology, tephra sample positions and GEOTEK geophysical measurements from core EW0408-40JC. (B) Volume magnetic susceptibility logs used to assist with identification of crytotephras in cores EW0408-22JC, -33JC, and -47JC; tephra presence was confirmed using smear slide light microscopy.

B — Volume Magnetic Susceptibility (SI units, x10⁻⁵)
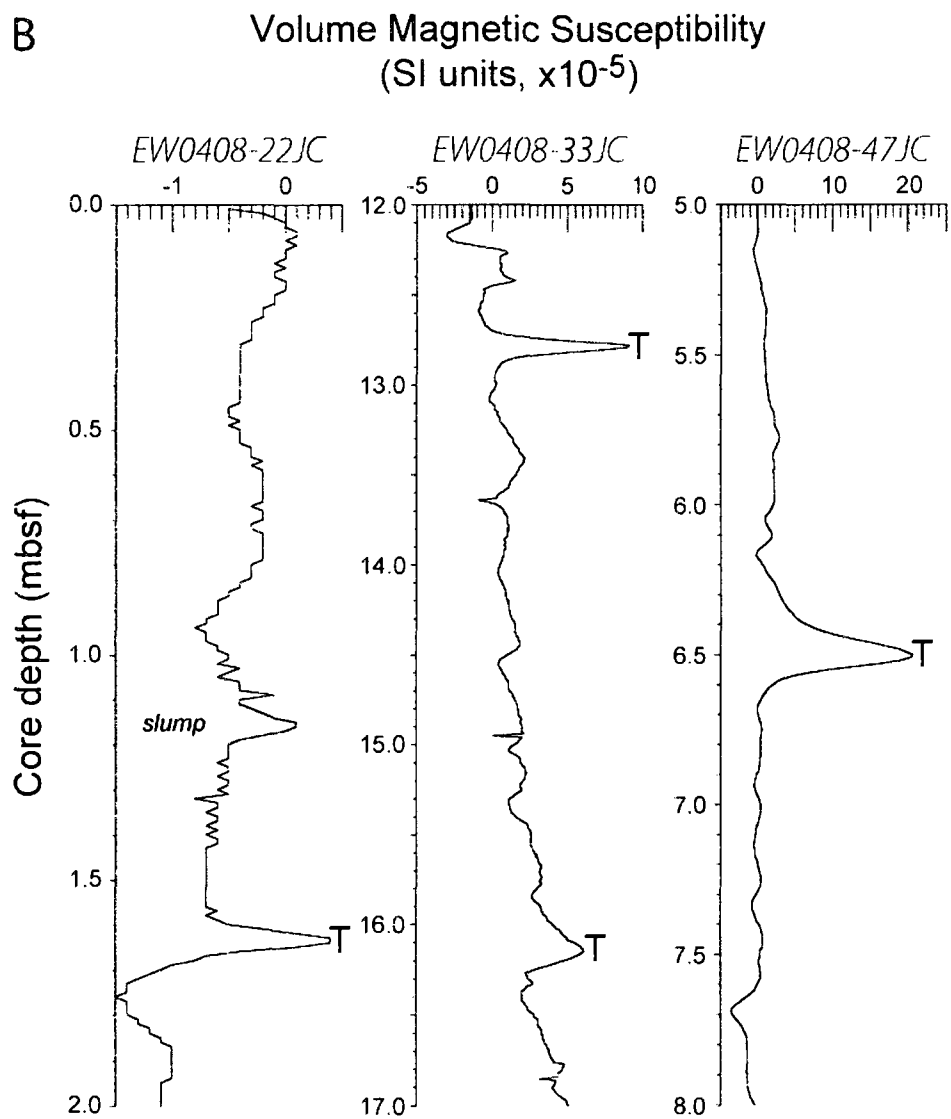
Figure 2.3 (continued).
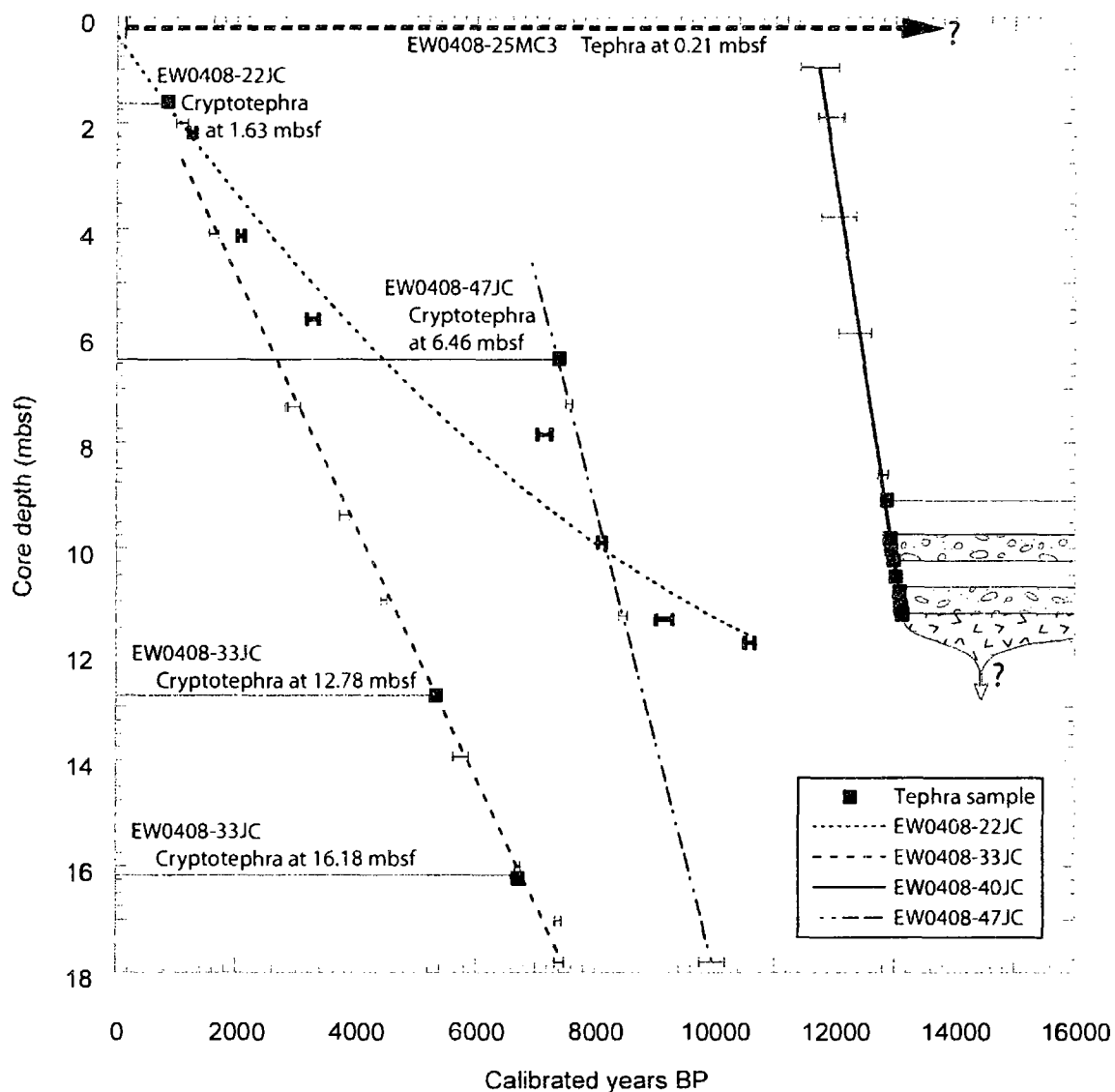
Figure 2.4: Depth-age relationships for EW0408 tephra-bearing marine sediment cores discussed in the text. Error bars represent the 2σ calibration range for dated AMS samples. Bold error bars correspond to EW0408-22JC age model. Because of poor age control, the EW0408-25MC3 tephra is only constrained beyond the depth of excess [210]Pb (>100 yr BP; Rosen et al., 2005; Walinsky et al., 2009). Depths of gravity and pyroclastic flow deposits are indicated for EW0408-40JC; lithologies are the same as in Figure 3. Thickness of basal EW0408-40JC pyroclastic deposit is unknown.
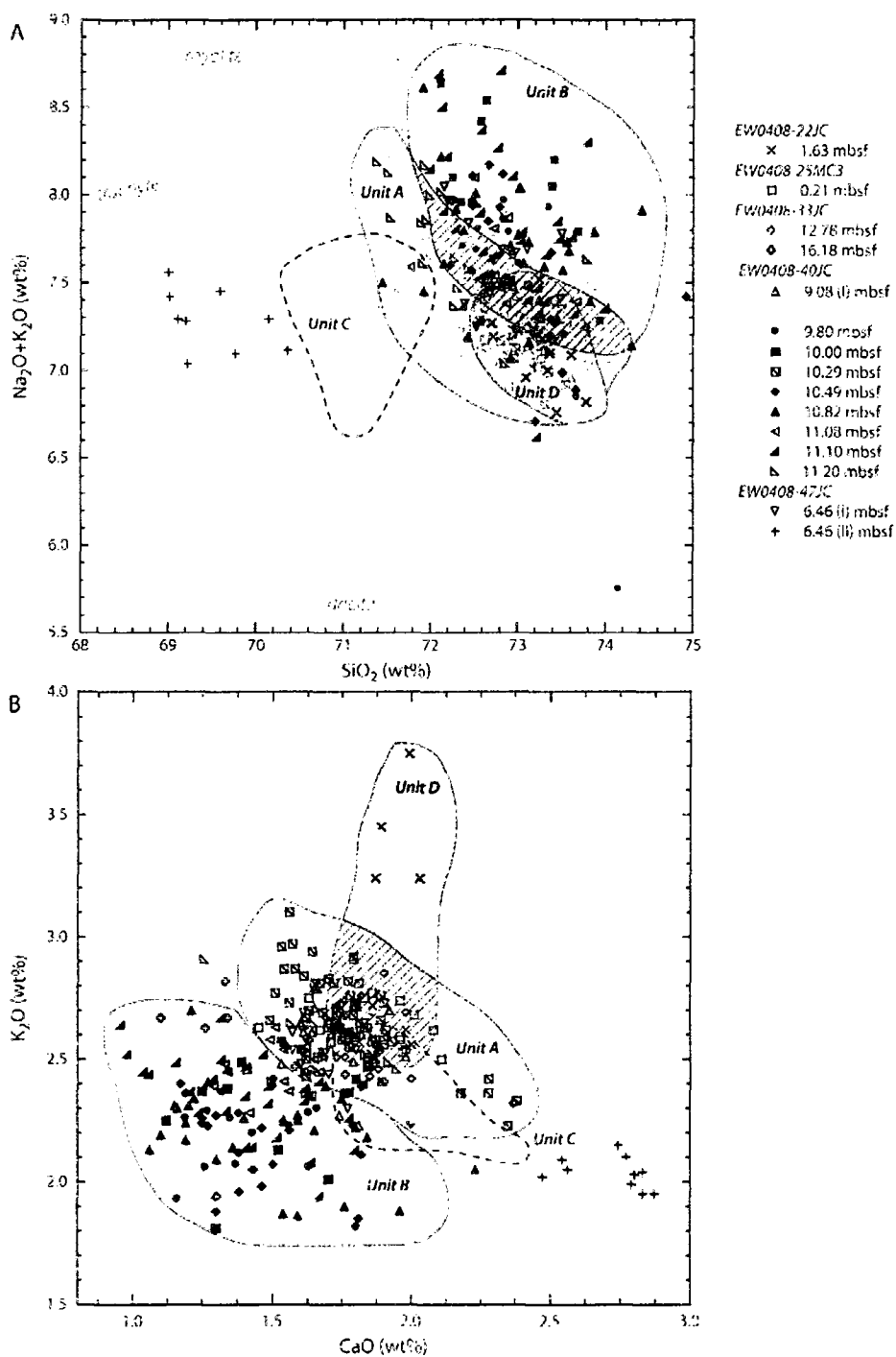
Figure 2.5: Total alkali-silica diagram (A) and oxide variation diagram (B) of individual EW0408 tephra glass shards. Classification based on the Le Bas et al. (1986) IUGS volcanic classification. Hollow symbols indicate geochemical affinities to SIMAN-identified Unit A; dark filled symbols represent Unit B; gray symbols represent Unit C; X symbols correspond to Unit D. Approximate compositional ranges are indicated; region of compositional overlap between Units A, B, and D indicated by slanted lines.
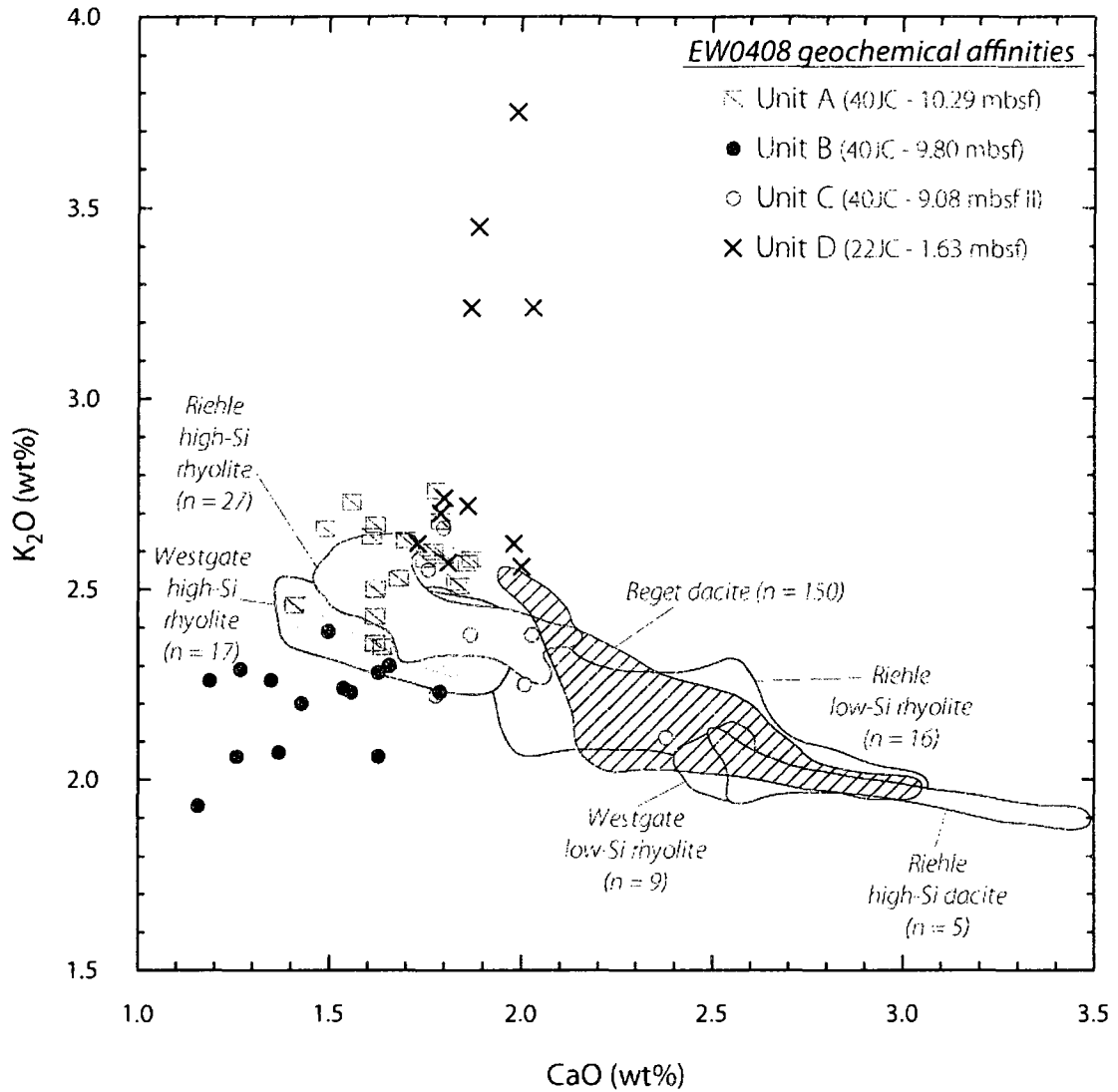
Figure 2.6: CaO-K₂O oxide variation diagram for representative EW0408 tephra geochemical units compared to previous published MEVF datasets (see text for references).
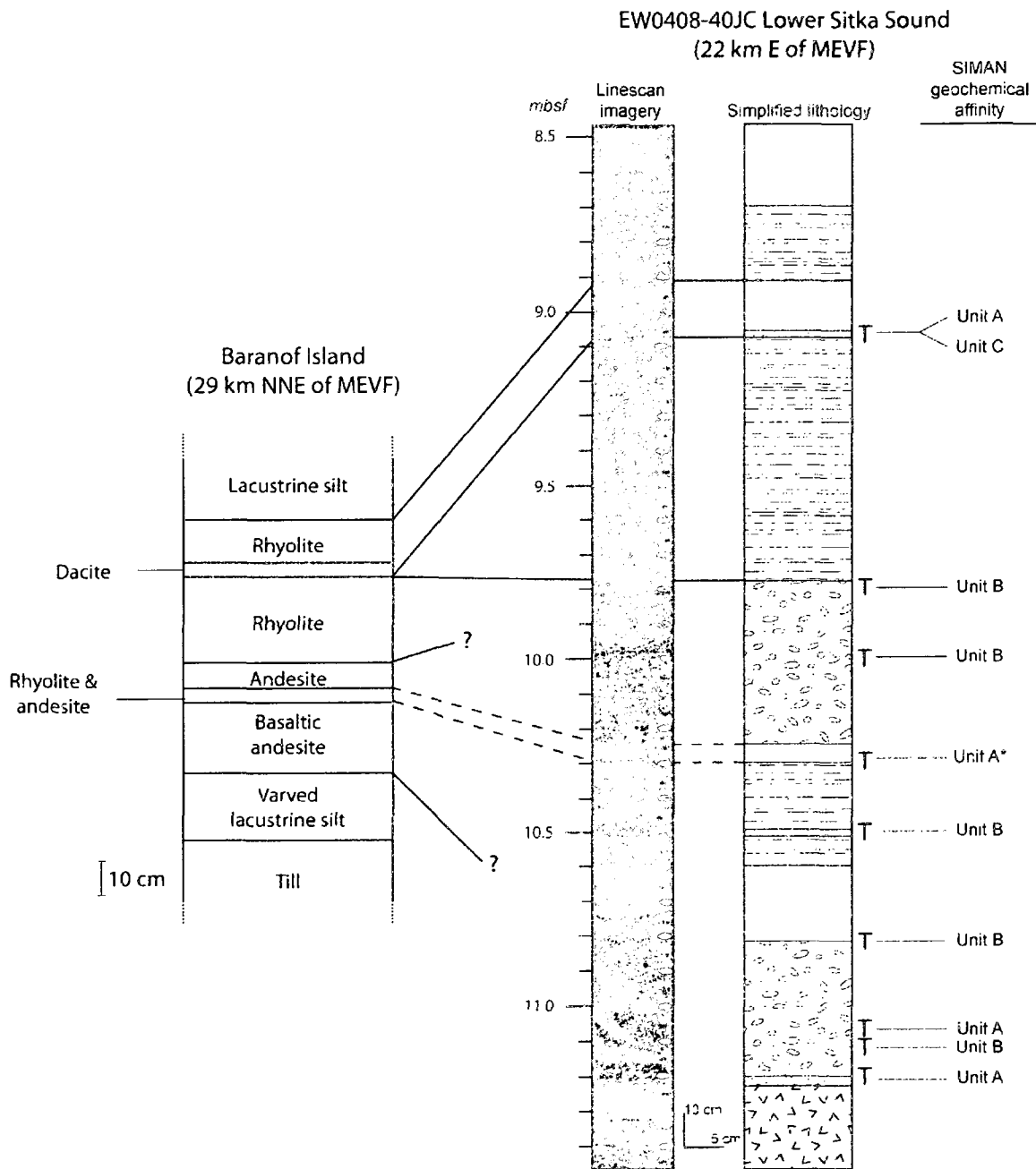
Figure 2.7: Correlation between published lake core from Baranof Island (Fig. 2.1; Riehle et al., 1992b) and EW0408-40JC. Based on the SIMAN similarity calculation, the Unit C chemistry is analogous to the dacite unit. * indicates a possible correlation; see text for explanation. Lithologies same as in Fig. 2.3.
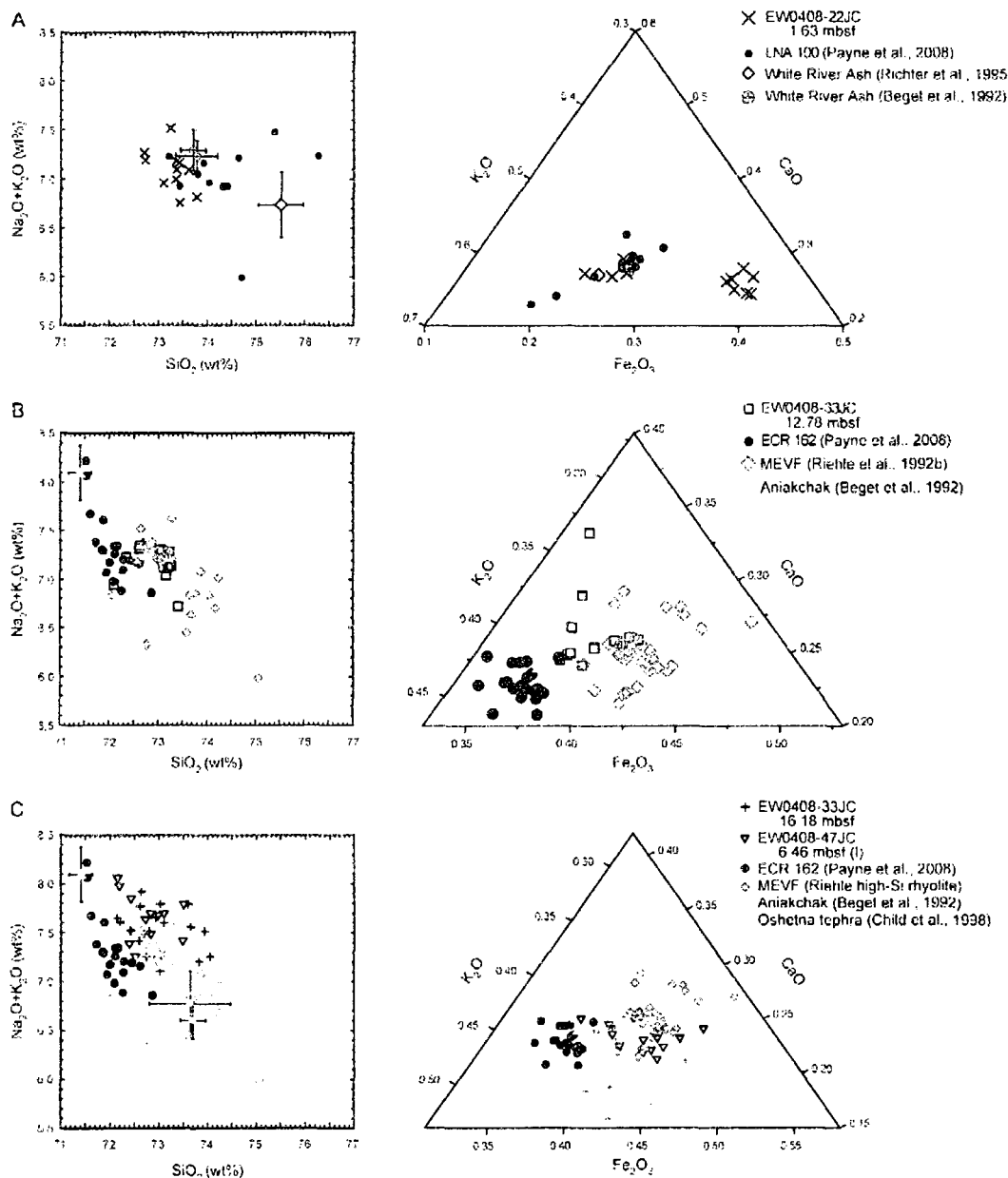
Figure 2.8: TAS and ternary oxide variation diagrams for EW0408 tephra deposits and regionally significant tephra deposits. (A) The composition of the cryptotephra from core EW0408-22JC appears similar to LNA 100, a cryptotephra from a peat deposit near Juneau, Alaska, that has been linked to the White River Ash. (B) Some compositional overlap exists between the cryptotephra at 12.78 mbsf in core EW0408-33JC and ECR 162; ECR 162 is compositionally similar to the 3400 cal yr BP eruption of Aniakchak (Beget et al., 1992), whereas EW0408-33JC at 12.78 mbsf bears similarities to MEVF activity. (C) The cryptotephras in cores EW0408-33JC (at 16.18 mbsf) and -47JC (at 6.46 msbsf [I]) are compositionally identical, and overlap somewhat with ECR 162 which has been attributed to a previously unidentified Aniakchak eruption by Payne et al. (2008). However, both cryptotephras in -33JC and -47JC more closely resemble rhyolitic deposits associated with MEVF activity. Error bars (where shown) indicate 1σ standard deviation of published population means where individual glass analyses were unavailable.
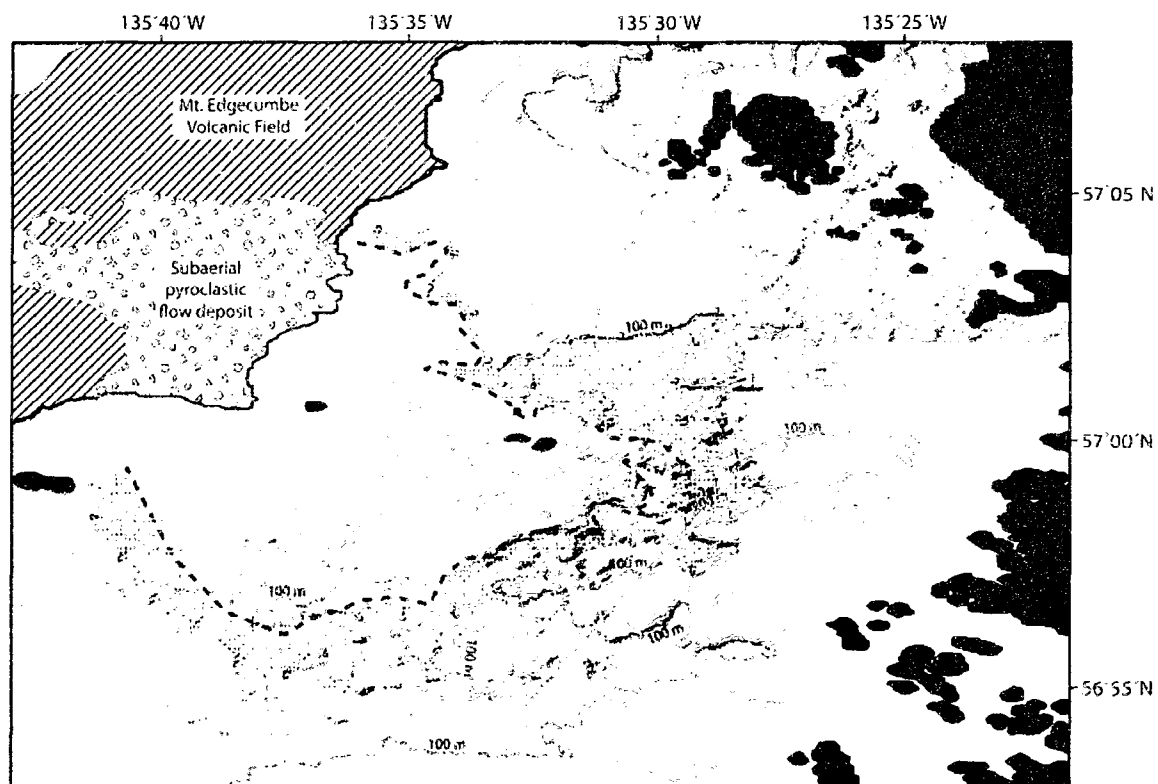
Figure 2.9: Bathymetry of Sitka Sound in relation to mapped subaerial pyroclastic flows from the MEVF (Riehle et al., 1989). The geometry of the lobe, as well as the sedimentology of EW0408-40JC, suggest this may be the submerged run-out of the adjacent subaerial flow. White contour line at 70 m water depth indicates eustatic sea level at the time of deposition of the MEd tephra (Fairbanks, 1989).

2.11 Appendix

Appendix 2.1 Individual tephra grain analyses.

Core: EW0408-22JC
Sample depth: 1.63 mbsf

UNNORMALIZED RAW DATA

Line Numbers	Na2O (%)	MgO (%)	Al2O3 (%)	SiO2 (%)	Cl (%)	K2O (%)	CaO (%)	TiO2 (%)	Fe2O3 (%)	Total	Formula H2O	100% Normalization factor
842	4.25	0.26	13.90	68.86	0.09	2.56	1.69	0.37	2.71	94.70	3.55	1.056015104
854	3.62	0.39	13.71	69.24	0.31	3.05	1.91	0.23	1.60	94.06	4.33	1.063161591
864	4.26	0.23	14.25	71.83	0.13	2.57	1.70	0.29	2.66	97.94	0.26	1.021045071
865	4.06	0.31	14.05	69.79	0.06	2.63	1.73	0.51	2.56	95.39	2.20	1.041760879
866	4.01	0.32	13.57	67.50	0.09	2.42	1.83	0.06	2.61	92.35	6.04	1.082813134
869	3.81	0.21	13.19	66.70	0.05	2.33	1.82	0.33	2.38	90.82	7.49	1.10105315
870	3.64	0.32	14.10	70.64	0.38	3.61	1.92	0.31	1.54	96.45	1.95	1.03683053
871	3.29	0.30	13.57	67.09	0.36	2.98	1.72	0.25	1.62	92.01	6.40	1.090032770
1020	3.42	0.50	13.51	67.20	0.34	3.16	1.73	0.18	1.59	91.52	6.84	1.091426198
1028	4.34	0.26	13.98	70.28	0.09	2.48	1.74	0.28	2.36	95.77	2.48	1.044212602
1029	4.06	0.20	13.35	67.10	0.07	2.49	1.70	0.10	2.33	91.40	7.00	1.094121555

NORMALIZED

Line Numbers	Na2O (%)	MgO (%)	Al2O3 (%)	SiO2 (%)	Cl (%)	K2O (%)	CaO (%)	TiO2 (%)	Fe2O3 (%)	Total	Formula H2O
842	4.48	0.28	14.68	72.72	0.10	2.70	1.79	0.39	2.86	100.00	3.55
854	3.85	0.41	14.58	73.61	0.33	3.24	2.03	0.25	1.70	100.00	4.33
864	4.37	0.24	14.55	73.34	0.13	2.62	1.73	0.30	2.72	100.00	0.26
865	4.54	0.32	14.64	72.70	0.06	2.74	1.80	0.53	2.67	100.00	2.20
866	4.34	0.34	14.70	73.09	0.10	2.62	1.98	0.00	2.82	100.00	6.04
869	4.20	0.23	14.52	73.44	0.05	2.56	2.00	0.37	2.62	100.00	7.49
870	3.77	0.33	14.61	73.24	0.39	3.75	1.99	0.32	1.59	100.00	1.95
871	3.58	0.33	14.75	73.76	0.41	3.24	1.87	0.26	1.78	100.00	6.40
1020	3.73	0.55	14.74	73.35	0.37	3.45	1.89	0.19	1.73	100.00	8.84
1028	4.53	0.27	14.59	73.36	0.10	2.57	1.81	0.29	2.47	100.00	2.48
1029	4.45	0.22	14.61	73.42	0.07	2.72	1.86	0.11	2.55	100.00	7.00

MEAN

n	Na2O (%)	MgO (%)	Al2O3 (%)	SiO2 (%)	Cl (%)	K2O (%)	CaO (%)	TiO2 (%)	Fe2O3 (%)	Total	H2O (%)
11	4.17	0.32	14.63	73.28	0.19	2.93	1.89	0.28	2.32	100.00	4.41
1 SD	0.36	0.09	0.08	0.33	0.15	0.41	0.10	0.14	0.51	-	2.48

Core: EW0408-25MC3
Sample depth: 0.21 mbsf

UNNORMALIZED RAW DATA

Line Numbers	Na2O (%)	MgO (%)	Al2O3 (%)	SiO2 (%)	Cl (%)	K2O (%)	CaO (%)	TiO2 (%)	Fe2O3 (%)	Total	Formula H2O	100% Normalization factor
426	4.56	0.37	13.94	73.40	0.25	2.47	1.85	0.46	2.93	100.23	-0.23	1.00
429	4.21	0.36	13.99	70.52	0.09	2.48	1.84	0.24	3.02	96.74	3.26	1.03
430	4.34	0.33	13.27	73.04	0.38	2.72	1.81	0.07	2.94	98.89	1.11	1.01
433	4.47	0.26	13.81	74.19	0.15	2.57	1.71	0.22	2.62	99.99	0.01	1.00
435	4.81	0.35	13.96	72.23	0.29	2.62	2.07	0.42	2.92	99.65	0.35	1.00
440	4.28	0.29	14.31	72.65	0.10	2.73	1.62	0.23	2.95	99.15	0.85	1.01
443	4.49	0.22	13.53	72.89	0.09	2.59	1.43	0.54	2.95	98.73	1.27	1.01
444	4.54	0.26	13.97	72.33	0.32	2.65	1.71	0.06	2.99	98.82	1.18	1.01
445	4.46	0.35	13.89	72.28	0.07	2.54	1.93	0.22	3.03	98.58	1.44	1.01
446	4.30	0.32	12.97	70.06	0.05	2.55	1.91	0.20	2.95	95.31	4.69	1.05
448	3.71	0.31	12.41	67.30	0.11	2.36	1.78	0.36	2.57	90.90	9.10	1.10
449	4.45	0.26	14.37	73.50	0.19	2.64	1.92	0.25	2.90	100.48	-0.48	1.00
451	4.44	0.30	13.99	73.07	0.08	2.52	1.96	0.21	3.04	99.60	0.40	1.00
452	4.59	0.27	14.70	72.97	0.15	2.61	1.66	0.08	2.71	99.72	0.28	1.00
454	4.60	0.30	14.30	72.46	0.06	2.50	2.11	0.56	2.95	99.84	0.16	1.00
457	4.28	0.32	13.77	73.64	0.07	2.75	1.85	0.13	2.66	99.45	0.54	1.01
459	4.56	0.33	14.64	72.91	0.08	2.59	1.91	0.23	3.13	100.37	-0.37	1.00
460	4.45	0.30	13.83	71.20	0.06	2.67	1.91	0.24	2.68	97.33	2.67	1.03
466	4.48	0.29	13.94	73.21	0.07	2.49	1.65	0.09	2.96	99.19	0.81	1.01
468	4.66	0.35	13.97	72.89	0.28	2.53	1.98	0.45	2.75	99.86	0.14	1.00

NORMALIZED

Line Numbers	Na2O (%)	MgO (%)	Al2O3 (%)	SiO2 (%)	Cl (%)	K2O (%)	CaO (%)	TiO2 (%)	Fe2O3 (%)	Total	Formula H2O
426	4.55	0.37	13.90	73.23	0.25	2.47	1.84	0.48	2.92	100.00	-0.23
429	4.35	0.38	14.46	72.90	0.09	2.56	1.90	0.25	3.12	100.00	3.26
430	4.38	0.33	13.42	73.87	0.39	2.75	1.83	0.07	2.97	100.00	1.11
433	4.47	0.26	13.81	74.20	0.15	2.57	1.71	0.22	2.62	100.00	0.01
435	4.83	0.35	14.00	72.48	0.29	2.62	2.08	0.42	2.93	100.00	0.35
440	4.32	0.29	14.43	73.27	0.10	2.75	1.63	0.23	2.98	100.00	0.85
443	4.55	0.23	13.70	73.82	0.09	2.63	1.45	0.55	2.99	100.00	1.27
444	4.59	0.26	14.14	73.19	0.32	2.68	1.73	0.06	3.02	100.00	1.18
445	4.52	0.36	13.89	73.32	0.07	2.58	1.96	0.22	3.08	100.00	1.44
446	4.51	0.33	13.60	73.51	0.05	2.68	2.01	0.21	3.10	100.00	4.69
448	4.08	0.34	13.65	74.03	0.12	2.59	1.96	0.39	2.83	100.00	9.10
449	4.43	0.26	14.30	73.14	0.19	2.62	1.91	0.25	2.89	100.00	-0.48
451	4.45	0.30	14.04	73.36	0.08	2.53	1.97	0.21	3.05	100.00	0.40
452	4.60	0.27	14.74	73.18	0.15	2.62	1.67	0.06	2.72	100.00	0.28
454	4.61	0.30	14.32	72.58	0.06	2.50	2.11	0.56	2.96	100.00	0.16
457	4.30	0.32	13.84	74.04	0.07	2.77	1.86	0.13	2.68	100.00	0.54
459	4.55	0.32	14.58	72.64	0.08	2.58	1.90	0.23	3.12	100.00	-0.37
460	4.57	0.31	14.21	73.15	0.06	2.74	1.96	0.24	2.76	100.00	2.67
466	4.52	0.30	14.05	73.81	0.07	2.51	1.63	0.09	2.98	100.00	0.31
468	4.86	0.35	13.99	72.93	0.28	2.54	1.98	0.45	2.75	100.00	0.14

MEAN

n	Na2O	MgO	Al2O3	SiO2	Cl	K2O	CaO	TiO2	Fe2O3	Total	H2O
20	4.49	0.31	14.05	73.34	0.15	2.61	1.86	0.27	2.92	100.00	1.36
1 SD	0.16	0.04	0.35	0.50	0.10	0.09	0.17	0.16	0.15	-	2.23

Core. EW0408-33JC
Sample depth 16.18 mbsf

UNNORMALIZED RAW DATA

Line Numbers	Na2O (%)	MgO (%)	Al2O3 (%)	SiO2 (%)	Cl (%)	K2O (%)	CaO (%)	TiO2 (%)	Fe2O3 (%)	Total	Formula H2O	100% Normalization factor
1333	5.10	0.22	14.05	71.49	0.11	1.88	1.20	0.21	2.53	96.85	3.15	1.033
1335	4.70	0.21	14.47	70.59	0.03	2.17	1.94	0.13	2.42	96.66	3.34	1.035
1336	4.90	0.28	14.38	71.45	0.07	2.40	1.74	0.33	2.89	98.43	1.57	1.016
1338	5.16	0.33	14.58	72.91	0.05	2.65	1.74	0.37	2.62	100.41	-0.41	0.996
1339	4.82	0.26	13.31	68.55	0.07	2.27	1.79	0.34	2.76	94.17	5.83	1.062
1340	5.03	0.31	14.50	70.97	0.12	2.49	1.85	0.39	2.72	98.39	1.61	1.016
1343	4.99	0.31	13.44	67.75	0.11	2.40	1.52	0.19	2.56	93.26	6.74	1.072
1345	4.90	0.21	14.23	71.70	0.08	2.56	1.69	0.17	2.57	98.09	1.91	1.019
1349	4.53	0.28	13.44	68.79	0.11	2.34	1.49	0.45	3.14	94.58	5.44	1.058
1351	5.08	0.28	14.01	70.82	0.11	2.47	1.50	0.07	2.64	96.98	3.02	1.031
1358	4.63	0.32	13.08	65.29	0.09	2.15	1.64	0.32	2.64	90.16	9.84	1.109
1359	5.07	0.20	13.77	72.88	0.13	2.65	1.09	0.51	2.74	99.03	0.97	1.010
1362	4.28	0.19	12.64	67.35	0.05	2.57	1.22	0.34	2.47	91.10	8.90	1.098
1365	4.73	0.30	13.90	68.97	0.12	2.38	1.64	0.34	2.50	94.89	5.11	1.054
1368	4.78	0.40	13.46	71.87	0.08	2.60	1.31	0.38	2.72	97.59	2.41	1.025
1370	4.84	0.31	14.19	69.10	0.08	2.45	1.70	0.44	2.58	95.70	4.30	1.045
1372	4.40	0.20	12.85	70.40	0.08	2.50	1.20	0.47	2.97	95.08	4.92	1.052
1373	4.87	0.23	13.84	71.41	0.12	2.63	1.72	0.31	2.79	97.91	2.09	1.021
1374	4.91	0.28	14.14	71.44	0.14	2.52	1.86	0.31	3.06	98.64	1.36	1.014

NORMALIZED

Line Numbers	Na2O (%)	MgO (%)	Al2O3 (%)	SiO2 (%)	Cl (%)	K2O (%)	CaO (%)	TiO2 (%)	Fe2O3 (%)	Total	Formula H2O
1333	5.27	0.23	14.51	73.82	0.11	1.94	1.30	0.21	2.61	100.00	3.15
1335	4.87	0.22	14.97	73.03	0.03	2.24	2.00	0.14	2.50	100.00	3.34
1336	4.98	0.28	14.61	72.59	0.07	2.44	1.76	0.33	2.94	100.00	1.57
1338	5.13	0.33	14.52	72.61	0.05	2.64	1.74	0.37	2.61	100.00	-0.41
1339	5.12	0.27	14.14	72.80	0.08	2.41	1.90	0.36	2.93	100.00	5.83
1340	5.12	0.31	14.74	72.14	0.12	2.53	1.88	0.40	2.77	100.00	1.61
1343	5.35	0.34	14.41	72.64	0.12	2.58	1.63	0.20	2.74	100.00	6.74
1345	5.00	0.21	14.50	73.10	0.08	2.61	1.72	0.17	2.62	100.00	1.91
1349	4.79	0.30	14.21	72.75	0.11	2.47	1.58	0.47	3.32	100.00	5.44
1351	5.24	0.28	14.45	73.03	0.11	2.55	1.55	0.07	2.73	100.00	3.02
1358	5.13	0.36	14.51	72.42	0.09	2.39	1.82	0.36	2.93	100.00	9.84
1359	5.12	0.20	13.90	73.59	0.13	2.67	1.10	0.52	2.76	100.00	0.97
1362	4.70	0.21	13.87	73.93	0.06	2.82	1.33	0.37	2.71	100.00	8.90
1365	4.99	0.31	14.65	72.69	0.13	2.51	1.73	0.36	2.64	100.00	5.11
1368	4.90	0.41	13.79	73.64	0.08	2.67	1.34	0.39	2.78	100.00	2.41
1370	5.05	0.33	14.83	72.20	0.08	2.56	1.78	0.46	2.70	100.00	4.30
1372	4.63	0.21	13.51	74.05	0.08	2.63	1.26	0.49	3.12	100.00	4.92
1373	4.97	0.23	14.13	72.93	0.13	2.68	1.76	0.31	2.85	100.00	2.09
1374	4.98	0.29	14.33	72.42	0.14	2.55	1.88	0.31	3.10	100.00	1.36

MEAN

n	Na2O	MgO	Al2O3	SiO2	Cl	K2O	CaO	TiO2	Fe2O3	Total	H2O
19	5.02	0.28	14.35	72.97	0.09	2.52	1.64	0.33	2.81	100.00	3.80
1 SD	0.19	0.06	0.38	0.58	0.03	0.19	0.25	0.12	0.21	-	2.71

Appendix 2.1 (continued)

Core: EW0408-33JC
Sample depth: 12.78 mbsf

UNNORMALIZED RAW DATA

Line Numbers	Na₂O (%)	MgO (%)	Al₂O₃ (%)	SiO₂ (%)	Cl (%)	K₂O (%)	CaO (%)	TiO₂ (%)	Fe₂O₃ (%)	Total	Formula H₂O	100% Normalization factor
877	4.36	0.25	14.30	70.44	0.13	2.76	1.84	0.14	2.77	96.98	1.32	1.031107889
879	4.47	0.24	15.17	69.53	0.05	2.24	2.28	0.10	2.36	96.43	1.86	1.037008602
880	4.47	0.37	14.01	70.18	0.07	2.60	1.92	0.12	2.93	96.66	1.63	1.034596121
881	4.32	0.23	13.79	63.62	0.07	2.28	1.73	0.08	2.65	93.77	4.55	1.066397957
882	4.30	0.24	13.90	68.65	0.07	2.40	1.67	0.14	2.54	93.91	4.41	1.064830501
283	4.52	0.26	13.93	70.45	0.16	2.33	1.93	0.27	2.41	96.25	1.97	1.038919641
890	4.57	0.40	14.82	71.15	0.09	2.54	1.87	0.04	2.85	98.34	-0.07	1.016850318
892	4.13	0.25	13.71	69.13	0.08	2.61	1.72	0.20	2.59	94.41	3.90	1.059249205
893	4.33	0.24	13.59	68.48	0.06	2.34	1.64	0.29	2.49	93.47	4.80	1.069810805
896	3.99	0.26	13.65	68.68	0.10	2.30	1.76	0.08	2.74	93.55	4.77	1.068933558
900	4.53	0.28	14.02	69.63	0.09	2.44	1.78	0.14	2.45	95.36	2.94	1.048649152
902	4.41	0.24	14.14	70.60	0.10	2.64	1.70	0.21	2.58	96.63	1.64	1.034920572
903	4.45	0.30	13.77	70.29	0.10	2.55	1.65	0.25	2.63	95.99	2.26	1.041743903

NORMALIZED

Line Numbers	Na₂O (%)	MgO (%)	Al₂O₃ (%)	SiO₂ (%)	Cl (%)	K₂O (%)	CaO (%)	TiO₂ (%)	Fe₂O₃ (%)	Total	Formula H₂O
877	4.50	0.26	14.74	72.63	0.13	2.85	1.90	0.14	2.85	100.00	1.32
879	4.63	0.25	15.73	72.10	0.05	2.32	2.37	0.10	2.45	100.00	1.86
380	4.63	0.38	14.49	72.61	0.07	2.69	1.98	0.12	3.03	100.00	1.63
881	4.60	0.24	14.70	73.17	0.08	2.43	1.85	0.08	2.83	100.00	4.55
882	4.58	0.26	14.80	73.10	0.08	2.55	1.78	0.15	2.71	100.00	4.41
883	4.70	0.27	14.47	73.19	0.16	2.42	2.00	0.28	2.50	100.00	1.97
890	4.64	0.41	15.07	72.35	0.09	2.59	1.91	0.04	2.90	100.00	-0.07
892	4.38	0.26	14.52	73.23	0.08	2.76	1.82	0.21	2.74	100.00	3.90
893	4.63	0.26	14.54	73.26	0.07	2.51	1.76	0.31	2.67	100.00	4.80
395	4.26	0.28	14.59	73.41	0.11	2.46	1.88	0.08	2.93	100.00	4.77
900	4.75	0.30	14.70	73.02	0.10	2.56	1.87	0.14	2.57	100.00	2.94
902	4.57	0.25	14.63	73.06	0.10	2.74	1.76	0.22	2.67	100.00	1.64
903	4.63	0.31	14.35	73.23	0.11	2.66	1.72	0.26	2.74	100.00	2.26

MEAN

n	Na2O	MgO	Al2O3	SiO2	Cl	K2O	CaO	TiO2	Fe2O3	Total	H2O
13	4.58	0.29	14.72	72.95	0.09	2.58	1.89	0.17	2.74	100.00	2.77
1 SD	0.13	0.05	0.35	0.40	0.03	0.15	0.17	0.09	0.17	-	1.57

Appendix 2.1 (continued)

Core   EW0403-40JC
Sample depth: 9.08 mbsf (I;

UNNORMALIZED RAW DATA

Line Numbers	Na$_2$O (%)	MgO (%)	Al$_2$O$_3$ (%)	SiO$_2$ (%)	Cl (%)	K$_2$O (%)	CaO (%)	TiO$_2$ (%)	Fe$_2$O$_3$ (%)	Total	Formula H$_2$O	100% Normalization factor
1671	5.08	0.30	14.34	69.18	0.10	2.51	1.76	0.14	3.03	96.43	3.57	1.037912096
1672	4.61	0.28	14.13	69.36	0.07	2.46	1.69	0.33	2.64	95.78	4.22	1.044011952
1673	4.80	0.30	14.20	70.06	0.03	2.40	1.72	0.14	2.68	96.35	3.65	1.037917233
1678	4.78	0.26	13.70	69.71	0.06	2.67	1.58	0.33	2.68	95.75	4.25	1.044367303
1682	4.73	0.22	13.90	69.29	0.10	2.66	1.58	0.28	2.53	95.28	4.72	1.049548574
1686	4.84	0.30	13.94	68.46	0.04	2.46	1.69	0.33	2.69	94.56	5.44	1.05751901
1689	5.33	0.33	14.06	69.23	0.12	2.61	1.85	0.37	2.88	95.80	3.20	1.033106312
1690	4.52	0.28	13.29	68.88	0.13	2.42	1.45	0.28	2.64	93.89	6.11	1.065091873
1691	4.21	0.09	14.12	69.19	0.10	2.33	1.44	0.37	2.15	94.00	6.00	1.063835851
1692	4.86	0.22	13.55	69.35	0.10	2.24	1.54	0.37	2.63	94.88	5.12	1.053973279
1697	5.37	0.25	13.99	68.75	0.07	2.49	1.56	0.19	2.53	95.18	4.82	1.050639874
1698	4.43	0.28	14.33	70.54	0.07	2.63	1.68	0.22	2.87	97.06	2.94	1.030262341
1699	4.57	0.24	13.94	69.06	0.07	2.12	1.72	0.30	2.87	94.88	5.12	1.054006608
1700	4.29	0.80	13.07	68.89	0.03	2.16	1.65	0.31	3.65	94.86	5.14	1.054163348
1702	4.55	0.33	13.87	68.88	0.08	2.39	1.89	0.43	3.02	95.44	4.56	1.047741479
1703	5.04	0.30	14.03	69.09	0.09	2.48	1.63	0.43	2.50	95.61	4.39	1.045913671
1704	4.99	0.32	14.43	69.91	0.08	2.43	1.81	0.45	2.85	97.24	2.76	1.028428798
1705	5.34	0.31	14.12	69.12	0.07	2.61	1.59	0.39	2.81	96.37	3.63	1.037691711
1706	4.16	0.28	13.30	66.99	0.10	2.43	1.46	0.24	2.62	91.58	8.42	1.091948952
1707	5.10	0.28	14.28	69.67	0.04	2.42	1.82	0.35	2.87	96.83	3.17	1.032722202
1709	4.84	0.27	13.67	69.49	0.06	2.50	1.54	0.37	2.99	95.74	4.26	1.044524521

NORMALIZED

Line Numbers	Na$_2$O (%)	MgO (%)	Al$_2$O$_3$ (%)	SiO$_2$ (%)	Cl (%)	K$_2$O (%)	CaO (%)	TiO$_2$ (%)	Fe$_2$O$_3$ (%)	Total	Formula H$_2$O
1671	5.26	0.31	14.87	71.74	0.10	2.60	1.82	0.14	3.14	100.00	3.57
1672	5.03	0.29	14.75	72.42	0.07	2.57	1.76	0.35	2.76	100.00	4.22
1673	4.98	0.32	14.74	72.72	0.04	2.49	1.79	0.14	2.79	100.00	3.65
1678	4.99	0.27	14.30	72.80	0.06	2.79	1.65	0.35	2.80	100.00	4.25
1682	4.96	0.23	14.59	72.72	0.10	2.79	1.66	0.29	2.65	100.00	4.72
1686	4.91	0.32	14.74	72.40	0.04	2.60	1.79	0.35	2.84	100.00	5.44
1689	5.50	0.35	14.52	71.52	0.13	2.70	1.92	0.39	2.97	100.00	3.20
1690	4.82	0.30	14.16	73.36	0.14	2.57	1.54	0.29	2.82	100.00	6.11
1691	4.48	0.09	15.02	73.61	0.11	2.48	1.53	0.40	2.29	100.00	6.00
1692	5.13	0.24	14.29	73.09	0.10	2.36	1.63	0.39	2.77	100.00	5.12
1697	5.64	0.26	14.70	72.23	0.07	2.61	1.64	0.19	2.66	100.00	4.82
1698	4.56	0.29	14.76	72.88	0.08	2.71	1.73	0.22	2.96	100.00	2.94
1699	4.82	0.25	14.69	72.79	0.07	2.23	1.81	0.31	3.02	100.00	5.12
1700	4.53	0.84	13.78	72.63	0.04	2.27	1.74	0.33	3.85	100.00	5.14
1702	4.77	0.35	14.53	72.16	0.08	2.51	1.98	0.45	3.16	100.00	4.56
1703	5.27	0.32	14.68	72.26	0.10	2.60	1.71	0.45	2.62	100.00	4.39
1704	5.13	0.33	14.84	71.90	0.08	2.50	1.86	0.47	2.93	100.00	2.76
1705	5.54	0.32	14.65	71.73	0.07	2.71	1.65	0.41	2.92	100.00	3.63
1706	4.54	0.31	14.53	73.15	0.11	2.65	1.60	0.26	2.87	100.00	8.42
1707	5.27	0.29	14.75	71.94	0.04	2.50	1.87	0.37	2.96	100.00	3.17
1709	5.05	0.28	14.28	72.59	0.07	2.61	1.61	0.39	3.12	100.00	4.26

MEAN

n	Na2O	MgO	Al2O3	SiO2	Cl	K2O	CaO	TiO2	Fe2O3	Total	H2O
21	5.01	0.31	14.58	72.50	0.08	2.56	1.73	0.33	2.90	100.00	4.55
1 SD	0.33	0.13	0.28	0.55	0.03	0.15	0.12	0.10	0.30	-	1.30

Core: EW0408-40JC
Sample depth: 9.08 mbsf (II)

UNNORMALIZED RAW DATA

Line Numbers	Na$_2$O (%)	MgO (%)	Al$_2$O$_3$ (%)	SiO$_2$ (%)	Cl (%)	K$_2$O (%)	CaO (%)	TiO$_2$ (%)	Fe$_2$O$_3$ (%)	Total	Formula H$_2$O	100% Normalization factor
734	4.36	0.30	13.80	69.09	0.08	2.51	1.75	0.51	2.70	95.09	3.10	1.05
744	4.35	0.30	14.39	70.91	0.11	2.45	1.75	0.43	2.69	97.40	0.76	1.03
759	4.60	0.79	13.59	66.90	0.10	2.09	1.93	0.19	3.64	93.83	4.40	1.07
762	3.85	1.14	12.50	67.70	0.11	2.07	1.71	0.33	4.50	93.91	4.19	1.06
766	4.62	0.26	14.17	67.65	0.10	2.21	1.95	0.23	2.54	93.74	4.55	1.07
786	4.10	0.39	13.53	67.62	0.10	2.21	1.79	0.56	3.26	93.59	4.55	1.07
795	4.84	0.19	15.24	69.05	0.13	2.01	2.34	0.35	2.14	96.29	1.92	1.04

NORMALIZED

Line Numbers	Na$_2$O (%)	MgO (%)	Al$_2$O$_3$ (%)	SiO$_2$ (%)	Cl (%)	K$_2$O (%)	CaO (%)	TiO$_2$ (%)	Fe$_2$O$_3$ (%)	Total	Formula H$_2$O
734	4.98	0.36	14.64	71.77	0.07	2.66	1.80	0.78	2.95	100.00	3.10
744	4.56	0.36	14.91	71.96	0.09	2.55	1.76	0.64	2.87	100.00	0.76
759	5.33	0.95	14.61	70.43	0.09	2.25	2.01	0.30	4.03	100.00	4.40
762	4.45	1.39	13.41	71.16	0.10	2.22	1.78	0.51	4.98	100.00	4.19
766	5.36	0.32	15.26	71.36	0.09	2.38	2.03	0.36	2.82	100.00	4.55
786	4.76	0.48	14.57	71.34	0.09	2.35	1.87	0.88	3.64	100.00	4.55
795	5.47	0.23	15.98	70.89	0.11	2.11	2.38	0.53	2.31	100.00	1.92

MEAN

n	Na2O	MgO	Al2O3	SiO2	Cl	K2O	CaO	TiO2	Fe2O3	Total	H2O
7	5.03	0.58	14.77	71.27	0.09	2.36	1.95	0.57	3.37	100.00	3.35
1 SD	0.37	0.43	0.78	0.52	0.01	0.19	0.22	0.21	0.91	-	1.50

Appendix 2.1 (continued)

Core: EW0408-40JC
Sample depth: 9.80 mbsf

UNNORMALIZED
unavailable; please contact JA Addison directly for this data

NORMALIZED

Line Numbers	Na₂O (%)	MgO (%)	Al₂O₃ (%)	SiO₂ (%)	Cl (%)	K₂O (%)	CaO (%)	TiO₂ (%)	Fe₂O₃ (%)	Total	Formula H₂O
1832	5.73	0.30	14.58	72.28	0.06	2.24	1.54	0.33	2.94	100.00	1.20
1829	5.45	0.35	14.66	72.37	0.08	2.26	1.18	0.48	3.16	100.00	-0.18
1831	5.31	0.29	14.84	72.53	0.08	2.39	1.50	0.25	2.81	100.00	1.89
1814	5.53	0.28	14.38	72.54	0.07	2.28	1.63	0.33	2.95	100.00	2.07
1815	5.34	0.22	14.53	72.79	0.12	2.30	1.66	0.45	2.57	100.00	1.68
1813	5.66	0.32	14.45	72.93	0.08	2.20	1.43	0.21	2.63	100.00	2.44
1822	6.04	0.26	14.37	72.84	0.04	1.93	1.18	0.52	2.84	100.00	-0.71
1821	5.30	0.29	14.67	72.88	0.09	2.23	1.56	0.17	2.81	100.00	4.63
1820	5.72	0.30	14.33	72.90	0.12	2.07	1.37	0.29	2.91	100.00	1.89
1827	5.38	0.25	14.85	72.94	0.10	2.29	1.27	0.29	2.81	100.00	3.21
1830	5.35	0.27	14.67	73.01	0.08	2.26	1.35	0.45	2.56	100.00	0.90
1823	5.88	0.21	14.35	73.35	0.06	2.06	1.26	0.20	2.65	100.00	-0.80
1819	4.79	0.22	14.31	73.57	0.07	2.06	1.63	0.21	3.04	100.00	1.84
1835	3.82	0.29	14.66	74.15	0.13	2.23	1.79	0.17	3.06	100.00	3.88

MEAN

n	Na2O	MgO	Al2O3	SiO2	Cl	K2O	CaO	TiO2	Fe2O3	Total	H2O
14	5.36	0.28	14.53	72.93	0.08	2.20	1.46	0.31	2.85	100.00	1.71
1 SD	0.61	0.04	0.17	0.50	0.03	0.13	0.19	0.12	0.18	-	1.59

Core: EW0408-40JC
Sample depth: 10.00 mbsf

UNNORMALIZED
unavailable; please contact JA Addison directly for this data

NORMALIZED

Line Numbers	Na₂O (%)	MgO (%)	Al₂O₃ (%)	SiO₂ (%)	Cl (%)	K₂O (%)	CaO (%)	TiO₂ (%)	Fe₂O₃ (%)	Total	Formula H₂O
1811	6.51	0.29	14.29	72.11	0.10	2.13	1.52	0.34	2.71	100	3.89
1790	5.68	0.37	14.60	72.25	0.07	2.42	1.80	0.17	2.63	100	5.24
1799	5.60	0.24	14.55	72.35	0.09	2.36	1.76	0.25	2.80	100	3.40
1788	5.95	0.32	14.59	72.47	0.08	2.01	1.70	0.09	2.79	100	4.68
1777	6.17	0.28	14.77	72.58	0.07	2.25	1.12	0.17	2.59	100	5.72
1802	6.08	0.34	14.39	72.84	0.13	2.49	1.39	0.21	2.35	100	4.16
1783	5.51	0.26	14.17	73.39	0.04	2.54	1.60	0.00	2.49	100	5.81
1792	5.82	0.36	13.82	73.41	0.07	2.38	1.34	0.04	2.76	100	4.30
1784	5.43	0.27	14.06	73.69	0.11	2.37	1.25	0.34	2.49	100	5.45
1793	5.48	0.23	14.13	73.93	0.10	1.81	1.30	0.63	2.40	100	3.61

MEAN

n	Na2O	MgO	Al2O3	SiO2	Cl	K2O	CaO	TiO2	Fe2O3	Total	H2O
10	5.82	0.29	14.34	72.88	0.09	2.28	1.48	0.22	2.60	100.00	4.61
1 SD	0.35	0.05	0.30	0.65	0.03	0.23	0.23	0.18	0.16	-	0.91

Core: EW0408-40JC
Sample depth: 10.29 mbsf

UNNORMALIZED
unavailable; please contact JA Addison directly for this data

NORMALIZED

Line Numbers	Na₂O (%)	MgO (%)	Al₂O₃ (%)	SiO₂ (%)	Cl (%)	K₂O (%)	CaO (%)	TiO₂ (%)	Fe₂O₃ (%)	Total	Formula H₂O
1592	6.16	0.28	14.57	71.85	0.06	2.59	1.75	0.10	2.65	100.00	3.19
1593	6.27	0.24	14.63	72.27	0.12	2.67	1.62	0.35	2.83	100.00	4.48
1594	4.81	0.25	14.41	73.05	0.09	2.43	1.62	0.60	2.74	100.00	5.28
1508	5.00	0.31	14.68	72.00	0.14	2.81	1.78	0.47	3.03	100.00	2.08
1600	5.59	0.30	14.60	71.71	0.13	2.76	1.78	0.38	2.76	100.00	6.51
1601	4.54	0.35	14.54	72.28	0.09	2.58	1.87	0.35	3.41	100.00	3.46
1802	5.37	0.32	14.62	72.29	0.09	2.51	1.84	0.19	2.81	100.00	4.80
1603	4.44	0.31	14.26	73.31	0.11	2.36	1.62	0.75	2.83	100.00	5.62
1605	4.95	0.33	14.73	72.66	0.13	2.50	1.62	0.30	2.79	100.00	7.18
1607	4.58	0.30	14.74	72.32	0.07	2.52	1.83	0.55	2.99	100.00	3.63
1610	4.75	0.25	14.43	73.11	0.07	2.73	1.58	0.41	2.68	100.00	4.63
1611	4.74	0.30	14.53	73.42	0.09	2.56	1.49	0.31	2.58	100.00	4.10
1614	4.58	0.32	14.88	72.81	0.05	2.59	1.80	0.12	2.86	100.00	5.35
1615	5.02	0.24	13.97	73.84	0.12	2.46	1.41	0.25	2.70	100.00	6.00
1620	5.48	0.26	14.61	71.95	0.07	2.53	1.66	0.45	3.09	100.00	7.37
1621	5.00	0.31	14.67	71.99	0.09	2.57	1.36	0.28	3.15	100.00	3.15
1622	4.09	0.30	14.58	72.85	0.09	2.68	1.79	0.50	3.13	100.00	5.15
1623	5.32	0.26	14.48	72.83	0.07	2.60	1.77	0.27	2.39	100.00	4.54
1624	5.60	0.29	14.21	72.52	0.12	2.35	1.64	0.32	2.95	100.00	2.72
1625	4.66	0.25	14.66	72.52	0.08	2.64	1.51	0.48	2.89	100.00	5.54
1626	4.93	0.31	14.63	72.52	0.06	2.63	1.70	0.19	2.96	100.00	4.55
387	4.58	0.27	14.71	72.59	0.14	2.66	1.53	0.46	2.65	100.00	0.61
388	4.73	0.32	14.67	72.63	0.08	2.67	1.82	0.37	2.90	100.00	1.20
395	4.56	0.28	14.60	73.16	0.12	2.69	1.68	0.17	2.75	100.00	2.66
396	4.57	0.29	14.63	72.85	0.05	2.73	1.80	0.23	2.84	100.00	0.11
397	4.52	0.29	14.74	72.56	0.10	2.76	1.89	0.23	2.90	100.00	0.25
398	4.53	0.29	14.69	72.86	0.16	2.66	1.89	0.16	2.82	100.00	0.57
399	4.81	0.31	14.66	72.50	0.14	2.61	1.79	0.16	3.03	100.00	1.37
402	4.27	0.33	14.40	72.89	0.12	2.82	1.77	0.38	3.02	100.00	2.52
403	4.36	0.29	14.61	72.94	0.13	2.87	1.94	0.63	2.64	100.00	1.38
405	4.84	0.25	14.44	72.90	0.05	3.10	1.56	0.28	2.78	100.00	2.94
407	4.56	0.28	14.53	72.54	0.08	2.81	1.81	0.37	3.02	100.00	0.82
408	4.54	0.33	14.50	72.95	0.08	2.87	1.53	0.18	2.86	100.00	0.70
410	4.46	0.30	14.50	72.63	0.07	2.73	1.90	0.44	2.69	100.00	0.54
412	4.42	0.23	14.46	73.23	0.08	2.81	1.72	0.31	2.73	100.00	4.14
413	4.70	0.24	14.37	72.67	0.09	2.81	1.65	0.34	3.14	100.00	4.85
414	4.45	0.28	14.54	72.98	0.11	2.58	1.73	0.53	2.70	100.00	0.59
421	4.48	0.24	14.37	73.20	0.10	2.72	1.80	0.21	2.86	100.00	0.51
422	4.58	0.29	14.35	72.99	0.05	2.84	1.61	0.03	2.97	100.00	2.00
423	4.38	0.24	14.33	73.29	0.11	2.83	1.70	0.43	2.85	100.00	-0.82
430	4.72	0.25	14.69	72.72	0.07	2.91	1.79	0.24	2.61	100.00	2.71
431	4.44	0.22	14.45	73.13	0.09	2.94	1.64	0.32	2.78	100.00	0.51
432	4.44	0.24	14.71	72.95	0.10	2.63	1.73	0.39	2.80	100.00	0.97
433	4.55	0.28	14.84	73.14	0.08	2.65	1.73	0.21	2.55	100.00	0.78
434	4.53	0.33	14.80	72.95	0.11	2.63	1.64	0.05	2.78	100.00	1.12
436	4.69	0.28	14.87	72.57	0.09	2.57	1.83	0.28	2.72	100.00	0.28
437	4.53	0.19	15.12	72.54	0.11	2.92	1.79	0.19	2.60	100.00	0.51
438	4.59	0.24	14.55	73.00	0.07	2.63	1.83	0.30	2.79	100.00	0.61
417	5.00	0.20	16.34	71.39	0.05	2.42	2.23	0.14	2.18	100.00	2.47
409	5.11	0.21	16.10	71.44	0.10	2.23	2.35	0.07	2.10	100.00	-0.20
427	5.08	0.21	15.69	71.63	0.07	2.36	2.28	0.14	2.55	100.00	0.77
408	5.20	0.20	15.91	71.68	0.07	2.33	2.38	0.23	2.01	100.00	2.14
416	4.90	0.20	15.36	72.37	0.07	2.36	2.18	0.09	2.48	100.00	2.03
424	4.69	0.24	14.31	73.42	0.07	2.71	1.73	0.26	2.57	100.00	2.72
429	4.53	0.29	14.05	73.49	0.07	2.81	1.67	0.28	2.77	100.00	0.16
392	4.32	0.56	13.63	73.54	0.09	2.70	1.68	0.38	3.28	100.00	2.20
401	4.29	0.27	14.23	73.56	0.07	2.97	1.57	0.45	2.59	100.00	3.49
420	4.48	0.25	14.18	73.81	0.13	2.77	1.51	0.05	2.84	100.00	1.48

MEAN

n	Na2O	MgO	Al2O3	SiO2	Cl	K2O	CaO	TiO2	Fe2O3	Total	H2O
58	4.76	0.28	14.65	72.72	0.09	2.66	1.76	0.31	2.79	100.00	2.66
1 SD	0.39	0.05	0.48	0.57	0.03	0.18	0.20	0.15	0.25	-	2.05

Appendix 2.1 (continued)

Core: *EW0408-40JC*
Sample depth *10.49 mbsf*

UNNORMALIZED
unavailable: please contact JA Addison directly for this data

NORMALIZED

Line Numbers	Na$_2$O (%)	MgO (%)	Al$_2$C$_3$ (%)	SiO$_2$ (%)	Cl (%)	K$_2$O (%)	CaO (%)	TiO$_2$ (%)	Fe$_2$O$_3$ (%)	Total	Formula H$_2$O
1883	5.31	0.28	14.34	73.37	0.05	1.98	1.46	0.30	2.91	100.00	5.98
1885	4.60	0.36	14.76	73.20	0.12	2.11	1.82	0.33	2.70	100.00	1.84
1887	5.46	0.20	14.19	73.38	0.11	2.21	1.56	0.21	2.68	100.00	1.82
1888	4.99	0.32	14.36	73.51	0.12	2.22	1.46	0.13	2.88	100.00	4.25
1889	6.10	0.26	14.37	72.67	0.09	2.07	1.50	0.24	2.70	100.00	0.61
1890	5.11	0.23	14.87	73.51	0.13	1.88	1.30	0.12	2.84	100.00	2.43
1892	6.00	0.26	14.43	72.83	0.04	2.12	1.38	0.21	2.74	100.00	2.27
1893	5.71	0.31	14.53	72.48	0.07	2.23	1.27	0.41	3.00	100.00	1.68
1894	5.07	0.33	14.57	72.70	0.08	2.40	1.17	0.33	3.34	100.00	1.33
1895	5.15	0.31	14.88	72.60	0.10	2.37	1.32	0.37	2.89	100.00	0.76
1896	5.28	0.30	14.46	72.71	0.08	2.27	1.30	0.57	3.02	100.00	0.32
1899	5.65	0.28	14.21	72.79	0.09	2.28	1.38	0.41	2.92	100.00	0.11
1904	5.16	0.09	13.93	74.92	0.07	2.26	1.25	0.38	1.94	100.00	3.56
1908	5.78	0.38	14.81	72.22	0.08	1.82	1.80	0.41	2.71	100.00	0.62
1912	5.22	0.27	14.19	73.42	0.13	2.05	1.43	0.12	3.17	100.00	0.33
1913	4.92	0.41	14.48	73.66	0.07	1.96	1.38	0.13	2.99	100.00	3.24
1920	5.61	0.35	14.51	72.66	0.10	2.24	1.25	0.41	2.86	100.00	1.49
1921	5.16	0.26	15.00	72.47	0.09	2.42	1.50	0.37	2.73	100.00	1.23
1922	5.43	0.18	15.73	72.58	0.12	1.85	1.81	0.42	1.88	100.00	4.03
1923	5.75	0.32	14.56	72.48	0.13	2.36	1.19	0.20	3.01	100.00	0.63

MEAN

n	Na2O	MgO	Al2O3	SiO2	Cl	K2O	CaO	TiO2	Fe2O3	Total	H2O
20	5.37	0.29	14.56	73.01	0.09	2.16	1.43	0.30	2.80	100.00	1.93
1 SD	0.38	0.07	0.38	0.62	0.03	0.18	0.20	0.13	0.35	-	1.57

Core: *EW0408-40JC*
Sample depth *10.82 mbsf*

UNNORMALIZED
unavailable; please contact JA Addison directly for this data

NORMALIZED

Line Numbers	Na$_2$O (%)	MgO (%)	Al$_2$O$_3$ (%)	SiO$_2$ (%)	Cl (%)	K$_2$O (%)	CaO (%)	TiO$_2$ (%)	Fe$_2$O$_3$ (%)	Total	Formula H$_2$O
1836	5.12	0.22	14.22	73.82	0.12	2.27	1.59	0.25	2.39	100.00	1.65
1837	4.94	0.22	15.13	73.13	0.11	2.22	1.80	0.04	2.41	100.00	2.92
1839	5.73	0.26	15.11	72.15	0.11	1.88	1.96	0.24	2.56	100.00	-0.27
1840	5.55	0.29	14.15	73.87	0.06	2.24	1.19	0.13	2.52	100.00	2.97
1841	4.89	0.36	14.96	72.92	0.08	2.18	1.84	0.00	2.78	100.00	2.52
1842	5.29	0.30	15.10	72.43	0.04	1.90	1.76	0.45	2.71	100.00	1.05
1843	6.35	0.25	14.44	72.12	0.09	1.86	1.59	0.28	3.00	100.00	-0.12
1844	5.78	0.21	13.68	74.41	0.07	2.13	1.06	0.13	2.53	100.00	3.45
1845	5.73	0.25	14.54	73.30	0.10	1.87	1.54	0.21	2.47	100.00	2.52
1847	6.26	0.30	14.87	71.91	0.09	2.34	1.22	0.00	3.00	100.00	0.08
1849	5.33	0.22	14.70	73.12	0.08	2.41	1.27	0.13	2.76	100.00	3.62
1850	5.30	0.24	14.34	73.06	0.08	2.31	1.20	0.41	3.05	100.00	2.28
1851	5.40	0.27	13.91	73.51	0.07	2.17	1.19	0.32	3.16	100.00	-1.35
1852	5.45	0.25	15.77	71.45	0.07	2.05	2.23	0.41	2.31	100.00	1.07
1853	5.49	0.24	14.51	73.58	0.09	2.19	1.10	0.00	2.81	100.00	1.99
1854	5.54	0.24	14.14	72.29	0.14	2.39	1.69	0.51	3.06	100.00	3.88
1860	5.28	0.33	14.54	72.82	0.10	2.21	1.65	0.13	2.94	100.00	3.90
1864	5.26	0.26	14.75	73.24	0.08	2.14	1.36	0.29	2.61	100.00	1.65
1865	5.05	0.26	14.39	74.30	0.08	2.09	1.30	0.00	2.53	100.00	2.81
1866	5.52	0.28	14.50	73.01	0.07	2.25	1.54	0.16	2.67	100.00	-0.17
1869	5.00	0.33	15.04	71.92	0.07	2.46	1.34	0.16	3.68	100.00	-0.75
1872	5.74	0.25	14.37	73.02	0.09	2.30	1.16	0.45	2.63	100.00	1.06
1873	4.98	0.27	14.78	73.45	0.04	2.31	1.15	0.30	2.72	100.00	4.91
1874	5.56	0.29	14.56	72.38	0.06	2.25	1.59	0.54	2.77	100.00	2.55
1875	5.67	0.18	14.82	72.51	0.05	2.34	1.75	0.00	2.68	100.00	1.36
1876	5.45	0.27	14.54	72.92	0.09	2.26	1.40	0.08	2.99	100.00	2.59
1877	5.02	0.19	14.13	73.56	0.11	2.70	1.21	0.37	2.70	100.00	0.02

MEAN

n	Na2O	MgO	Al2O3	SiO2	Cl	K2O	CaO	TiO2	Fe2O3	Total	H2O
27	5.43	0.26	14.59	72.97	0.08	2.21	1.47	0.22	2.76	100.00	1.81
1 SD	0.37	0.04	0.44	0.74	0.02	0.19	0.30	0.17	0.29	-	1.60

Appendix 2.1 (continued)

Core: EW0408-40JC
Sample depth: 11.08 mbsf

UNNORMALIZED RAW DATA

Line Numbers	Na₂O (%)	MgO (%)	Al₂O₃ (%)	SiO₂ (%)	Cl (%)	K₂O (%)	CaO (%)	TiO₂ (%)	Fe₂O₃ (%)	Total	Formula H₂O	100% Normalization factor
1387	4.74	0.23	13.74	68.95	0.15	2.32	1.54	0.38	2.49	94.54	5.46	1.05777703
1389	4.64	0.39	13.28	68.26	0.10	2.36	1.52	0.26	2.93	93.75	6.25	1.06665347
1391	5.32	0.30	13.69	70.81	0.16	2.58	1.47	0.26	2.83	97.40	2.60	1.026675546
1392	4.74	0.29	14.13	70.20	0.15	2.45	1.49	0.45	2.71	96.60	3.40	1.035222772
1394	4.68	0.22	13.95	71.93	0.09	2.39	1.31	0.31	2.66	97.52	2.48	1.025391335
1397	4.88	0.45	14.19	68.92	0.08	2.41	1.79	0.25	3.06	96.03	3.97	1.04133652
1398	4.92	0.22	14.36	70.71	0.05	2.31	1.25	0.23	2.87	96.72	3.28	1.033938814
1399	4.35	0.29	14.45	72.87	0.07	2.40	1.53	0.35	2.67	99.49	0.51	1.005174993
1401	4.90	0.29	14.40	70.92	0.05	2.45	1.64	0.29	2.56	97.49	2.51	1.025694814
1402	4.93	0.30	14.39	70.98	0.11	2.42	1.30	0.45	2.94	97.83	2.17	1.022132407
1403	5.24	0.27	14.21	71.80	0.06	2.47	1.63	0.20	2.84	98.72	1.28	1.012932627
1404	4.96	0.29	14.44	72.23	0.05	2.35	1.54	0.25	3.00	99.11	0.89	1.008944261
1406	4.94	0.26	13.81	71.17	0.04	2.20	1.37	0.22	2.59	96.60	3.40	1.03514972
1410	4.89	0.27	14.39	72.16	0.07	2.55	1.51	0.42	2.83	99.11	0.89	1.008967624
1412	4.78	0.23	12.56	65.84	0.09	2.33	1.35	0.40	2.69	90.33	9.67	1.107066799
1413	4.97	0.32	14.14	71.92	0.07	2.43	1.65	0.32	3.18	99.00	1.00	1.010119366
1414	4.73	0.29	13.51	69.29	0.04	2.44	1.54	0.41	3.12	95.38	4.62	1.048468233
1415	4.98	0.30	13.93	69.51	0.09	2.25	1.56	0.28	2.76	95.66	4.34	1.045367748
1417	5.21	0.29	13.69	69.77	0.13	2.49	1.69	0.27	3.08	96.62	3.38	1.034997959

NORMALIZED

Line Numbers	Na₂O (%)	MgO (%)	Al₂O₃ (%)	SiO₂ (%)	Cl (%)	K₂O (%)	CaO (%)	TiO₂ (%)	Fe₂O₃ (%)	Total	Formula H₂O
1387	5.01	0.24	14.53	72.93	0.16	2.46	1.63	0.40	2.63	100.00	5.46
1389	4.95	0.42	14.16	72.81	0.11	2.52	1.62	0.28	3.12	100.00	6.25
1391	5.46	0.30	14.26	72.50	0.16	2.63	1.51	0.27	2.91	100.00	2.60
1392	4.91	0.30	14.63	72.67	0.15	2.54	1.54	0.46	2.80	100.00	3.40
1394	4.80	0.23	14.30	73.76	0.09	2.45	1.34	0.32	2.72	100.00	2.48
1397	5.08	0.46	14.77	71.77	0.09	2.51	1.86	0.27	3.19	100.00	3.97
1398	5.08	0.23	14.85	73.11	0.05	2.39	1.29	0.24	2.76	100.00	3.28
1399	4.88	0.29	14.52	73.25	0.08	2.41	1.54	0.35	2.69	100.00	0.51
1401	5.03	0.30	14.77	72.74	0.05	2.51	1.68	0.30	2.62	100.00	2.51
1402	5.04	0.31	14.71	72.55	0.12	2.48	1.33	0.46	3.01	100.00	2.17
1403	5.31	0.27	14.39	72.73	0.06	2.50	1.65	0.21	2.88	100.00	1.28
1404	5.01	0.29	14.57	72.87	0.05	2.37	1.56	0.25	3.03	100.00	0.89
1406	5.11	0.27	14.30	73.67	0.04	2.28	1.42	0.23	2.69	100.00	3.40
1410	4.93	0.28	14.52	72.81	0.07	2.57	1.53	0.42	2.86	100.00	0.89
1412	5.29	0.32	13.90	72.89	0.10	2.58	1.49	0.44	2.98	100.00	9.67
1413	5.02	0.32	14.28	72.65	0.07	2.45	1.67	0.32	3.21	100.00	1.00
1414	4.96	0.31	14.17	72.65	0.04	2.55	1.62	0.43	3.27	100.00	4.62
1415	5.20	0.31	14.56	72.67	0.09	2.35	1.63	0.29	2.88	100.00	4.34
1417	5.39	0.30	14.17	72.21	0.13	2.58	1.75	0.28	3.19	100.00	3.38

MEAN

n	Na2O	MgO	Al2O3	SiO2	Cl	K2O	CaO	TiO2	Fe2O3	Total	H2O
19	5.08	0.30	14.44	72.80	0.09	2.48	1.56	0.33	2.92	100.00	3.27
1 SD	0.18	0.06	0.25	0.45	0.04	0.09	0.15	0.08	0.21	-	2.23

Core: EW0408-40JC
Sample depth: 11.10 mbsf

UNNORMALIZED
unavailable; please contact JA Addison directly for this data

NORMALIZED

Line Numbers	Na₂O (%)	MgO (%)	Al₂O₃ (%)	SiO₂ (%)	Cl (%)	K₂O (%)	CaO (%)	TiO₂ (%)	Fe₂O₃ (%)	Total	Formula H₂O
1926	5.40	0.25	13.52	73.49	0.08	2.35	1.41	0.47	3.02	100	4.00
1929	6.21	0.10	14.41	72.82	0.09	2.50	1.32	0.54	2.02	100	1.47
1930	5.34	0.22	14.59	72.30	0.07	2.47	1.85	0.62	2.54	100	1.08
1931	6.31	0.31	14.33	72.10	0.05	2.38	1.52	0.08	2.81	100	0.37
1932	5.64	0.19	14.28	72.58	0.11	2.26	1.78	0.49	2.68	100	1.42
1934	4.99	0.29	14.81	73.12	0.10	2.41	1.67	0.00	2.61	100	1.52
1935	5.14	0.23	14.90	73.23	0.08	2.33	1.62	0.21	2.27	100	2.07
1936	5.02	0.28	14.66	73.24	0.04	2.32	1.49	0.25	2.72	100	1.10
1937	5.37	0.28	14.78	72.93	0.10	2.14	1.43	0.25	2.73	100	0.97
1938	4.68	0.43	14.47	73.22	0.08	1.94	1.67	0.53	2.87	100	3.73
1940	4.95	0.18	14.88	73.65	0.05	2.37	1.21	0.45	2.26	100	0.47
1941	5.72	0.25	14.36	72.96	0.03	2.39	1.49	0.16	2.63	100	1.53
1942	5.55	0.28	14.75	72.62	0.10	2.13	1.80	0.00	2.77	100	2.54
1943	6.01	0.35	14.64	72.00	0.11	2.14	1.41	0.41	2.92	100	1.79
1944	5.46	0.25	14.54	72.71	0.10	2.18	1.52	0.21	3.02	100	2.34
1945	5.15	0.29	13.96	73.34	0.10	2.52	1.47	0.37	2.80	100	1.60
1947	5.31	0.28	14.93	73.04	0.06	2.44	1.06	0.45	2.45	100	-0.30
1949	5.85	0.24	14.35	72.60	0.13	2.52	0.98	0.37	2.96	100	1.50
1951	5.31	0.32	14.29	73.63	0.08	2.45	1.04	0.00	2.88	100	2.24
1952	4.93	0.21	14.07	74.00	0.13	2.42	1.29	0.04	2.91	100	1.05
1953	5.54	0.23	14.34	72.16	0.10	2.37	1.78	0.50	2.99	100	1.82
1954	5.29	0.19	15.31	72.38	0.11	2.08	1.64	0.37	2.63	100	0.54
1955	5.50	0.25	14.39	73.08	0.14	2.29	1.34	0.29	2.74	100	1.45
1957	5.76	0.34	14.78	72.20	0.07	2.47	1.41	0.08	2.90	100	1.41
1958	5.60	0.22	14.60	72.79	0.06	2.67	1.32	0.21	2.53	100	1.06
1959	6.10	0.32	14.53	72.14	0.03	2.40	1.63	0.13	2.52	100	3.07
1960	5.67	0.21	13.82	73.80	0.12	2.64	0.96	0.29	2.50	100	3.31
1961	5.57	0.24	15.27	73.46	0.09	2.28	1.24	0.00	1.86	100	1.66
1964	4.90	0.28	14.67	73.32	0.09	2.49	1.16	0.38	2.71	100	4.91

MEAN

n	Na2O	MgO	Al2O3	SiO2	Cl	K2O	CaO	TiO2	Fe2O3	Total	H2O
29	5.46	0.26	14.53	72.93	0.09	2.36	1.44	0.28	2.66	100.00	1.79
1 SD	0.41	0.06	0.39	0.55	0.03	0.17	0.26	0.19	0.29	-	1.14

Appendix 2.1 (continued)

Core   *EW0408-40JC*
Sample depth.   *11.20 mbsf*

UNNORMALIZED
unavailable: please contact JA Addison directly for this data

NORMALIZED

Line Numbers	Na₂O (%)	MgO (%)	Al₂O₃ (%)	SiO₂ (%)	Cl (%)	K₂O (%)	CaO (%)	TiO₂ (%)	Fe₂O₃ (%)	Total	Formula H₂O
1630	5.47	0.29	14.68	72.10	0.06	2.55	1.77	0.20	2.88	100.00	3.51
1631	5.55	0.28	14.70	71.97	0.08	2.45	1.66	0.27	3.04	100.00	3.80
1632	5.75	0.30	14.76	71.91	0.01	2.41	1.89	0.25	2.71	100.00	4.28
1635	4.32	0.29	14.79	72.84	0.11	2.72	1.79	0.10	3.03	100.00	5.65
1637	6.85	0.38	14.72	72.29	0.07	2.82	1.90	0.33	2.84	100.00	4.63
1639	4.99	0.35	14.78	71.69	0.13	2.62	1.76	0.47	3.01	100.00	3.05
1640	4.99	0.33	14.60	72.26	0.14	2.65	1.81	0.43	2.80	100.00	3.80
1641	5.41	0.63	14.49	71.52	0.08	2.46	1.94	0.41	3.07	100.00	3.57
1642	5.35	0.29	14.76	71.87	0.08	2.49	1.91	0.36	2.89	100.00	2.69
1644	5.28	0.27	14.29	72.60	0.11	2.68	1.09	0.26	2.90	100.00	2.76
1645	4.71	0.53	14.07	73.35	0.14	2.41	1.49	0.15	3.36	100.00	5.83
1646	5.36	0.34	14.68	71.90	0.11	2.50	1.86	0.35	2.86	100.00	4.83
1649	5.60	0.30	14.78	71.36	0.08	2.59	1.86	0.28	3.15	100.00	2.19
1650	5.22	0.29	14.63	72.84	0.12	2.65	1.64	0.27	2.33	100.00	4.48
1654	4.72	0.32	13.62	73.77	0.06	2.91	1.25	0.43	2.92	100.00	7.64
1656	4.55	0.25	14.32	73.39	0.11	2.65	1.56	0.35	2.82	100.00	5.52
1657	4.86	0.28	14.48	72.42	0.08	2.71	1.74	0.43	3.00	100.00	3.98
1659	4.74	0.25	14.47	73.24	0.09	2.45	1.61	0.34	2.82	100.00	7.75
1662	4.79	0.28	14.72	72.62	0.10	2.68	1.74	0.19	2.88	100.00	4.66
1663	5.57	0.35	14.78	71.49	0.05	2.55	1.86	0.43	2.90	100.00	3.50
1666	4.83	0.28	14.78	72.25	0.08	2.48	1.84	0.49	2.91	100.00	4.63

MEAN

n	Na2O	MgO	Al2O3	SiO2	Cl	K2O	CaO	TiO2	Fe2O3	Total	H2O
21	5.09	0.32	14.57	72.37	0.09	2.58	1.74	0.32	2.91	100.00	4.43
1 SD	0.40	0.08	0.29	0.67	0.03	0.12	0.17	0.11	0.19	-	1.46

Core: *EW0408-17JC*
Sample depth: *6.46 mbsf (I) & (II)*

UNNORMALIZED RAW DATA

Line Numbers	Na₂O (%)	MgO (%)	Al₂O₃ (%)	SiO₂ (%)	Cl (%)	K₂O (%)	CaO (%)	TiO₂ (%)	Fe₂O₃ (%)	Total	Formula H₂O	100% Normalization factor	POPULATION
1132	4.639512	0.669479	13.59266	65.27638	0.133375	1.903853	2.514588	0.324226	3.737479	90.69203	9.307987	1.102633687	2
1133	5.218019	0.289653	14.63042	71.36729	0.053928	2.656304	1.595417	0.22144	2.821501	98.65397	1.146027	1.01159313	1
1134	5.363358	0.358111	13.82792	70.10425	0.098702	2.460503	1.646287	0.343623	2.966036	97.16679	2.83121	1.029137031	1
1135	4.994672	0.297357	14.20361	71.79261	0.134324	2.580903	1.698829	0.230572	2.640594	93.57387	1.426126	1.014467586	1
1136	5.052862	0.248736	13.99744	71.15466	0.113892	2.482777	1.75927	0.160179	2.762254	97.71223	2.287712	1.023412736	1
1140	5.216774	0.639237	15.01425	67.46873	0.081598	1.901022	2.797999	0.625031	3.877088	97.62172	2.278276	1.024362159	2
1141	5.062311	0.247083	15.16947	68.45419	0.019558	2.136793	2.717689	0.375757	4.229073	99.2119	0.783103	1.007943634	2
1143	4.650997	0.23639	14.46952	72.2223	0.10223	2.511715	1.55269	0.273262	2.957364	98.95643	1.043566	1.010545711	1
1144	4.875326	0.275281	13.98459	71.88999	0.058059	2.865132	1.718012	0.315945	2.482591	98.06492	1.935081	1.019752653	1
1146	5.385819	0.675773	15.05863	67.31763	0.061339	1.993885	2.761721	0.592131	3.713735	97.55465	2.435347	1.024961386	2
1147	4.776947	0.638433	13.86938	63.57019	0.060065	1.832491	2.234034	0.343386	3.303253	90.62828	9.371723	1.103406377	2
1154	5.113704	0.248069	13.55251	72.28371	0.100552	2.53874	1.593831	0.270068	2.625784	98.31477	1.885234	1.017141209	1
1156	5.177392	0.268111	13.9987	70.02615	0.122845	2.399768	1.549567	0.381441	2.751375	96.67595	3.324052	1.034383454	1
1157	4.723346	0.489432	13.10366	65.79337	0.113451	2.494534	1.808608	0.211895	3.060787	94.59926	5.400736	1.057090677	1
1159	4.659259	0.251916	13.5423	71.28478	0.048391	2.632148	1.522287	0.273233	2.902681	97.01709	2.982913	1.030746264	1
1162	5.000344	0.286048	14.41063	72.62708	0.193352	2.31227	1.776368	0.371961	3.285299	100.3336	-0.333549	0.996674605	1
1163	5.019041	0.330905	14.0709	72.48049	0.115921	2.431634	1.692285	0.235511	3.163083	99.54698	0.450019	1.004520533	1
1164	4.642804	0.315924	14.54281	73.29491	0.06436	2.682478	1.949466	0.409627	3.259817	101.052	-1.061995	0.98949184	1
1165	5.036411	0.259306	13.64008	72.05222	0.060588	2.538942	1.515055	0.400163	3.041084	98.74185	1.258145	1.01274177	1
1166	5.20251	0.726469	14.61813	66.02523	0.051693	1.899853	2.67395	0.378198	3.904176	95.6802	4.319799	1.045148306	2
1167	5.215014	0.729963	15.28028	63.73936	0.054351	2.013593	2.781174	0.43886	4.111455	99.33435	0.865855	1.008701157	2
1168	5.002598	0.766992	15.26115	87.96509	0.099046	1.913875	2.777103	0.724692	3.69661	98.23676	1.763242	1.017949903	2
1170	5.325482	0.644897	14.85213	69.11549	0.086038	2.078936	2.520346	0.601388	4.09872	99.32312	0.676877	1.006814893	2
1171	4.765526	0.541742	14.29866	69.1376	0.056395	1.931032	2.402129	0.378676	3.514881	94.00494	5.995065	1.063773939	2

POPULATION 1

NORMALIZED

Line Numbers	Na₂O (%)	MgO (%)	Al₂O₃ (%)	SiO₂ (%)	Cl (%)	K₂O (%)	CaO (%)	TiO₂ (%)	Fe₂O₃ (%)	Total	Formula H₂O
1133	5.28	0.29	14.80	72.19	0.05	2.69	1.61	0.22	2.85	100.00	1.15
1134	5.52	0.37	14.23	72.15	0.10	2.53	1.69	0.35	3.05	100.00	2.83
1135	5.07	0.30	14.41	72.83	0.14	2.62	1.72	0.23	2.68	100.00	1.43
1136	5.15	0.25	14.33	72.82	0.12	2.54	1.90	0.16	2.83	100.00	2.29
1143	4.68	0.24	14.62	72.98	0.10	2.54	1.57	0.28	2.98	100.00	1.04
1144	4.97	0.28	14.26	73.10	0.06	2.72	1.75	0.32	2.53	100.00	1.94
1154	5.20	0.25	13.78	73.50	0.10	2.58	1.62	0.28	2.67	100.00	1.69
1156	5.36	0.28	14.48	72.43	0.13	2.48	1.60	0.39	2.85	100.00	3.32
1157	4.99	0.52	13.85	72.72	0.12	2.64	1.79	0.22	3.24	100.00	5.40
1159	4.80	0.26	13.96	73.48	0.05	2.61	1.57	0.28	2.99	100.00	2.98
1162	5.07	0.27	14.36	72.39	0.19	2.30	1.77	0.37	3.27	100.00	-0.33
1163	5.04	0.33	14.13	72.82	0.12	2.44	1.70	0.24	3.18	100.00	0.45
1164	4.59	0.31	14.39	72.52	0.06	2.65	1.93	0.41	3.23	100.00	-1.06
1165	5.10	0.26	14.02	72.97	0.06	2.57	1.53	0.41	3.08	100.00	1.26

MEAN

n	Na2O	MgO	Al2O3	SiO2	Cl	K2O	CaO	TiO2	Fe2O3	Total	H2O
14	5.06	0.30	14.26	72.78	0.10	2.57	1.68	0.30	2.96	100.00	1.74
1 SD	0.25	0.07	0.29	0.42	0.04	0.11	0.09	0.08	0.23	-	1.62

POPULATION 2

NORMALIZED

Line Numbers	Na₂O (%)	MgO (%)	Al₂O₃ (%)	SiO₂ (%)	Cl (%)	K₂O (%)	CaO (%)	TiO₂ (%)	Fe₂O₃ (%)	Total	Formula H₂O
1132	5.01	0.74	14.99	69.77	0.15	2.10	2.77	0.36	4.12	100.00	9.01
1140	5.34	0.65	15.38	69.11	0.08	1.95	2.87	0.64	3.97	100.00	2.58
1141	5.40	0.75	15.26	69.00	0.02	2.15	2.74	0.38	4.26	100.00	0.79
1146	5.52	0.70	15.43	69.00	0.06	2.04	2.83	0.61	3.81	100.00	2.44
1147	5.27	0.70	15.30	70.14	0.07	2.02	2.47	0.38	3.64	100.00	9.37
1166	5.44	0.76	15.28	69.01	0.05	1.99	2.79	0.60	4.03	100.00	4.52
1167	5.25	0.73	15.38	69.20	0.05	2.03	2.30	0.41	4.14	100.00	0.87
1168	5.09	0.73	15.54	69.22	0.10	1.95	2.83	0.74	3.76	100.00	1.75
1170	5.36	0.65	14.95	69.59	0.09	2.09	2.54	0.61	4.13	100.00	0.68
1171	5.07	0.58	15.21	70.36	0.04	2.05	2.56	0.40	3.74	100.00	5.00

MEAN

n	Na2O	MgO	Al2O3	SiO2	Cl	K2O	CaO	TiO2	Fe2O3	Total	H2O
10	5.29	0.70	15.28	69.44	0.07	2.04	2.72	0.51	3.97	100.00	3.77
1 SD	0.17	0.06	0.18	0.50	0.04	0.07	0.14	0.14	0.21	-	3.39

Chapter 3 Holocene evolution of the Pacific Decadal Oscillation in the Gulf of Alaska[1]

3.1 Abstract

Sediment core EW0408-33JC is the first high-resolution marine record from the Subarctic Northeast Pacific Ocean that demonstrates environmental variability at decadal- to centennial-timescales over the last 7,500 years. This variability is likely associated with the Pacific Decadal Oscillation (PDO). By comparing the biogeochemical record of this marine core with terrestrial records from the adjacent continent, we are able to interpret the composite record in terms of both atmosphere/ocean variability and marine ecosystem change. Our analysis indicates that the onset of modern PDO variability began about 4,000 years ago with the onset of the Holocene Neoglacial cooling period. Furthermore, we also provide evidence that shows the current binary model of PDO regime shifts is inadequate to fully encompass the Holocene record of environmental and ecosystem change in the North Pacific Ocean.

---

[1]J.A. Addison, and B.P. Finney, prepared for submission to *Science*.

3.2 Introduction

The Subarctic Northeast Pacific Ocean is a unique area where atmospheric circulation and oceanography are linked with marine ecosystem variability. This region, dominated by the Gulf of Alaska basin (Fig. 3.1), is the modern terminus of the global thermohaline circulation system yet its significance as a key contributor to global climate remains largely overlooked. Instrumental data of Northern Hemisphere sea level pressure (SLP) show evidence of teleconnections between the Subarctic North Pacific, the Equatorial Pacific, the American Midwest and Southeast, and the Sonora Desert regions (*1-3*). Outputs from coupled atmosphere-ocean general circulation models have also shown that changes in the Northeast Pacific can be an important driver for Northern Hemisphere climate, particularly during periods of abrupt climate change (*4*).

Seasonal atmospheric dynamics in the Gulf of Alaska are controlled by the position and intensity of the Aleutian Low (AL) pressure cell (Fig. 3.1; *5*). During the winter, the center of the AL is located in the central Northeast Pacific Ocean where it contributes to reduced sea surface temperatures (SST) and SLP, increased precipitation, and intensification of the northeastern storm track (*2*). The AL-driven reduced SLP also leads to enhanced upwelling in the Alaska Gyre, a high-nitrate-low-chlorophyll zone (HNLC; *6*). The cyclonic rotation of the Alaska Gyre leads to horizontal advection of shallow nutrient-rich water towards the continental shelf of the Gulf of Alaska where it contributes to large phytoplankton blooms in the spring and summer (*7*). Concurrent with the spring bloom is the spring freshet along the margin when freshwater discharge into the Gulf of Alaska is at a maximum (*8*). This low-salinity Alaska Coastal Current water circumnavigates the inner shelf of the Gulf of Alaska in a cyclonic fashion (Fig. 3.1), and leads to the development of a pronounced halocline (*7*). The advected nutrients from the Alaska Gyre, and the enhanced stratification present along the shelf due to reduced salinity from freshwater discharge, are thought to trigger the high seasonal primary productivity and the associated economically valuable Gulf of Alaska commercial fisheries, particularly in the case of Pacific salmon populations (*7, 9*). The high fluvial discharge also contributes significant amounts of the micronutrient iron to the

HNLC Gulf of Alaska, which likely plays a role in stimulating the strong seasonal productivity signal as well (*6, 10, 11*).

Interdecadal variability in the atmosphere and Gulf of Alaska ocean conditions has been recognized in instrumental records of SST, SLP, precipitation, freshwater river discharge, and wind stress fields. These physical parameters indicate several shifts between decadal-scale regimes during the last century, with the most distinctive recent shift occurring during AD 1976/1977 (*1, 2, 12*). The marine ecosystem also underwent contemporaneous changes in the abundance of phytoplankton and zooplankton (*13*), and contributed to a notable increase in Alaskan salmon catch records likely due to bottom-up forcing (*14*).

These historical regime shifts have been linked to the PDO, defined as the leading principal component of variability in North Pacific SST, and have been used to characterize shifts on 40-to-70 year time scales throughout the 20th century (*15, 16*). The primary forcing mechanism of the PDO is the strength and position of the AL pressure system (*2, 3*). The AL cell oscillates between an intensified locus in the eastern Aleutian Islands, while the less intense locus occurs in the western Aleutian Islands (Fig. 3.1; *17*). AL activity is more directly described by the North Pacific Index which exhibits decadal-scale variability (*2*), and strongly correlates with the PDO (*15*). PDO-associated downstream variability has also been observed in the tropical Pacific, with changes in the volume and heat transport of the Indonesian Throughflow during PDO regime shifts (*18*), reinforcing the notion that marine conditions in the Subarctic Northeast Pacific Ocean are strongly linked with global circulation and climate.

Records of PDO and AL variability extending beyond 20th century observations are rare. Several annually-resolved datasets exist from the Gulf of Alaska margin that describe terrestrial and marine variability, but these capture only the last 1,300 years of regional climate variability (*19-21*). Older paleoenvironmental records from the region are confounded by a lack of high temporal resolution. A notable exception is the Prospector Ridge Col ice core from Mt. Logan in the St. Elias Range (Fig. 3.1; *22*). In this study, we present the first high-resolution marine sediment record from the Gulf of

Alaska that exhibits decadal-scale behavior, and interpret this record in terms of AL variability and ecosystem change. We combine these new findings with other regionally important datasets to develop an integrated model of climate-ocean dynamics and associated ecosystem linkages for the last 7,500 years.

Marine sedimentary records from the Gulf of Alaska margin contain extremely high accumulation rates throughout the Holocene, permitting rare high-resolution reconstructions of North Pacific climate. The highest non-glacially-driven rates (0.1 – 0.4 cm·yr^{-1}) occur in the hundreds of shallow-silled fjords located along the eastern North Pacific coast, many of which have been ice-free since the early Holocene. Fjord sediments favor excellent organic matter preservation because (i) shallow sills restrict water exchange and can facilitate seasonal bottom-water anoxia, and (ii) fjords tend to be seasonal hotspots of biological primary productivity (23). Such basins can thus preserve exceptional high-resolution records of marine paleoproductivity (24). Sediment core EW0408-33JC, recovered from Katlian Bay, an ice-free temperate fjord on Baranof Island, Alaska (Fig. 3.1), preserves the last 7,500 years of paleoenvironmental change along the Gulf of Alaska margin at decadal timescales (25).

Measurements of biogenic silica (opal), total organic carbon (TOC), C/N weight ratios and carbonate-free sedimentary δ^{13}C ratios (26, 27) on EW0408-33JC provide insight into organic matter dynamics. Both highly depleted bulk sedimentary stable δ^{13}C isotope values and high C/N ratios (28) suggest the TOC is dominantly terrestrial organic matter, transported into Katlian Bay by fluvial discharge or freshwater runoff from the adjacent watershed (Appendix 3.1). The application of a linear mixing model (Appendix 3.1) allows the extraction of terrigenous TOC contributions as a precipitation-driven terrestrial erosion proxy. When combined with the opal mass accumulation rate (MAR) as a proxy for marine primary productivity, these two independent datasets in EW0408-33JC document decadal-scale environmental and ecological variability in the Gulf of Alaska environment since the early Holocene.

3.3 Comparison between EW0408-33JC and regional paleoclimate records

Primary productivity records in EW0408-33JC show a strong relationship to the PDO over the last millennium (Fig. 3.2a). With the exception of an out-of-phase period beginning around AD 1840, the opal MAR correlates significantly ($n = 43$, $r = 0.41$, $p < 0.01$) with a tree-ring derived composite PDO reconstruction (20). This result implies that prior to AD 1840, positive PDO phases favored enhanced Gulf of Alaska marine productivity, and is consistent with modern positive feedback models linking precipitation, ocean stratification, and marine productivity (13, 14). While the AD 1840 anomaly introduces some doubt about the relationship between the PDO and EW0408-33JC opal data over millennial timescales, this specific time interval has been recognized as an irregularity in other long terrestrial paleoclimate records from the Gulf of Alaska margin (22, 29; Appendix 3.2). The EW0408-33JC opal MAR record thus appears to be sensitive to past PDO variability, and suggests that this dataset may be useful as a PDO proxy for interpretation of the longer Holocene record.

Previous paleoclimate compilations of PDO and AL dynamics indicate nearly synchronous behavior attributed to atmospheric forcing. Comparison with records sensitive to these past dynamics, and the record preserved in EW0408-33JC, can be used to differentiate between regional processes and local signals unique to Katlian Bay. The in-phase relationship between $\delta^{18}O$ records from Mt. Logan (22) and the EW0408-33JC terrestrial erosion proxy (Fig. 3.2b, c) correspond with modern observations, namely that periods of enhanced/eastern AL cells tend to favor meridional atmospheric circulation patterns that bring moisture derived from the tropical Pacific Ocean northwards into the Gulf of Alaska, and lead to increased precipitation and terrestrial runoff along the continental margin. This in-phase relationship appears to hold for the last 2,000 years, as well as periods between 3,100-4,800 and 5,800-7,100 years ago (Fig. 3.2b, c). The carbonate $\delta^{18}O$ record from Jellybean Lake in the Yukon Territory (29) shows similar trends to these results, further confirming the EW0408-33JC terrestrial erosion data as a sensitive proxy for Aleutian Low intensity.

Combining the record of siliceous productivity from EW0408-33JC (Fig. 3.2d) with these proxies of atmospheric dynamics yields additional insight into the linked atmosphere-climate-ecosystem structure at work in the Gulf of Alaska. Surprisingly, there is no correlation between the opal MAR data and either Mt. Logan (n = 305, r = 0.083, p < 0.150) or the terrestrial TOC MAR of EW0408-33JC (n = 304, r = -0.100, p < 0.100). These observations are not consistent with current models of the PDO and its influence on the Northeast Pacific Ocean ecosystem. This lack of coherency in the mid- and early Holocene also conflicts with our earlier findings that the EW0408-33JC opal MAR record is correlated with PDO reconstructions for the last millennia (Fig. 3.2a).

Applying wavelet time-series techniques (*30, 31*) to the EW0408-33JC opal MAR and Mt. Logan δ^{18}O records highlights high power in the 40-to-70-yr period for the last 1,000 years, with the Mt. Logan spectrum continuing to display significant power until about 3,300 calibrated years before present (cal yrs BP; Appendix 3.3). In contrast, the EW0408-33JC opal MAR has a noticeable reduction in power from about 800 – 2,000 cal yrs BP but returns to higher power from 2,000 – 3,500 cal yrs BP. The cross-wavelet coherence pattern of both spectrums (Appendix 3.3c) also exhibits periodic power increases in the decadal band for the last 4,000 years. Prior to this period, however, there is little relationship between the two records, suggesting that the environmental linkage between the independent datasets does not occur before this point. We hypothesize that this decadal-scale wavelet coherence pattern reflects an abrupt baseline change-of-state in AL-driven conditions in the North Pacific about 4,000 years ago. The somewhat regular pattern of in-phase and out-of-phase behavior between Mt. Logan and EW0408-33JC, particularly in light of our understanding of simple binary PDO phases, suggests that this model of North Pacific environmental variability may be insufficient to describe Holocene conditions for this region.

A key example of the need for better models of decadal-scale North Pacific climate variability is exemplified with the anomalous regional behavior in various paleoclimate records that started around AD 1840. This period coincides with the termination of the Little Ice Age and the onset of 20th century warming across the Arctic

(*32*), and is a time of global climate reorganization (*33*). Specifically within the Gulf of Alaska region, the proxy evidence points to an intensification of the AL pressure cell and increased delivery of tropical Pacific moisture (Fig. 3.2*b*, *c*), while marine paleoproductivity data suggest a decrease in both primary producers (Fig. 3.2*d*) and some marine consumers (e.g. pelagic fish and pinnipeds; (*34-36*). This anti-phase behavior is in direct contrast to modern observational data of SST, SLP, and biological productivity as exemplified by the North Pacific regime shift during AD 1976/1977 (*15*). An important distinction between these differing types of datasets is that reliable SST and SLP records for the North Pacific only extend back in time to AD 1900 (*2*), while robust plankton and fisheries data cover only the last fifty years at best (*37*). In other words, the time span of human scientific observation is probably too small to account for the full range of potential North Pacific environmental variability.

The phase changes observed between the EW0408-33JC opal MAR record and the Mt. Logan δ^{18}O data suggest a disconnect between AL-driven forcings (e.g. Alaska Gyre upwelling) and marine ecosystem variability as understood by a simple binary PDO model. Recent SLP, SST, and fisheries catch data has identified a similar disconnect between North Pacific climate and ecosystem response between AD 1990-2002, termed the "Victoria Pattern" (*38, 39*). By using three independent paleoenvironmental records influenced by Aleutian Low variability, and by inference PDO regime changes, we provide evidence for such alternate modes of North Pacific variability.

3.4   Role of the Intertropical Convergence Zone in the North Pacific Ocean

Our integrated analysis indicates that the Aleutian Low pressure cell, the dominant control on PDO variability, undergoes its earliest period of intensification in the Gulf of Alaska region around 4,000 years ago, during the onset of Neoglacial conditions. Global data compilations suggest this period favored cooler, wetter high-latitude conditions, while equatorial regions tended towards increased aridity (*40*), attributed to a southward shift of the Intertropical Convergence Zone (ITCZ) associated with the onset of modern El Nino – Southern Ocean (ENSO) periodicity (*41*). The

negative anomaly in the Mt. Logan $\delta^{18}O$ data at 4,200 cal yrs BP (Fig. 3.2c) indicates an active meridional circulation pattern that agrees with the suggested ITCZ shift. The location of the ITCZ is sensitive to interhemispheric temperature contrasts (42), and high-latitude cooling promotes the expansion of sea ice which has a feedback on ITCZ conditions (43). Variability in Bering Sea ice cover since AD 1947 has been linked to PDO regime shifts (44), suggesting a possible feedback mechanism linking North Pacific Aleutian Low dynamics with the equatorial ITCZ. We speculate that the onset of mid-Holocene Gulf of Alaska AL intensification is related to the increase in the meridional temperature gradient between the equatorial and high-latitude regions. This north-south gradient is responsible for controlling Hadley cell heat transport to the poles, and is the ultimate driver of atmospheric meridional convective circulation. This hypothesis is also consistent with modeling efforts that describe the 4,000 cal yr BP onset of ENSO dynamics (45).

To test the hypothesis that the ITCZ-Aleutian Low linkage is responsible for these alternate modes of North Pacific climate variability, we combined our Alaskan high-resolution paleoenvironmental records (Fig. 3.2b-d) with two additional lower latitude high-resolution records: (i) a subdecadally-resolved speleothem from the Guadalupe Mountains in the Sonoran Desert (Fig. 3.2e; 46), and (ii) the equally high-resolution titanium concentration record recovered from Ocean Drilling Program (ODP) Site 1002 in the Cariaco Basin (Fig. 3.2f; 47). The speleothem record is sited in a region of strong atmospheric teleconnection with the Aleutian Low through the Pacific North America Pattern (2, 48), while ODP Site 1002 reflects the latitude of the ITCZ. Using the combined paleoclimate datasets in a principal component analysis (PCA), we find two components alone account for 50% of the variance within this composite dataset, with high loadings on PC1 in records that reflect an Arctic – Equator linkage possibly via intensification of the Hadley cell circulation, while PC2 is strongly associated with records of Aleutian Low intensity in the Gulf of Alaska (Fig. 3.3a). Plotting individual values of PC1 and PC2 shows that the composite PCA dataset breaks into four zones, two of which are the likely classic binary PDO modes, while two alternate regime patterns are

also identified (Fig. 3.3*b*). One of these alternate modes is likely synonymous with the Victoria Pattern as it is currently understood (*38, 39*). PC1 shows a distinctive shift at approximately 4000 cal yrs BP towards regimes characteristic of an enhanced meridional temperature gradient (Fig. 3.3*c*), consistent with our hypothesis that the ITCZ is forcing the AL strength during mid- and late Holocene times. Linking these shifts in the ITCZ with the composite Aleutian Low intensity record derived from PC2 (Fig. 3.3*c*) shows that between 3,500 – 1,800 cal yrs BP, the North Pacific climate alternated at decadal timescales between positive PDO regimes and the Victoria Pattern, and that most positive PDO states (e.g. strengthened AL regimes) have occurred since only 4,000 years ago.

It is becoming clear from the mounting evidence that the onset of mid-Holocene Neoglacial conditions are truly the beginning of modern North Pacific atmospheric and oceanic variability, and that subsequent climate events (e.g. the Little Ice age termination) have intensified these cycles. In conclusion, reorganization of atmospheric dynamics occurred several times throughout the Holocene, and that greater occurrences of positive PDO states since 4,000 years ago argues that the PDO is a direct manifestation of cooling of the high latitudes. If true, then modern greenhouse warming may ultimately suppress PDO cycles in the future.

3.5   References

1.   K. E. Trenberth, *Bulletin of the American Meteorological Society* **71**, 988 (1990).
2.   K. E. Trenberth, J. W. Hurrell, *Climate Dynamics* **9**, 303 (1994).
3.   M. Latif, T. P. Barnett, *Science* **266**, 634 (1994).
4.   D. M. Peteet, A. Del Genio, K. K. W. Lo, *Journal of Geophysical Research-Atmospheres* **102**, 23781 (1997).
5.   P. R. Mundy, P. Olsson, in *The Gulf of Alaska: biology and oceanography* P. R. Mundy, Ed. (Alaska Sea Grant College Program, University of Alaska Fairbanks, 2005) pp. 25-34.
6.   P. J. Harrison, P. W. Boyd, D. E. Varela, S. Takeda, *Progress in Oceanography* **43**, 205 (1999).
7.   A. R. Childers, T. E. Whitledge, D. A. Stockwell, *Deep-Sea Research Part II-Topical Studies in Oceanography* **52**, 193 (2005).
8.   T. C. Royer, *Deep-Sea Research Part II-Topical Studies in Oceanography* **52**, 267 (2005).
9.   A. E. Gargett, *Fisheries Oceanography* **6**, 109 (1997).

10. Z. Chase, P. G. Strutton, B. Hales, *Geophysical Research Letters* **34**, doi:10.1029/2006GL028069 (2007).

11. P. J. Lam, J. K. B. Bishop, *Geophysical Research Letters* **35**, 5 (2008).

12. T. J. Weingartner, S. L. Danielson, T. C. Royer, *Deep-Sea Research Part II-Topical Studies in Oceanography* **52**, 169 (2005).

13. G. A. McFarlane, R. J. Beamish, *Canadian Journal of Fisheries and Aquatic Sciences* **49**, 743 (1992).

14. R. J. Beamish, D. R. Bouillon, *Canadian Journal of Fisheries and Aquatic Sciences* **50**, 1002 (1993).

15. N. J. Mantua, S. R. Hare, Y. Zhang, J. M. Wallace, R. C. Francis, *Bulletin of the American Meteorological Society* **78**, 1069 (1997).

16. N. J. Mantua, S. R. Hare, *Journal of Oceanography* **58**, 35 (2002).

17. S. N. Rodionov, J. E. Overland, N. A. Bond, *Fisheries Oceanography* **14**, 3 (2005).

18. L. Wainwright, G. Meyers, S. Wijffels, L. Pigot, *Geophysical Research Letters* **35**, 5 (2008).

19. J. Halfar *et al.*, *Geophysical Research Letters* **34**, 5 (2007).

20. G. M. MacDonald, R. A. Case, *Geophysical Research Letters* **32** (2005).

21. R. Wilson, G. Wiles, R. D'Arrigo, C. Zweck, *Climate Dynamics* **28**, 425 (2007).

22. D. Fisher *et al.*, *Holocene* **18**, 667 (2008).

23. D. C. Burrell, *Biogeochemistry of a boreal fjord: Boca de Quadra, Southeast Alaska.* H. Stockholm, Ed., Occasional publication (Institute of Marine Science, University of Alaska Fairbanks, 1989), pp. 454.

24. R. Gilbert, *Geomorphology* **32**, 295 (2000).

25. Core EW0408-32MC3 is a 40-cm-long surface multicore, and is constrained by ^{137}Cs and excess ^{210}Pb concentrations. The longer EW0408-33JC is an 18.2-m-long piston core, and is constrained by ten AMS ^{14}C dated wood macrofossils (Appendix 3.4). Sub-cm-scale scanning of gamma-ray-attenuated wet bulk density and magnetic susceptibility of both cores indicates coherent overlap of physical properties between EW0408-32MC3 and -33JC with no obvious loss of sediment or core compression. The sedimentary accumulation rate for both cores exceeds 4 yrs·cm^{-1}, and combined with a 5-cm sampling interval, yields an average temporal sampling resolution in both cores of 21.2 yrs, well below the observed 40-to-70 yr frequency of modern PDO regime shifts.

26. J. A. Addison, B. P. Finney, W. E. Dean, J. M. Jaeger, *Continental Shelf Research* (in prep.).

27. Diatoms are the dominant phytoplankton in the Gulf of Alaska region. Diatom frustules are composed of opal (biogenic silica), and because the Subarctic North Pacific Ocean has the highest silicic acid concentration and highest opal export rates in the world ocean, sedimentary opal concentrations represent a robust record of primary productivity for this region.

28. P. A. Meyers, *Chemical Geology* **114**, 289 (1994).

29. L. Anderson, M. B. Abbott, B. P. Finney, S. J. Burns, *Quaternary Research* **64**, 21 (2005).

30. C. Torrence, G. P. Compo, *Bulletin of the American Meteorological Society* **79**, 61 (1998).

31. A. Grinsted, J. C. Moore, S. Jevrejeva, *Nonlinear Processes in Geophysics* **11**, 561 (2004).

32. J. Overpeck *et al.*, *Science* **278**, 1251 (1997).

33. M. E. Mann, R. S. Bradley, M. K. Hughes, in *El Nino and the Southern Oscillation* H. F. Diaz, V. Markgraf, Eds. (Cambridge University Press, Cambridge, UK, 2000) pp. 321-372.

34. B. P. Finney, I. Gregory-Eaves, J. Sweetman, M. S. V. Douglas, J. P. Smol, *Science* **290**, 795 (2000).

35. N. Misarti, B. P. Finney, H. D. G. Maschner, M. J. Wooller, *Holocene* **19**, 1 (2009).

36. B. P. Finney *et al.*, *Journal of Marine Systems* (in press).

37. B. W. Frost, *Progress in Oceanography* **32**, 17 (1993).

38. N. A. Bond, J. E. Overland, M. Spillane, P. Stabeno, *Geophysical Research Letters* **30** (2003).

39. E. Di Lorenzo *et al.*, *Geophysical Research Letters* **35**, 6 (2008).

40. P. A. Mayewski *et al.*, *Quaternary Research* **62**, 243 (2004).

41. D. T. Rodbell *et al.*, *Science* **283**, 516 (1999).

42. A. J. Broccoli, K. A. Dahl, R. J. Stouffer, *Geophysical Research Letters* **33**, 4 (2006).

43. J. C. H. Chiang, C. M. Bitz, *Climate Dynamics* **25**, 477 (2005).

44. H. J. Niebauer, *Journal of Geophysical Research* **103**, 27717 (1998).

45. D. Sun, in *El Nino and the Southern Oscillation: Multiscale Variability and Global and Regional Impacts* H. F. Diaz, V. Markgraf, Eds. (Cambridge University Press, 2000) pp. 443-463.

46. Y. Asmerom, V. Polyak, S. Burns, J. Rassmussen, *Geology* **35**, 1 (2007).

47. G. H. Haug, K. A. Hughen, D. M. Sigman, L. C. Peterson, U. Rohl, *Science* **293**, 1304 (2001).

48. J. M. Wallace, D. S. Gutzler, *Monthly Weather Review* **109**, 784 (1981).

49. The authors thank the crew and scientific party of the R/V *Maurice Ewing* during cruise EW0408, Bobbi Conard and Mysti Weber of the OSU core repository, and Andrea Krumhardt and Tara Borland for analytical assistance. All biogeochemical samples were analyzed at the Alaska Stable Isotope Facility under the direction of Matthew J. Wooller. JAA was funded by the Cooperative Institute for Arctic Research through cooperative agreement NA17RJ1224 with the National Oceanic and Atmospheric Administration. BPF was supported through NSF Grant OCE-0351075.
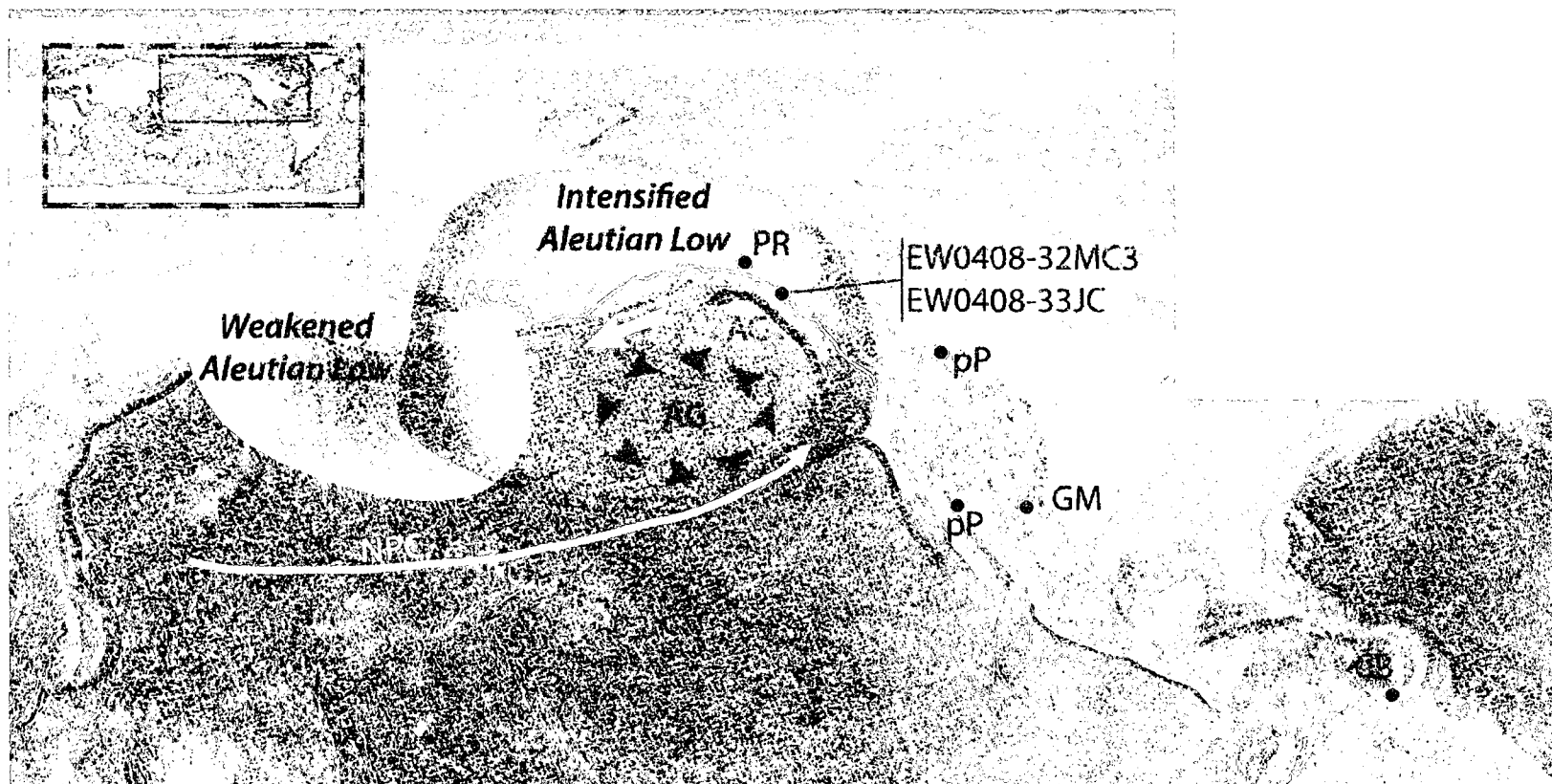
Figure 3.1 Location of cores EW0408-32MC3 and -33JC, high-resolution regional paleoclimate records, and generalized atmospheric and oceanographic circulation of the Subarctic North Pacific Ocean. PR = Prospector Ridge Col ice core from Mt. Logan (22); GM = record from Pink Panther Cave in the Guadalupe Mountains, New Mexico (46); CB = Ocean Drilling Program Site 1002 in the Cariaco Basin (47); pP = tree-ring sites used in paleoPDO reconstruction (20); NPC = North Pacific Current; CC = California Current; AG = Alaska Gyre; AC = Alaska Current; AS = Alaska Stream; ACC = Alaska Coastal Current. Location of Aleutian Low extents defined by SLP during positive and negative North Pacific Index phases (17). Base ETOPO2 topography courtesy National Geophysical Data Center.
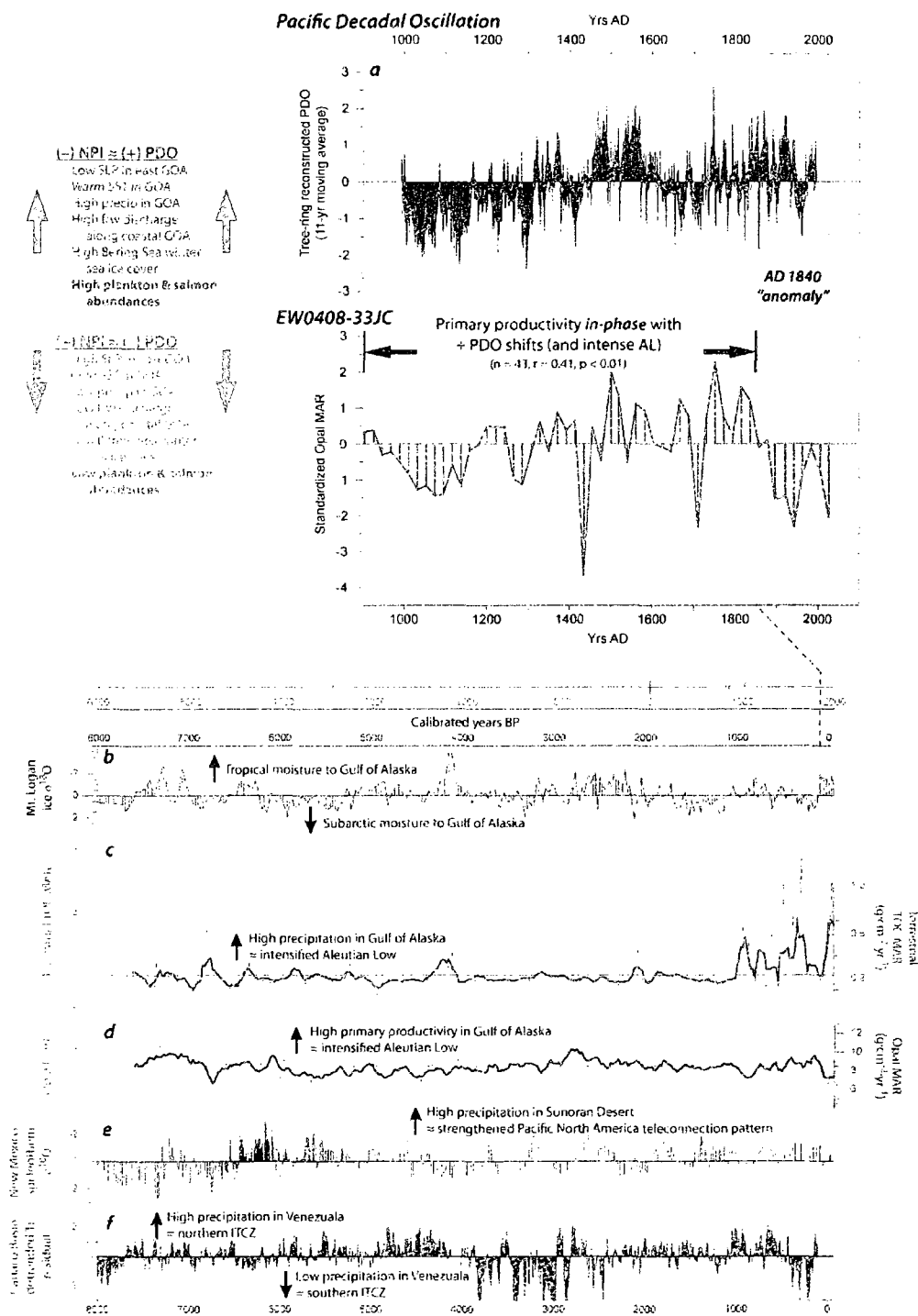
Figure 3.2 Biogeochemical proxy data from EW0408-33JC compared against: (a) tree-ring-based PDO reconstruction (*20*); (b) standardized Mt. Logan ice core $\delta^{18}O$ (*22*); (c) terrestrial TOC MAR from EW0408-33JC; (d) marine productivity opal MAR from EW0408-33JC; (e) standardized New Mexico speleothem $\delta^{18}O$ (*46*); and (f) standardized detrended titanium accumulation residual from ODP Site 1002 in the Cariaco Basin (*47*).
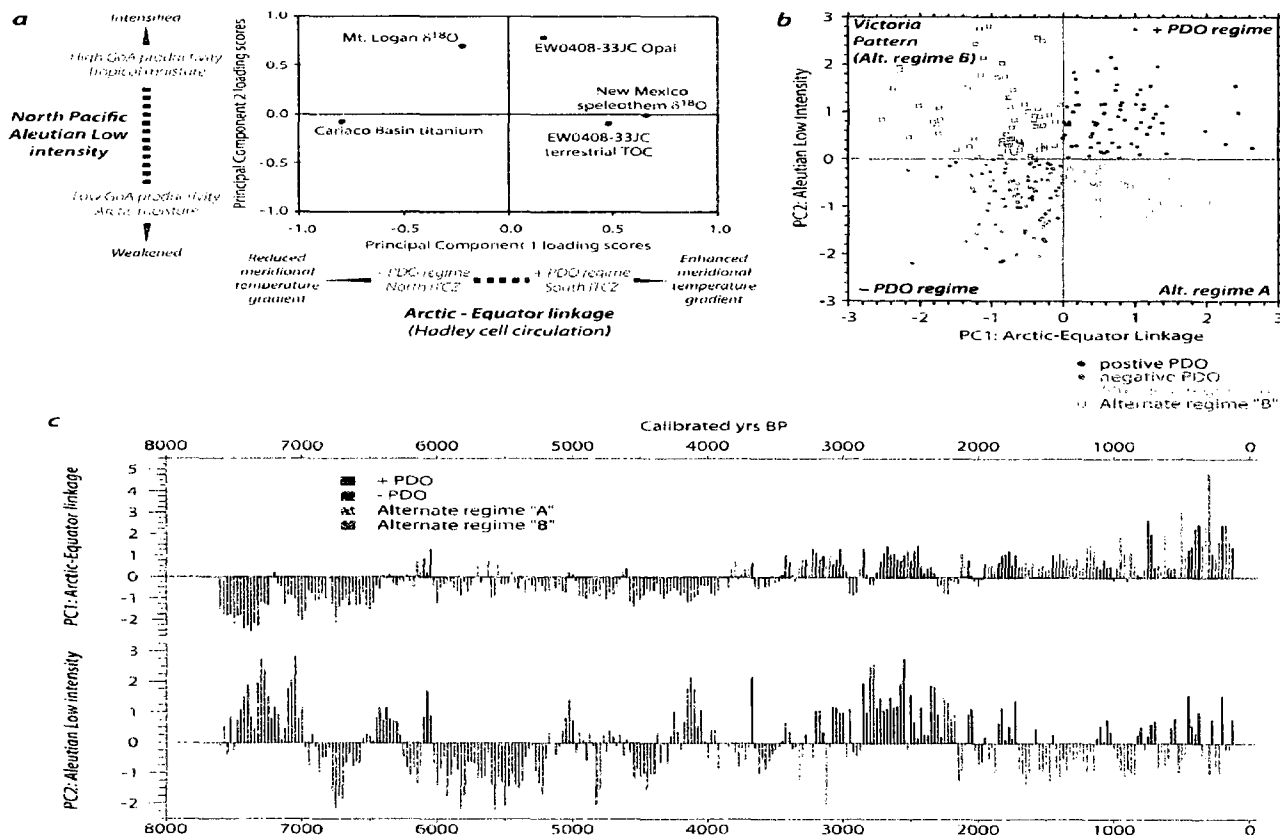
Figure 3.3 Principal component analysis of high-resolution paleoclimate data series from Fig. 3.2*b-f*. (a) Loading scores indicate strong affinities between PC1 and EW0408-33JC terrestrial TOC, a New Mexico speleothem, and the Cariaco Basin titanium record, suggesting PC1 is a measure of the Arctic-Equator atmospheric linkage, likely through the Hadley circulation. High loadings on PC2 for EW0408-33JC opal MAR and Mt. Logan $\delta^{18}O$ indicate PC2 is a measure of Aleutian Low intensity in the Gulf of Alaska. Factors were rotated using the Kaiser varimax method. (b) Plot of PC1 and PC2 scores indicate a quadropole climate system, composed of a mix of the traditional binary PDO regime systems as well as two alternate regimes. (c) PC1 and PC2 plotted as time-series data show major paleoenvironmental shifts have occurred between the four potential regimes, with a notable shift in PC1 at 4,000 cal yrs BP.

67

3.6   Appendix

Appendix 3.1: Bulk sedimentary organic matter (OM) provenance diagram after (28). Marine-derived OM is indicated by (i) relatively enriched $\delta^{13}C$ values due to photosynthetic fractionation associated with the use of dissolved HCO_3^- as a substrate and (ii) C/N ratios near the Redfield ratio of ~6.6. This figure suggests that, while there is some marine OM incorporated within the sediment, there are also major contributions from terrigenous sources as well.
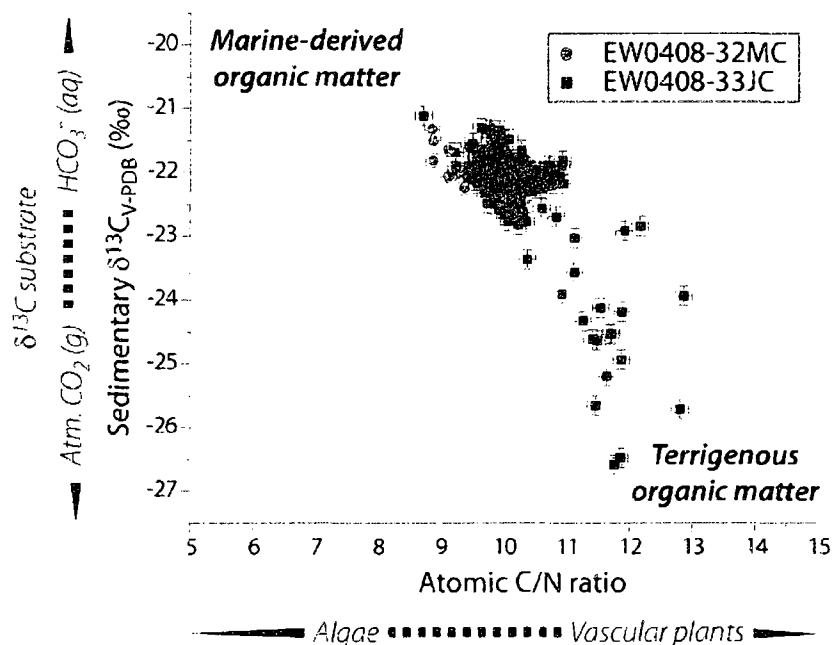
This pattern of marine- versus terrigenous organic matter was utilized to extract the percent contribution of terrestrial TOC from the total measured TOC in EW0408-33JC by use of the equation

$$TOC_{terrestrial} = \frac{\delta^{13}C_{sample} - \delta^{13}C_{marine}}{\delta^{13}C_{terrestrial} - \delta^{13}C_{marine}} \times TOC_{sample}$$

where $TOC_{terrestrial}$ is the calculated terrigenous-derived TOC (in wt%) for any given sample, $\delta^{13}C_{sample}$ is the measured $\delta^{13}C$, $\delta^{13}C_{marine}$ is the fully marine endmember $\delta^{13}C$, $\delta^{13}C_{terrestrial}$ is the fully terrestrial endmember $\delta^{13}C$, and TOC_{sample} is the measured total TOC for a sample. $\delta^{13}C$ values of -21‰ (modern marine particulate organic matter) and -27‰ (modern pollen) were used as the marine and terrestrial $\delta^{13}C$ endmember values, respectively, as measured by McQuoid et al. (2001) in Saanich Inlet, British Columbia.

Appendix 3.2: Correlation coefficients of EW0408-32MC biogeochemical proxies and decadal-scale North Pacific climate indices. Because the -32MC population size is small (n = 8), none of the correlations are significant at the 95% confidence level. Bold type indicates significance at the 85% confidence level. SLP = sea level pressure; SST = sea surface temperature; SSH = sea surface height.

	NPI[a]	PDO[b]	NPGO[c]
Defining oceanic parameter			
SLP	X		
SST		X	
SSH			X
EW0408-32MC3			
GRA wet bulk density	0.09	-0.03	-0.16
Opal	**0.70**	-0.26	-0.30
Opal MAR	**0.58**	-0.21	-0.29
TOC	**-0.58**	0.27	-0.10
TOC MAR	**-0.66**	0.30	-0.16
Atomic C/N ratio	0.14	-0.11	-0.04
Sedimentary $\delta^{13}C$	0.13	0.11	-0.02
Sedimentary $\delta^{15}N$	-0.10	-0.13	0.34

[a] North Pacific Index (*2*)

[b] Pacific Decadal Oscillation (*15*)

[c] North Pacific Gyre Oscillation (*39*)

Appendix 3.3: Morlet wavelet time-series analyses for (a) EW0408-33JC opal MAR data and (b) Mt. Logan $\delta^{18}O$ record (*30*). Diamond pattern indicates range of modern PDO periods; thick lines indicate 95% significance level against red noise and cone of influence where edge effects bias analysis. (c) Wavelet coherence (*31*) between standardized EW0408-33JC opal MAR and Mt. Logan records; relative phase relationship indicated by arrow directions. Relative wavelet power indicated by vertical color bars on right of each frame.

Calibrated years BP
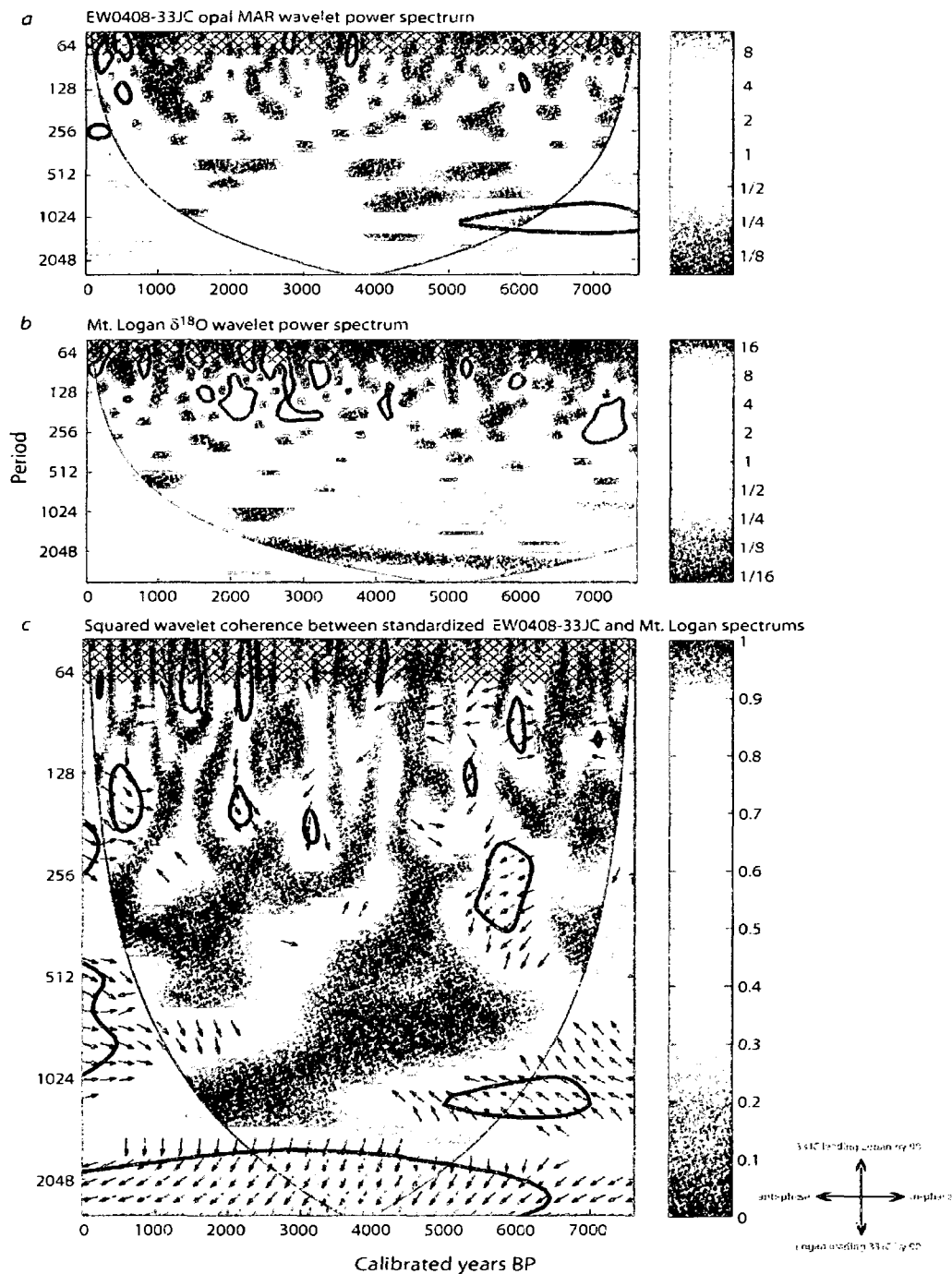
Appendix 3.4: Depth-age models for marine sediment cores (*a*) EW0408-32MC and (*b*) EW0408-33JC. EW0408-32MC is constrained by the AD 1964 peak in anthropogenic fallout from atmospheric testing of nuclear weapons and the minimum detectable activity of ^{210}Pb; the presence of a mixed surface layer from 0 – 10 cm indicates full recovery of modern sediment. Core EW0408-33JC is constrained by nine AMS ^{14}C dated wood macrofossils; overlap in the geophysical properties of both EW0408-32MC and the top of -33JC permits the application of the -32MC chronological constraints to the top of the -33JC age model. Error bars in *b* are 2σ; red dashed lines indicate the 95% confidence interval for the ^{14}C-constrained age model.
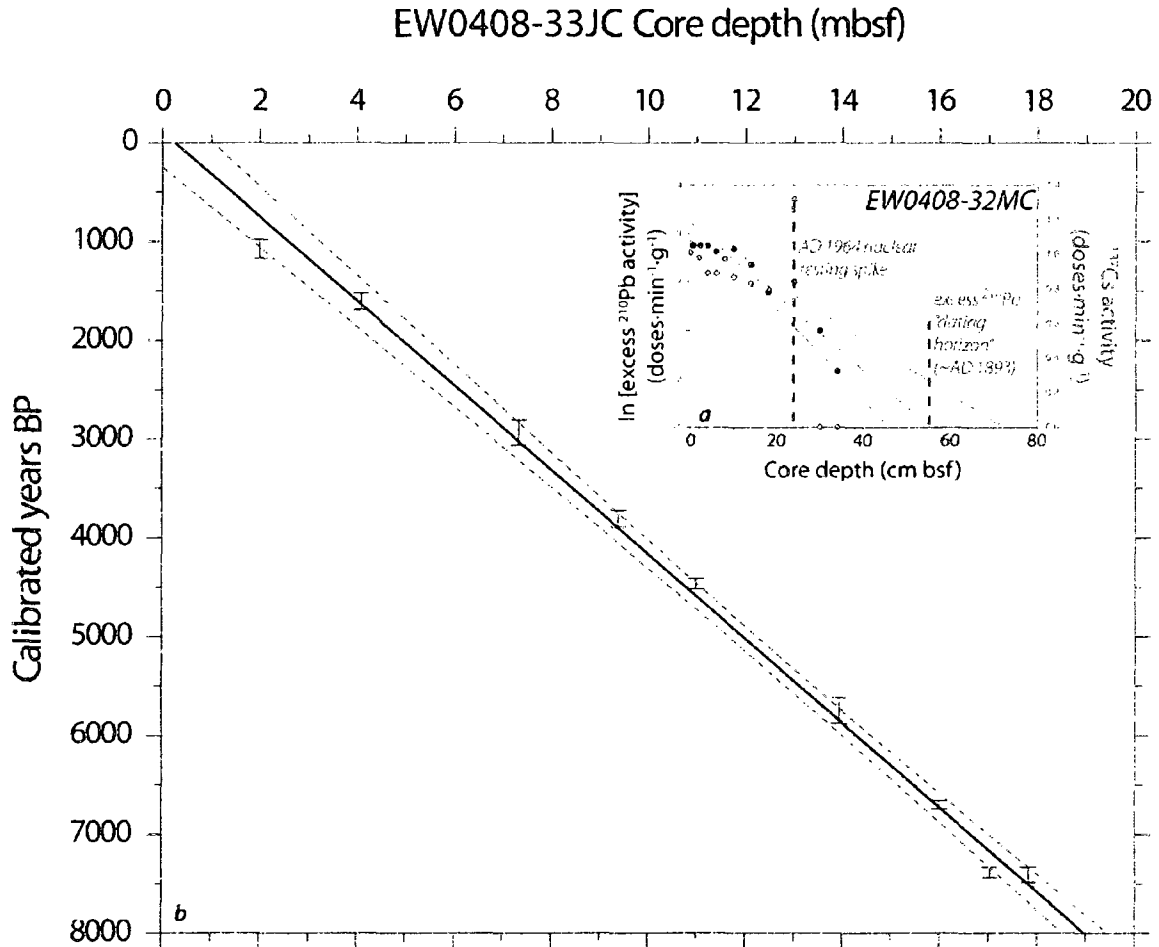
EW0408-33JC Core depth (mbsf)

Chapter 4 High-resolution paleoproductivity evidence for Holocene evolution of the Aleutian Low Pressure System from coastal fjords in the Subarctic Northeast Pacific Ocean[1]

4.1 Abstract

Environmental conditions in the Subarctic Northeast Pacific Ocean are an important component of North American climate patterns, as well as a potential driver of Northern Hemisphere climate variability. This region experiences a dynamic linkage between the atmospheric Aleutian Low pressure cell and the Alaska Gyre upwelling zone that contributes to the maintenance of a highly productive nearshore marine ecosystem. The paleoclimatic record of Aleutian Low dynamics since the Last Glacial Maximum are explored using biogeochemical proxies of paleoproductivity, freshwater discharge, and ocean circulation preserved in four fjords from the southeast Alaskan margin. Major results indicate (i) the onset of modern fjord-style reverse estuary circulation begins around 12000 years ago; (ii) an intensification of the Aleutian Low between 4800 – 2700 years ago initiated regional increases in productivity and freshwater discharge; and (iii) a decoupling between the marine ecosystem and the Aleutian Low-Alaska Gyre system from 8000 – 6500 years ago argue against a simple binary dipole model for environmental and ecological regime shifts in the North Pacific Ocean. A high-resolution analysis of variability present within the productivity records also indicate significant power in the 40-100 yr·cycle^{-1} range of periodicity consistent with the short historical record. This study highlights the need for longer datasets of climate and ocean phenomena to better identify the full range of variability possible within a given region.

4.2 Introduction

A dynamic linkage exists between Northern Hemisphere atmospheric circulation and oceanographic conditions in the Subarctic Northeast Pacific Ocean. A key component of this system is the Aleutian Low (AL) pressure cell, a coherent sea level pressure (SLP) feature located near the Aleutian Islands, which controls both seasonal and multi-decadal environmental variability at multiple spatial scales, ranging from local effects within the Bering Sea and Gulf of Alaska to teleconnections with Mexico and the southeastern United States (Latif and Barnett, 1994; Trenberth and Hurrell, 1994; Rodionov et al., 2007).

Seasonal atmospheric dynamics in the Gulf of Alaska are controlled by the position and intensity of the AL (Mundy and Olsson, 2005). During the winter, the center of the AL is located in the central northeast Pacific Ocean where it reduces sea surface temperature (SST) and SLP, increases precipitation, and intensifies the northeastern Pacific storm track (Trenberth and Hurrell, 1994). The AL-driven SLP reduction leads to enhanced upwelling in the Alaska Gyre (Harrison et al., 1999). Cyclonic Alaska Gyre circulation leads to horizontal advection of shallow nutrient-rich water towards the continental shelf of the Gulf of Alaska where it contributes to large phytoplankton blooms in the spring and summer (Childers et al., 2005). Concurrent with the spring bloom is the seasonal freshet along the margin when freshwater discharge into the Gulf of Alaska is at a maximum (Royer, 2005). The summer runoff maxima (Royer et al., 2001) thus reflects atmospheric conditions driven by the preceding wintertime AL.

Interdecadal climate variability has also been recognized in the Gulf of Alaska. Instrumental records of SST, SLP, precipitation, freshwater discharge, and wind stress all indicate an environmental regime shift during the late 1970s (Carleton et al., 1990; Trenberth, 1990; Trenberth and Hurrell, 1994; Weingartner et al., 2005). In the Gulf of Alaska, the marine ecosystem underwent a significant change in the abundances of plankton populations (McFarlane and Beamish, 1992), and contributed to a notable increase in Alaskan salmon catch records (Mantua et al., 1997). Instrumental and observational evidence for environmental regime shifts in the Gulf of Alaska extend to

the early twentieth century, and document three to four shifts since AD 1900 (Mantua et al., 1997). The Pacific Decadal Oscillation (PDO), defined as the leading principal component of variability in SST anomalies in the North Pacific Ocean (Mantua et al., 1997; Mantua and Hare, 2002), operates on time scales ranging from 40-80 years. The primary forcing mechanism of the PDO is the position and strength of the AL pressure system (Latif and Barnett, 1994; Trenberth and Hurrell, 1994). Royer et al. (2001) developed a hydrological model describing coastal Gulf of Alaska circulation, and found significant variability at seasonal and decadal timescales, with the latter pattern being attributed to PDO regime shifts, respectively.

While the interactions between the modern atmosphere, ocean, and marine ecosystem have been fairly well characterized, the long-term evolution and variability of the AL remains an area of active research. Recent work has established contemporaneous environmental changes at millennial and centennial scales in ice, terrestrial, and marine datasets that record different AL parameters for the last 7500 years from the Gulf of Alaska margin (Addison and Finney, *in prep.*). The carbonate $\delta^{18}O$ record from Jellybean Lake in the Canadian Yukon (Anderson et al., 2005), the $\delta^{18}O$ record in an ice core recovered from Mt. Logan (Fisher et al., 2004; Fisher et al., 2008), and terrestrially-derived total organic carbon (TOC) preserved in marine sediment core EW0408-33JC from Katlian Bay in coastal southeast Alaska (Addison and Finney, *in prep.*) have all been interpreted directly in terms of atmospheric dynamics controlled by the AL. Changes in the $\delta^{18}O$ records of Jellybean Lake and Mt. Logan reflect variations in moisture source and pathway, while the Katlian Bay terrestrial influx dataset is representative of coastal precipitation intensity. Prior to ~AD 1000, AL existed in a weakened state and/or more westerly location with a northern zonal moisture source, and reduced precipitation along the Gulf of Alaska margin that limited marine productivity. During the Little Ice Age, between AD 1200 – 1850, the dynamics of this system altered drastically; the Aleutian Low became more intensified and/or easterly with tropical moisture delivered by meridional circulation. These changes resulted in increased precipitation and enhanced marine productivity within the Gulf of Alaska. These shifts in

state are unprecedented in magnitude relative to the AL regime shifts documented historically (Trenberth and Hurrell, 1994).

In this paper, high-resolution paleoceanographic records preserved in three southeast Alaskan fjords, along with the EW0408-33JC record from Katlian Bay, are studied to determine patterns of regional coastal change since the Late glacial/Holocene transition. The oceanography of fjords tend to favor excellent organic matter (OM) preservation because (i) shallow sills restrict water exchange and can facilitate seasonal bottom-water anoxia, and (ii) fjords tend to be seasonal hotspots of biological primary productivity (Burrell, 1989). Fjord basins can thus preserve exceptional high-resolution records of marine paleoproductivity (Gilbert, 2000). This innovative approach benefits from the use of multiple fjord records such that the influence of local effects on an individual fjord's sedimentary record can be identified by cross-referencing across the larger data compilation. Because of differing sedimentary accumulation rates (SARs) within this subset of Alaskan fjords, multiple temporal patterns of change can be distinguish, ranging from subdecadal through millennial timescales. Parameters of interest include (i) marine primary productivity; (ii) erosion intensity of the adjacent terrestrial landscape; and (iii) water column anoxia. These parameters will then be used to investigate regional mechanisms of millennial- and decadal-scale change attributable to Aleutian Low-Alaska Gyre linkages throughout the Holocene.

4.2.1   Site descriptions

The Subarctic Northeast Pacific Ocean is dominated by the Gulf of Alaska basin, and is bordered by the Kenai – St. Elias – Chugach Range complex along its eastern margin (Fig. 4.1a). These mountains are significant orographic barriers, with the tallest peak at Mt. St. Elias exceeding five kilometers in elevation. The coast of southeast Alaska was extensively glaciated during the Last Glacial Maximum (LGM; Fig. 4.1a). Tidewater glaciers were common throughout the region (Mann et al., 1998) and the evidence of their extents include the complex network of fjords that now cover the region. A fjord is a deep, high-latitude estuary that has been (or is presently being) excavated or modified by land-based ice (Syvitski et al., 1987). A shallow sill at the

mouth of a fjord tends to restrict water exchange with the open ocean, and often leads to seasonal or permanent anoxia in the bottom waters within the fjord particularly when vertical mixing is minimal (Skei et al., 2003). Many of these southeast Alaska fjords are now completely free of perennial ice with no evidence of Holocene ice within their terrestrial watersheds. The sediment fill of many of these fjords thus represent a continuous Holocene record of sedimentation derived from autochthonous marine organic material, allochthonous terrestrial organic and detrital material from either fluvial systems draining into the fjord or precipitation run-off, and episodic disturbance events (e.g. seismic or aseismic debris flows and turbidity currents; Syvitski et al., 1987).

This study focuses on three fjords from western Baranof Island (Fig. 4.1b), as well as a site in the Gulf of Esquibel (Fig. 4.1c). All four locations share several characteristics, including either a single sill at the head of a basin, or multiple sills within a complex basin (Table 4.1). Hydrographic profiles of temperature (t) and salinity (s) collected in August 2004 during coring operations indicate strongly stratified water columns (Fig. 4.2), consistent with fjord estuarine circulation patterns characteristic of the North Pacific coast (Fig. 4.3). Comparison with a deepwater profile at the continental slope adjacent to Baranof Island exhibits similar t-s properties between shallow offshore and nearshore fjord water columns.

Previous oceanographic time-series observations in Boca de Quadra (Burrell, 1989), a fjord 170 km east-south-east of the Gulf of Esquibel, suggest the fjord sites presented in this study are approaching the autumn period of greatest stratification, driven by seasonal maxima in precipitation and fluvial discharge (Fig. 4.2c). However, the surface salinity in these fjords appears to be higher than other locations around the Alaskan coast, particularly compared to fjords and inlets within Prince William Sound (Gay and Vaughan, 2001), probably as a result of (i) smaller rivers at the fjord heads, and (ii) no upland glaciers or icefields present within the terrestrial drainage basins. Nevertheless, this stratified condition will most likely be disrupted during the subsequent winter when vertical mixing within the surface layer is enhanced by the combination of

minimal freshwater flux and strong down-fjord winds funneled by the high relief
topography along the fjord margin (Nebert, 1982).

The intermediate zone, characterized as the depth range between the surface water
mass and the sill depth, is unique in fjord-style estuary circulation because it is a major
influx of water and nutrients into a fjord from the open ocean (Syvitski et al., 1987). The
presence of Gulf of Alaska-derived intermediate zone water is suggested in the
relationship between the offshore hydrographic data and the fjord data in the *t-s* diagram
(Fig. 4.2c), where the continental slope site crosses the fjords' trends above sill depth. In
the multiple-basin Boca de Quadra fjord, the outermost (seaward) basin intermediate
zone is in continuous contact with Gulf of Alaska shelf water throughout the year, while
up-fjord transport into successive basins occurs during the winter as a function of
Aleutian Low-driven onshore convergence and Ekman transport (Burrell, 1989;
Weingartner et al., 2005). The up-fjord transport of this nutrient-rich water allows for the
annual replacement of nutrients at depth. Coupled with increased vertical mixing during
the winter due to the reduction in freshwater accumulation in the surface layer, this
combination of processes allows for the 'priming' of the euphotic zone with new
nutrients to sustain the high levels of primary productivity during the following spring
bloom (Childers et al., 2005). Increasing stratification from precipitation and solar
radiative heating in the spring of the surface layer may also help to contribute to the high
levels of primary productivity associated with the Northeast Pacific coast (Gargett, 1997).

An important component of all four fjord profiles is the presence of the
homogenous water mass at the bottom of each fjord below sill depth (Fig. 4.2). This
bottom water is derived from summer advection of denser water from the Gulf of Alaska
shelf across the sill into the fjord basin. The Boca de Quadra study (Burrell, 1989) shows
that this replacement usually occurs annually in response to diffusive salt loss from the
bottom fjord waters to the overlying intermediate waters. However, Burrell also
emphasizes that this cycle of bottom water renewal during the summer is not always the
case if sufficiently dense waters are not present outside the fjord.

A key difference exists between Boca de Quadra and two of the fjords in this study. The shallowest sill in Boca de Quadra is at 85 m water depth, while Deep Inlet and Katlian Bay have sills at 24 and 31 m water depth, respectively (Table 4.1). These shallow sills most likely restrict bottom water renewal events, and probably contribute to multi-annual residence times for these bottom water masses. Indeed, the divergence between the t-s properties of the fjord water masses below sill depth and the continental shelf suggests that none of the Baranof Island fjord bottom waters have undergone exchange with the shelf during the 2004 summer (Fig. 4.2c). This contrasts with the Gulf of Esquibel profile, in that given the t-s properties of its bottom water, it probably has experienced bottom-water exchange relatively recently.

The episodic replacement of fjord bottom waters, coupled with the high primary productivity of the overlying euphotic zone and subsequent export to the stagnant bottom water and sediment, suggests that fjord sedimentary records can serve as excellent high-fidelity repositories of paleoceanographic information (Gilbert, 2000). Indeed, low dissolved oxygen concentrations, rapid export rates and low microbial respiration rates all tend to favor high organic matter preservation (Hartnett et al., 1998; Hedges et al., 1999). While direct dissolved oxygen concentration data are not available from any of the fjord sites considered in this study, several Norwegian and British Columbian fjords are known to become seasonally anoxic (Syvitski et al., 1987; Skei et al., 2003), as is Skan Bay on Unalaska Island in the Aleutian Archipelago (Sugai et al., 1994), and Saanich Inlet on Vancouver Island (Timothy and Soon, 2001). Dissolved oxygen measurements within the bottom waters of Boca de Quadra, however, were never less than 3 ml/L over a three-year observational period, and this is due largely to the high dissolved O_2 concentrations in the residual water mass following the conclusion of the summer flushing sequence by O_2-rich Gulf of Alaska shelf water (Burrell, 1989). The dissolved O_2 minima in both Boca de Quadra and Skan Bay occur during the winter. Additionally, low dissolved O_2 water masses may occasionally be upwelled from the abyssal Gulf of Alaska, and advect into coastal areas (Burrell, 1989).

4.2.2 Philosophy of approach

These modern observations of Northeast Pacific fjord oceanographic dynamics suggest that a sedimentary record derived from fjord depocenters can potentially preserve evidence of several regional and local processes. When combined with a diverse multi-proxy analysis of paleoceanographic parameters, a complex dataset can be developed that details the effects of changing environmental conditions on marine primary producers, terrigenous sedimentation regimes, and bottom-water circulation dynamics. Because each proxy has its own assumptions and limitations for use, this multi-proxy approach allows for cross-validation and an increasingly robust interpretation. Furthermore, due to the use of multiple fjord sediment records, local basin effects and regional forcings can be distinguished across the Subarctic Northeast Pacific Ocean coastal zone as a whole.

The influx of intermediate zone water from the nutrient-rich Gulf of Alaska (Fig. 4.3) provides a pathway to relate fjord paleoproductivity records to shelf conditions. Sedimentary opal is derived primarily from the tests of diatoms, the dominant phytoplankton group in the North Pacific Ocean (Miller, 1993), and presents a resilient record of export production that has been recognized at all ocean depths, latitudes, and climate zones of the ocean (Ragueneau et al., 2000). However, additional proxies are necessary due to potential uncoupling of the Si:C cycle and differential opal dissolution (Ragueneau et al., 2000; Dezileau et al., 2003). Therefore, as an additional independent paleoproductivity proxy, bulk sedimentary total organic carbon (TOC) will also be measured. These results will then be compared against measurements of total nitrogen (TN), $\delta^{13}C$ of organic matter, and TOC/TN weight ratios (for brevity, C/N ratio hereafter) to evaluate changes in the TOC composition as indicative of either (i) past water column nutrient dynamics, or (ii) changes in the proportions of marine algal material versus terrestrial vascular plant debris to the sediment (Meyers, 1994; Bickert, 2006).

Terrigenous sedimentation within the ice-free fjords of southeast Alaska is driven primarily by freshwater runoff from the adjacent terrestrial watershed. This runoff manifests itself as the shallow low-salinity surface water present in fjord circulation regimes (Fig. 4.3). Therefore, terrigenous sediment accumulation can be utilized as a

proxy for seasonal runoff (Haug et al., 2001). Terrigenous sedimentation is evaluated using concentrations of lithophilic elements known to accumulate as detrital phases, due to physical weathering of primary igneous or secondary sedimentary lithologies. These include Zr (as zircon or baddeleyite), Ti (as rutile or anatase), and Al (as representative of the bulk aluminosilicate fraction) (Marshall and Fairbridge, 1999). The primary similarity between all of these elements is that they are classified as either highly refractory or super refractory (McLennan, 1999), and thus are associated predominantly with the detrital mineral flux, though some authigenic precipitation of Al-bearing clays and oxyhydroxides is known to occur in aqueous environments (e.g. Langmuir, 1997). Nevertheless, detrital accumulation behavior is inferred for these elements due to the (i) highly insoluble nature of the carrier mineral phases as imposed by thermodynamic constraints (Faure, 1998), (ii) rapid transport of sediment from the terrestrial margin to the Gulf of Alaska basin (Hallet et al., 1996; Jaeger et al, 1998; Walinsky et al., 2009) thus minimizing chemical weathering reaction times, and (iii) limited X-ray diffraction analysis of the bulk mineral assemblage contained in EW0408-33JC shows highly immature mineral phases dominated by chlorite, quartz, illite, plagioclase, and amphibole (R. Newberry, pers. comm., 2006).

Without knowing the dissolved oxygen concentration of the fjords considered in this study *a priori*, past redox conditions of these fjords can be reconstructed using the accumulation of redox-sensitive elements contained within the bulk sediment. These elements are derived from two sources, either associated with terrestrially-derived detrital mineral phases and organic matter via substitution or adsorption processes (Calvert and Pedersen, 1993), or direct precipitation from seawater as reduced sulphide phases sensitive to prevailing redox potential (Eh) conditions within the water column (Crusius et al., 1996; Piper and Dean, 2002). Following the guidelines described by Piper (2001) and Piper and Calvert (2009), a suite of elements are studied that cover a range of environmental Eh values, as determined by empirical thermodynamic constraints on half-cell reactions. Authigenic Mn^{4+}-bearing oxides, oxyhydroxides and carbonates precipitate under oxidizing conditions from dissolved Mn^{2+} at Eh values exceeding 0.704

eV in seawater, which is an Eh value only slightly higher than that associated with denitrification of nitrate (Piper and Calvert, 2009). Therefore, enrichments of excess Mn can be used to infer oxic water conditions, while depletions indicate suboxic or anoxic conditions (Tribovillard et al., 2006). Similarly, both excess Cr and excess V are adsorbed onto sinking particles as oxyanions or precipitate as $Cr(OH)_3$ or vanadium-bearing oxides or oxyhydroxides [V_2O_3, V_2O_4, $V(OH)_3$] at Eh values below 0.545 eV and -0.040 eV, respectively (Piper, 2001). This latter value is only slightly higher than the predicted Eh value of -0.055 eV for sulfate reduction, thus implying that both excess Cr and excess V enrichments are indicative of suboxic or anoxic conditions, while depletions suggest an oxic water column. Enrichments of excess Mo and excess U are used to infer full anoxia. Dissolved MoO_4^{2-} and $UO_2(CO_3)_3^{4-}$ are the predominant species in oxygenated seawater (Calvert and Pedersen, 1993), and are reduced to solid-phase MoS_2 and several U-bearing oxides of which UO_2 is the dominant form, or as the particle-reactive MoO_2^+ species.

4.3 Methods

4.3.1 Core descriptions

Sediment cores were recovered by the *R/V Maurice Ewing* from four fjords along the Gulf of Alaska margin in 2004 (Fig. 4.1). Each station was sampled with either short gravity- or multicore-type cores, and longer piston-type jumbo cores (Table 4.2). Following retrieval, each core was sectioned and analyzed shipboard using a GEOTEK Multi-Sensor Core Logger (MSCL) for high spatial resolution geophysical properties at 1-cm intervals. Cores were then subsequently split, lithologies described and high-resolution linescan imagery was collected. All EW0408 sediment cores are stored at the Oregon State University core repository.

4.3.2 Geochronological approach

To develop a chronological framework for this study, a complementary approach was employed using excess ^{210}Pb, ^{137}Cs, and ^{226}Rn activities, ^{14}C accelerator-mass-

spectrometry (AMS) dating of terrestrial and marine macrofossils, and tephrochronological correlations to previously dated terrestrial volcaniclastic deposits. Furthermore, due to the tendency towards core top loss during piston coring operations, multi-cores or benthos gravity cores were used to recover surface sediment. These short cores were then correlated to the appropriate longer piston core using radionuclide activities, MSCL geophysical properties or biogeochemical marker horizons to generate a composite record for each site. Excess ^{210}Pb, ^{137}Cs, and ^{226}Rn activities were measured following the methods described in Walinsky et al. (2009).

4.3.3 Biogeochemical approach

Bulk 1-cm-thick sediment samples were collected from each core (Table 4.2). Samples were then freeze-dried, homogenized by hand with a ceramic mortar and pestle, and subsampled. One split for all jumbo piston core samples (except EW0408-44JC due to insufficient sample masses) was pressed into 5 g pellets under a confining pressure of ten metric tonnes for two minutes. The pressed pellets were then analyzed for major, minor, and trace element concentrations using a PANalytical Axios wavelength dispersive x-ray fluorometer (XRF). The XRF analytical routine was calibrated using 40 international standards, standardized fused disks were run as machine drift monitors, and two internal standards (MAG-1 and SDO-1) were run alongside each analytical set of 20 samples. Replicate analyses of the internal standards yielded standard deviations less than 5% of the mean for 28 elements. The geochemistry of core EW0408-11JC was analyzed by inductively coupled plasma mass spectrometry (ICP-MS). A full description of ICP-MS methods and analytical precision, as well as the coulometric method for measuring $CaCO_3$ concentrations, are all presented in Addison et al. (in prep.).

Concentrations of inorganic elements were interpreted in terms of their respective geochemical behaviors. In the case of the refractory elements Al, Ti, and Zr, these were used in bivariate and ternary plots to identify detrital element provenance. If it was found that only a single geochemical source contributed detrital sediment, then the concentration of Ti was used as a proxy for terrigenous erosion (e.g. fluvial discharge

and/or terrestrial run-off). However, if multiple detrital sources were indicated, then a more general approach was used to estimate the bulk terrigenous content,

$$L = 100 - (opal + CaCO_3 + (2 \times TOC))$$ [Eqn. 1]

where L is the total lithic concentration, and the other components are assumed to fully account for the biogenic phases. Because $CaCO_3$ was not measured in core EW0408-22JC directly, $CaCO_3$ content was estimated by multiplying the total Ca concentration by a factor of 2.01, based on the mean Holocene $CaCO_3$/Ca ratio observed in EW0408-11JC ($n = 52$, $r = 0.754$, $p < 0.01$).

The concentrations of the redox-sensitive elements Mn, V, Cr, U, and Mo were used to estimate the authigenic precipitate fraction as a qualitative proxy for dissolved oxygen content in the ambient water column, according to the equation

$$excess\ X = X_{measured} - \left(Al_{measured} \times \left[\frac{X}{Al} \right]_{avg\ sed} \right)$$ [Eqn. 2]

where $X_{measured}$ is the measured XRF or ICP-MS sample concentration of the element of interest, and $(X/Al)_{avg\ sed}$ is the global mean sediment Al-normalized ratio for element X (McLennan, 1995). This calculation has been used extensively in many different sedimentary environments, including nearshore continental margins (e.g. Dymond, 1981). This approach assumes a constant element/Al ratio, implying only one source of terrigenous sediment (Anderson and Winckler, 2005). Based on the detrital provenance analysis results presented in the next section, this assumption is violated for cores EW0408-11JC and -22JC due to mixing between different sources; this complexity is addressed by examining a full gamut of redox-sensitive elements.

The second sample split was treated in 2 N HCl overnight, rinsed with Millipore distilled water three times, and freeze-dried. A subsample was then measured for biogenic silica (opal) using a wet-alkali extraction method (Mortlock and Froelich, 1989), with an estimated error of 11% based on replicate measurements of an internal sediment standard. A second subsample was combusted with a Costech 4010 HCNS elemental analyzer for TOC and TN concentrations that was coupled to a Finnigan Delta^{plus}XP

isotope ratio mass spectrometer for stable $\delta^{13}C$ measurement. All isotope values are reported in permil units (‰) according to the relationship

$$\delta X = \frac{R_{sample} - R_{standard}}{R_{standard}} \times 1000 \qquad \text{[Eqn. 3]}$$

where X is the element of interest and R is the measured isotopic ratio. All carbon measurements are relative to the V-PDB standard ($\delta^{13}C$ = 0.0‰). Replicate measurements (n > 100) of internal standards run alongside TOC, TN, and sedimentary $\delta^{13}C$ samples yielded one standard deviation from the mean of 2.6%, 3.8%, and 1.0%, respectively.

A linear mixing model approach was used to estimate the terrestrial TOC contribution to the fjord sediment because of the high proportions of terrestrially-derived TOC likely present within the total TOC measurements at these nearshore sites using the equation

$$\% \text{ terrestrial C} = \frac{\delta^{13}C_{sample} - \delta^{13}C_{marine}}{\delta^{13}C_{terrestrial} - \delta^{13}C_{marine}} \times 100 \qquad \text{[Eqn. 4]}$$

where $\delta^{13}C_{sample}$ is the measured $\delta^{13}C$, $\delta^{13}C_{marine}$ is the fully marine endmember $\delta^{13}C$, and $\delta^{13}C_{terrestrial}$ is the fully terrestrial endmember $\delta^{13}C$. Normal application of Eqn. 4 places values of approximately -21.0‰ (modern marine phytoplankton) and -27.0‰ (modern pollen) as the marine and terrestrial $\delta^{13}C$ endmember values, respectively, (Meyers, 1994; McQuoid et al., 2001). In this study, the endmember ranges were broadened slightly to -20.0 (marine) and -28.0‰ (terrestrial) because many of the EW0408 samples considered here exceeded the customary range of $\delta^{13}C$ values. Such variability is not unusual for continental margin sediments (e.g. Nuwer and Keil, 2005; Walsh et al., 2008).

To estimate the export flux of biogenic and terrigenous material for each core, mass accumulation rates (MAR) were calculated according to the relationship

$$\text{Bulk MAR} = \rho_{bulk} \times \text{SAR} \qquad \text{[Eqn. 5a]}$$

where bulk MAR is the bulk mass accumulation rate (in units $g/cm^2/yr$), ρ_{bulk} was estimated from the gamma-ray-attenuated bulk density measurements from the MSCL (in

units g/cm^3), and SAR is the interval sedimentation rate (in units cm/yr) calculated between each biogeochemical sample using the interpolated ages for each sample based on the respective age-depth model for each core. Then, to determine the flux of specific sediment phases

$$X_{MAR} = \text{Bulk MAR} \times X_{measured} \qquad \qquad \text{[Eqn. 5b]}$$

where X_{MAR} is the mass accumulation rate of component X (in units g/cm^2/yr or µg/cm^2/yr), and $X_{measured}$ is the concentration of the phase of interest (either in units ppm = µg/g, or wt% = g/g).

4.3.4   Statistical treatment

Statistical considerations were limited chiefly to correlation calculations, data reduction, and time-series analyses. Bivariate Pearson correlation coefficients were calculated for natural-log-transformed datasets to ensure normal distributions (Davis, 2002). Natural-log transformation has the added benefit of circumventing the constant-sum problem (Aitchison, 1986; Aitchison, 1999). In the case of core EW0408-33JC that was sampled at extremely high temporal resolution and yielded more than 350 individual samples, bivariate correlations were not realistic. Instead, principal component analysis was used to simplify the redox-sensitive element concentration data into three factors with eigenvalues ≥ 1, using a varimax rotation to maximize the variance of the element loadings onto the extracted factors (Davis, 2002). These extracted factors were then interpreted in terms of the environmental processes that may control the observed elemental loading patterns.

Time-series analysis was performed using the REDFIT analysis software package (Schulz and Mudelsee, 2002). Briefly, this program utilizes a bias-corrected Lomb-Scargle Fourier transform appropriate for unevenly-spaced data with no need for interpolation to equal time steps. To assess the significance of resulting spectral peaks, REDFIT calculates a first-order autoregressive (AR1) process representing stochastic variability in the dataset, and then tests the data time-series against the AR1 time-series using a Monte Carlo ensemble. For the time-series analysis of the high-resolution opal

MAR datasets from cores EW0408-22JC, -33JC, and -44JC, peaks exceeding the 95% confidence level were considered significant. The REDFIT approach inherently assumes that the AR1 process approximates the background noise in the respective datasets, and that the distribution of data along the time axis is not too clustered (Schulz and Mudelsee, 2002).

4.4   Results

4.4.1   Lithologies and geochronology

Radiometric dating results are presented in Table 4.3. AMS ^{14}C dates were calibrated to calendar ages (denoted as cal yrs BP, or cal kyrs BP) using the CALIB 5.01 software (Stuiver and Reimer, 1993) and the INTCAL04 calibration curve (Reimer et al., 2004). All ages are reported as the 2σ median probability age with uncertainties of one-half of the 2σ calibrated age range. In the case of marine macrofossils, a marine carbonate reservoir age of 732 years was subtracted from the ^{14}C date prior to calibration. This reservoir age is based on the mean ^{14}C date discrepancy between paired marine bivalve and terrestrial wood samples from three different EW0408 cores. In an effort to minimize the use of reservoir corrections, terrestrial-derived wood fragments, spruce needles, leaves and seeds were preferentially selected for AMS radiocarbon dating where available following wet sieving with a 250-μm-screen of approximately 10 cm^3 bulk sediment samples. To determine if older macrofossils were inadvertently sampled with this strategy, each AMS ^{14}C date was evaluated against both the lithostratigraphy and the full age-depth model for each respective core.

EW0408-11JC

The piston core EW0408-11JC recovered from the Gulf of Esquibel is composed of three major lithologic units (Fig. 4.4). The uppermost Unit 1 is an olive-gray silty clay marked with faint laminations that extends from 0 – 1230 cm bsf, and conformably overlies a massive dark gray silty clay (Unit 2) with moderate bioturbation from 1230 – 1314 cm below sea floor (cm bsf). Within this massive silty clay at 1295 – 1298 cm bsf,

a black tephra bed with a graded top contact and sharp bottom contact is present. Below 1314 cm bsf is a conformable contact with a color interstratified (reddish-brown/light gray/dark gray) silty clay containing rare dropstones (Unit 3) that extends to the bottom of core EW0408-11JC at 1762 cm bsf.

The suite of geophysical and biogeochemical analyses conducted on the multi-core EW0408-10MC indicates no overlap with the longer EW0408-11JC piston core, nor with its accompanying trigger core, indicating a gap of unknown length exists between the bottom of the multicore and the top of the piston core. Using a suite of 11 AMS ^{14}C samples and a tephra correlation to a nearby lake core (Barron et al., 2009), a fifth-order polynomial age model was generated that explained >99% of the variance in the depth-age relationship for the dated samples in the EW0408-11JC piston core (Fig. 4.5). This age model places the top of EW0408-11JC at ~1600 cal yrs BP, corresponding to approximately 1 m loss of core top material. Additional dating efforts are underway to constrain the age of this core more fully. This geochronological approach differs from that presented by Barron et al. (2009), in that (i) their age model is based on a 3-part linear fit to these dates and (ii) assumes no core top loss. The practical result of these differences in age models is that the late Holocene dates discussed in this paper are older than those reported by Barron et al. (2009).

Linear estimations of the polynomial age-depth model were required for the calculation of bulk mass accumulation rates (Fig. 4.6a). In particular, the rapid shift in sedimentation rates between 11.8 – 10.8 cal kyrs BP presents a considerable problem for this approach. Linearization removes distortion induced in the accumulation rate calculations by the presence of inflection points within the age model, though at the cost of imposing abrupt changes in sedimentation. Opal concentrations are also highly correlated with density (Fig. 4.6b; n = 93, r = -0.921, p < 0.01), which further biases mass accumulation calculations and indicates opal is a key component of the bulk sedimentation regime. To resolve these complications, the EW0408-11JC age model required three different linear sedimentation rates for a somewhat realistic bulk MAR:

0.022 cm/yr between 21.0 to 11.8 cal kyrs BP; 0.563 cm/yr between 11.8 to 10.8 cal kyrs BP; and 0.102 cm/yr younger than 10.8 cal kyrs BP.

EW0408-22JC

EW0408-22JC is 11.84 m long, and is composed of three lithologic units (Fig. 4.4). The uppermost massive olive gray clay unit extends from the core top to 50 cm bsf. It conformably overlies a slightly coarser massive dark olive gray clay that extends to 460 cm bsf. The lowermost conformable unit is a massive dark grayish-brown silty clay with dispersed sand grains from 460 – 1184 cm bsf. EW0408-22JC also contains six thin sand beds, and rare sand pods or gravel clasts (Fig. 4.4). For the biogeochemical analyses, these coarser units were avoided during sampling.

Both geophysical and biogeochemical analyses indicate an overlap between the benthos gravity core EW0408-21GC and EW0408-22JC that corresponds to a loss of the upper 30 cm from the EW0408-22JC piston core. Measurements of excess ^{210}Pb activity from EW0408-21GC are consistent with a maximum apparent steady-state accumulation rate of 2.4 – 4.5 mm/yr ($p < 0.05$); this rate is corroborated with ^{137}Cs activities that indicate a maximum apparent mean accumulation rate based on the first appearance of ^{137}Cs of 3.0 – 3.7 mm/yr. For the purposes of generating a composite age-depth model for EW0408-22JC, the first appearance of ^{137}Cs at 13.5 cm bsf was considered as equivalent to AD 1964, and the first appearance of excess ^{210}Pb activities at 40 cm bsf as AD 1893 (Table 4.3).

Seven AMS ^{14}C samples and the White River Ash (Addison et al., *accepted*) constrain EW0408-22JC (Table 4.3). Due to an apparent age reversal, an additional AMS sample at 1.28 mbsf was rejected. While the lithostratigraphic unit associated with this sample does not suggest emplacement of reworked material from upslope, there are numerous broken shell fragments and dispersed sand grains throughout the core implying episodic cryptic turbidites or iceberg-rafted debris (IRD) accumulation within the homogenous silty clay sections (Fig. 4.6). Nevertheless, the ordered chronology of the remainder of the AMS ^{14}C samples gives us confidence in the geochronological method employed in this study.

The composite age-depth model generated from the complementary geochronological approaches utilized for EW0408-22JC is a quadratic fit forced through AD 2004 at the core top ($R^2 = 0.983$). To evaluate the most appropriate age-depth model for these data, the significance of two alternate models (linear and cubic) were tested using an analysis of variance (ANOVA) coupled with an F-test (Davis, 2002). While all three models are statistically significant ($p < 0.05$) in describing the age control points, the quadratic model was a significant improvement over the linear model, while the cubic model was not a significant improvement ($p > 0.05$) over the quadratic model. The curvature of the quadratic model suggests non-steady-state accumulation throughout the Holocene, with rates highest during the late Holocene (Fig. 4.6a). There is a strong negative correlation between opal concentrations and the bulk density (Fig. 4.6b; n = 243, $r = -0.578$, p < 0.01). Because Eqn. 5a relies on both sedimentation rate and bulk density, this result indicates opal accumulation is intimately related to the sedimentation regime at this site. The mean accumulation rate for the full core is 1.25 mm/yr, which is less than half the rate suggested by either excess ^{210}Pb or ^{137}Cs activities measured in recent sediment.

EW0408-33JC

Core EW0408-33JC is 18.19 m long, and composed of a massive olive gray clay that coarsens slightly to a silty clay at 497 cm bsf that extends to the bottom of the core (Fig. 4.4). No sand lenses are present, though several shell hash layers are evident. The major chronological constraints for core EW0408-33JC have been presented previously (Addison and Finney, *in prep.*). Briefly, EW0408-33JC is constrained by nine terrestrial AMS ^{14}C dated macrofossils, and the corresponding multicore EW0408-32MC by excess ^{210}Pb and ^{137}Cs activities. To these age control points, two cryptotephras recently identified in EW0408-33JC (Addison et al., *accepted*) were included. These cryptotephras are derived from previously dated explosive activity from nearby Mt. Edgecumbe (Riehle and Brew, 1984) The cryptotephras are geochemically identical to macroscopic tephra deposits that are constrained by conventional ^{14}C dates on underlying peat deposits. The new age-depth model constructed for this work is linear and describes

>99% of the variance within the dataset. This excellent fit to the data indicates that, despite the shell hash horizons suggesting episodic turbidite deposition, the full EW0408-33JC core is a continuously accumulating record of hemipelagic sedimentation. The mean sedimentary accumulation rate for the full core is 2.4 mm/yr (Fig. 4.6b).

EW0408-44JC

Core EW0408-44JC is 15.61 m long following correction for gas voids (Table 4.2). EW0408-44JC is composed of a laminated black silty clay that fines slightly to clay at 724 cm bsf and below (Fig. 4.4). This core contains several prominent graded dark laminations that consist of coarser sediment including several noted terrestrial macrofossil-rich horizons.

Radiometric dating (excess ^{210}Pb and ^{226}Rn activities) indicates a surface mixed layer 20 cm thick in EW0408-43MC, with a steady-state maximum apparent accumulation rate of 5.2 – 6.7 mm/yr ($p < 0.05$). The same radionuclide measurements from the top of EW0408-44JC indicate approximately 25 cm was lost during core recovery. Unlike the other cores considered in this study, the uppermost sections of EW0408-44JC suffered from excessive gas expansion, such that correlations of the high-resolution MSCL geophysical data between cores EW0408-43MC and EW0408-44JC were impractical.

The EW0408-44JC piston core is constrained by 8 AMS ^{14}C dates on terrestrially-derived organic macrofossils (Table 4.3). An additional AMS ^{14}C sample from 1.21 mbsf was rejected due to an anomalously old date, suggesting emplacement of upslope older sediment at the coring location. The age-depth model selected for the indicated EW0408-44JC chronological constraints is a cubic model with an R^2 value of >0.99 (Fig. 4.5). A linear model ($R^2 = 0.96$) was tested as a less complicated alternate age-depth model, but it was discarded due to the results of an ANOVA test that indicated the cubic model was a significantly better fit ($p < 0.05$) for the data. However, as with EW0408-11JC, the cubic age-depth model for EW0408-44JC also contains an inflection point that bias the bulk mass accumulation rate (Fig. 4.6c) calculations necessary for evaluating productivity. To circumvent this problem, a simplifying linear sedimentation rate of 0.40 cm/yr was used.

4.4.2 Paleoproductivity and organic matter trends

The record of sedimentary organic matter accumulation preserved within the fjords of southeast Alaska is complex. Both TOC and opal accumulation rates vary by an order of magnitude between fjord sites (Figs. 4.7 and 4.8), and the relationship between these components is not straightforward. Cores EW0408-11JC and EW0408-22JC both show strong positive correlations between TOC and opal ($r > 0.85$), but lack of a correlation for EW0408-33JC, and a negative correlation for EW0408-44JC (Fig. 4.7a), indicate a complicated relationship between siliceous export productivity and organic carbon accumulation in these different fjords. Organic matter source analysis using bulk sedimentary $\delta^{13}C$ isotopic values and C/N ratios (Meyers, 1994) also show variable contributions of both terrestrial vascular plant material and marine algae (Fig. 4.7b).

Core EW0408-11JC has both low opal and TOC concentrations prior to ~14 cal kyrs BP (Appendix 4.5). Following 14 cal kyrs BP, these data begin a steady monotonic increase that reaches maximum values of 40% and 7.5%, respectively, at the top of the core, corresponding to ~1600 cal yrs BP. The lowest values in sedimentary $\delta^{13}C$ also occur prior to 14 cal kyrs BP (-29.0 ± 0.3‰), and are contemporaneous with the highest C/N ratios (15.3 ± 1.9). Between 10 – 14 cal kyrs BP, the $\delta^{13}C$ values increase rapidly by +7‰, and then slowly increase to a late Holocene maximum of -21.0‰; the C/N ratio data show the opposite trend, with a late Holocene minimum of 9.6.

EW0408-22JC contains similar trends as -11JC, albeit with greater variability in opal concentrations (Appendix 4.6). Both TOC and opal values increase from minima during the early Holocene (prior to ~7000 cal yrs BP), and culminate in late Holocene maxima. With the exception of a few isolated peaks, the C/N ratio remains fairly constant throughout the entire core (9.82 ± 0.82), while the sedimentary $\delta^{13}C$ data show a steady increase to late Holocene values, similar to both the opal and TOC trends. There are significant correlations between $\delta^{13}C$ and both TOC ($n = 69$, $r = 0.808$, $p < 0.01$) and the C/N ratio ($n = 69$, $r = -0.312$, $p < 0.01$).

The high-resolution productivity record in EW0408-33JC (Appendix 4.7) differs from both -11JC and -22JC in many aspects. The presence of decadal-scale variability is

indicated in several proxies throughout the entire core length. During the early Holocene (from ~7500 to ~5500 cal yrs BP), decadal-scale opal concentration variability is superimposed over a millennial-scale background decline of approximately ~10%. Between 5500 to 2700 cal yrs BP, the opal background increases by ~10%, but then declines again from 2700 to 1000 cal yrs BP The late Holocene sees a short-lived increase to opal concentration values exceeding 35%, and then gives way to an abrupt decline in the most recent sediment. These trends in biogenic silica are largely not seen in any other proxy from core EW0408-33JC. Instead, there is considerable coherency in the relationships between $\delta^{13}C$ and both TOC (n = 362, r = 0.265, p < 0.01) and the C/N ratio (n = 362, r = -0.713, p < 0.01). The most striking behavior in these related proxies is seen between the core top and ~1000 cal yrs BP, when TOC, the C/N ratio and sedimentary $\delta^{13}C$ data show large magnitude in-phase oscillations.

Opal, TOC, the C/N ratio, and sedimentary $\delta^{13}C$ data are all highly correlated in core EW0408-44JC. As described above for EW0408-33JC, core -44JC contains high-frequency variability in all organic proxies superimposed over lower frequency changes in the millennial-scale background. All four proxies are correlated at the 99% confidence level. For both opal and $\delta^{13}C$ (n = 128, r = 0.791, p < 0.01), the oldest part of the core at ~4000 cal yrs BP contains a background maxima that decreases to a minima around 3000 cal yrs BP. The opal and $\delta^{13}C$ background then increases again until 2000 cal yrs BP. This interval is then followed by a reduction to minimum values around 1200 cal yrs BP, and then a second increase that terminates in the modern core top sediment. These millennial-scale trends are anti-correlated with the patterns observed in both TOC and C/N ratio data, particularly with respect to opal where both TOC (n = 128, r = -0.743, p < 0.01) and the C/N ratio (n = 128, r = -0.837, p < 0.01) exceed the 99% confidence level.

The strong correlation between TOC and both C/N and sedimentary $\delta^{13}C$ ratios in all four cores, as well as the lack of a positive correlation between opal and TOC in both cores EW0408-33JC and -44JC, suggest TOC MARs as calculated by Eqn. 5 are unlikely to faithfully indicate only marine productivity. The results of the linear mixing model using the measured sedimentary $\delta^{13}C$ data from cores EW0408-11JC, -22JC, -33JC, and -

44JC indicate mean Holocene terrestrial-derived C proportions of 16.8 ± 5.5%, 17.9 ± 6.2%, 27.8 ± 9.5%, and 15.8 ± 10.1%, respectively. Therefore, opal MAR calculations alone are considered as key to describing changes in siliceous marine primary productivity (e.g. diatoms) in these fjord cores.

The effects of the Holocene/LGM transition on nearshore siliceous productivity, as preserved in EW0408-11JC, indicate a shift from relatively low LGM values to a peak during the deglacial transition (Fig. 4.8a). This deglacial peak, driven partly by a short-lived rapid bulk accumulation rate change (Fig. 4.6a), is a real productivity maxima as evidenced by the same peak in the unmodified opal concentration data. The deglacial peak then gives way to an early Holocene minimum at 10.7 cal kyrs BP. At 10.0 cal kyrs BP, siliceous productivity increases in EW0408-11JC, and then transitions to a more gradual increase from 9500 – 2600 cal yrs BP (Fig. 4.8b).

The joint Holocene record of productivity recorded within the overlapping time periods preserved within the four fjords is complex (Fig. 4.8b). For example, between 10000 – 4000 cal yrs BP, core EW0408-22JC shows a prolonged opal MAR minima that is only disrupted (i) between 8500 – 8000 cal yrs BP, when values show several rapid fluctuations within a relatively narrow time range, and (ii) during a diffuse peak between 7000 to 6500 cal yrs BP. Opal accumulation rates then increase monotonically into the late Holocene starting around 4000 cal yrs BP. Core EW0408-33JC shows a similar trend to that of EW0408-11JC, with increasing productivity beginning around 5500 cal yrs BP and terminating at 2800 cal yrs BP. Finally, while the accumulation rate of core EW0408-44JC is extremely high, it only preserves the last 3800 years of export productivity within Deep Inlet. Nevertheless, during this period, it shows several periods of elevated productivity beginning at approximately 3500, 2700, 1900, and 1200 cal yrs BP.

4.4.3   Terrestrial OM and detrital accumulation

Proxy datasets for describing the accumulation of terrigenous sediment are based on (i) geochemical assays of bulk untreated sediment samples using either ICP-MS or XRF techniques (EW0408-11JC, -22JC, and -33JC), (ii) bulk lithic calculations based on

Eqn. 1, and (iii) terrestrially-derived organic matter as determined by carbonate-free bulk sedimentary $\delta^{13}C$ isotope data and C/N ratios. This third approach indicates sustained changes in the relative proportions of marine- and terrestrially-derived organic matter in core EW0408-11JC (Fig. 4.7). Due to the greater prevalence of marine-derived organic matter in the other sediment cores discussed in the previous section, the organic matter provenance records from EW0408-22JC, -33JC and -44JC will not be examined as records of long-term terrestrial OM erosion.

Inorganic geochemistry and bulk lithic trends in EW0408-11JC, -22JC, and -33JC

The elements Al, Ti, and Zr occur dominantly within independent, highly insoluble mineral phases and are commonly associated with the sedimentary lithogenic fraction. When the Ti and Zr concentration data are plotted against Al in bivariate diagrams, both cores EW0408-22JC and -33JC follow an average shale composition (Fig. 4.9a, b). EW0408-11JC is more complex; while the Holocene (< 11 cal kyrs BP) Ti/Al ratio data is similar to that of the global average shale (Fig. 4.9a; Turekian and Wedepohl, 1961), the LGM values are depleted relative to Ti. The Zr/Al ratio is also very different from an average shale composition (Fig. 4.9b); however, an extrapolation of the Zr/Al data back to the origin suggests both elements are still associated with a lithogenic source.

Examining the concentrations of Al, Ti, and Zr in ternary space (Fig. 4.9c) indicates the presence of multiple geochemically-distinctive detrital sources within cores EW0408-11JC and -22JC, while the small degree of scatter in the EW0408-33JC dataset suggests only one sediment source. The overlap between the EW0408-22JC and -33JC ranges suggests related sources, and that the composition of EW0408-33JC is likely representative of one of the two endmembers present along the EW0408-22JC mixing line. The bedrock geology of the EW0408-22JC site in West Crawfish Inlet is composed exclusively of the Crawfish Inlet pluton complex (Loney et al., 1975; Reifenstuhl, 1986), with only tonalite and granodiorite exposures in outcrop along the shoreline of the fjord, suggesting that the variability indicated in the refractory element concentrations in EW0408-22JC may be related to magmatic processes.

The detrital provenance analysis also indicates different sediment sources present within the EW0408-11JC dataset (Fig. 4.9c). While there is excellent agreement between the Zr and Al data (Fig. 4.9b), the relationship between Ti and Al suggests two potential sediment sources, with one source substantially depleted in Ti relative to the other (Fig. 4.9a). Reconnaissance geological mapping of adjacent Prince of Wales Island (Brew, 1996) indicates many geochemically diverse source lithologies may be contributing sediment to the Gulf of Esquibel, and that an assignment of representative lithologies based on the detrital geochemical data is not straightforward. Nonetheless, the provenance diagram also indicates little mixing between the two sources, and that the relative contribution of these sources is time-transgressive (Fig. 4.9c). Therefore, this "detrital switch" between sources is likely related to paleoenvironmental conditions, and occurs between 12.4 – 10.2 cal kyrs BP.

Given these inorganic geochemical results, it appears that the mass accumulation rates of refractory elements is likely only applicable for reconstructing terrigenous flux in core EW0408-33JC. The Ti concentration data was used for this approach, though Zr would have been equally appropriate given the high correlation between these two datasets (n = 364, r = 0.874, p < 0.01). The refractory element complications were circumvented for cores EW0408-11JC and -22JC by using the bulk lithic calculation described in Eqn. 1. While this equation does not account for authigenic sedimentation, it is likely that contributions by such processes would be minimal due to the greater proportions of the biogenic and terrigenous sediment fractions. Authigenic sedimentation is evaluated in greater detail in a following section.

The downcore trends in terrigenous accumulation rates from cores EW0408-11JC, -22JC, and -33JC are complex. EW0408-11JC contains high concentrations of lithic components during the LGM (mean 88%; Fig. 4.10a) until approximately 12 cal kyrs BP, when the concentrations begin a steep decline to 50% around 9.5 cal kyrs BP. Holocene lithic concentrations continue to decline steadily to a minimum lithic concentration of 37% at the core-top. The lithic MAR calculation indicates the lowest flux was associated with the LGM (mean 2.96 g/cm^2/yr), with a short-lived increase to 58.58 g/cm^2/yr

between 11.8 – 10.8 cal kyrs BP, and a Holocene mean value of 6.38 g/cm^2/yr. The elevated deglacial flux rate is likely an artifact of the bulk MAR given there is no such increase indicated in the lithic concentration data.

EW0408-22JC has greater variability in both lithic concentations and the lithic MAR than core EW0408-11JC in the overlapping time period (Fig. 4.10a). There is a distinctive increase in both datasets between 10.0 – 8.2 cal kyrs BP, followed by a reduction that lasts until 5.5 cal kyrs BP. This interval is the lowest lithic MAR period in the entire core, with a mean rate of 5.64 g/cm^2/yr. This minima then rapidly transitions to the highest lithic MAR of 9.29 g/cm^2/yr at 4300 cal yrs BP. Between 4300 – 2500 cal yrs BP, both the lithic concentration and lithic MAR undergo a series of rapid oscillations that ultimately end in minima for both data around 1800 cal yrs BP. At this point, the lithic concentration data and the lithic MAR rates diverge, with the lowest lithic concentration in EW0408-22JC occurring in the modern sediment, while the lithic MAR increases to a late Holocene mean of 6.59 g/cm^2/yr. The late Holocene divergence between the lithic concentrations and the lithic MAR seem likely related to the late Holocene increase in both opal concentrations and the bulk MAR (Fig. 4.6a, b), suggesting the apparent increase in the lithic MAR is an artifact of the MAR calculation.

As in the case with productivity, both Ti concentrations and the Ti MAR in EW0408-33JC indicate high frequency decadal-scale variability superimposed over lower frequency millennial- and centennial-scale oscillations (Fig. 4.10b). Because both Ti concentrations and the Ti MAR record are highly correlated (n = 363, r = 0.772, p < 0.01) due to the linear bulk MAR calculated for this core (Fig. 4.6c), only the millennial-scale Ti MAR results will be addressed for brevity. Low-frequency Ti MAR increases are seen between 7500 – 5500, 2400 – 1500, and 600 – recent. Several higher-frequency increases in Ti MAR also occur throughout the mid- and late Holocene sections of EW0408-33JC, including the highest Ti MAR value at 0.16 g/cm^2/yr occurring between 6800 – 6600 cal yrs BP.

The three cores considered here show a number of contemporaneous increases in terrigenous accumulation fluxes, as determined either by Ti-based or lithic-based MAR

calculations (Fig. 4.10). There are several periods when all three cores indicate broadly consistent increases in terrigenous accumulation: 6300 – 5600, 4600 – 2500, and 2400 – 1500 cal yrs BP. Based on this consistent multi-basin record of terrigenous accumulation, these results are likely representative of enhanced precipitation and associated fluvial discharge throughout the southeastern Alaska region during the Holocene.

Organic geochemistry trends in EW0408-11JC

The EW0408-11JC OM record indicates several sustained shifts in the proportions of marine- and terrerstrially-derived OM sources throughout the last 18000 years (Fig. 4.11). The major deglacial change in OM provenance occurs in steps, beginning with a gradual enrichment from an LGM $\delta^{13}C$ value of -29.0‰ to -26.8‰ between 14,300 – 12,500 cal yrs BP (phase I), with no obvious changes in the high C/N values during this interval. This time interval is associated with a mean terrestrial-derived C contribution of 89%, as indicated by Eqn. 4. The second deglacial shift (phase II) occurs between 12.5 – 10.8 cal kyrs BP, and during this period of rapid increase of $\delta^{13}C$ values, C/N values increase abruptly, perhaps associated with selective degradation of N compounds, or more likely, a period of increased productivity (Fig. 4.8a). This is the same time frame associated with the EW0408-11JC detrital 'switch' as described previously. The third phase of the deglacial shift (phase III) is marked by a final increase in $\delta^{13}C$ to -21.7‰, and a reduction in the C/N ratio to 9.5, both of which are clear indicators of predominantly marine-derived OM, and an estimated terrestrial contribution of only 20%. Throughout the rest of the EW0408-11JC record into the late Holocene, both $\delta^{13}C$ and C/N values are relatively constant with long-term trends towards increasing marine-derived OM with the exception of two perturbations at 8200 and 2600 cal yrs BP, respectively (Fig. 4.11).

4.4.4   Bottom-water anoxia

Several redox-sensitive elements exhibit high enrichments in cores EW0408-11JC, -22JC, and -33JC (Fig. 4.12). Enrichments above standard shale values (Turekian

and Wedepohl, 1961) in Mn (Fig. 4.12*a*) and Mo (Fig. 4.12*c*) are strong indications of oxic and anoxic conditions, respectively, such that a plot of Mn versus Mo can be used to qualitatively identify dominant sedimentary oxygenation regimes (Fig. 4.12*d*). In particular, all Mo concentrations in EW0408-22JC are above the average shale values suggesting dominantly anoxic or suboxic conditions. Conversely, both cores EW0408-11JC and -33JC show Mo concentrations both above and below the average shale, suggesting that these fjords have experienced periods of either enhanced bottom-water renewal or stagnation. The linear behavior of V in all three cores suggests V is related to terrigeneous clastic material (Fig. 4.12*b*). Unlike both EW0408-11JC and -33JC, however, extrapolation of the EW0408-22JC vanadium concentrations to 0% Al concentration yields a value of 43 ppm V, indicating some authigenic precipitation of V occurred, likely associated with suboxic or anoxic conditions as inferred from the Mo data (Fig. 4.12*c, d*).

These qualitative results are further substantiated with statistical results associated with the excess elemental concentration calculations. In particular, negative correlations between natural-log-transformed concentrations of solid-phases that accumulate under oxic (Mn) and anoxic (U and Mo) conditions are statistically significant (U: $n = 492$, $r = -.398$, $p < 0.01$; Mo: $n = 519$, $r = -.214$, $p < 0.01$), and are consistent with thermodynamic predictions (Piper, 2001). The identification of suboxic conditions is more difficult (Fig. 4.12*b*). There are inconsistent relationships between excess V, oxic, and anoxic proxy elements in EW0408-11JC and -22JC that complicate its use as a proxy for suboxia. In the case of EW0408-11JC, excess V exhibits a positive correlation with excess Mn ($n = 95$, $r = 0.737$, $p < 0.01$) and a negative correlation with excess Mo ($n = 95$, $r = -0.729$, $p < 0.01$), suggesting that V is accumulating under dominantly oxic conditions. The other important suboxia indicator, excess Cr, also has a negative correlation with V ($n = 95$, $r = -0.501$, $p < 0.01$), suggesting that the oxic-suboxic boundary in the Gulf of Esquibel lies somewhere between the Eh potentials of these two elements. Therefore, the accumulation of excess Cr in EW0408-11JC appears to be more diagnostic of suboxic conditions while excess V reflects oxic conditions. On the other hand, the low

correlation values in core EW0408-22JC between excess V, and both the excess Mn and Mo datasets (Fig. 4.12b), indicates V is a reliable indicator of suboxia because of its low range of variability relative to either Mn or Mo, suggesting that processes independent of those controlling excess Mn or Mo accumulation (e.g. exclusively oxia or anoxia, respectively) are dominant.

The large number of samples in EW0408-33JC makes simple qualitative interpretations more difficult. To simplify this process, a PCA method was applied to a geochemical dataset composed of the excess contributions of Mn, Fe, Cr, U, V, Mo, Cu, Zn, and Ni (Piper and Calvert, 2009). The PCA identified three principal components that described 65% of the variance within this suite of redox-sensitive elements. The loading scores for each element (Table 4.4) agree with previous assumptions about the behavior of these elements, namely that PC 1 dominantly reflects oxic accumulation conditions, PC 2 is controlled by suboxia, and the accumulation of solid-phase elements associated with PC3 are driven by bottom-water anoxia. This interpretation is somewhat complicated by nearly equal loadings between components 1 and 2 for excess Fe and Cu, as well as Ni being contained almost entirely within PC 1; these results suggest that, in addition to oxic environmental conditions, some detrital-associated accumulation may also be reflected within these data that is not completely addressed by the excess accumulation calculations. Nevertheless, the identification of the three dissolved oxygen conditions, as well as high correlations between excess Mn and PC 1 ($n = 364, r = 0.873$, $p < 0.01$), excess V and PC 2 ($n = 364, r = 0.929, p < 0.01$), and excess Mo and PC 3 ($n = 364, r = 0.776, p < 0.01$), gives us confidence in this approach.

Examining the history of water column anoxia preserved within cores EW0408-11JC, -22JC, and -33JC presents a detailed record of fjord paleocirculation. At the coarsest temporal resolution, core EW0408-11JC indicates two distinctive periods of intense anoxia (Fig. 4.13). The earliest period of anoxia occurs immediately prior to the Holocene/LGM transition, between 15.6 – 14.0 cal kyrs BP, and corresponds to a reduction in the accumulation of excess Mn, and increases in the accumulation of excess U and V. A second period of intense anoxia occurs during the mid-Holocene, from about

7000 – 4000 cal yrs BP. This intense mid-Holocene anoxia is bracketed by periods of suboxia from 7500 – 7000 and 4000 – 2000. Two additional periods of dominantly suboxic conditions occur around 12.0 and 9.5 cal kyrs BP.

Increasing the temporal resolution of the bottom-water anoxia record using core EW0408-22JC provides additional information. Three periods of intense anoxia are evident in the redox-sensitive elemental concentration data, from 7700 – 7500, 6500 – 5500, and 4700 – 4200 cal yrs BP (Fig. 4.14). Several short-lived periods of dominantly suboxic conditions are also evident around 9400, 6800, 3100, and for the most recent 600 cal yrs BP. However, the interpretation of bottom-water anoxia is confounded by an apparent decrease in all redox-sensitive elements between 8500 – 8000 cal yrs BP. The highest resolution record of bottom-water anoxia is contained within EW0408-33JC, and is resolved at multiple timescales. The PCA analysis indicates three millennial-scale regimes. During the early Holocene, oxic bottom-water conditions appear to have dominated, as evidenced by the consistently high values associated with PC1 (Fig. 4.15). From approximately 5300 to 3500 cal yrs BP, anoxia appears to have become more dominant as implied by high PC 2 and PC 3 values. These conditions then gradually transitioned to suboxia starting around 2400 cal yrs BP.

Lastly, while there were no direct measurements of redox-sensitive geochemical components in EW0408-44JC, anoxic conditions are suggested throughout this entire core by the presence of mm-scale laminated sediments (Fig. 4.4). The frequent occurrence of prominent dark fibrous organic-rich horizons indicates minimal organic degradation has occurred within Deep Inlet. Thus, at least suboxic conditions appear to have been dominant in Deep Inlet since approximately 4000 cal yrs BP.

All four cores indicate consistent patterns of anoxia. In particular, the period from about 6500 – 3500 appears to have been dominantly anoxic in Katlian Bay, West Crawfish Inlet, and the Gulf of Esquibel. This period of regional anoxia appears to have weakened during the late Holocene, when either suboxic or oxic conditions became more common in these three deeper-silled fjord records. Furthermore, the period between about 10.0 – 9.0 cal kyrs BP was likely dominated by regional suboxia, as evidenced by

an increase in either excess Cr or excess V in cores EW0408-11JC and EW0408-22JC, respectively.

4.5   Discussion

4.5.1   Site-specific variability in fjord sites

The four cores examined in this study exhibit a large degree of site-specific variability in accumulation as evidenced by the need for four different age-depth models (Fig. 4.5). Some of this variability can be ascribed to differences related to fjord geomorphology (Table 4.1). For example, the Holocene Gulf of Esquibel is not fed directly by any large fluvial systems, unlike the other fjords considered in this study so it has one of the lowest bulk MARs (Fig. 4.6a). Both depth and number of sill(s) also likely play a role in mass accumulation. This relationship is particularly highlighted by the laminated nature of EW0408-44JC, as well as its extremely high OM content (mean opal 64% and TOC 8.5%; Appendix 4.8) and high bulk MAR (Fig. 4.6c). Deep Inlet has the shallowest sill of any fjord in this study, which contributes to the maintenance of anoxic bottom-water conditions that enhance OM preservation in this fjord.

Small differences in sill depth and fluvial discharge rates seem enough to cause very different sedimentation regimes in southeast Alaskan fjords. Both Deep Inlet and Katlian Bay are small tributary fjords opening into the larger Sitka Sound (Fig. 4.1b). The sill at the mouth of Katlian Bay is approximately 7 m deeper than the Deep Inlet sill. However, Katlian Bay has greater fluvial discharge as evidenced by its deeper halocline (Table 4.1).   Together, the slightly deeper sill and the increased river flow is sufficient to generate a homogenous silty clay in Katlian Bay, while the shallower sill and reduced fluvial discharge lead to laminations in Deep Inlet.

The marine ecosystem plays an important role in sediment accumulation in the fjords as well. Cores EW0408-11JC, -22JC, and -33JC all show significant correlations between opal concentrations and the bulk sediment density (Fig. 4.6b, d). Because the bulk MAR calculation [Eqn. 5a] contains a density term, changes in the opal concentration can exert a control on the bulk MAR given a high enough opal

concentration. Such is the case with both EW0408-11JC (post 10 cal kyrs BP) and -22JC. In the latter example, the bulk MAR indicates a monotonic increase in accumulation during the late Holocene (Fig. 4.6a); this increase is mirrored in the bulk opal concentration as well as the bulk density. However, such an increase is not observed in the lithic fraction concentrations, yet the lithic MAR records an increase during this same late Holocene period (Fig. 4.10b).

Ultimately, these site-specific differences in accumulation highlight the importance of recognizing the role local effects can have in these fjord records. However, by combining these different datasets into a composite reconstruction, regional changes can be identified that are common to all four sites considered here, and extrapolate these results across the larger southeast Alaskan margin.

4.5.2   The Holocene/LGM deglaciation

Core EW0408-11JC is unique in this study of southeastern Alaskan fjord sediment cores, in that it preserves paleoenvironmental conditions during the Holocene/LGM deglacial transition from the nearshore North Pacific Ocean margin. This core presents a rare opportunity to study this major change in the linked atmosphere-ocean system in a region where this transition remains poorly understood. The suite of biogeochemical data available adds further detail previously unknown from this region. While the focus of this paper is to describe past Aleutian Low dynamics and associated Gulf of Alaska circulation patterns, and their impact on the marine ecosystem, a solely climatic interpretation from EW0408-11JC is not simple during the Holocene/LGM transition because of the role of changing sea level, due to both eustasy and regional glacial isostatic crustal adjustments. While the Gulf of Esquibel itself exceeds a water depth of 300 m, it is connected to the Gulf of Alaska via several shallow channels, none of which exceed 70 m in depth (Fig. 4.1c). Eustatic sea level rise did not breach the 70-m-isobath until approximately 13.0 cal kyrs BP (Fairbanks, 1989). A recent analysis of the siliceous microfossil communities preserved in EW0408-11JC during the deglacial transition indicates a significant presence of both freshwater and sea-ice associated diatoms, together making up more than 40% of the total diatom assemblage in some

samples, as well as numerous oceanic and coastal species (Barron et al., 2009). The presence of mixed salinities inferred from the different diatom populations clearly indicates EW0408-11JC was never disconnected from the North Pacific Ocean during the LGM deglaciation. However, fine-scale vertical adjustments of these channels driven by ice loading feedbacks, coupled with disruptions in water column dynamics by changes in freshwater discharge and bottom-water ventilation events, most likely contributed to the diverse conditions preserved in EW0408-11JC throughout the LGM/Holocene transition. While no direct data exists for reconstructing relative sea level during the LGM/Holocene deglaciation adjacent to the Gulf of Esquibel from Prince of Wales Island or nearby Heceta Island, there is good evidence that the area was not extensively glaciated and that several ice-free refugia existed during the LGM (Heaton and Grady, 2003; Carrara et al., 2007), contrary to reconstructions of regional ice margins in southeast Alaska (Clague and James, 2002; Kaufman and Manley, 2004).

Examining the detailed biogeochemical proxy evidence in EW0408-11JC alongside the diatom and silicoflagellate population data of Barron et al. (2009) allows a detailed analysis of the Gulf of Esquibel paleoenvironment during the deglacial transition, and presents several distinct periods of change (Fig. 4.16). At about 15.3 cal kyrs BP (t_0; Table 4.5), there is a major conformable lithologic change from a dropstone-rich color interstratified silty clay to a moderately bioturbated massive silty clay, presumably representing a sedimentation regime shift from somewhat proximal glaciomarine-dominated conditions to hemipelagic conditions. During this transition, there was also a shift towards bottom-water anoxia which suggests an increase in water-column stability, possibly due to a reduction in bottom-water renewal events.

The next major deglacial shift in EW0408-11JC occurs at 14.3 cal kyrs BP (t_1), as indicated by (i) the sudden appearance of a diverse diatom and silicoflagellate community, with freshwater, oceanic, and coastal marine diatoms present (Barron et al., 2009); (ii) a modest increase in opal concentration; (iii) prevalent oxic bottom-waters; and (iv) the initiation of a shift towards greater inputs of marine-derived OM (Fig. 4.16). Collectively, these proxy changes seem to be best explained as indicative of a river-

dominated estuary (Reading and Collinson, 1996). This suggests the channels connecting the Gulf of Esquibel to the North Pacific Ocean were thus probably dominated by an outflux of low-salinity waters reminiscent of the modern surface waters now present throughout the fjords of southeast Alaska (Burrell, 1989). Furthermore, these channels were likely shallow enough to restrict major influxes of both nutrient-rich intermediate zone water and suboxic-to-anoxic bottom-waters from the Gulf of Alaska, thus limiting both productivity and bottom-water ventilation. The reduction in bottom-water renewal events suggests anoxia should be dominant, yet the enrichments in excess Mn and depletions in excess U indicate oxic bottom waters, both of which seem likely tied to a combination of oxygen-rich fluvial discharge and low export productivity. During the t_1 interval, eustatic sea level surpassed the 70 m isobath, yet no noticeable change in the relative proportions of freshwater and marine diatoms occurred during this phase (Barron et al., 2009), implying regional isostatic subsistence was maintaining a shallow depth in the seagoing channels in the Gulf of Esquibel during this phase.

At 12.4 cal kyrs BP (t_2), several radical shifts occur: (i) a conformable lithology change from the massive very dark gray bioturbated silty clay to a faintly laminated olive gray silty clay; (ii) a small increase in opal concentrations; (iii) a major reduction in both freshwater and sea ice diatom populations; (iv) a decrease in subarctic, and warm and/or deep thermocline silicoflagellates; (v) an increase in upwelling-associated silicoflagellates; (vi) a possible change to suboxic bottom-water conditions; (vii) the 'detrital switch' in refractory elements as described above, reflected in the increase of the Ti/Zr ratio; and (viii) an enrichment in sedimentary $\delta^{13}C$ and a decrease in the C/N ratio (Fig. 4.16). These changes in multiple datasets are consistent with a reconfiguration of sea level in the Gulf of Esquibel and adjacent channels. The reduction in both freshwater and sea-ice diatoms indicates an increase in salinity, while increases in upwelling-related silicoflagellates suggests the advection of intermediate zone waters into the Gulf of Esquibel (Fig. 4.3; Burrell, 1989). The increases in marine productivity, as evidenced by the opal increase and isotopic enrichment, could thus be explained by an influx of this nutrient-rich water. The higher $\delta^{13}C$ values may also indicate the influx of older North

Pacific water containing enriched ^{13}C into the Gulf of Esquibel (Kroopnick, 1985).

Collectively, these proxies therefore represent the onset of modern fjord-style reverse circulation (Syvitski et al., 1987) during the LGM/Holocene deglaciation. Considering these conditions as a function of sea level requires deepening of the seagoing channels to facilitate intermediate zone water advection beneath the fluvially-dominated surface waters. The Barbados eustatic sea level reconstruction of Fairbanks (1989) shows global sea level deepening from 60 to 55 m below present sea level during interval t_2. While this deepening was in the correct direction of sea level change required for intermediate zone water advection from the Gulf of Alaska, it seems unlikely that only a 5 m change would effect such a drastic shift in microfossil community structure and biogeochemical proxy data. Continued isostatic subsidence seems necessary as well.

Between 11.7 – 10.8 cal kyrs BP (t_3), there was a productivity spike indicated in both opal concentrations and opal MAR calculations (Fig. 4.16). Accompanying the abrupt productivity maxima, there was also an increase in temperate oceanic diatoms, and a gradual reduction in sea-ice related diatoms, as well as a total loss of both subarctic and warm and/or deep thermocline-associated silicoflagellates, and all freshwater-associated diatoms. Additionally, the "detrital switch" completes during this period, the lithic MAR increases abruptly while the concentration of lithic material decreases from 90 to 70%, and bottom-waters appear to be dominantly oxic. Interval t_3 also has the highest bulk accumulation rate for the entire EW0408-11JC core (Fig. 4.6a), suggesting the high lithic MAR is an artifact of the bulk MAR that is biased by opal (Fig. 4.6b). The collective evidence points to (i) an increase in local SST as evidenced by the loss of cryophilic marine microfossils and (ii) an increase in advection of intermediate zone water, which was the ultimate cause of the massive productivity spike observed during interval t_3. It is unusual that bottom-water anoxia is not indicated at this time since this condition should be favored by both high export productivity and high accumulation rates. Enhanced winter vertical mixing may account for this seeming contradiction, though modern observations of warmer SSTs tend to be associated with periods of reduced winter storm activity, which are necessary for seasonal mixing along the Gulf of Alaska coast

(Childers et al., 2005; Rodionov et al., 2005). Alternatively, the increase in temperate oceanic diatoms and total absence of freshwater diatoms suggest the Gulf of Esquibel has attained full connection to the Subarctic Northeast Pacific Ocean with advection of both nutrient-rich intermediate zone waters, and regular bottom-water renewal events. This explanation is supported by the observation that there is little change in upwelling-associated silicoflagellates, suggesting interval t_3 is a period of intensification of fjord-style circulation, requiring additional deepening of the seaward channels connecting the Gulf of Esquibel to the Pacific. The decrease in lithic concentrations and the "detrital switch" phenomenon can both be attributed to increasing distance from the local Cordilleran Icesheet margin. This increasing distance would have led to the establishment of dominantly local sediment sources, as well as a reduction of glaciomarine sediment accumulation. By this time, isostatic subsidence would also have ceased due to the widespread retreat of the Cordilleran Icesheet along the Pacific coast (Clague and James, 2002). Field data and modeling studies for the Queen Charlotte Islands 150 km to the SSE indicate rapid crustal displacement changes from +30 m above modern sea level between 12.8 – 11.8 cal kyrs BP, to -30 m below sea level between 11.80 – 11.17 cal yrs BP (Hetherington et al., 2004). The drastic change in crustal elevation was associated with a forebulge collapse due to the retreat of the Cordilleran Icesheet, yet the location of associated shorelines during this time interval exhibit little change (Fedje and Christensen, 1999; Hetherington et al., 2004; Carrara et al., 2007). Extrapolating these results to the Gulf of Esquibel area suggests that this time period saw rapid deepening of the seagoing channels connecting the Gulf of Esquibel to the North Pacific Ocean, which is consistent with the biogeochemical results suggesting intensification of fjord-style reverse circulation during interval t_3.

EW0408-11JC deglacial interval t_4 occurred between approximately 10.8 – 10.0 cal kyrs BP, and is the final period of dramatic shifts in biogeochemical paleoproxies. In particular, the bulk accumulation rate slowed dramatically (Fig. 4.6a), and with it, there was a productivity decline in both opal MAR calculations and opal concentrations (Fig. 4.16). In the diatom assemblage data, there was a continued reduction in sea-ice related

forms, and a major reduction in temperate oceanic forms. There was also a minor return of subarctic, and warm and/or deep thermocline silicoflagellates. In terms of refractory elements, the "detrital switch" is now complete, and both the lithic MAR and lithic concentrations imply decreased terrigenous sedimentation, and by implication, a decrease in precipitation and freshwater runoff. Bottom-waters remain fully oxic during this phase, most likely due to the reduction in export productivity. Besides the decline in productivity, the second-most drastic proxy change observed during this phase is the transition towards a fully marine-dominated OM system, as evidenced by rapid shifts in both carbonate-free sedimentary $\delta^{13}C$ and C/N ratios. The marine OM signature suggests t_4 is the final phase of channel deepening adjacent to the Gulf of Esquibel, but with a climatic overprint indicated by the final drawdown of cryophilic microfossils. The warming climate signal is consistent with onset of the Holocene Thermal Maximum in southern Alaska (Kaufman et al., 2004).

Deglaciation appears to be complete around 10.0 cal kyrs BP in core EW0408-11JC (Fig. 4.16). At this point, siliceous productivity begins a slow increase towards a culmination during the mid-Holocene; temperate oceanic diatom forms become common once again; lithic accumulation rates and concentrations are low; and suboxic bottom-water conditions appear to become more regular as indicated by increasing concentrations of excess U. It is also significant that the OM provenance is dominated by marine contributions, perhaps as high as 85%. Taken as a group, these data all appear consistent with the onset of the Holocene Thermal Maximum (e.g. warm and dry conditions), with no indication of further changes related to isostatic dynamics. Nevertheless, an elevated paleoshoreline at 12.5 m above present sea level on Prince of Wales Island has been dated to 9200 – 9700 ^{14}C yrs BP (Putnam and Fifield, 1995); correcting these bivalve dates using a marine reservoir correction of 732 yrs and calibrating against the INTCAL04 curve (Reimer et al., 2004) places the formation of this shoreline between approximately 9500 – 10200 cal yrs BP, and suggests some continued isostatic rebound during the early Holocene. The impact of this vertical motion on circulation in the Gulf of Esquibel appears to be minimal, suggesting that the seagoing

channels were sufficiently deep to facilitate continued fjord-style reverse estuary circulation following the LGM/Holocene deglaciation despite isostatic adjustments. Therefore, it appears that paleoclimate inferences based on the EW0408-11JC biogeochemical record are valid after about 10.0 cal kyrs BP due to a lack of appreciable impact by continued isostatic effects.

The chronology of many of these site-specific events correspond to large-scale paleoclimate changes recognized in the Greenland NGRIP ice core (Table 4.5; Rasmussen et al., 2006; Steffensen et al., 2008). In particular, the sudden appearance of a diverse diatom and silicoflagellate community at 14.3 cal kyrs BP in EW0408-11JC is nearly contemporaneous with the onset of Bølling-Allerød warming in Greenland. The rapid opal productivity increase during deglacial phase t_3 (11.7 – 10.8 cal kyrs BP) is contemporaneous with a similar increase observed along the Gulf of Alaska continental slope (Addison et al., *in prep.*), both of which correspond with the Preboreal Oscillation identified throughout the North Atlantic (Rasmussen et al., 2007). These observations suggest that the complex deglaciation events preserved in EW0408-11JC may record global paleoclimate signals as well as local environmental signals. However, the current age-depth model for EW0408-11JC is limited by a lack of dated AMS ^{14}C samples beyond 11.5 cal kyrs BP (Fig. 4.5). The older portions of the core are constrained purely by the tephra at 1295 cm bsf; additional dating efforts are currently underway to improve the chronology presented in this paper.

4.5.3   Common Holocene trends in fjord-based paleoenvironmental reconstructions

The results indicate several distinct periods of nearshore Holocene environmental change common throughout our analyses of southeast Alaskan fjord sediment cores at multiple time resolutions. The broadest temporal approach that allow us to distinguish sub-millennial patterns common in all four fjord records suggest a variable coupling behavior between marine productivity, terrestrial erosion, and ocean circulation (Fig. 4.17). In particular, there are two prominent periods of high productivity between 2700 – 4800 and 6500 – 8000 cal yrs BP.

The mid- to late Holocene productivity enhancement from 2700 – 4800 cal yrs BP corresponds to a distinctive increase in terrestrial erosion and implied freshwater run-off. Pollen-based reconstructions suggest this interval is associated with low summer air temperatures and increasing mean annual precipitation (Heusser et al., 1985). These environmental conditions, combined with the fjord results, suggest that the increased freshwater runoff, probably driven by a millennial-scale enhancement of the AL, likely stimulated an increase in nearshore primary productivity due to a more strongly stratified euphotic zone as envisioned by the stratification-productivity positive feedback model of Gargett (1997). This same time interval is also associated with a regional increase in anoxic or sub-oxic conditions in all four fjords. The enhancement of both paleoproductivity and reduced dissolved oxygen concentrations imply that increased export of organic matter to the benthos stimulated enhanced microbial consumption of oxygen, as suggested by the observed increases in excess U and Mo accumulation from these fjords (Figs. 4.13 - 4.15). This anoxia may also suggest a reduction in ventilation of fjord bottom waters, and that across-sill transport of oxic water masses is slowed during this time period, though this seems unlikely since an enhanced AL would favor increased bottom-water renewal at the deeper silled sites due to increased upwelling of deep waters in the Alaska Gyre. Though the anoxia data may be inconclusive, the synchronous increases in both primary productivity and precipitation are most readily explained by the modern stratification-productivity feedback paradigm as it is understood for the modern Gulf of Alaska.

The early Holocene period between 8000 – 6500 cal yrs BP is also an interval of enhanced productivity in all four fjords. Unlike the mid-Holocene productivity maxima, however, this early Holocene productivity increase occured during a period of reduced terrestrial runoff (Fig. 4.17), seen both in regional pollen reconstructions (Heusser et al., 1985) and the independent composite record of fjord terrigenous sedimentation. This early Holocene period also sees enhanced bottom-water oxygen concentrations. Collectively, these relationships are more difficult to reconcile with known observations of AL – Gulf of Alaska dynamics. A decrease in freshwater runoff is consistent with a

weaker and/or more westerly AL pressure cell (Rodionov et al., 2005; Weingartner et al., 2005). The enhanced regional productivity associated with this period is in direct contrast with modern observations of atmosphere-ocean-ecosystem linkages between the AL and the Gulf of Alaska. Modern weak/westerly AL cells favor reduced productivity due to reduced Alaska Gyre upwelling of deep water and reduced euphotic zone stratification (Francis et al., 1998). A possible explanation for this dichotomy of high productivity during a weak AL regime is that enhanced preservation in anoxic bottom-waters maintained high concentrations of OM, and that the paleoproductivity proxies actually reflect this preservation signal instead of true enhanced productivity. This possibility seems remote, however, because an increase in bottom-water oxygenation would likely favor enhanced OM degradation through microbially-mediated oxidative respiration pathways within both the water column and the shallower portions of the sediment (Froelich et al., 1979; Hedges et al, 1999). Furthermore, the preservation of biogenic silica is driven by dissolved silica concentrations, not oxygen concentration (Ragueneau et al., 2000). Therefore, the lack of appreciable bottom-water anoxia implies (i) that seasonal export productivity was not high enough to drive benthic microbial respiration to consume all available dissolved oxygen, or (ii) the rate of ventilation of the deep fjord bottom-waters occurred regularly to minimize anoxia.

An alternative explanation for this early Holocene pattern of enhanced productivity and reduced freshwater discharge could indicate an increased influence of "intermediate zone" water flux into the fjords of nearshore southeast Alaska (Fig. 4.3). Because the intermediate zone water is derived ultimately from the nutrient-rich Alaska Gyre upwelling center, enhanced across-sill advection would lead to an increase in nutrient delivery to the constricted fjord marine environment. While the reduction in freshwater discharge would reduce stratification of the euphotic zone and potentially lead to deleterious growth conditions for diatoms and other phytoplankton, the increased influx of nutrients may offset this effect. Taken together, the increase in intermediate zone water transport and the increase in productivity would then be sufficient to (i) decrease across-sill transport of bottom-waters and reduce ventilation events and (ii)

drive the available bottom-waters to at sub-oxic levels due to the enhanced OM flux. Unlike the previous explanation, this mechanism would be consistent with a stronger AL, in that it favors both higher productivity and increased Alaska Gyre upwelling; however, the decline in precipitation remains inconsistent with known patterns of AL dynamics.

Modern observations of physical dynamics and productivity dichotomies in the Subarctic Northeast Pacific Ocean have only recently been observed. The "Victoria Pattern" (Bond et al., 2003; Peterson and Schwing, 2003) reflects such a change in behavior of the linked atmosphere-ocean system in the North Pacific. Unlike the traditional binary dipole relationship between SLP, SST, and marine productivity observed between the subarctic and temperate sectors of the Northeast Pacific Ocean described by the Pacific Decadal Oscillation (Trenberth and Hurrell, 1994; Mantua et al., 1997), the Victoria Pattern indicates a period of decoupling in these environmental parameters between AD 1999-2002. This data indicates the Victoria Pattern can occur over millennial timescales, and has done so for long periods of time during the Holocene. The hemispheric comparison of EW0408-33JC and other sensitive, high-resolution paleoclimate datasets from the Pacific margin (Addison and Finney, *in prep.*) further support this observation of mid-Holocene decoupling between the linked atmosphere-ocean structure and the marine ecosystem. In the fjord synthetic record presented here, as well as the larger Pacific margin reconstruction paleoclimate dataset, the period associated with the onset of the Northern Hemisphere Neoglaciation (between 4,000 – 5,000 cal yrs BP) is highlighted as a key transition in the fundamental behavior of Holocene climate dynamics. The consistency between the fjord records further support this analysis, and further the assertion that instrumental observations of North Pacific climate from the last century are inadequate to encompass the full range of climatic variability within this region.

4.5.4   High-resolution time-series analysis of fjord paleoenvironmental data

The combination of high accumulation rates and high spatial sampling intensity provides a rare opportunity to examine the Holocene paleoproductivity record preserved in cores EW0408-22JC, -33JC, and -44JC at decadal timescales, with mean sampling

resolutions of 44, 21, and 30 yrs per sample, respectively. Application of the REDFIT time-series analytical program (Schulz and Mudelsee, 2002) yields dominant periods in both the decadal and centennial ranges at the 95% and 99% significance levels (Fig. 4.18).

All three cores exhibit several significant spectral amplitude peaks within the 40-100 yr/cycle range. This period corresponds with the PDO/AL variability identified from modern instrument data in the Gulf of Alaska (Trenberth and Hurrell, 1994; Mantua et al., 1997; Minobe and Mantua, 1999), as well as shifts in marine ecosystem productivity levels in the North Pacific Ocean (Mantua and Hare, 2002). The use of multiple fjord records of paleoproductivity give us confidence in these results being indicative of regional decadal-scale variability present in the marine ecosystem of southeast Alaska. While it is difficult to evaluate the effects of these prehistoric high-frequency shifts in primary productivity on primary and tertiary consumers that provide limited biogeochemical evidence in marine sedimentary records, bottom-up ecological forcing principles suggest these alternating periods of relatively high and low primary productivity would have maintained similar shifts throughout multiple trophic levels within the marine ecosystem (Finney et al., 2000; Finney et al., 2002), as well as coastal terrestrial ecosystems that incorporate marine-derived nutrients from spawning salmonids (Heaton and Grady, 2003; Misarti et al., 2009). Indeed, high-frequency fluctuations have been observed in the late Holocene paleoabundance record of Pacific sockeye salmon at Karluk Lake on Kodiak Island (Finney et al., 2002), which exhibit similar behavior as that of the EW0408-33JC opal MAR dataset. These independent corroborating records thus indicate consistent forcing of the Subarctic Northeast Pacific marine ecosystem by AL dynamics throughout the Holocene.

Though the productivity records along the Gulf of Alaska margin appear to exhibit similar behavior throughout the Holocene, other biogeochemical proxies do not appear to be as easily interpretable. Further examination of the high-resolution record of terrestrial erosion and inferred freshwater discharge preserved within the Ti MAR data of EW0408-33JC indicates that a period of 47 yrs/cycle exceeds the 95% Monte Carlo

significance level (plot not shown). The same REDFIT approach used for the opal MAR dataset in EW0408-33JC yields roughly equivalent periodicity (Fig. 4.18b), yet the relatively poor correlation between the two datasets ($n = 362$, $r = -0.310$, $p < 0.01$) suggests processes beyond the simple stratification-productivity model are also at work. Following the earlier argument that accumulation of Ti within the sediment of Katlian Bay is attributed purely to erosion of subaerial lithic material driven by precipitation, then it may be necessary to partition the precipitation between rainwater and snow accumulation within the adjacent alpine areas to reconcile this apparent disconnect. Such an analysis is beyond the scope of this work. Nevertheless, the longer residence time of precipitation stored within the alpine snowpack relative to the geologically instantaneous delivery of rainwater to the fjord environment may provide a likely explanation to this anomalous behavior.

4.6 Conclusions

Using a comprehensive set of biogeochemical proxies from four fjords along the southeast Alaskan margin, a detailed record of productivity, freshwater discharge, and circulation since the LGM/Holocene deglaciation was presented at multiple time resolutions. This data indicates the nearshore LGM/Holocene transition occurred in several phases along this margin, and that a straightforward climatic interpretation is complicated by changes in relative sea level caused by proximity to the Cordilleran Ice Sheet. Despite these complexities, periods of major environmental change appear to correlate with both regional offshore sediment records, as well as hemispheric climate records. During the Holocene, there are several trends consistent amongst the fjord records, with two intervals standing out. The period from 4800 – 2700 cal yrs BP is consistent with a millennial-scale intensification of the AL-Alaska Gyre linkage, while the period 8000 – 6500 cal yrs BP appears to be similar to the recently identified Victoria Pattern, in that intense marine productivity is favored during a period of less intense AL dynamics. Finally, there is also clear evidence of high-frequency decadal-scale variability present within the ultrahigh-resolution siliceous productivity datasets of EW0408-22JC, -33JC, and -44JC, attributable to consistent decadal-scale influences of

the marine ecosystem by the AL pressure cell This decadal variability overprint of millennial-scale features suggests that the relatively short period of available regional instrument data is likely insufficient to encompass the full range of variability possible in the Subarctic Northeast Pacific Ocean, and its accompanying marine ecosystem. This study highlights the need for longer datasets of climate and ocean phenomena to better identify the full range of variability possible within a given region.

4.7   Acknowledgements

4.8   Figures

Figure 4.1 (*a*) Location map of EW0408 sites along Gulf of Alaska margin. Dashed insets indicate extents of (*b*) Baranof Island fjord sites and (*c*) the Gulf of Esquibel. The depths in (*c*) are derived from a digital bathymetry model of available NOAA digital sounding data; contours at 50 m intervals. Note the shallow channels that connect the Gulf of Esquibel to the open North Pacific Ocean.
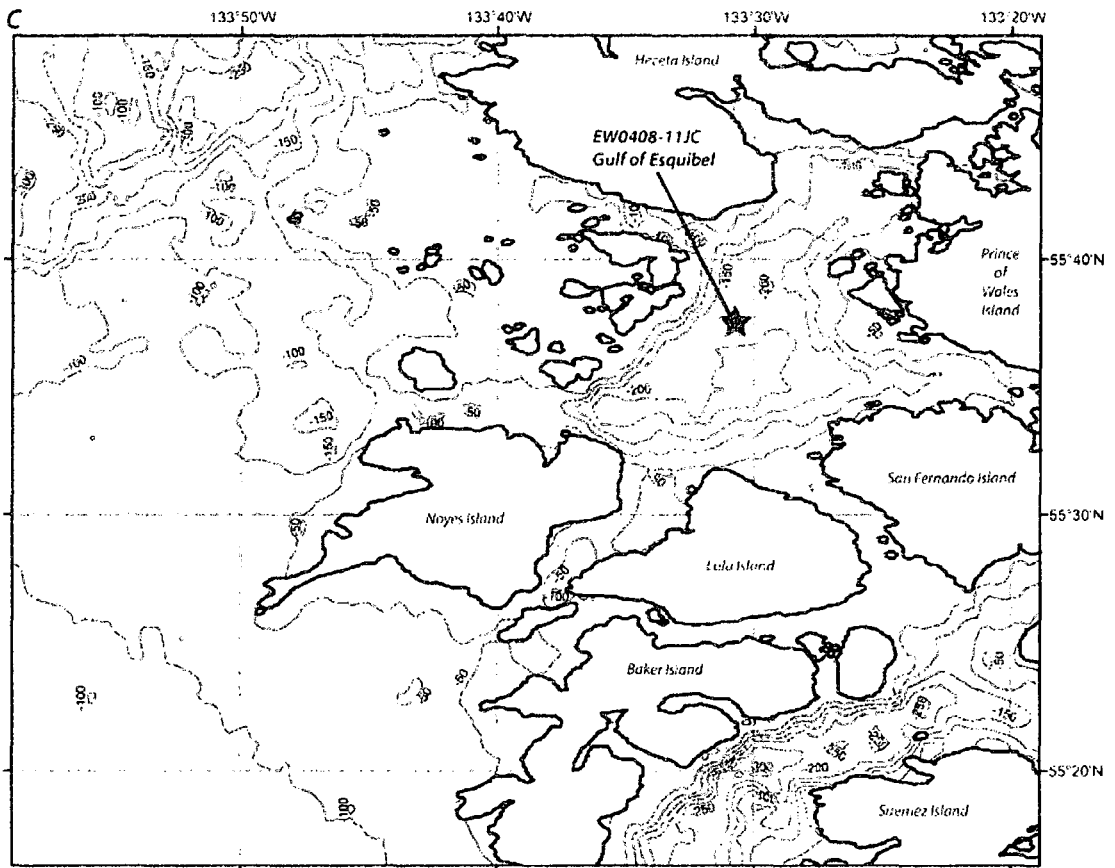
Figure 4.1 (continued)
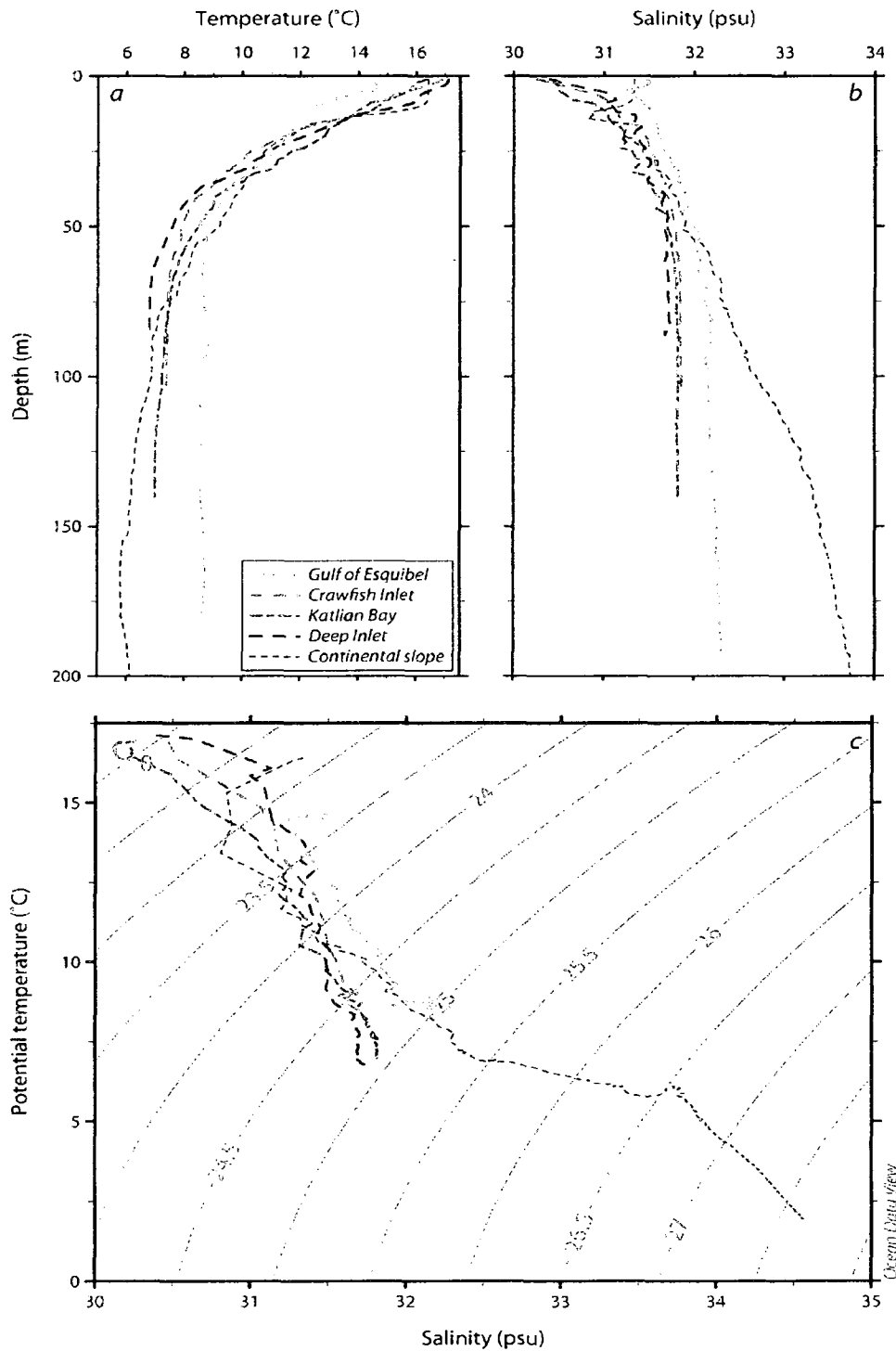
Figure 4.2 August 2004 (*a*) temperature and (*b*) salinity water column data from the coring sites presented in this study. (*c*) Potential temperature-salinity diagram. Contours are potential density (σ_0) isopycnals. Continental slope refers to a location west of Baranof Island at 56.792°N, 136.253°W with a maximum water depth of 1784 m.

fjord head | fjord mouth

river mouth

Surface mixed layer
low salinity
relatively shallow depths (5-20 m depth range)
derived from fluvial and/or run-off inputs
strongly stratified during summer & autumn

Intermediate zone
influx from Gulf of Alaska shelf
nutrient-rich
normal salinity
transport into fjord during winter
vertical mixing during winter brings nutrients to
surface layer

Bottom water
most dense water mass in fjord
may be seasonally or permanently anoxic
episodic renewal events (e.g. oxygenation) by
advection of denser water across sill
diffusive salt loss to overlying intermediate zone
decreases density and increases likelihood of
renewal event

Gulf of Alaska

sill

Figure 4.3 Idealized circulation in a temperate ice-free fjord from southeast Alaska. Arrows at right indicate dominant direction of water flux between fjord and the coastal Gulf of Alaska.

Figure 4.4 Southern Alaskan fjord EW0408 core lithologies.
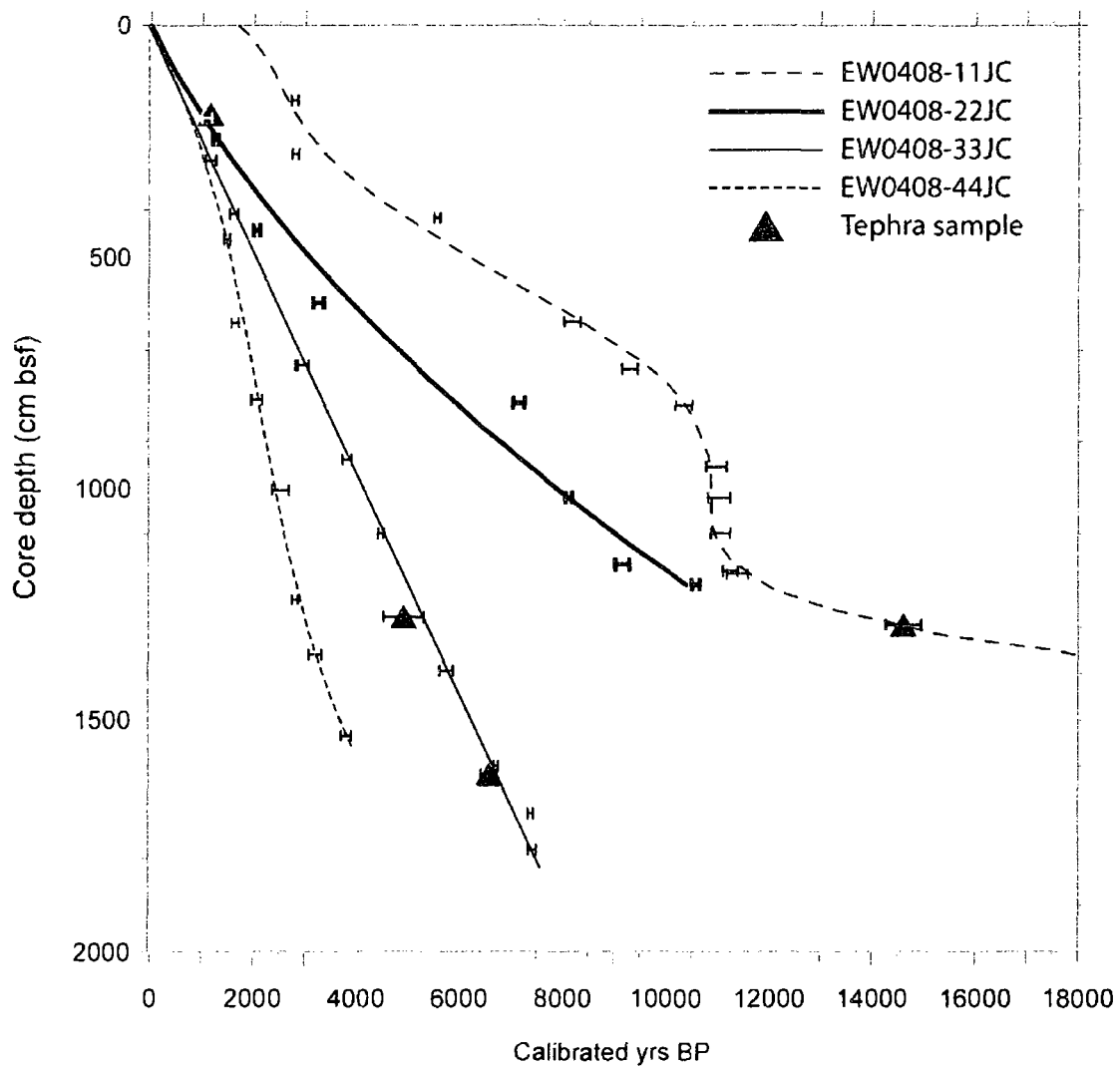
Figure 4.5 Composite age-depth models for EW0408 marine sediment cores. Error bars represent 2σ calibrated age range; bold error bars correspond to the EW0408-22JC model only.
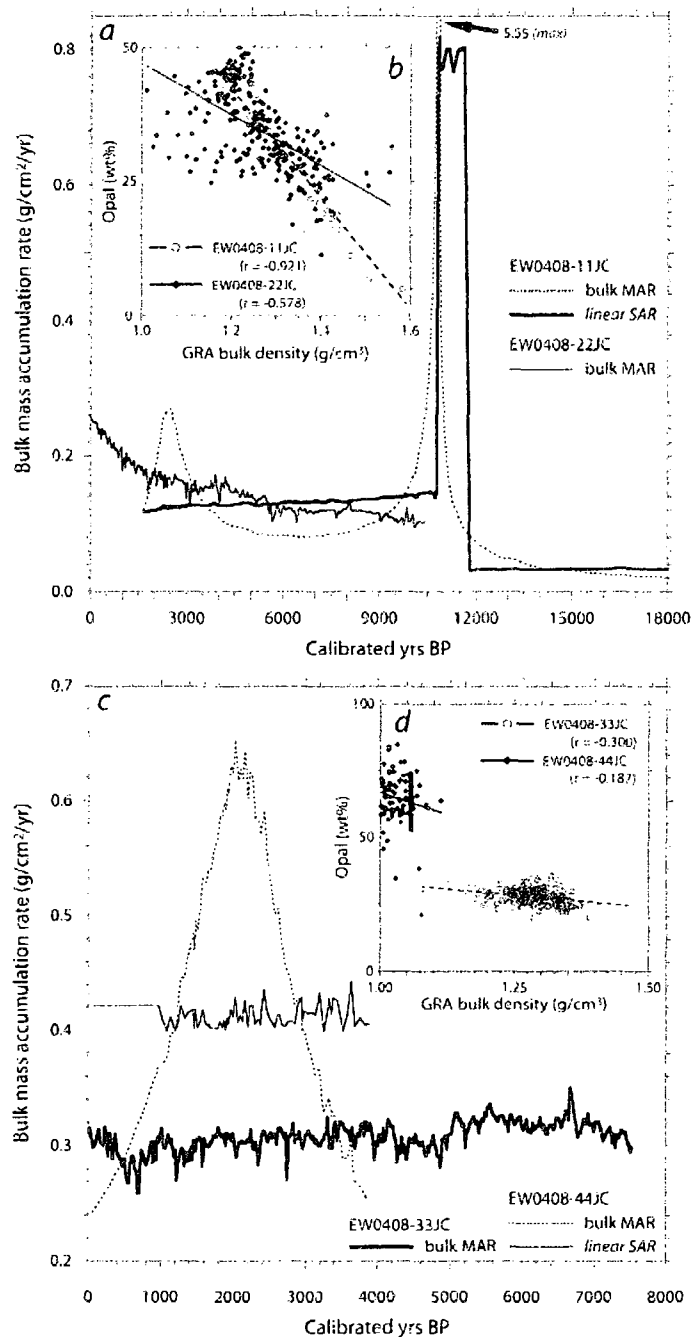
Figure 4.6 Bulk mass accumulation rates calculated based on composite AMS ^{14}C age-depth models for cores (a) EW0408-11JC and -22JC, and (c) EW0408-33JC and -44JC. The relationships between bulk density and opal concentration are also shown (b, d), all of which correlate at the 95% significance level except EW0408-44JC. Due to non-steady-state accumulation patterns, a linear sedimentation rate (SAR) approximation was imposed for cores EW0408-11JC and -44JC. This approach was not used for EW0408-22JC due to the strong correlation between opal and bulk MAR (b), suggesting that opal accumulation is intimately related with the sedimentation regime. The linear MAR for EW0408-44JC over the most recent 1000 yrs is due to the use of a constant mean density due to poor data quality from the MSCL instrument.
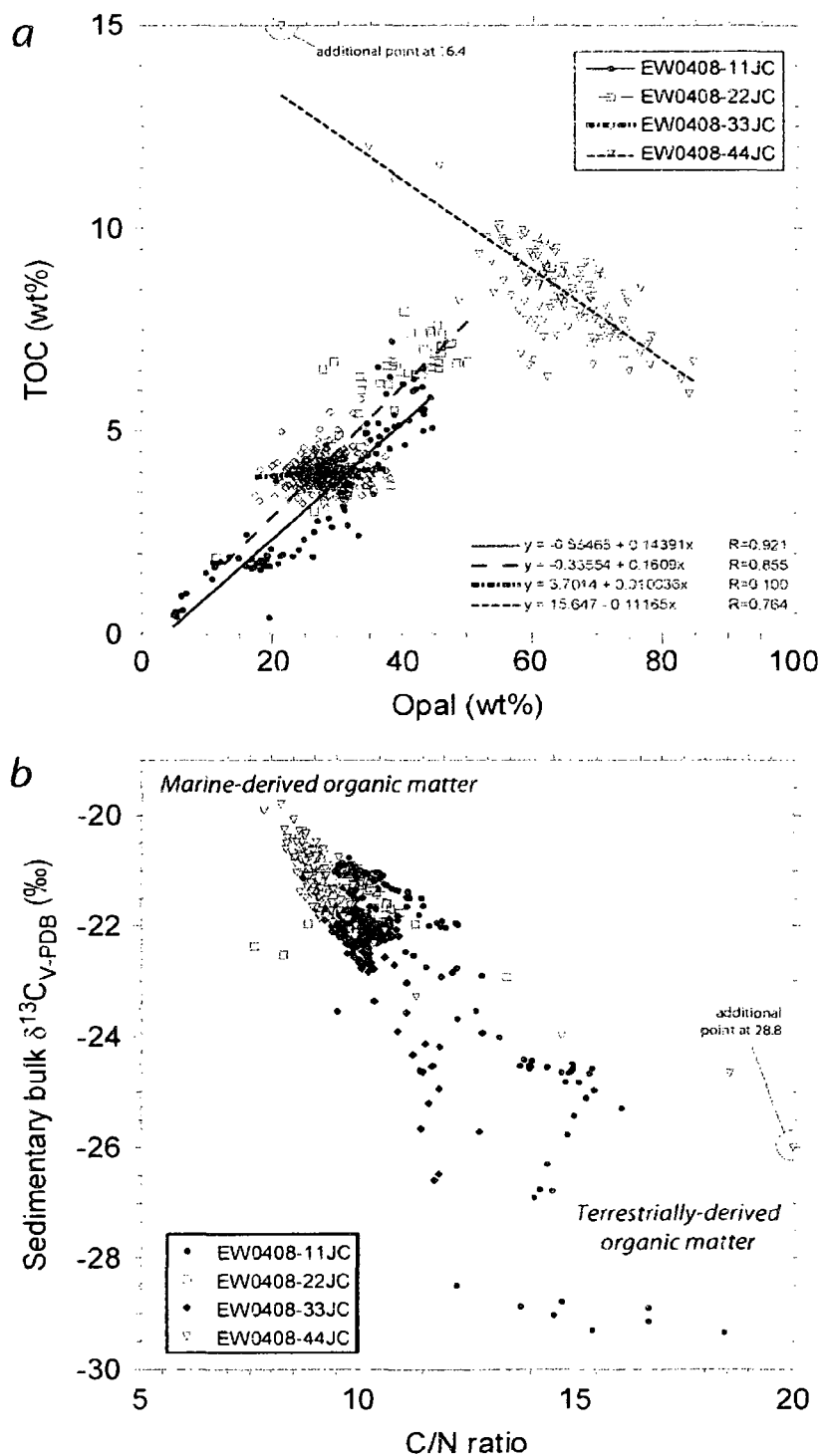
Figure 4.7 Sedimentary organic matter biogeochemical relationships. (*a*) Limited correspondence between carbonate-free TOC and opal values suggests TOC is not a robust indicator of export productivity. (*b*) OM provenance analysis (Meyers, 1994) shows southeast Alaskan fjords accumulate a mixture of both terrigenous and marine OM.
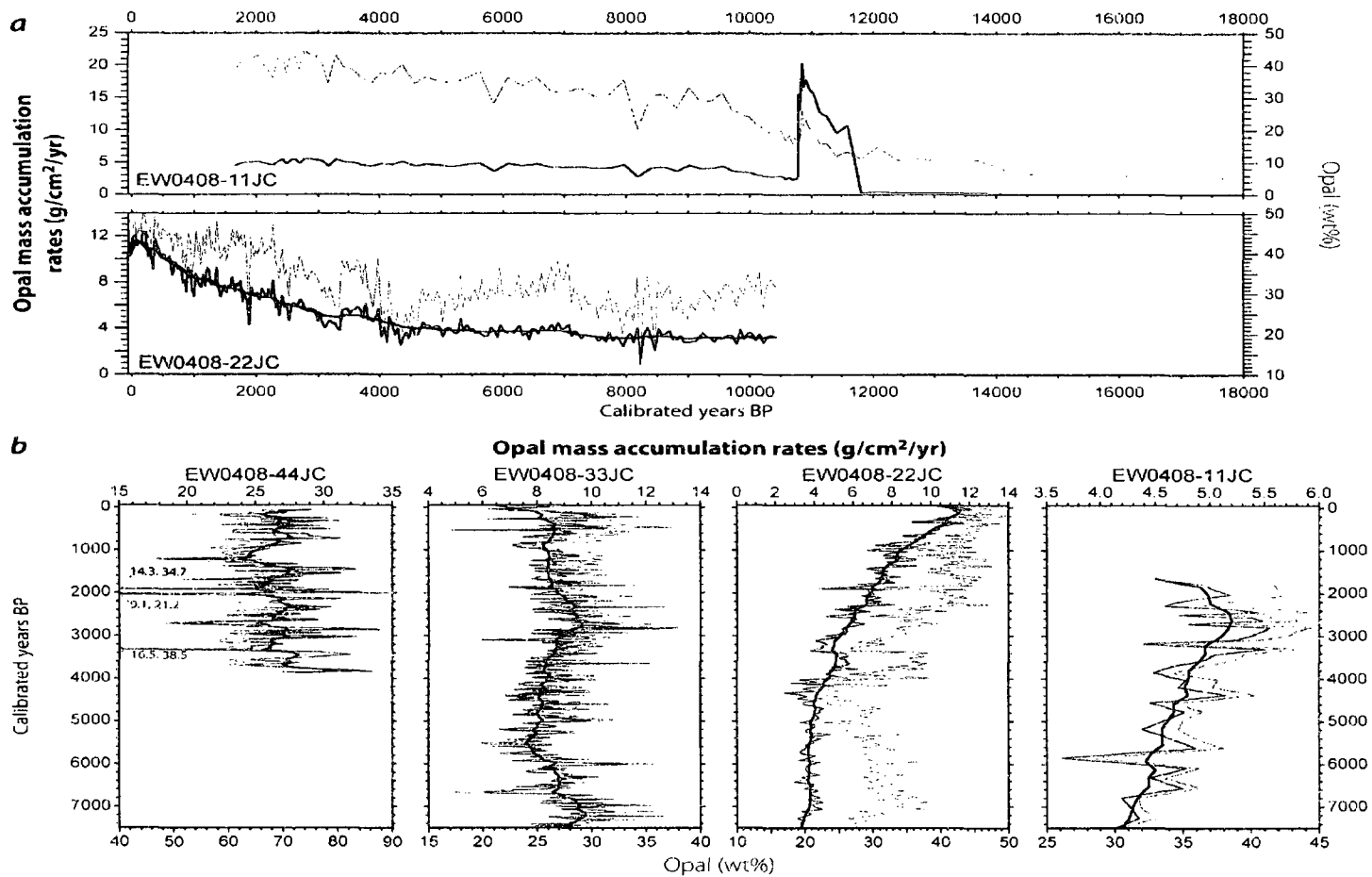
Figure 4.8 Opal productivity proxy data for nearshore southeast Alaska fjord sites. Opal mass accumulation rates (thick lines) and opal concentrations (thin lines) for (a) cores EW0408-11JC and EW0408-22JC for the last 18,000 years, and (b) all cores considered in this study for the last 7,500 years. Due to inflection points in the age-depth models for cores EW0408-11JC and EW0408-44JC, the accumulation rates for these cores have been calculated based on linear sedimentation rates. Thick bold lines are a 5-pt running mean of the opal mass accumulation rates. Shaded regions indicate sustained periods of increasing export productivity.
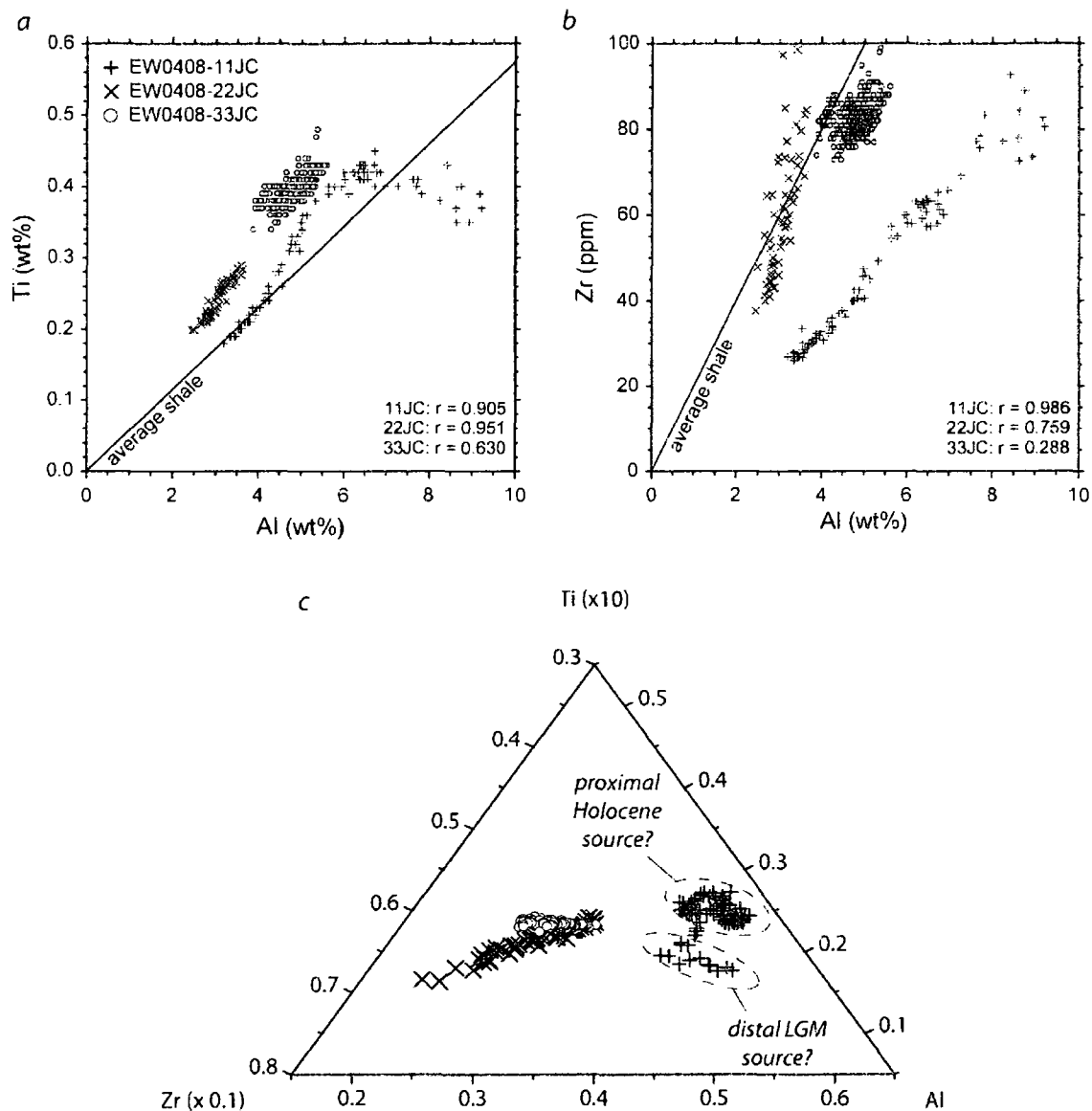
Figure 4.9 Refractory element bivariate diagrams (*a, b*) for cores EW0408-11JC, -22JC, and -33JC. All Pearson correlation r values are statistically significant at the 99% significance level, and were calculated on natural-log-transformed concentration data. Average shale values from Turekian and Wedepohl (1961). (*c*) Detrital provenance ternary diagram highlighting relationships between sedimentary sources for cores EW0408-11JC, -22JC, and -33JC. The overlap between cores -22JC and -33JC suggest similar sources, while the divergence in the -11JC geochemical data corresponding to Holocene and LGM intervals indicate different sedimentary sources.
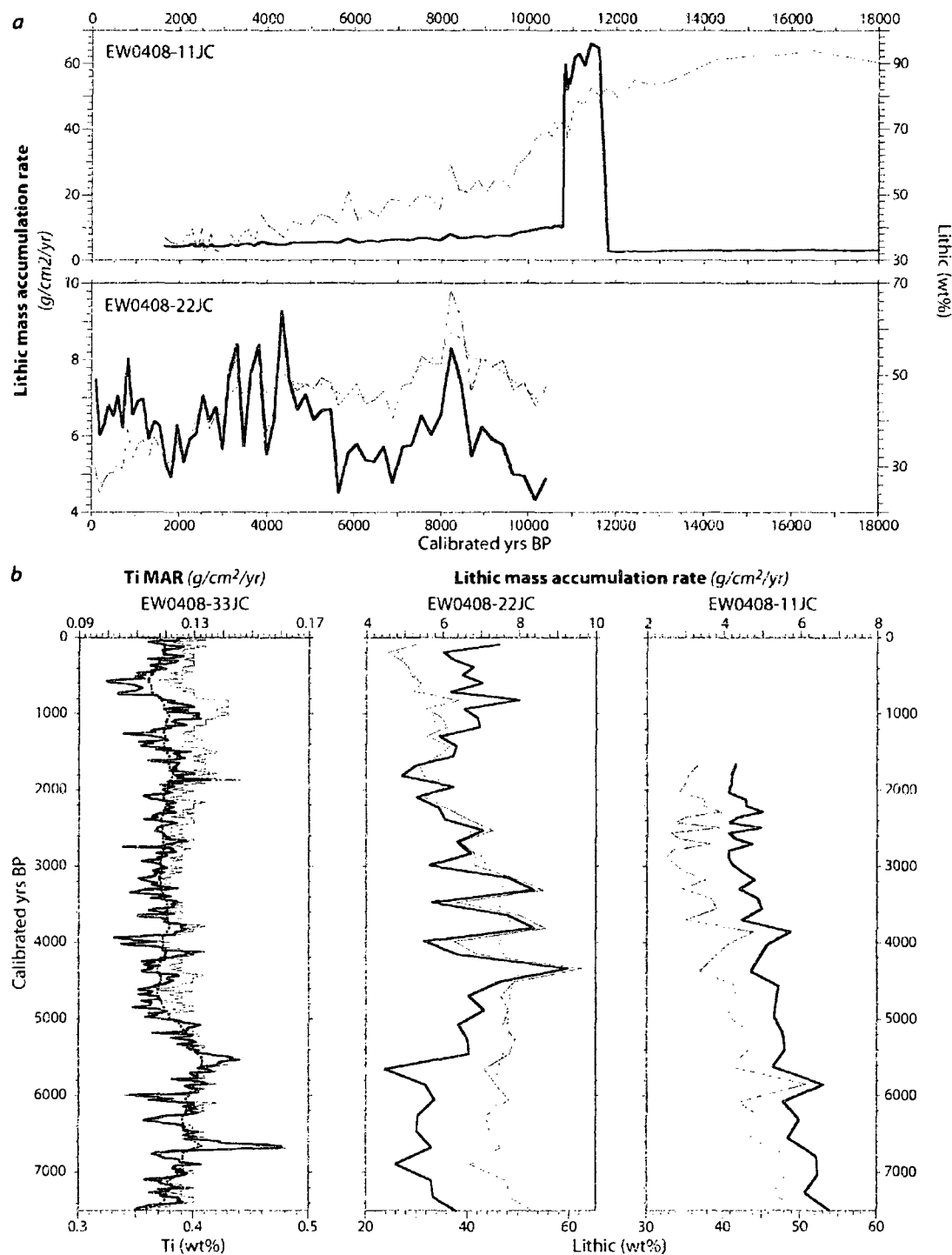
Figure 4.10 Lithic mass accumulation rates (thick lines) and lithic concentrations (thin lines) for (a) cores EW0408-11JC and -22JC for the last 18,000 years, and (b) cores EW0408-11JC, -22JC, and -33JC for the last 7,500 years. Gray shading indicates centennial-scale periods of increased terrigenous accumulation. Dashed lines are a 5-pt running mean where indicated. Because only one detrital source was indicated by Fig. 4.9 for core EW0408-33JC, titanium MARs were calculated in lieu of bulk lithic MARs.
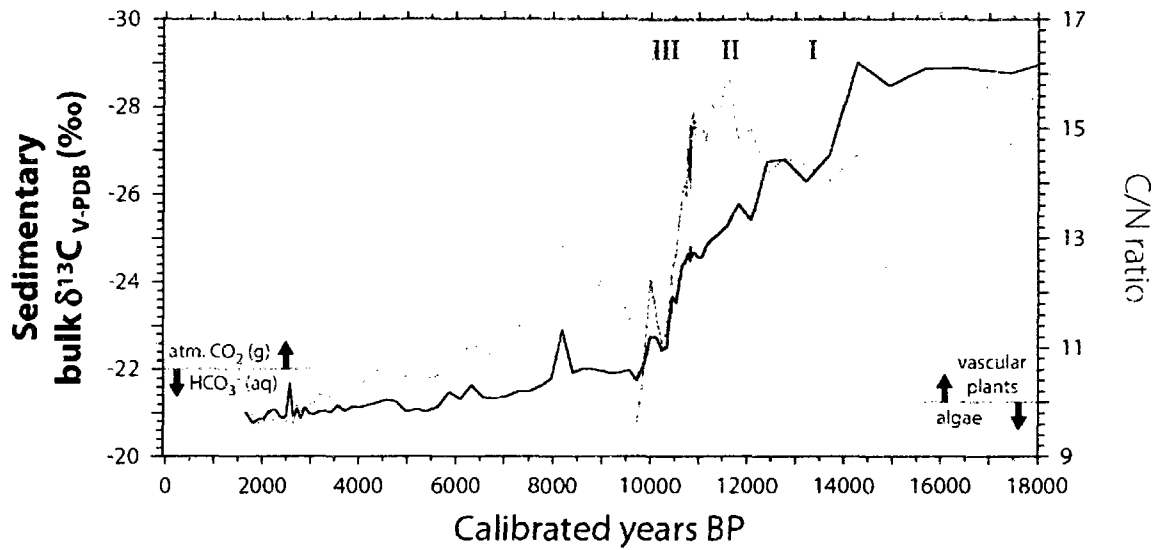
Figure 4.11 EW0408-11JC record of sedimentary $\delta^{13}C$ (thick line) and C/N ratio (thin line) of carbonate-free organic matter. Light gray shaded regions indicate periods of increased terrestrially-derived OM. Gray shaded boxes with Roman numerals indicate deglacial phases as described in the text. Suggested biogeochemical boundaries as suggested by Meyers (1994). Note $\delta^{13}C$ axis is reversed.
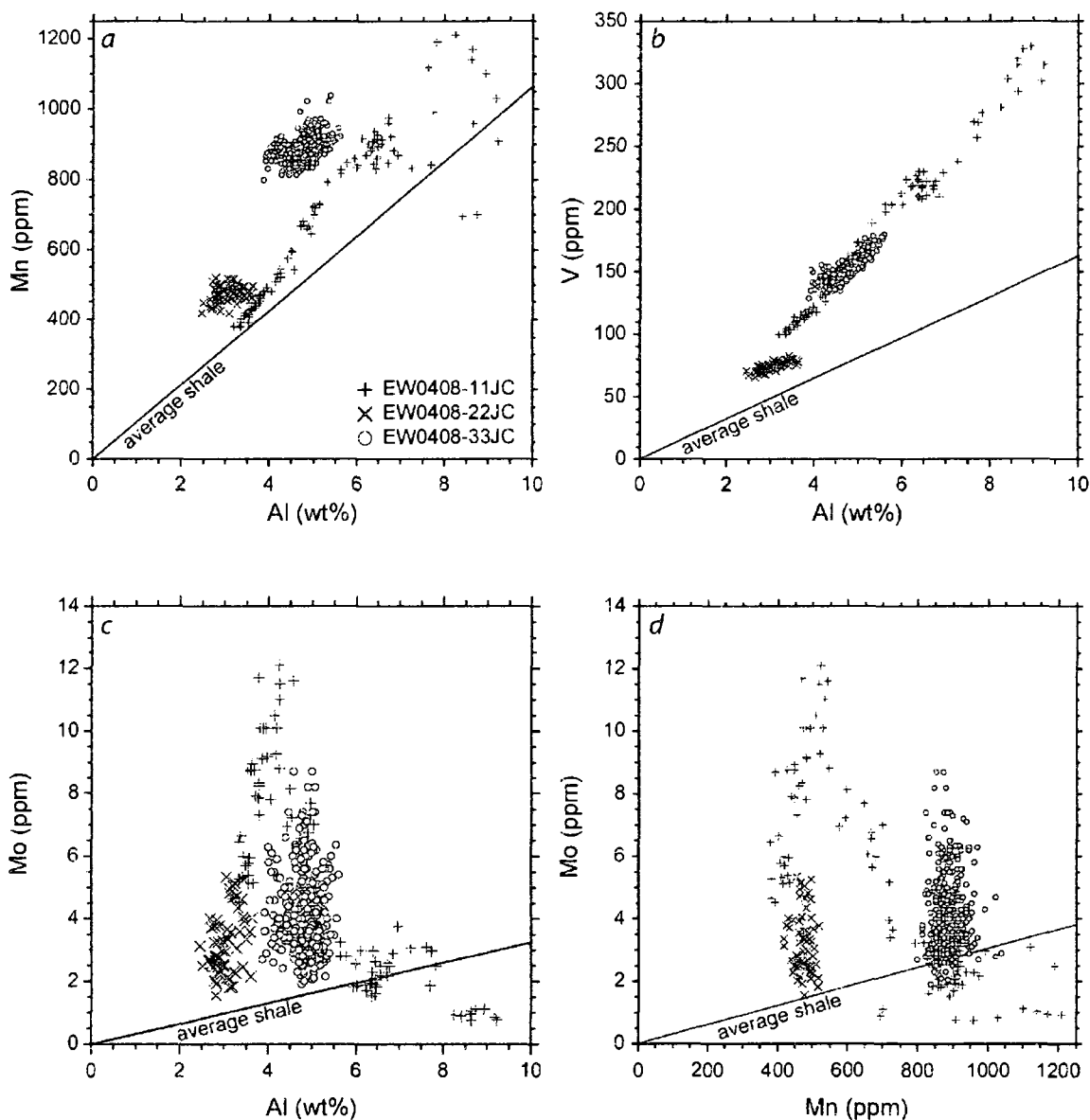
Figure 4.12 Redox-sensitive element concentrations for cores EW0408-11JC, -22JC, and -33JC. Enrichments above average shale values (Turekian and Wedepohl, 1961) suggest authigenic precipitation with enrichments in Mn indicating oxic conditions (a), V enrichments suggesting suboxic conditions (b), and Mo diagnostic of anoxic conditions (c). A comparison between the concentrations of Mn and Mo (d) indicate past changes between oxic (Mo depletion) and anoxic (Mo enrichment) regimes preserved within cores EW0408-11JC and -33JC.

EW0408-11JC
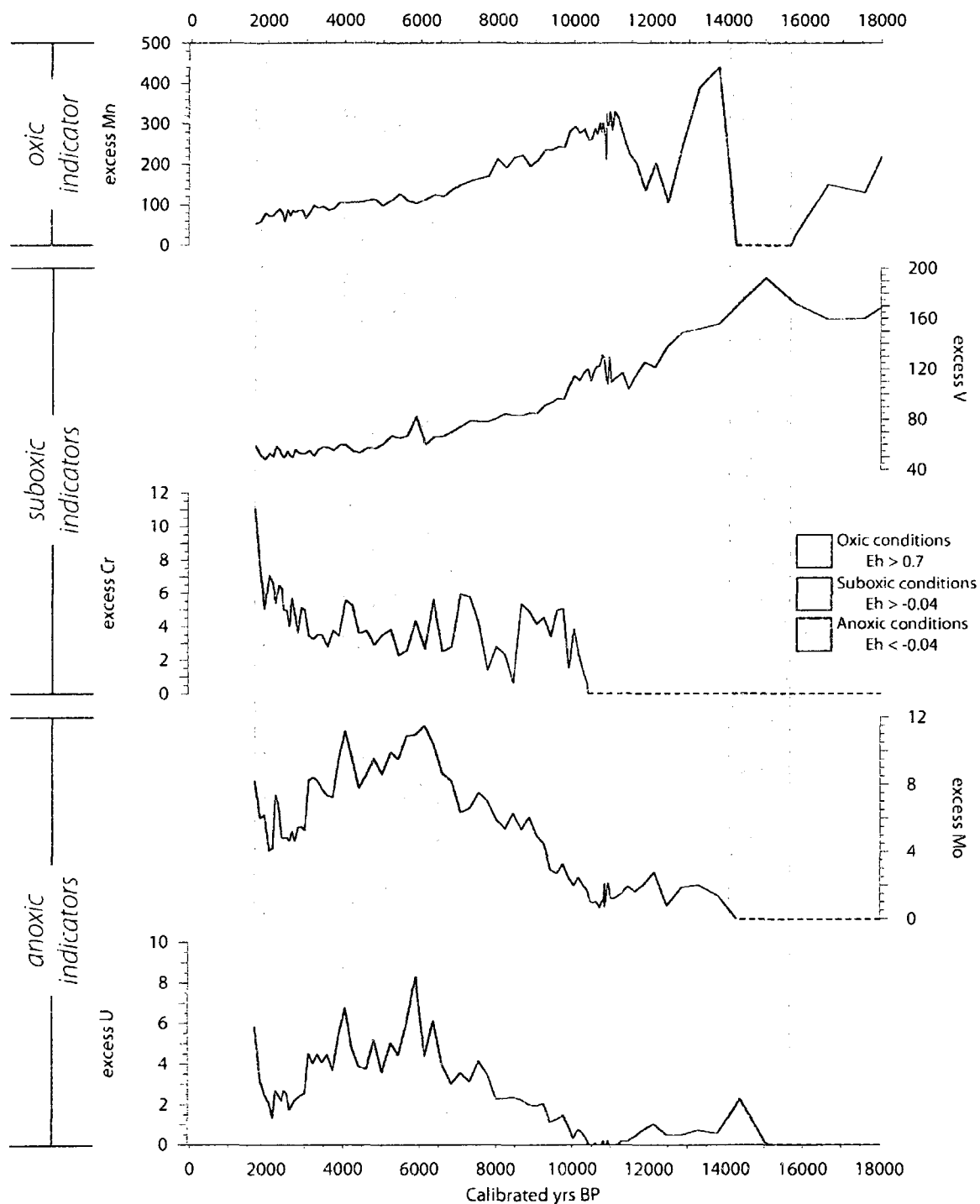
Figure 4.13 Paleoanoxia record from EW0408-11JC. The oxic, suboxic, and anoxic boundaries are defined by thermodynamic calculations (Piper, 2001). Dashed lines indicate calculated excess concentrations either below analytical detection limits, or negative values relative to a global mean sediment composition (McLennan, 1995).

EW0408-22JC
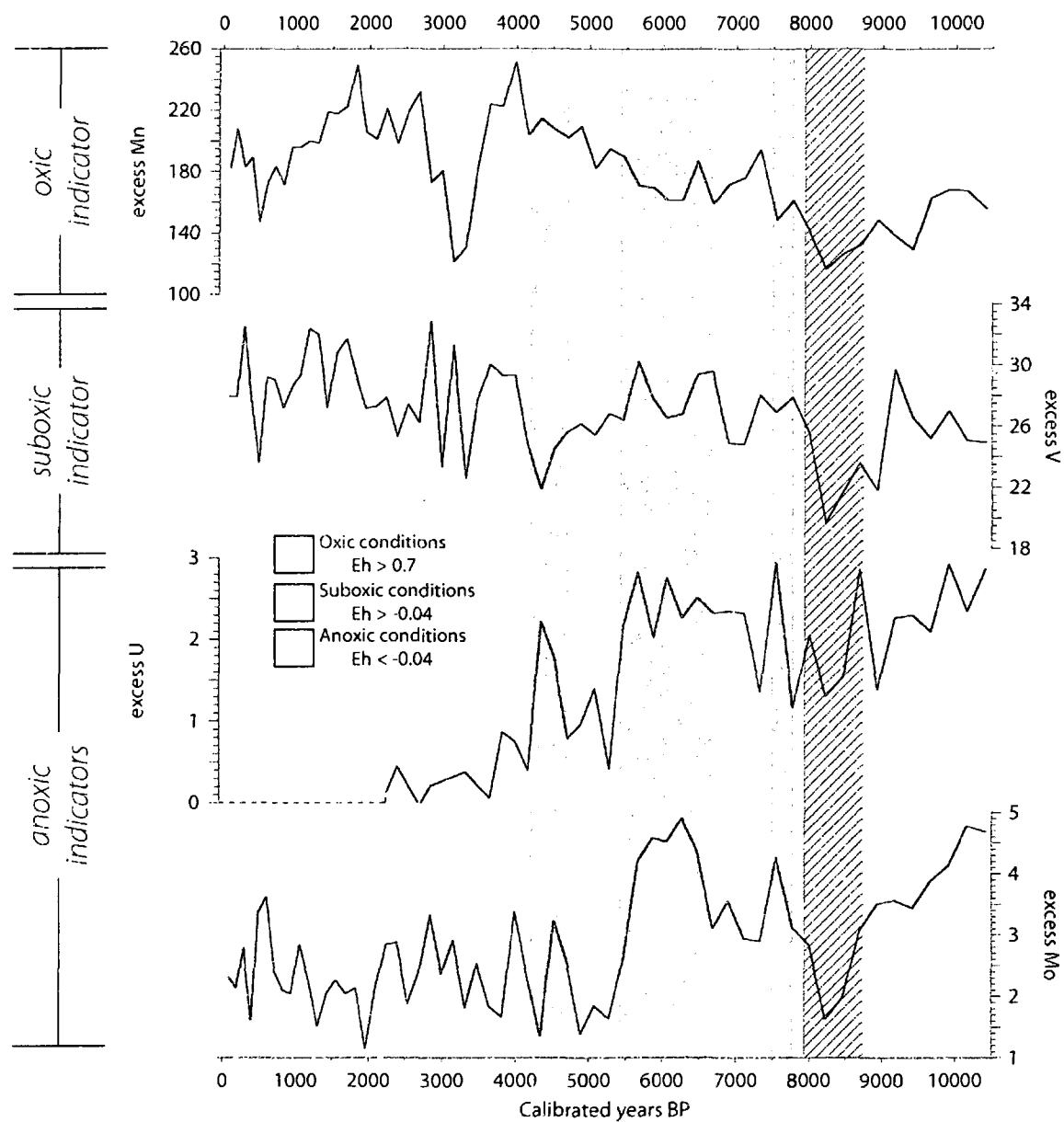
Figure 4.14 Paleoanoxia record from EW0408-22JC. The decoupling behavior observed between 8700-8000 cal yrs BP (indicated by the diagonal lines) is discussed in the text. Dashed lines same as in Fig. 4.13.

EW0408-33JC
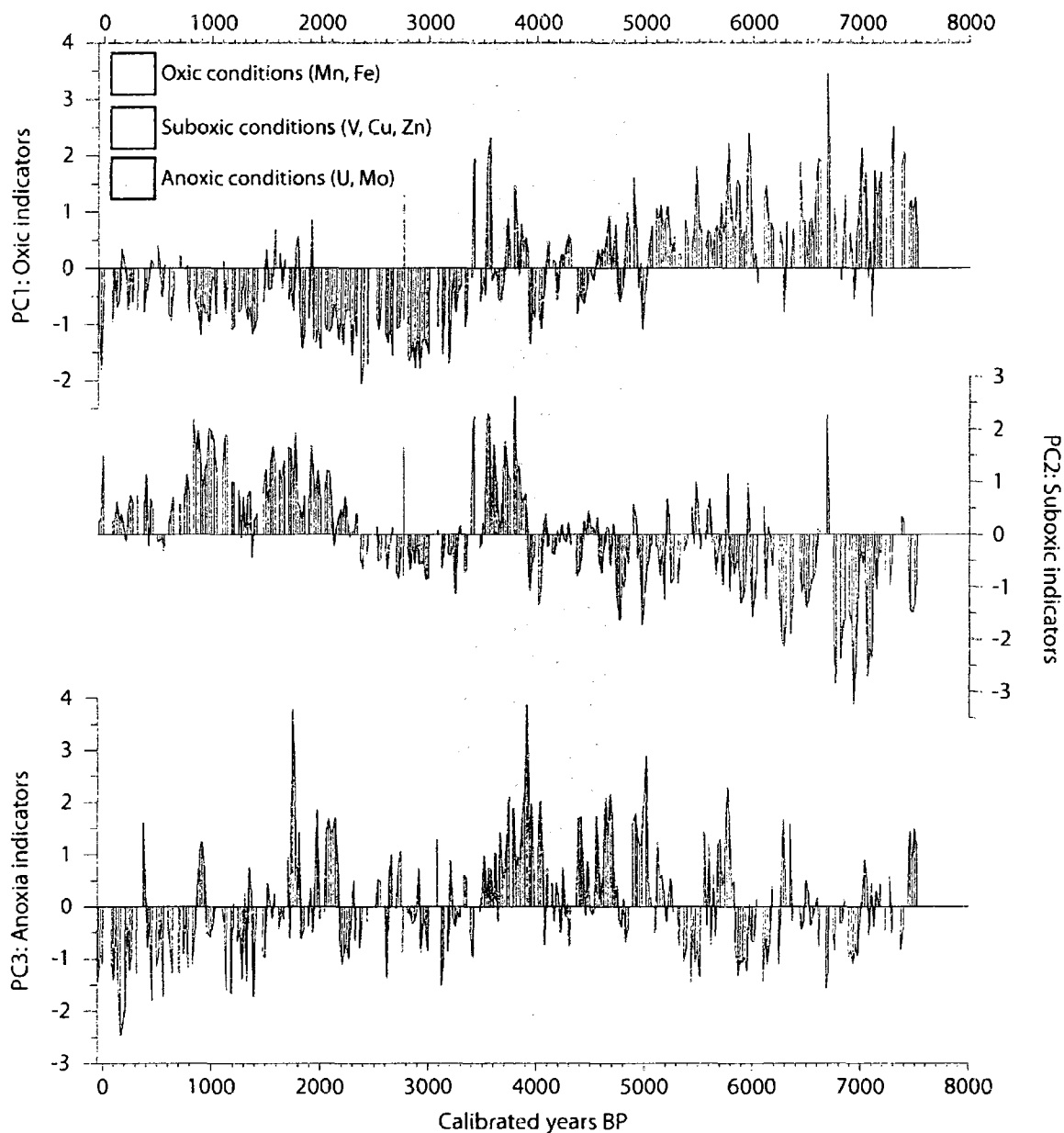
Figure 4.15 Paleoanoxia record from EW0408-33JC. Elements indicated in the legend are assigned to the different principal components based on their highest loading value. Shading transitions between 5300-4800 and 3500-2500 cal yrs BP indicates uncertainty in millenial-scale shifts in dominant dissolved oxygen regime. Excess Ni and Cr were included in the principal component analysis, but both had their highest loadings associated with PC1. This result is suspect given the Eh ranges associated with authigenic precipitation, suggesting an alternative process is responsible for the accumulation of these elements.
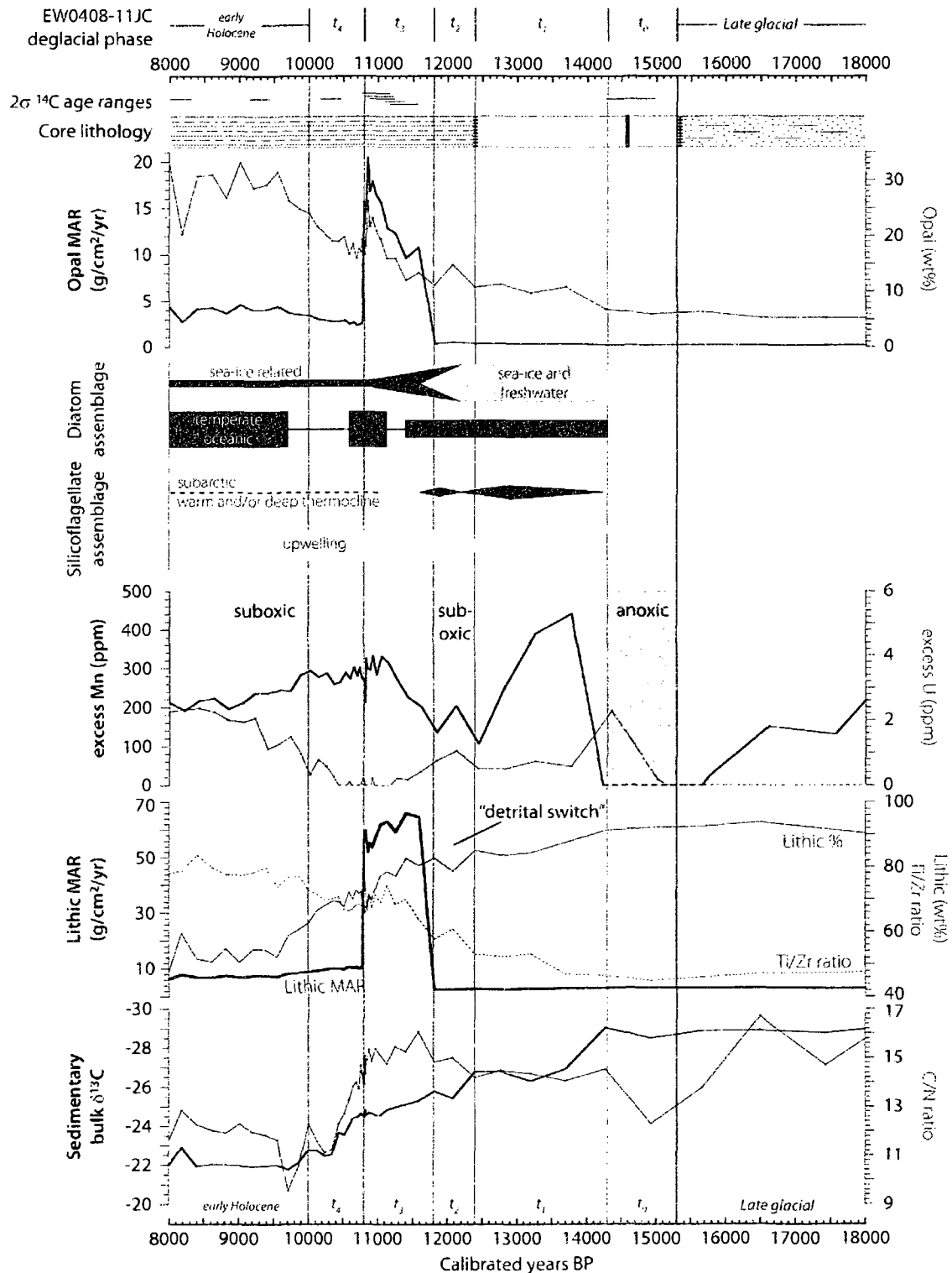
Figure 4.16 The Late glacial/Holocene transition recorded in EW0408-11JC. Diatom and silicoflagellate assemblage data from Barron et al. (2009). Core lithology same as Fig. 4.4; dashed lines in excess Mn and U datasets indicate values less than 0 ppm.
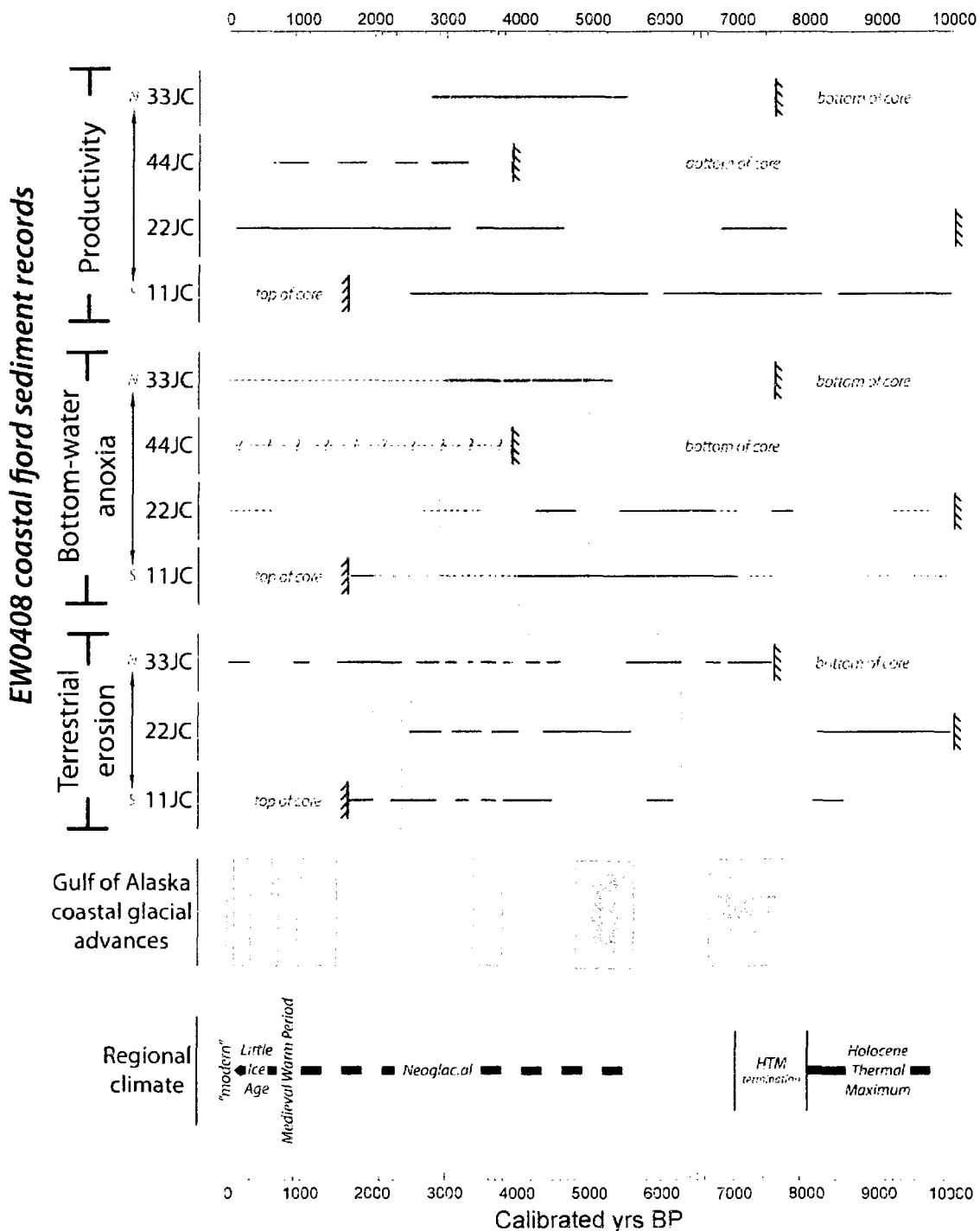
Figure 4.17 Regional Holocene sub-millenial reconstruction of the nearshore Gulf of Alaska marine environment. Thick lines indicate periods of enhanced (i) primary productivity, (ii) bottom-water anoxia, or (iii) terrestrial erosion. Thin dashed lines correspond to periods of suboxic water conditions. Some uncertainty exists for bottom-water anoxic conditions in EW0408-44JC as discussed in the text. Gray shading indicates periods when at least 2 cores indicate synchronous increases in the same proxy.
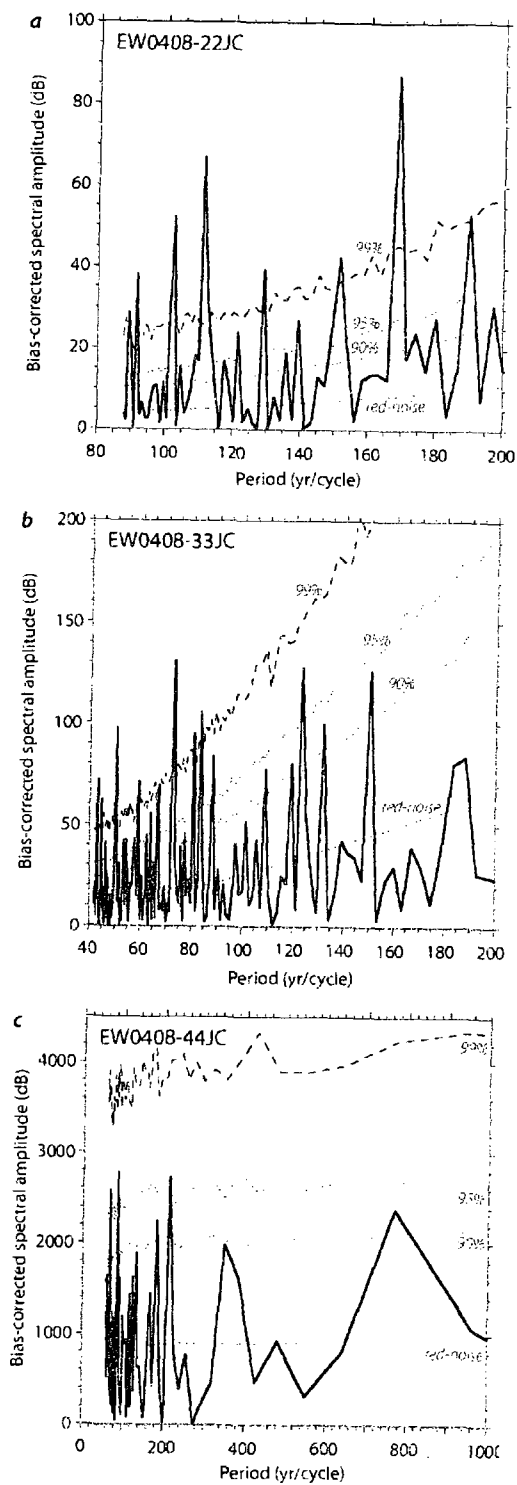
Figure 4.18 REDFIT Lomb-Scargle Fourier transform time-series analyses of high-resolution EW0408 opal mass accumulation rate data from cores (a) EW0408-22JC, (b) -33JC, and (c) -44JC. Significance of spectral amplitudes (thick lines) evaluated against the theoretical red-noise spectrum, and by using a Monte Carlo test at the 90, 95, and 99% significance levels (dashed lines).

Table 4.1 Modern physical fjord characteristics of core sites.

Location	Morphology	Maximum depth (m)	Depth of sill (m)	Depth of surface mixed layer (m)	Depth of thermocline (m)	Depth of halocline (m)	River present at head?
Gulf of Esquibel	Complex-basin fjord	340	20-70 (multiple channels)	5	48	37	n/a
Deep Inlet	Single basin fjord	91	24	8	35	25	Y
Katlian Bay	Single basin fjord	146	31	10	40	36	Y
West Crawfish Inlet	Single basin fjord	267	80	17	37	18	Y

Table 4.2 EW0408 core details.

Location	Core ID	Core type	Latitude (°N)	Longitude (°W)	Water depth of core (m)	Core length (mbsf)	Sampling resolution (cm)
Gulf of Esquibel	EW0408-10MC	Multicore	55.6266	133.512	184	0.41	5
	EW0408-11TC	Trigger core	55.6267	133.511	183	1.48	5
	EW0408-11JC	Jumbo piston core	55.6267	133.511	183	17.52	15
Deep Inlet	EW0408-43MC	Multicore	56.965	135.268	90	0.68	5
	EW0408-44JC	Jumbo piston core	56.965	135.268	90	18.14	5 or 10
Katlian Bay	EW0408-32MC	Multicore	57.162	135.357	141	0.40	5
	EW0408-33TC	Trigger core	57.162	135.357	144	0.71	5
	EW0408-33JC	Jumbo piston core	57.162	135.357	144	18.19	5
West Crawfish Inlet	EW0408-21GC	Gravity core	56.802	135.212	185	1.10	5
	EW0408-22JC	Jumbo piston core	56.802	135.211	188	11.84	5 or 20

Table 4.3 Geochronology results for EW0408 cores.

Core depth (mbsf)	Material	Reported ^{14}C age (yrs BP)	Corrected ^{14}C age (yrs BP)	2σ calibrated range (yrs BP)
EW0408-11JC				
1.62	terrestrial organics	2640 ± 35	2640 ± 35	2722 - 2844
2.78	wood fragment	2690 ± 40	2690 ± 40	2747 - 2861
4.15	terrestrial organics	4815 ± 25	4815 ± 25	5477 - 5601
5.13	wood fragment**	3565 ± 40	3565 ± 40	3722 - 3975
6.39	terrestrial organics	7350 ± 70	7350 ± 70	8016 - 8329
7.42	plant material	8306 ± 47	8306 ± 47	9138 - 9442
8.20	terrestrial organics	9110 ± 70	9110 ± 70	10176 - 10492
9.52	terrestrial organics	9615 ± 35	9615 ± 35	10780 - 11167
10.20	wood fragment	9707 ± 49	9707 ± 49	10009 - 11234
10.97	plant material	9733 ± 49	9733 ± 49	10878 - 11244
10.97	bivalve shell*	10399 ± 52	9733 ± 52	10874 - 11246
11.78	wood fragment	9812 ± 62	9812 ± 62	11109 - 11390
11.85	bivalve shell	10597 ± 54	9865 ± 54	11184 - 11590
12.98	Leech Lake tephra	12505 ± 40	12975 ± 40	14266 - 14952
EW0408-22JC				
0.00	sediment surface (multicore)			-54
0.14	f.a.d [137]Cs (multicore)			-14 - -4
0.40	f.a.d excess [210]Pb (multicore)			46 - 66
1.28	terrestrial organics**	1505 ± 20	1505 ± 20	1336 - 1480
1.93	White River Ash			1147
2.47	terrestrial organics	1335 ± 20	1335 ± 20	1185 - 1300
4.42	terrestrial organics	2070 ± 20	2070 ± 20	1989 - 2116
5.98	wood fragment	3045 ± 35	3045 ± 35	3161 - 3359
8.15	terrestrial organics	6220 ± 20	6220 ± 20	7020 - 7243
10.19	terrestrial organics	7305 ± 20	7305 ± 20	8037 - 8174
11.65	bivalve shell	8931 ± 48	8199 ± 48	9018 - 9294
12.08	terrestrial organics	9350 ± 25	9350 ± 25	10501 - 10656
EW0408-33JC				
0.00	sediment surface (multicore)			-54
0.24	f.a.d [137]Cs (multicore)			-14 - -4
0.55	f.a.d excess [210]Pb (multicore)			46 - 66
2.00	terrestrial organics	1155 ± 35	1155 ± 35	978 - 1172
4.08	wood fragment	1685 ± 35	1685 ± 35	1528 - 1692
7.33	wood fragment	2818 ± 35	2816 ± 35	2806 - 3061
7.33	bivalve shell*	3559 ± 38	2827 ± 38	2849 - 3064
9.38	wood fragment	3540 ± 20	3540 ± 20	3724 - 3892
10.99	terrestrial organics	3980 ± 20	3980 ± 20	4416 - 4517
12.78	MEVF tephra	4310 ± 140	4310 ± 140	4523 - 5307
13.94	wood fragment	4985 ± 30	4985 ± 30	5619 - 5878
16.00	terrestrial organics	5880 ± 20	5880 ± 20	6659 - 6743
16.18	MEVF tephra	5760 ± 70	5760 ± 70	6407 - 6726
17.03	wood fragment	6485 ± 20	6485 ± 20	7327 - 7434
17.82	wood fragment	6510 ± 30	6510 ± 30	7328 - 7483

AMS ^{14}C Laboratory	Sample ID	Notes
Keck - UCI	50805	
CAMS - LLNL	127764	
Keck - UCI	50806	
CAMS - LLNL	127765	
Keck - UCI	50807	
NSF - AAMS	WW6105	
Keck - UCI	50808	
Keck - UCI	50809	
NSF - AAMS	WW6106	
NSF - AAMS	WW6107	
NSF - AAMS	WW6108	
NSF - AAMS	WW5485	
NSF - AAMS	WW5468	
		Barron et al., 2009
		AD 2004
		AD 1964-1954
		AD 1884-1904
Keck - UCI	50810	
		Clague et al., 1995;
Keck - UCI	50811	Addison et al., *accepted*
Keck - UCI	50812	
CAMS - LLNL	127833	
Keck - UCI	50813	
Keck - UCI	50814	
NSF - AAMS	WW5471	
Keck - UCI	50815	
		AD 2004
		AD 1964-1954
		AD 1904-1884
Keck - UCI	50816	
CAMS - LLNL	127767	
NSF - AAMS	WW6110	
NSF - AAMS	WW6109	
Keck - UCI	50817	
Keck - UCI	50818	
		Riehle & Brew, 1984;
CAMS - LLNL	127768	Addison et al., *accepted*
Keck - UCI	50819	
		Riehle & Brew, 1984;
Keck - UCI	50820	Addison et al., *accepted*
CAMS - LLNL	127769	

Table 4.3 (continued).

Core depth (mbsf)	Material	Reported ^{14}C age (yrs BP)	Corrected ^{14}C age (yrs BP)	2σ calibrated range (yrs BP)	AMS ^{14}C Laboratory	Sample ID	Notes
EW0408-44JC [†]							
0.00	sediment surface (multicore)			-54			AD 2004
0.86	f.a.d. excess ^{210}Pb (multicore)			46 - 66			AD 1904-1884
1.21	terrestrial organics[**]	1585 ± 20	1585 ± 20	1413 - 1525	Keck - UCI	50821	
2.92	wood fragment	1225 ± 30	1225 ± 30	1065 - 1260	CAMS - LLNL	127770	
4.62	terrestrial organics	1600 ± 20	1600 ± 20	1416 - 1534	Keck - UCI	50822	
6.42	terrestrial organics	1735 ± 30	1735 ± 30	1562 - 1712	Keck - UCI	50823	
8.08	wood fragment	2090 ± 35	2090 ± 35	1951 - 2150	CAMS - LLNL	12/831	
10.03	terrestrial organics	2415 ± 20	2415 ± 20	2353 - 2673	Keck - UCI	50824	
12.40	wood fragment	2700 ± 40	2700 ± 40	2749 - 2868	CAMS - LLNL	127832	
13.59	terrestrial organics	2995 ± 20	2995 ± 20	3079 - 3317	Keck - UCI	50825	
15.35	wood fragment	3530 ± 30	3530 ± 30	3708 - 3891	CAMS - LLNL	127771	

[*] sample not included in age model calculations due to use as marine carbonate correction
[**] sample rejected from age model; see text for details
[†] corrected core depths, see text for details

CAMS - LLNL = Center for Accelerator Mass Spectrometry, Lawrence Livermore National Lab
Keck - UCI = Keck Carbon Cycle AMS facility, University of California - Irvine
NSF AAMSF = National Science Foundation - Arizona AMS facility, Tucson

f.a.d. = first appearance datum
MEVF = Mt. Edgecumbe Volcanic Field

Table 4.4 Principal component analysis of redox-sensitive elements in EW0408-33JC. Analysis included components with eigenvalues ≥1, and loadings were rotated using the Varimax method with a Kaiser normalization. Bold values indicate loadings that exceed 0.4 units.

	Component 1 oxic	Component 2 suboxic	Component 3 anoxic
excess Mn	**0.879**	-0.241	0.103
excess Fe	**0.622**	**0.470**	0.064
excess Cr	**0.686**	0.230	-0.271
excess U	0.012	0.042	**0.738**
excess V	-0.099	**0.917**	-0.036
excess Mo	0.053	0.096	**0.780**
excess Cu	**0.508**	**0.697**	0.082
excess Zn	0.077	**0.482**	0.321
excess Ni	**0.823**	0.100	0.187

Table 4.5 Late glacial/Holocene deglacial transition phases in EW0408-11JC and inferred paleoenvironmental conditions.

EW0408-11JC deglacial phase	Onset (cal yrs BP)	Termination (cal yrs BP)	Inferred Gulf of Esquibel paleoenvironment	Approximate NGRIP chronozone boundary[†] (date of boundary in parentheses)
LGM	?	15,300	CIS glacimarine depocenter	LGM
t_0	15,300	14,300	Rapid retreat of CIS ice margin	LGM/Bølling-Alleröd transition (14,700)
t_1	14,300	12,400	River-dominated estuary with shallow channels	Bølling-Alleröd/Younger Dryas transition (12,900)
t_2	12,400	11,700	Onset of fjord-style reverse estuary circulation with deepening channels	Younger Dryas/Preboreal transition (11,700)
t_3	11,700	10,800	Intensification of fjord-style circulation due to rapid deepening of channels: collapse of regional forebulge?	Preboreal termination (11,300); onset of Holocene Thermal Maximum (11,300±1.500)*
t_4	10,800	10,000	Continued deepening of channels; evidence of warming SST	-
early Holocene	10,000	-	Modern fjord-style circulation; only minor isostatic adjustments	-

† dates from GICC05 timescale (Rasmussen et al., 2006; Steffensen et al., 2008)
* Central-eastern Beringian synthesis from Kaufman et al., 2004
CIS: Cordilleran Ice Sheet

4.10 References

Addison, J.A., Beget, J.E., Ager, T.A. and Finney, B.P., *accepted*. Marine tephrochronology of the Mt. Edgecumbe Volcanic Field, Southeast Alaska, USA. Quaternary Research.

Addison, J.A. and Finney, B.P., *in prep.*, Holocene evolution of the Pacific Decadal Oscillation in the Gulf of Alaska. Science.

Addison, J.A., Finney, B.P., Dean, W.E. and Davies, M.H., *in prep.*, Decoupling of the coastal marine ecosystem and glaciomarine Cordilleran Ice Sheet dynamics in the Gulf of Alaska during the Last Glacial Maximum/Holocene transition. Paleoceanography.

Aitchison, J., 1986. The statistical analysis of compositional data. Chapman and Hall, London, 416 pp.

Aitchison, J., 1999. Logratios and natural laws in compositional data analysis. Mathematical Geology 31(5): 563-580.

Anderson, L., Abbott, M.B., Finney, B.P. and Burns, S.J., 2005. Regional atmospheric circulation change in the North Pacific during the Holocene inferred from lacustrine carbonate oxygen isotopes, Yukon Territory, Canada. Quaternary Research 64(1): 21-35.

Anderson, R.F. and Winckler, G., 2005. Problems with paleoproductivity proxies. Paleoceanography 20, PA3012: doi:10.1029/2004PA001107.

Barclay, D.J., Calkin, P.E. and Wiles, G.C., 2001. Holocene history of Hubbard Glacier in Yakutat Bay and Russell Fiord, southern Alaska. Geological Society of America Bulletin 113(3): 388-402.

Barron, J.A., Bukry, D., Dean, W.E., Addison, J.A. and Finney, B.P., 2009. Paleoceanography of the Gulf of Alaska during the past 15,000 years: results from diatoms, silicoflagellates, and geochemistry. Marine Micropaleontology 72: 176-195.

Bickert, T., 2006. Influences of geochemical processes on stable isotope distribution in marine sediments. In: H.D. Schulz and M. Zabel (Editors), Marine geochemistry. Springer-Verlag, Berlin, Germany, pp. 339-370.

Bond, N.A., Overland, J.E., Spillane, M. and Stabeno, P., 2003. Recent shifts in the state of the North Pacific. Geophysical Research Letters 30(23): doi:10.1029/2003GL018597.

Brew, D.A., 1996. Geologic map of the Craig, Dixon Entrance, and parts of the Ketchikan and Prince Rupert Quadrangles, southeastern Alaska, USGS Miscellaneous Field Studies Map MF-2319.

Burrell, D.C., 1989. Biogeochemistry of a boreal fjord: Boca de Quadra, Southeast Alaska. Occasional publication 6. Institute of Marine Science, University of Alaska Fairbanks, 454 pp.

Calvert, S.E. and Pedersen, T.F., 1993. Geochemistry of recent oxic and anoxic marine sediments - implications for the geological record. Marine Geology 113(1-2): 67-88.

Carleton, A.M., Carpenter, D.A. and Weser, P.J., 1990. Mechanisms of interannual variability of the Southwest United States summer rainfall maximum. Journal of Climate 3(9): 999-1015.

Carrara, P.E., Ager, T.A. and Baichtal, J.F., 2007. Possible refugia in the Alexander Archipelago of southeastern Alaska during the late Wisconsin glaciation. Canadian Journal of Earth Sciences 44: 229-244.

Childers, A.R., Whitledge, T.E. and Stockwell, D.A., 2005. Seasonal and interannual variability in the distribution of nutrients and chlorophyll a across the Gulf of Alaska shelf: 1998-2000. Deep-Sea Research Part II-Topical Studies in Oceanography 52(1-2): 193-216.

Clague, J.J. and James, T.S., 2002. History and isostatic effects of the last ice sheet in southern British Columbia. Quaternary Science Reviews 21: 71-87.

Crusius, J., Calvert, S.E., Pedersen, T.F. and Sage, D., 1996. Rhenium and molybdenum enrichments in sediments as indicators of oxic, suboxic and sulfidic conditions of deposition. Earth and Planetary Science Letters 145(1-4): 65-78.

Davis, J.C., 2002. Statistics and data analysis in geology. John Wiley and Sons, Inc., New York, 638 pp.

Dezileau, L., Reyss, J.L. and Lemoine, F., 2003. Late Quaternary changes in biogenic opal fluxes in the southern Indian Ocean. Marine Geology 202(3-4): 143-158.

Dymond, J., 1981. Geochemistry of Nazca plate surface sediments: An evaluation of hydrothermal, biogenic, detrital, and hydrogenous sources. In: L.D. Kulm, J. Dymond, E.J. Dasch, D.M. Hussong and R. Roderick (Editors), Nazca Plate: crustal formation and Andean convergence. Memoir - Geological Society of America. Geological Society of America, Boulder, CO, pp. 133-173.

Fairbanks, R.G., 1989. A 17,000-year glacio-eustatic sea-level record - influence of glacial melting rates on the Younger Dryas event and deep-ocean circulation. Nature 342(6250): 637-642.

Faure, G., 1998. Principles and applications of geochemistry. Prentice Hall, Upper Saddle River, New Jersey, 600 pp.

Fedje, D.W. and Christensen, T., 1999. Modeling paleoshorelines and locating early Holocene coastal sites in Haida Gwaii. American Antiquity 64(4): 635-652.

Finney, B.P., Gregory-Eaves, I., Douglas, M.S.V. and Smol, J.P., 2002. Fisheries productivity in the northeastern Pacific Ocean over the past 2,200 years. Nature 416(6882): 729-733.

Finney, B.P., Gregory-Eaves, I., Sweetman, J., Douglas, M.S.V. and Smol, J.P., 2000. Impacts of climatic change and fishing on Pacific salmon abundance over the past 300 years. Science 290(5492): 795-799.

Fisher, D. et al., 2008. The Mt Logan Holocene-late Wisconsinan isotope record: Tropical Pacific-Yukon connections. Holocene 18(5): 667-677.

Fisher, D.A. et al., 2004. Stable isotope records from Mt. Logan, Eclipse Ice Cores and nearby Jellybean Lake - Water cycle of the North Pacific over 2000 years and over five vertical kilometers: sudden shifts and tropical connections. Geographie Physique Et Quaternaire 58(2-3).

Francis, R.C., Hare, S.R., Hollowed, A.B. and Wooster, W.S., 1998. Effects of interdecadal climate variability on the oceanic ecosystems of the NE Pacific. Fisheries Oceanography 7(1): 1-21.

Froelich, P.N. et al., 1979. Early oxidation of organic matter in pelagic sediments of the eastern equatorial Atlantic: suboxic diagenesis. Geochimica Et Cosmochimica Acta 43: 1075-1090.

Gargett, A.E., 1997. The optimal stability 'window': a mechanism underlying decadal fluctuations in North Pacific salmon stocks? Fisheries Oceanography 6(2): 109-117.

Gay, S.M. and Vaughan, S.L., 2001. Seasonal hydrography and tidal currents of bays and fjords in Prince William Sound, Alaska. Fisheries Oceanography 10: 159-193.

Gilbert, R., 2000. Environmental assessment from the sedimentary record of high-latitude fiords. Geomorphology 32: 295-314.

Hallet, B., Hunter, L. and Bogen, J., 1996. Rates of erosion and sediment evacuation by glaciers: A review of field data and their implications. Global and Planetary Change 12(1-4): 213-235.

Harrison, P.J., Boyd, P.W., Varela, D.E. and Takeda, S., 1999. Comparison of factors controlling phytoplankton productivity in the NE and NW subarctic Pacific gyres. Progress in Oceanography 43(2-4): 205-234.

Hartnett, H.E., Keil, R.G., Hedges, J.I. and Devol, A.H., 1998. Influence of oxygen exposure time on organic carbon preservation in continental margin sediments. Nature 391(6667): 572-574.

Haug, G.H., Hughen, K.A., Sigman, D.M., Peterson, L.C. and Rohl, U., 2001. Southward migration of the intertropical convergence zone through the Holocene. Science 293(5533): 1304-1308.

Heaton, T.H. and Grady, F., 2003. The Late Wisconsin vertebrate history of Prince of Wales Island, Southeast Alaska. In: B.W. Schubert, J.I. Mead and R.W. Graham (Editors), Ice Age Cave Faunas of North America. Indiana University Press, Bloomington, pp. 17-53.

Hedges, J.I. et al., 1999. Sedimentary organic matter preservation: A test for selective degradation under oxic conditions. American Journal of Science 299(7-9): 529-555.

Hetherington, R., Barrie, J.V., Reid, R.G.B., MacLeod, R. and Smith, D.J., 2004. Paleogeography, glacially induced crustal displacement, and Late Quaternary coastlines on the continental shelf of British Columbia, Canada. Quaternary Science Reviews 23(3-4): 295-318.

Heusser, C.J., Heusser, L.E. and Peteet, D.M., 1985. Late Quaternary climatic change on the American North Pacific Coast. Nature 315(6019): 485-487.

Jaeger, J.M., Nittrouer, C.A., Scott, N.D. and Milliman, J.D., 1998. Sediment accumulation along a glacially impacted mountainous coastline: north-east Gulf of Alaska. Basin Research 10(1): 155-173.

Kaufman, D. and Manley, W.F., 2004. Pleistocene Maximum and Late Wisconsinan glacier extents across Alaska, U.S.A. In: J. Ehlers and P.L. Gibbard (Editors), Quaternary Glaciations - Extent and chronology, Part II: North America. Elsevier, Amsterdam, pp. 9-27.

Kaufman, D.S. et al., 2004. Holocene thermal maximum in the western Arctic (0-180 degrees W). Quaternary Science Reviews 23(5-6): 529-560.

Kroopnick, P.M., 1985. The distribution of ^{13}C of ΣCO_2 in the world oceans. Deep-Sea Research 32(1): 57-84.

Latif, M. and Barnett, T.P., 1994. Causes of decadal climate variability over the North Pacific and North America. Science 266(5185): 634-637.

Langmuir, D., 1997. Aqueous environmental geochemistry. Prentice Hall, Upper Saddle River, New Jersey, p. 600.

Loney, R.A., Brew, D.A., Muffler, L.J.P. and Pomeroy, J.S., 1975. Reconnaissance geologic map of Chichagof, Baranof, and Kruzof Islands, southeastern Alaska, Geological Survey Professional Paper 792. United States Government Printing Office, Washington D.C.

Mann, D.H., Crowell, A.L., Hamilton, T.D. and Finney, B.P., 1998. Holocene geologic and climatic history around the Gulf of Alaska. Arctic Anthropology 35(1): 112-131.

Mantua, N.J. and Hare, S.R., 2002. The Pacific decadal oscillation. Journal of Oceanography 58(1): 35-44.

Mantua, N.J., Hare, S.R., Zhang, Y., Wallace, J.M. and Francis, R.C., 1997. A Pacific interdecadal climate oscillation with impacts on salmon production. Bulletin of the American Meteorological Society 78(6): 1069-1079.

Marshall, C.P. and Fairbridge, R.W. (Editors), 1999. Encyclopedia of geochemistry. Kluwer Academic Publishers, Dordrecht, The Netherlands, 712 pp.

McFarlane, G.A. and Beamish, R.J., 1992. Climatic influence linking copepod production with strong year-classes in sablefish, Anoplopoma-Fimbria. Canadian Journal of Fisheries and Aquatic Sciences 49(4): 743-753.

McLennan, S.M., 1995. Sediments and soils: chemistry and abundances. In: T.J. Ahrens (Editor), Rock physics and phase relations - a handbook of physical constants. American Geophysical Union, Washington D.C., pp. 8-19.

McLennan, S.M., 1999. Geochemical classification of the elements. In: C.P. Marshall and R.W. Fairbridge (Editors), Encyclopedia of geochemistry. Kluwer Academic Publishers, Dordrecht, The Netherlands, pp. 263-266.

McQuoid, M.R., Whiticar, M.J., Calvert, S.E. and Pedersen, T.F., 2001. A post-glacial isotope record of primary production and accumulation in the organic sediments of Saanich Inlet, ODP Leg 169S. Marine Geology 174(1-4): 273-286.

Meyers, P.A., 1994. Preservation of elemental and isotopic source identification of sedimentary organic matter. Chemical Geology 114(3-4): 289-302.

Miller, C.B., 1993. Pelagic production processes in the sub-arctic Pacific. Progress in Oceanography 32(1-4): 1-15.

Minobe, S. and Mantua, N., 1999. Interdecadal modulation of interannual atmospheric and oceanic variability over the North Pacific. Progress in Oceanography 43(2-4): 163-192.

Misarti, N., Finney, B.P., Maschner, H.D.G. and Wooller, M.J., 2009. Changes in northeast Pacific marine ecosystems over the last 4500 years: evidence from stable isotope analysis of bone collagen from archaeological middens. Holocene 19: 1-13.

Mortlock, R.A. and Froelich, P.N., 1989. A simple method for the rapid determination of biogenic opal in pelagic marine sediments. Deep-Sea Research 36(9): 1415-1426.

Mundy, P.R. and Olsson, P., 2005. Climate and weather. In: P.R. Mundy (Editor), The Gulf of Alaska: biology and oceanography. Alaska Sea Grant College Program, University of Alaska Fairbanks, pp. 25-34.

Nebert, D.L., 1982. The circulation of the Smeaton Bay and Boca de Quadra fjord systems. In: D.V. Ellis (Editor), Marine tailings disposal. Ann Arbor Science Publications, Ann Arbor, pp. 291-310.

Nuwer, J.M. and Keil, R.G., 2005. Sedimentary organic matter geochemistry of Clayoquot Sound, Vancouver Island, British Columbia. Limnology and Oceanography 50(4): 1119-1128.

Peterson, W.T. and Schwing, F.B., 2003. A new climate regime in northeast pacific ecosystems. Geophysical Research Letters 30(17): doi:10.1029/2003GL017528.

Piper, D.Z., 2001. Marine chemistry of the Permian Phosphoria Formation and Basin, Southeast Idaho. Economic Geology 96: 599-620.

Piper, D.Z. and Calvert, S.E., 2009. A marine biogeochemical perspective on black shale deposition. Earth-Science Reviews 95: 63-96.

Piper, D.Z. and Dean, W.E., 2002. Trace-element deposition in the Cariaco Basin, Venezuela Shelf, under sulfate-reducing conditions - a history of the local hydrography and global climate, 20 ka to the present, US Geological Survey Professional Paper P1670. US Geological Survey, Reston, VA, pp. 41.

Putnam, D.E. and Fifield, T., 1995. Estuarine archaeology and Holocene sea-level change on Prince of Wales Island, Alaska, Proceedings of Hidden Dimensions: the cultural significance of wetland archaeology, Vancouver, British Columbia, Canada, pp. 1-15.

Ragueneau, O. et al., 2000. A review of the Si cycle in the modem ocean: recent progress and missing gaps in the application of biogenic opal as a paleoproductivity proxy. Global and Planetary Change 26(4): 317-365.

Rasmussen, S.O., Andersen, K.K., Svensson, A.M., Steffensen, J.P., Vinther, B.M., Clausen, H.B., Siggaard-Andersen, M.L., Johnsen, S.J., Larsen, L.B., Dahl-Jensen, D., Bigler, M., Rothlisberger, R., Fischer, H., Goto-Azuma, K., Hansson, M.E., and Ruth, U., 2006. A new Greenland ice core chronology for the last glacial termination. Journal of Geophysical Research-Atmospheres 111(D06102): doi:10.1029/2005JD006079.

Rasmussen, S.O., Vinther, B.M., Clausen, H.B. and Andersen, K.K., 2007. Early Holocene climate oscillations recorded in three Greenland ice cores. Quaternary Science Reviews 26(15-16): 1907-1914.

Reading, H.G. and Collinson, J.D., 1996. Clastic coasts. In: H.G. Reading (Editor), Sedimentary environments: processes, facies, and stratigraphy. Blackwell Science Ltd., Oxford, pp. 154-231.

Reifenstuhl, R.R., 1986. Geology of the Goddard Hot Spring area, Baranof Island, Southeastern Alaska. Public-Data File (Alaska) Report 86-2. Alaska Division of Geological and Geophysical Surveys, Fairbanks, AK, p. 83

Reimer, P.J. et al., 2004. IntCal04 terrestrial radiocarbon age calibration, 0-26 cal kyr BP. Radiocarbon 46(3): 1029-1058.

Riehle, J.R. and Brew, D.A., 1984. Explosive latest Pleistocene(?) and Holocene activity of the Mount Edgecumbe volcanic field, Alaska. In: K.M. Reed and S. Bartsch-Winkler (Editors), The United States Geological Survey in Alaska: accomplishments during 1982, pp. 111-115.

Rodionov, S.N., Bond, N.A. and Overland, J.E., 2007. The Aleutian Low, storm tracks, and winter climate variability in the Bering Sea. Deep-Sea Research Part II-Topical Studies in Oceanography 54: 2560-2577.

Rodionov, S.N., Overland, J.E. and Bond, N.A., 2005. Spatial and temporal variability of the Aleutian climate. Fisheries Oceanography 14: 3-21.

Royer, T.C., 2005. Hydrographic responses at a coastal site in the northern Gulf of Alaska to seasonal and interannual forcing. Deep-Sea Research Part Ii-Topical Studies in Oceanography 52(1-2): 267-288.

Royer, T.C., Grosch, C.E. and Mysak, L.A., 2001. Interdecadal variability of Northeast Pacific coastal freshwater and its implications on biological productivity. Progress in Oceanography 49(1-4): 95-111.

Schulz, M. and Mudelsee, M., 2002. REDFIT: estimating red-noise spectra directly from unevenly spaced paleoclimatic time series. Computers and Geosciences 28: 421-426.

Skei, J.M., McKee, B. and Sundby, B., 2003. Fjords. In: K.D. Black and G.B. Shimmield (Editors), Biogeochemistry of marine systems. Biological Sciences Series. Blackwell Publishing Ltd., Oxford, UK, pp. 65-90.

Steffensen, J.P., Andersen, K.K., Bigler, M., Clausen, H.B., Dahl-Jensen, D., Fischer, H., Goto-Azuma, K., Hansson, M., Johnsen, S.J., Jouzel, J., Masson-Delmotte, V., Popp, T., Rasmussen, S.O., Rothlisberger, R., Ruth, U., Stauffer, B., Siggaard-Andersen, M.L., Sveinbjornsdottir, A.E., Svensson, A., and White, J.W.C., 2008. High-resolution Greenland ice core data show abrupt climate change happens in few years. Science 321(5889): 680-684.

Stuiver, M. and Reimer, P.J., 1993. Extended ^{14}C data base and revised CALIB 3.0 radiocarbon age calibration program. Radiocarbon 35(1): 137-189.

Sugai, S.F., Alperin, M.J. and Reeburgh, W.S., 1994. Episodic deposition and ^{137}Cs immobility in Skan Bay sediments: a ten-year ^{210}Pb and ^{137}Cs time series. Marine Geology 116: 351-372.

Syvitski, J.P.M., Burrell, D.C. and Skei, J.M., 1987. Fjords: processes and products. Springer-Verlag.

Timothy, D.A. and Soon, M.Y.S., 2001. Primary production and deep-water oxygen content of two British Columbian fjords. Marine Chemistry 73(1): 37-51.

Trenberth, K.E., 1990. Recent observed interdecadal climate changes in the Northern Hemisphere. Bulletin of the American Meteorological Society 71(7): 988-993.

Trenberth, K.E. and Hurrell, J.W., 1994. Decadal atmosphere-ocean variations in the Pacific. Climate Dynamics 9(6): 303-319.

Tribovillard, N., Algeo, T.J., Lyons, T. and Riboulleau, A., 2006. Trace metals as paleoredox and paleoproductivity proxies: An update. Chemical Geology 232(1-2): 12-32.

Turekian, K.K. and Wedepohl, K.H., 1961. Distribution of the elements in some major units of the Earth's crust. Geological Society of America Bulletin 72: 175-192.

Van der Weijden, C.H., 2002. Pitfalls of normalization of marine geochemical data using a common divisor. Marine Geology 184(3-4): 167-187.

Walinsky, S.E. et al., 2009. Distribution and composition of organic matter in surface sediments of coastal southeast Alaska. Continental Shelf Research 29(13): 1565-1579.

Walsh, E.M., Ingalls, A.E. and Keil, R.G., 2008. Sources and transport of terrestrial organic matter in Vancouver Island fjords and the Vancouver-Washington Margin: A multiproxy approach using $\delta^{13}C_{org}$, lignin phenols, and the ether lipid BIT index. Limnology and Oceanography 53(3): 1054-1063.

Weingartner, T.J., Danielson, S.L. and Royer, T.C., 2005. Freshwater variability and predictability in the Alaska Coastal Current. Deep-Sea Research Part Ii-Topical Studies in Oceanography 52(1-2): 169-191.

Appendix 4.1 EW0408-11JC biogeochemical data.

Isotopic and biogeochemical data				Sedimentary	Inorganic geochemical data		
Sample depth (cm bsf)		Opal (wt%)	TOC (wt%)	C/N ratio	$\delta^{13}C$ (‰ VPDB)	Sample depth (cm bsf)		Al (wt%)

Sample depth (cm bsf)		Opal (wt%)	TOC (wt%)	C/N ratio	$\delta^{13}C$ (‰ VPDB)	Sample depth (cm bsf)		Al (wt%)
0	- 1	38.22	7.23	9.44	-21.02	2	- 3	3.54
15	- 16	41.67	6.31	9.76	-20.76	17	- 18	3.33
30	- 31	42.08	6.07	9.61	-20.86	32	- 33	3.35
45	- 46	43.12	6.11	9.65	-20.89	47	- 48	3.35
60	- 61	40.14	6.19	9.84	-21.03	62	- 63	3.20
75	- 76	38.07	6.35	9.68	-21.08	77	- 78	3.70
90	- 91	36.29	6.59	9.54	-21.07	92	- 93	3.79
105	- 106	41.64	6.01	9.56	-20.91	107	- 108	3.43
120	- 121	44.32	5.85	9.54	-20.89	122	- 123	3.36
135	- 136	37.48	5.93	9.51	-20.96	137	- 138	3.55
150	- 151	43.24	6.57	10.41	-21.68	152	- 153	3.55
165	- 166	43.36	5.56	9.59	-20.88	167	- 168	3.48
180	- 181	38.72	5.42	9.95	-21.10	182	- 183	3.66
195	- 196	44.61	5.10	9.81	-20.89	197	- 198	3.58
210	- 211	43.31	5.44	9.95	-21.12	212	- 213	3.44
225	- 226	42.92	5.55	9.95	-20.98	227	- 228	3.55
240	- 241	41.07	5.28	9.98	-20.97	242	- 243	3.60
255	- 256	34.52	5.20	10.14	-21.03	257	- 258	3.62
270	- 271	43.18	5.03	10.16	-21.05	272	- 273	3.69
285	- 286	39.51	5.17	10.09	-21.02	287	- 288	3.79
300	- 301	38.80	5.13	10.37	-21.18	302	- 303	3.76
315	- 316	36.29	5.20	10.22	-21.06	317	- 318	4.05
330	- 331	34.28	4.95	10.34	-21.15	332	- 333	3.89
345	- 346	37.59	5.05	10.29	-21.14	347	- 348	3.78
360	- 361	37.20				362	- 363	3.81
375	- 376	40.31	4.68	10.58	-21.24	377	- 378	3.78
390	- 391	34.51	4.96	10.44	-21.31	392	- 393	3.86
405	- 406	36.42	4.88	10.63	-21.26	407	- 408	3.94
420	- 421	35.02	4.80	10.47	-21.05	422	- 423	3.98
435	- 436	34.67	4.42	10.56	-21.09	439	- 440	4.14
450	- 451	35.98	4.46	10.41	-21.04	452	- 453	4.19
465	- 466	37.97	4.58	10.49	-21.15	467	- 468	4.26
480	- 481	28.15	4.67	11.11	-21.48	482	- 483	4.57
495	- 496	36.24	4.68	10.75	-21.32	497	- 498	4.25
510	- 511	33.71	4.31	11.13	-21.65	512	- 513	4.26
525	- 526	36.29	4.19	10.91	-21.36	527	- 528	4.17
540	- 541	31.78	3.97	10.87	-21.35	542	- 543	4.24
555	- 556	31.92	3.70	11.13	-21.38	557	- 558	4.42
570	- 571	33.10	3.90	11.45	-21.49	572	- 573	4.53
585	- 586	30.34	3.50	11.17	-21.49	587	- 588	4.49
600	- 601	31.06	3.68	11.51	-21.63	602	- 603	4.95
615	- 616	35.44	3.45	11.40	-21.80	617	- 618	4.72
630	- 631	20.35	3.80	12.85	-22.91	632	- 633	4.86
645	- 646	30.78	3.14	12.26	-21.94	647	- 648	5.02
660	- 661	31.00	3.06	12.04	-22.03	662	- 663	4.76

Ti (wt%)	Zr (ppm)	Mn (ppm)	V (ppm)	Cr (ppm)	Mo (ppm)	U (ppm)
0.20	33.5	392	114	48	8.70	7.0
0.19	27.7	379	103	42	6.46	4.3
0.19	26.0	401	100	40	6.65	3.6
0.19	28.0	393	105	42	4.53	3.2
0.18	26.8	381	100	40	4.66	2.4
0.21	30.0	438	116	44	7.92	3.9
0.22	30.6	453	115	46	7.31	3.7
0.19	27.5	410	104	42	5.33	3.3
0.19	26.3	381	102	40	5.28	3.8
0.21	30.1	429	110	42	5.38	3.7
0.20	26.6	414	106	41	5.13	2.9
0.19	26.9	419	104	42	5.71	3.1
0.21	29.1	433	113	43	5.15	3.4
0.20	27.9	430	109	41	5.95	3.5
0.19	26.8	417	106	41	5.98	3.6
0.20	28.5	407	108	42	5.77	3.7
0.20	27.7	426	111	41	8.76	5.7
0.20	28.7	446	107	41	8.94	5.2
0.21	29.8	446	113	42	8.75	5.7
0.21	29.9	460	117	43	8.25	5.3
0.21	30.1	447	116	42	7.86	5.7
0.23	30.9	479	118	46	7.81	5.0
0.22	31.3	479	120	44	10.10	6.7
0.21	31.1	467	118	45	11.70	8.0
0.21	30.5	472	114	45	10.10	6.0
0.22	30.7	468	112	43	8.33	5.1
0.23	32.4	481	117	44	9.13	5.0
0.22	31.9	491	118	44	10.10	6.5
0.23	32.8	480	122	45	9.17	4.9
0.24	35.1	509	131	47	10.50	6.4
0.24	34.0	529	130	46	10.10	5.8
0.24	33.9	518	133	47	11.50	7.4
0.26	36.2	542	153	52	11.60	9.8
0.24	33.1	521	126	47	12.10	5.8
0.25	34.0	533	132	50	11.00	7.5
0.25	32.5	520	131	46	9.27	5.3
0.26	35.9	545	136	47	8.80	4.4
0.28	37.1	574	143	52	6.96	5.0
0.29	37.7	593	149	53	7.23	4.6
0.28	37.7	596	148	51	8.15	5.6
0.31	40.3	645	155	53	7.70	5.1
0.31	39.9	666	154	52	6.56	3.8
0.32	40.6	657	160	53	6.07	3.9
0.34	40.6	698	161	53	7.01	4.0
0.32	40.1	679	157	55	5.99	3.8

Appendix 4.1 (continued)

Isotopic and biogeochemical data					Inorganic geochemical data								
Sample depth (cm bst)	Opal (wt%)	TOC (wt%)	C/N ratio	Sedimentary δ¹³C (‰, VPDB)	Sample depth (cm bsf)	Al (wt%)	Ti (wt%)	Zr (ppm)	Mn (ppm)	V (ppm)	Cr (ppm)	Mo (ppm)	U (ppm)
675 - 676	26.81	2.80	11.92	-22.02	677 - 678	4.90	0.33	42.5	665	161	56	6.75	3.6
690 - 691	33.20	2.43	12.30	-21.97	692 - 693	4.78	0.33	42.6	669	159	54	5.64	3.5
705 - 706	28.65	2.87	11.94	-21.91	707 - 708	5.03	0.36	46.0	718	169	57	5.18	3.7
720 - 721	29.16	2.64	11.83	-21.95	722 - 723	5.14	0.36	45.1	729	173	57	3.64	2.8
735 - 736	31.49	2.69	11.64	-22.00	737 - 738	4.99	0.35	47.4	722	174	57	3.41	2.9
750 - 751	26.32	2.52	9.56	-21.76	752 - 753	4.98	0.35	45.6	719	173	57	3.97	3.1
765 - 766	24.85	2.32	10.57	-22.12	767 - 768	5.32	0.38	49.4	792	189	57	3.23	2.7
780 - 781	24.03	2.10	12.27	-22.75	782 - 783	5.77	0.40	55.0	847	204	64	2.80	2.2
795 - 796	21.70	1.98	11.57	-22.74	797 - 798	5.63	0.39	54.5	817	198	61	3.25	2.6
810 - 811		1.84	11.09	-22.46	812 - 813	5.63	0.40	57.4	827	204	60	2.79	2.4
825 - 826	19.09	1.85	11.27	-22.53	827 - 828	5.99	0.42	60.0	833	213	63	2.56	2.2
840 - 841	19.02	1.70	12.29	-23.67	842 - 843	6.02	0.41	58.0	840	204	60	1.85	1.9
855 - 856	19.83	2.11	12.71	-23.54	857 - 858	5.94	0.40	59.9	858	211	60	1.81	1.9
870 - 871	16.76	1.84	13.26	-24.02	872 - 873	6.21	0.42	63.2	869	218	61	1.89	2.1
885 - 886	18.56	1.75	13.81	-24.42	887 - 888	6.25	0.42	62.6	901	219	60	1.70	1.9
900 - 901	15.98	1.68	14.00	-24.44	902 - 903	6.36	0.43	63.1	889	224	59	1.53	1.9
915 - 916	17.72	1.76	13.73	-24.53	917 - 918	6.39	0.43	62.9	914	230	57	1.91	2.0
930 - 931	17.19	1.67	14.69	-24.65	932 - 933	6.33	0.42	61.8	884	227	57	1.94	2.1
945 - 946	19.32	1.94	14.36	-24.55	947 - 948	6.49	0.43	63.1	893	230	57	2.05	2.3
960 - 961	19.63	1.68	13.96	-24.55	962 - 963	6.56	0.42	63.3	900	222	54	2.48	2.3
975 - 976	18.80	1.83	14.94	-24.49	977 - 978	6.45	0.42	63.8	859	219	53	2.06	2.2
990 - 991	18.18	1.61	13.94	-24.58	992 - 993	6.44	0.43	63.5	829	217	50	1.60	2.1
1005 - 1006	16.72	1.63	13.92	-24.53	1007 - 1008	6.47	0.42	63.8	864	218	52	1.82	1.9
1020 - 1021	19.08	1.95	15.07	-24.82	1022 - 1023	6.40	0.43	62.4	843	222	51	2.98	2.0
1035 - 1036	18.16	1.83	14.34	-24.56	1037 - 1038	6.38	0.41	62.3	937	210	51	2.29	2.0
1050 - 1051	21.19	1.93	14.93	-24.58	1052 - 1053	6.45	0.41	60.8	925	217	52	1.89	2.0
1065 - 1066	26.22	1.92	14.90	-24.61	1067 - 1068	6.35	0.41	59.2	907	211	49	1.95	1.9
1080 - 1081	21.67	1.98	15.33	-24.67	1082 - 1083	6.45	0.41	57.3	914	208	49	2.63	2.0
1095 - 1096	23.21	1.92	14.85	-24.66	1097 - 1098	6.11	0.39	57.9	917	224	51	2.99	2.2
1110 - 1111	20.92	1.75	15.38	-24.57	1112 - 1113	6.56	0.41	57.5	912	211	53	2.18	1.9
1125 - 1126	19.50	0.41		-24.57	1127 - 1128	6.72	0.45	65.3	974	216	57	2.16	2.1
1140 - 1141	15.97	1.67	14.76	-24.83	1142 - 1143	6.71	0.43	58.0	958	218	55	2.28	2.1
1155 - 1156	15.96	2.46	15.45	-24.97	1157 - 1158	6.77	0.42	61.3	920	222	56	2.48	2.4
1170 - 1171	12.03	1.79	15.26	-25.10	1172 - 1173	6.85	0.42	60.1	882	210	55	2.89	2.4
1185 - 1186	13.38	1.92	16.07	-25.29	1187 - 1188	6.72	0.40	62.7	845	219	55	2.58	2.6
1200 - 1201	11.18	1.66	14.83	-25.77	1202 - 1203	7.26	0.40	69.3	831	238	57	3.07	3.1
1215 - 1216	14.81	1.88	14.98	-25.42	1217 - 1218	6.95	0.40	65.8	869	229	59	3.76	3.3
1230 - 1231	10.79	1.37	14.19	-26.76	1232 - 1233	7.69	0.40	75.6	842	257	60	1.86	3.0
1245 - 1246	11.32	1.73	14.47	-26.79	1247 - 1248	7.73	0.41	78.4	992	269	60	2.97	3.0
1260 - 1261	9.77	1.52	14.35	-26.30	1262 - 1263	7.62	0.41	77.2	1120	270	61	3.09	3.2
1275 - 1276	10.83	1.78	14.05	-26.91	1277 - 1278	7.82	0.39	83.3	1190	277	62	2.49	3.1
1290 - 1291	6.78	1.01	14.52	-29.02	1292 - 1293	8.41	0.43	92.8	693	304	62	0.89	5.0
1305 - 1306	5.97	0.95	12.29	-28.49	1307 - 1308	8.74	0.40	89.1	700	328	64	1.11	3.0
1320 - 1321	6.36	0.58	13.76	-28.87	1322 - 1323	9.22	0.37	80.5	908	315	78	0.77	2.1
1335 - 1336	5.30	0.42	16.69	-28.90	1337 - 1338	9.18	0.39	82.7	1030	302	84	0.84	2.2
1350 - 1351	5.30	0.56	14.70	-28.78	1352 - 1353	8.64	0.40	84.4	958	294	71	0.75	2.4
1365 - 1366	5.08	0.56	16.68	-29.13	1367 - 1368	8.63	0.35	72.6	1170	315	73	0.95	2.1
1380 - 1381	4.81	0.47	18.43	-29.34	1382 - 1383	8.25	0.38	77.3	1210	281	69	0.94	2.2
1395 - 1396	6.07	0.59	15.39	-29.29	1392 - 1393	8.93	0.35	73.5	1100	330	74	1.12	2.1
					1396 - 1397	8.62	0.37	78.0	1140	320	77	1.03	2.3

Appendix 4.2 EW0408-22JC biogeochemical data. * indicates composite depth due to splicing of EW0408-21GC with -22JC between 57 and 62 cm bsf.

Isotopic and biogeochemical data

Sample depth* (cm bsf)	Opal (wt%)	TOC (wt%)	C/N ratio	Sedimentary δ13C (‰, VPDB)
0 - 1	40.28	7.97	9.08	-21.26
2 - 3	45.28	7.63	9.03	-21.22
7 - 8	41.24	7.43	9.03	-21.23
12 - 13	44.23	7.50	8.92	-21.00
17 - 18	47.07	7.15	8.82	-21.10
22 - 23	47.53	7.18	8.84	-21.02
27 - 28	44.32	7.43	9.03	-20.96
32 - 33	45.01	6.95	8.91	-20.96
37 - 38	45.93	7.09	8.87	-20.75
42 - 43	45.21	7.12	8.83	-20.82
47 - 48	48.40	6.69	8.63	-20.72
52 - 53	49.95	6.72	8.73	-20.78
57 - 58	48.64	6.68	8.66	-20.70
62 - 63	45.01			
67 - 68	43.68			
72 - 73	46.12	7.38	10.18	-21.36
77 - 78	42.10			
82 - 83	40.22			
87 - 88	48.81			
92 - 93	46.00	6.93	9.74	-21.07
97 - 98	47.30			
102 - 103	44.56			
107 - 108	43.65			
112 - 113	46.01	7.14	9.96	-21.06
117 - 118	45.62			
122 - 123	45.29			
127 - 128	44.17			
132 - 133	44.99	6.73	10.03	-21.11
137 - 138	43.68			
142 - 143	40.52			
147 - 148	44.62			
152 - 153	45.63	6.71	9.86	-21.02
157 - 158	41.52			
162 - 163	44.56			
167 - 168	43.68			
172 - 173	37.67	6.62	9.88	-21.10
177 - 178	39.53			
182 - 183	36.25			
187 - 188	44.87			
192 - 193	43.16	7.03	9.79	-20.96
197 - 198	34.23			
202 - 203	37.88			
207 - 208	45.36			
212 - 213	40.44	6.63	9.76	-20.97
217 - 218	42.60			
222 - 223	36.73			

Inorganic geochemical data

Sample depth (cm bsf)	Al (wt%)	Ti (wt%)	Zr (ppm)	Mn (ppm)	V (ppm)	Cr (ppm)	Mo (ppm)	U (ppm)
32 - 33	2.67	0.21	41.41	438	69.3	41.1	2.69	
52 - 53	2.51	0.20	47.84	448	66.8	35.3	2.49	
72 - 73	2.46	0.20	37.52	418	70.5	33.4	3.13	
92 - 93	2.79	0.22	44.66	456	70.8	40.1	2.01	
112 - 113	2.89	0.22	43.20	425	68.5	37.1	3.78	
132 - 133	2.68	0.21	39.98	430	70.8	38.9	4.00	
152 - 153	2.82	0.22	48.85	454	72.8	34.7	2.82	
172 - 173	2.99	0.23	46.01	458	73.5	44.8	2.53	
192 - 193	2.98	0.23	48.95	482	74.7	41.7	2.47	
212 - 213	2.79	0.21	44.49	463	72.6	41.0	3.24	
232 - 233	2.82	0.22	48.17	470	76.1	45.0	2.66	
252 - 253	2.82	0.22	44.47	469	75.8	40.5	1.92	
272 - 273	2.86	0.22	46.18	493	71.5	41.5	2.45	
292 - 293	2.79	0.21	41.04	485	74.0	32.9	2.67	
312 - 313	2.76	0.22	42.58	487	74.5	36.4	2.44	
332 - 333	2.71	0.21	43.87	509	71.2	39.6	2.53	
352 - 353	2.82	0.22	46.53	475	70.8	37.0	1.55	
372 - 373	2.82	0.22	45.79	472	71.0	38.5	2.55	
392 - 393	2.87	0.22	43.02	496	72.4	41.5	3.26	1.06
412 - 413	2.98	0.22	73.67	483	71.5	34.7	3.30	1.41
432 - 433	2.86	0.22	50.00	493	71.7	39.6	2.28	
452 - 453	2.79	0.21	52.31	500	69.5	38.0	2.79	0.88
472 - 473	2.71	0.21	64.49	433	74.9	38.4	3.72	1.09
492 - 493	2.88	0.22	48.42	457	68.0	34.8	2.77	
512 - 513	3.09	0.23	53.76	417	79.2	39.5	3.36	
532 - 533	3.26	0.24	54.15	443	73.1	43.8	2.27	1.44
552 - 553	3.03	0.23	52.58	473	74.6	43.0	2.96	1.21
572 - 573	2.88	0.23	60.12	500	74.7	41.2	2.24	0.99
592 - 593	3.06	0.25	58.78	516	76.8	42.5	2.10	1.87
612 - 613	2.78	0.23	54.08	518	72.5	38.8	3.77	1.66
632 - 633	2.65	0.21	55.35	458	65.8	31.5	2.66	1.26
652 - 653	3.13	0.26	85.07	515	70.5	44.0	1.81	3.24
672 - 673	3.08	0.25	58.08	502	72.2	41.9	3.67	2.78
692 - 693	2.96	0.24	72.43	486	71.6	37.0	2.97	1.75
712 - 713	3.18	0.27	77.25	514	75.5	38.7	1.83	1.99
732 - 733	3.22	0.27	68.66	491	75.4	40.6	2.31	2.44
752 - 753	3.13	0.27	73.47	494	75.3	45.9	2.08	1.43
772 - 773	3.28	0.27	73.03	504	77.3	42.0	3.06	3.25
792 - 793	3.19	0.26	59.09	477	79.7	36.8	4.66	3.86
813 - 814	3.21	0.26	57.58	477	77.5	41.5	5.04	3.07
832 - 833	3.14	0.25	61.52	462	75.2	42.5	3.78	3.78
852 - 853	3.06	0.25	54.58	454	74.1	34.4	5.34	3.26
872 - 873	3.13	0.26	57.20	487	78.0	37.0	4.82	3.54
892 - 893	3.15	0.25	64.76	461	78.4	39.2	3.56	3.35
912 - 913	2.83	0.24	64.78	443	68.8	32.7	3.96	3.27
932 - 933	3.08	0.26	97.41	471	72.5	43.1	3.38	3.33

Appendix 4.2 (continued)

Isotopic and biogeochemical data

Sample depth* (cm bsf)	Opal (wt%)	TOC (wt%)	C/N ratio	Sedimentary δ¹³C (‰, VPDB)
227 - 228	45.10			
232 - 233	39.42	6.29	9.89	-21.00
237 - 238	46.69			
242 - 243	46.59			
247 - 248	41.28			
252 - 253	42.88	6.41	10.00	-21.11
257 - 258	40.38			
262 - 263	47.92			
267 - 268	43.56			
272 - 273	38.57	6.74	10.02	-21.03
277 - 278	40.07			
282 - 283	41.83			
287 - 288	38.04			
292 - 293	42.04	6.42	9.83	-20.91
297 - 298	41.44			
302 - 303	45.90			
307 - 308	41.77			
312 - 313	45.55	6.55	9.88	-20.96
317 - 318	42.84			
322 - 323	44.61			
327 - 328	42.05			
332 - 333	44.58	6.59	9.88	-21.06
337 - 338	37.79			
342 - 343	26.80			
347 - 348	44.19			
352 - 353	38.54	6.61	9.98	-21.01
357 - 358	40.89			
362 - 363	39.79			
367 - 368	41.42			
372 - 373	44.12	6.51	9.87	-20.98
377 - 378	39.88			
382 - 383	40.67			
387 - 388	41.89			
392 - 393	40.95	6.45	10.25	-21.32
397 - 398	47.28			
402 - 403	37.80			
407 - 408	36.82			
412 - 413	33.75	6.18	10.10	-21.21
417 - 418	40.86			
423 - 424	34.60			
427 - 428	35.90			
432 - 433	29.53	6.72	9.98	-21.11
437 - 438	36.69			
442 - 443	37.31			
447 - 448	33.95			
452 - 453	36.55	6.19	10.08	-21.27
457 - 458	39.43			
462 - 463	37.33			

Inorganic geochemical data

Sample depth (cm bsf)	Al (wt%)	Ti (wt%)	Zr (ppm)	Mn (ppm)	V (ppm)	Cr (ppm)	Mo (ppm)	U (ppm)
952 - 953	3.09	0.25	61.94	491	75.9	40.3	3.34	2.37
972 - 973	3.29	0.26	64.06	463	77.8	39.1	4.73	4.02
992 - 993	3.35	0.27	66.01	482	79.8	47.2	3.60	2.24
1012 - 1013	3.51	0.29	79.76	477	80.0	42.8	3.34	3.19
1032 - 1033	3.61	0.28	83.53	462	75.6	44.9	2.14	2.48
1052 - 1053	3.43	0.26	98.63	455	74.8	45.2	2.46	2.65
1072 - 1073	3.59	0.29	69.12	476	79.3	48.7	3.59	4.02
1092 - 1093	3.63	0.28	84.57	496	78.1	40.5	4.02	2.56
1112 - 1113	3.44	0.28	71.69	468	82.9	43.5	4.06	3.38
1132 - 1133	3.46	0.27	73.74	461	80.3	40.2	3.93	3.42
1152 - 1153	3.32	0.27	63.12	481	76.6	40.1	4.35	3.18
1172 - 1173	3.40	0.28	81.18	494	79.7	43.1	4.62	4.04
1192 - 1193	3.44	0.27	66.23	496	78.3	46.1	5.26	3.47
1212 - 1213	3.24	0.26	60.03	466	75.2	39.7	5.14	3.92

Isotopic and biogeochemical data

Sample depth* (cm bsf)	Opal (wt%)	TOC (wt%)	C/N ratio	Sedimentary δ¹³C (‰, VPDB)
467 - 468	34.36			
472 - 473	33.45	6.37	10.04	-21.20
477 - 478	34.91			
482 - 483	35.51			
487 - 488	34.80			
492 - 493	33.59	6.02	10.01	-21.28
497 - 498	32.52			
502 - 503	30.48			
507 - 508	31.43			
512 - 513	27.75	6.54	13.43	-22.93
517 - 518	31.68			
522 - 523	29.22			
527 - 528	27.14			
532 - 533	26.42	3.03	10.70	-21.92
537 - 538	26.90			
542 - 543	38.13			
547 - 548	36.36			
552 - 553	37.90	6.15	9.98	-20.97
557 - 558	35.42			
562 - 563	36.20			
567 - 568	35.86			
572 - 573	38.09			
577 - 578	36.76			
582 - 583	32.24			
587 - 588	37.49			
592 - 593	31.43			
597 - 598	30.07			
602 - 603	26.57			

Appendix 4.2 (continued)

Isotopic and biogeochemical data

Sample depth* (cm bsf)	Opal (wt%)	TOC (wt%)	C/N ratio	Sedimentary δ^{13}C (‰ VPDB)
607 - 608	32.52			
612 - 613	38.81	5.52	10.38	-21.07
617 - 618	24.82			
622 - 623	25.73			
627 - 628	17.92			
632 - 633	33.17	5.44	10.30	-21.10
637 - 638	24.19			
642 - 643	21.81			
647 - 648	25.33			
652 - 653	16.98	1.98	10.20	-22.35
657 - 658	22.46			
662 - 663	24.97			
667 - 668	21.56			
672 - 673	27.35	4.25	10.51	-21.45
677 - 678	23.38			
682 - 683	23.38			
687 - 688	28.90			
692 - 693	31.45	3.44	10.38	-21.68
697 - 698	28.32			
702 - 703	30.08			
707 - 708	28.50			
712 - 713	28.16	4.19	10.42	-21.41
717 - 718	30.55			
722 - 723	29.03			
727 - 728	22.72			
732 - 733	29.09	4.63	10.98	-21.76
737 - 738	29.54			
742 - 743	29.99			
747 - 748	25.82			
752 - 753	27.04	4.45	10.66	-21.60
757 - 758	34.78			
762 - 763	26.63			
767 - 768	30.34			
772 - 773	28.07	4.72	11.33	-21.97
777 - 778	30.08			
782 - 783	30.99			
787 - 788	28.45			
792 - 793	33.54	4.62	10.77	-21.69
797 - 798	29.63			
802 - 803	28.64			
807 - 808	31.54			
813 - 814	30.21	4.89	10.65	-21.60
817 - 818	29.06			
822 - 823	36.48			
827 - 828	29.75			
832 - 833	29.95	3.95	9.37	-21.71
843 - 844	29.11			
847 - 848	31.24			
852 - 853	34.56	3.69	9.17	-21.71
857 - 858	28.69			
862 - 863	30.96			
867 - 868	29.38			
872 - 873	33.09	4.11	9.63	-21.75
877 - 878	31.43			
882 - 883	29.18			
887 - 888	35.18			
892 - 893	30.34	4.19	10.30	-22.11
897 - 898	33.68			
902 - 903	36.72			
907 - 908	30.84			
912 - 913	38.13	3.67	9.19	-21.77

Isotopic and biogeochemical data

Sample depth* (cm bsf)	Opal (wt%)	TOC (wt%)	C/N ratio	Sedimentary δ^{13}C (‰ VPDB)
917 - 918	33.97			
922 - 923	33.59			
927 - 928	37.69			
932 - 933	27.96	3.29	8.85	-21.96
937 - 938	31.76			
942 - 943	29.76			
947 - 948	26.04			
952 - 953	29.60	3.75	9.32	-21.83
957 - 958	27.37			
962 - 963	27.47			
967 - 968	27.64			
972 - 973	23.85	4.03	9.62	-21.77
977 - 978	27.54			
982 - 983	26.03			
987 - 988	30.93			
992 - 993	25.20	3.90	9.80	-22.08
997 - 998	27.74			
1002 - 1003	24.60			
1007 - 1008	19.90			
1012 - 1013	25.39	3.59	9.62	-22.17
1017 - 1018	26.67			
1022 - 1023	23.11			
1027 - 1028	34.27			
1032 - 1033	11.41	1.91	8.28	-22.52
1037 - 1038	29.34			
1042 - 1043	34.25			
1047 - 1048	26.07			
1052 - 1053	17.68	1.72	7.60	-22.36
1057 - 1058	33.64			
1062 - 1063	29.01			
1067 - 1068	30.70			
1072 - 1073	32.16	4.13	10.66	-21.80
1077 - 1078	25.92			
1082 - 1083	26.26			
1087 - 1088	29.43			
1092 - 1093	24.31	3.57	10.03	-21.76
1097 - 1098	23.81			
1102 - 1103	27.48			
1107 - 1108	25.92			
1112 - 1113	27.49	3.83	10.48	-21.93
1117 - 1118	31.29			
1122 - 1123	29.98			
1127 - 1128	29.10			
1132 - 1133	25.86	3.74	10.14	-21.78
1137 - 1138	31.04			
1142 - 1143	28.77			
1147 - 1148	32.43			
1152 - 1153	31.95	3.79	10.20	-21.84
1157 - 1158	30.54			
1162 - 1163	26.93			
1167 - 1168	31.45			
1172 - 1173	29.86	3.48	10.01	-21.83
1177 - 1178	34.89			
1182 - 1183	31.88			
1187 - 1188	30.78			
1192 - 1193	35.59	3.57	10.11	-21.93
1197 - 1198	26.55			
1202 - 1203	32.01			
1207 - 1208	33.50			
1212 - 1213	31.78	3.58	10.27	-22.22

Appendix 4.3 EW0408-33JC biogeochemical data.

Isotopic and biogeochemical data				Sedimentary	Inorganic geochemical data							
Sample depth (cm bsf)	Opal (wt%)	TOC (wt%)	C/N ratio	δ¹³C (‰ VPDB)	Al (wt%)	Ti (wt%)	Zr (ppm)	Mn (ppm)	V (ppm)	Cr (ppm)	Mo (ppm)	U (ppm)
2 - 3	25.29	3.83	9.74	-21.90	5.24	0.40	81	905	166	126	2.8	1.7
7 - 8	25.35	3.92	11.42	-24.61	5.49	0.42	88	912	172	128	3.5	2.3
12 - 13	27.23	5.06	11.47	-25.66	5.32	0.40	82	899	172	132	3.8	1.8
17 - 18	24.69	3.23	11.72	-24.53	5.23	0.39	77	892	167	133	3.7	1.5
22 - 23	20.34	3.40	12.81	-25.72	5.30	0.41	82	912	168	128	2.2	1.7
27 - 28	23.89	3.36	10.10	-22.47	5.07	0.38	77	872	157	123	2.8	1.3
33 - 34	23.10	3.73	10.00	-22.30	5.09	0.39	78	879	162	129	3.7	1.9
37 - 38	28.51	3.38	10.05	-22.33	5.14	0.39	80	879	163	136	2.8	2.5
42 - 43	27.43	3.52	10.13	-22.04	5.28	0.41	82	899	165	129	3.3	2.8
47 - 48	31.13	3.31	10.11	-22.34	5.17	0.40	80	879	163	129	3.0	1.9
52 - 53	33.56	3.89	9.93	-22.29	5.00	0.39	79	885	161	139	2.1	1.8
57 - 58	29.17	3.66	10.43	-22.31								
62 - 63	31.05	4.56	10.38	-23.37	5.04	0.39	80	879	159	134	2.3	1.9
67 - 68	34.45	4.08	9.75	-22.49	5.18	0.40	82	899	160	126	2.8	2.4
72 - 73	30.21	3.94	9.41	-22.10	5.18	0.40	80	892	165	127	3.5	1.7
77 - 78	21.38	4.99	9.87	-22.15	5.04	0.40	81	872	162	128	3.2	2.4
82 - 83	29.96	3.74	10.01	-22.29	5.02	0.39	81	872	160	127	3.1	1.6
87 - 88	32.12	3.66	9.84	-22.17	5.13	0.40	80	892	165	125	3.2	1.8
92 - 93	26.94	5.48	11.76	-26.59	5.10	0.40	81	885	163	125	4.2	1.7
97 - 98	28.31	4.59	10.92	-23.91								
102 - 103	27.63	3.76	9.78	-22.07	5.06	0.40	82	879	160	130	8.2	2.6
107 - 108	32.42	3.90	9.75	-22.14	5.03	0.39	81	885	163	131	4.1	2.7
112 - 113	33.23	4.46	11.64	-25.20	4.93	0.39	79	879	156	133	3.8	2.5
117 - 118	27.80	4.08	10.08	-22.77	4.94	0.39	81	899	163	126	3.2	2.6
122 - 123	34.58	4.72	9.53	-22.03	5.04	0.40	80	899	163	131	2.8	1.7
126 - 127	37.34	3.91	10.03	-22.16	4.86	0.38	78	866	159	127	3.0	
132 - 133	27.97	3.92	9.75	-22.04	5.05	0.39	80	885	158	136	3.0	2.2
137 - 138	32.52	5.45	11.86	-26.48	4.93	0.39	79	879	155	130	3.3	2.3
142 - 143	18.11	4.06	9.57	-22.18	5.04	0.39	79	879	160	123	4.4	2.2
147 - 148	34.42	4.14	9.91	-21.82	4.72	0.37	76	859	152	123	2.2	1.6
152 - 153	31.25	4.15	9.70	-21.86	4.80	0.37	76	852	153	126	2.3	1.5
157 - 158	32.41	4.10	10.12	-21.98	4.91	0.39	79	859	157	126	4.7	2.0
162 - 163	28.88	4.07	10.10	-21.93	4.95	0.38	78	852	159	125	4.6	1.8
167 - 168	32.86	4.49	11.49	-24.64	4.85	0.38	78	846	159	128	3.6	1.8
172 - 173	29.95	3.99	9.94	-22.04	4.90	0.39	79	872	159	124	3.6	1.0
177 - 178	28.77	4.21	10.93	-21.82	4.94	0.40	80	885	163	133	3.1	1.6
182 - 183	29.30	4.25	9.23	-21.69	4.95	0.39	79	879	162	130	3.4	1.9
187 - 188	30.52	3.86	9.95	-21.89	5.15	0.40	83	906	165	130	3.7	1.0
192 - 193	30.81	4.44	11.70	-24.54	5.08	0.40	80	872	164	126	3.5	2.1
197 - 198	31.45	4.63	11.88	-24.94	5.06	0.40	79	872	166	129	4.6	2.6
202 - 203	29.88	3.89	9.92	-22.26	5.14	0.40	81	885	168	130	3.5	2.4
207 - 208	29.56	3.97	10.08	-22.09	5.34	0.41	84	905	171	130	3.3	1.4
212 - 213	25.23	3.79	10.66	-22.13	5.56	0.43	88	945	177	136	4.0	1.9
217 - 218	26.78	3.67	10.91	-21.90	5.45	0.43	86	912	175	140	5.3	2.7
222 - 223	23.59	4.20	10.45	-22.12	5.60	0.43	90	922	180	138	5.4	3.2
227 - 228	24.88	4.15	11.88	-24.19	5.54	0.43	88	918	178	131	6.4	3.4
232 - 233	24.40	3.81	10.56	-22.06	5.43	0.43	88	905	172	135	6.0	3.8
237 - 238	25.26	4.31	11.13	-23.57	5.36	0.42	86	885	171	133	5.7	3.1
242 - 243	25.13	4.40	11.26	-24.33	5.37	0.42	87	905	173	131	4.7	2.2
247 - 248	26.58	4.53	11.55	-24.13	5.34	0.42	87	905	179	129	3.5	2.8
252 - 253	27.01	3.65	9.86	-22.02	5.34	0.43	89	925	174	136	4.0	2.6
257 - 258	26.19	3.43	9.85	-22.15	5.39	0.43	90	925	175	137	5.6	2.7
262 - 263	29.92	4.06	9.76	-22.00	5.24	0.42	87	835	167	129	4.6	2.5
267 - 268	29.90	4.01	9.62	-21.97	5.32	0.42	86	905	174	130	2.7	1.2
272 - 273	28.44	3.57	9.81	-22.05	5.28	0.41	83	899	175	131	4.6	1.1
277 - 278	27.60	3.48	10.01	-22.22	5.29	0.41	84	912	172	131	5.6	1.8
282 - 283	31.49	3.70	9.74	-21.93	5.26	0.41	83	879	173	130	3.1	3.4
287 - 288	27.88	3.84	9.63	-21.97	5.25	0.41	84	872	173	130	2.6	1.7
292 - 293	29.07	4.10	9.63	-21.75	5.04	0.40	82	852	164	126	3.3	1.0
297 - 298	31.36	3.93	9.43	-21.91	5.05	0.40	82	846	164	126	2.5	1.7
302 - 303	29.78	3.39	9.73	-22.12	5.06	0.40	81	846	167	126	3.7	3.0
307 - 308	30.96	4.34	9.65	-21.72	5.01	0.40	81	866	159	130	3.9	1.3
312 - 313	27.14	3.69	10.21	-21.96	5.03	0.39	80	866	163	124	4.5	1.7
317 - 318	30.70	3.60	9.78	-21.81	5.06	0.39	80	872	160	127	5.4	1.8
322 - 323	28.73	4.00	10.14	-21.97	5.06	0.40	81	872	161	131	3.1	1.9
327 - 328	29.12	3.93	10.22	-22.07	5.09	0.40	81	872	160	128	5.5	2.4
332 - 333	30.87	3.75	9.85	-21.96	5.06	0.40	83	866	160	126	2.8	1.9
337 - 338	25.99	4.22	10.13	-21.92	5.09	0.41	84	872	165	129	6.2	2.6
342 - 343	28.37	4.04	10.74	-22.19	4.97	0.39	81	859	157	123	4.6	2.8

Appendix 4.3 (continued)

Isotopic and biogeochemical data				Sedimentary	Inorganic geochemical data							
Sample depth (cm bsf)	Opal (wt%)	TOC (wt%)	C/N ratio	$\delta^{13}C$ (‰ VPDB)	Al (wt%)	Ti (wt%)	Zr (ppm)	Mn (ppm)	V (ppm)	Cr (ppm)	Mo (ppm)	U (ppm)
347 - 348	29.05	3.59	10.37	-21.93	4.90	0.39	81	846	158	126	2.6	1.7
352 - 353	28.30	3.11	10.88	-22.06	4.95	0.39	80	852	162	122	4.0	2.5
357 - 358	27.53	3.78	10.41	-22.00	5.01	0.39	81	859	160	125	3.6	0.9
362 - 363	31.22	3.68	10.30	-21.90	5.25	0.41	84	906	164	126	2.7	0.9
367 - 368	28.63	4.00	10.19	-22.11	5.14	0.41	83	892	165	128	3.0	2.4
372 - 373	26.11	3.43	10.73	-22.12	5.42	0.42	87	929	167	135	3.5	2.2
377 - 378	26.89	3.74	10.48	-21.97	5.33	0.42	85	912	165	132	5.2	3.1
382 - 383	30.45	3.90	10.62	-22.12	5.23	0.41	83	899	171	130	4.3	3.0
387 - 388	27.83	3.71	10.42	-22.07	5.14	0.40	82	875	168	127	5.1	1.9
392 - 393	31.47	3.86	10.44	-22.10	5.23	0.41	84	914	165	133	5.1	2.5
397 - 398	29.55	3.69	10.32	-22.06	5.11	0.41	83	899	166	129	4.2	1.5
402 - 403	26.92	4.15	10.23	-22.12	5.06	0.40	81	899	165	128	4.6	1.9
407 - 408	26.71	4.60	10.20	-22.12	5.11	0.41	82	899	167	128	3.8	3.0
412 - 413	25.97	4.04	10.44	-22.18	5.15	0.41	84	905	171	136	3.1	3.4
417 - 418	27.61	4.37	10.28	-22.12	5.17	0.41	84	899	169	132	2.5	1.1
422 - 423	26.22	4.56	10.07	-21.99	5.15	0.41	83	892	169	129	4.3	3.5
427 - 428	30.59	4.32	10.14	-22.03	5.13	0.41	83	892	169	129	4.3	1.7
432 - 433	27.13	4.41	10.29	-21.91	4.99	0.40	82	872	165	124	8.7	4.6
437 - 438	31.28	4.48	10.17	-22.14	5.23	0.41	87	922	170	127	5.6	4.3
442 - 443	27.41	3.91	10.51	-22.02	5.01	0.42	90	929	165	131	3.2	3.3
447 - 448	28.32	4.58	10.56	-21.99	5.01	0.40	83	860	162	127	4.9	3.8
452 - 453	33.96	5.10	10.01	-22.05	5.00	0.40	82	852	162	123	4.3	1.7
457 - 458	27.98	4.47	10.05	-21.96	4.94	0.40	83	852	164	128	3.3	2.7
462 - 463	22.38	3.33	11.93	-22.92	5.16	0.44	91	971	177	137	2.7	1.3
467 - 468	29.80	4.24	9.95	-22.01	4.98	0.39	80	859	157	120	4.6	1.7
472 - 473	24.35	4.48	10.00	-22.19	5.04	0.41	84	922	164	130	6.2	2.1
477 - 478	29.19	4.34	9.72	-21.73	5.00	0.39	80	866	166	126	4.2	2.3
482 - 483	28.94	4.08	9.51	-21.55	5.03	0.39	80	869	164	122	4.4	3.0
487 - 488	28.28	3.94	9.64	-21.78	5.00	0.39	82	859	169	128	6.4	3.8
492 - 493	26.65	4.13	9.93	-21.93	4.83	0.38	80	839	161	119	3.9	2.3
497 - 498	27.01	4.00	10.21	-21.87	4.97	0.40	82	866	163	125	4.5	1.5
502 - 503	26.74	4.82	9.79	-21.94	4.93	0.39	82	844	160	123	4.9	1.9
507 - 508	32.03	4.03	10.48	-22.19	4.92	0.39	82	852	163	120	5.2	3.3
512 - 513	33.69	5.80	12.18	-22.85	4.89	0.39	79	846	162	120	8.2	1.9
517 - 518	30.11	4.88	9.93	-22.09	4.81	0.38	80	844	160	120	7.0	2.4
522 - 523	30.57	4.12	10.19	-22.37	4.80	0.38	78	859	154	124	5.8	3.4
527 - 528	25.53	4.20	10.13	-21.81	5.05	0.40	83	891	159	125	7.4	2.6
532 - 533	28.74	4.79	10.19	-21.90	5.15	0.41	85	875	163	124	4.4	3.1
537 - 538	32.44	4.63	10.11	-21.82	5.06	0.40	84	859	161	122	2.6	2.3
542 - 543	29.09	4.27	10.06	-21.76	5.00	0.40	81	852	159	123	2.8	2.0
547 - 548	26.67	3.73	10.13	-21.81	5.10	0.40	83	872	162	123	2.7	2.1
552 - 553	30.53	4.34	9.86	-21.81	4.98	0.40	80	859	156	125	2.6	2.6
557 - 558	30.18	4.43	9.70	-21.91	4.95	0.39	81	852	155	126	2.9	2.0
562 - 563	28.25	4.44	9.45	-21.61	4.99	0.39	82	859	158	119	4.0	2.1
567 - 568	29.16	4.12	9.66	-21.81	5.00	0.40	83	885	159	123	3.4	3.3
572 - 573	37.38	4.36	9.46	-21.93	4.91	0.39	80	866	154	120	2.6	1.7
577 - 578	29.01	3.66	10.71	-21.91	4.88	0.38	79	852	149	118	2.9	1.1
582 - 583	27.33	4.11	9.57	-21.81	5.05	0.40	81	866	159	119	3.4	1.8
587 - 588	25.30	4.05	9.65	-21.92	5.00	0.40	84	852	152	119	3.1	2.5
592 - 593	31.24	4.20	9.76	-21.81	5.03	0.40	84	866	157	120	2.1	1.6
597 - 598	26.65	3.90	9.69	-21.95	5.12	0.40	83	869	160	121	3.8	2.3
602 - 603	25.69	3.92	9.72	-22.32	5.06	0.39	81	872	154	123	3.8	0.7
607 - 608	31.42	3.40	9.87	-22.39	5.00	0.38	80	879	154	118	2.7	
612 - 613	29.59	4.32	9.40	-22.01	4.89	0.38	79	872	152	116	4.2	0.9
617 - 618	30.42	3.59	9.74	-21.98	4.84	0.39	80	872	159	122	4.3	2.3
622 - 623	33.79	3.42	9.99	-21.85	4.80	0.38	79	866	155	121	5.3	2.4
627 - 628	30.90	3.17	9.73	-21.90	4.88	0.38	80	883	154	120	4.6	2.5
632 - 633	30.73	3.81	9.77	-22.01	4.96	0.39	80	879	161	123	3.3	
637 - 638	29.40	3.63	9.83	-22.02	4.89	0.38	81	860	155	121	3.2	2.9
642 - 643	26.69	4.29	9.81	-22.06	5.06	0.39	82	879	155	126	3.2	1.7
647 - 648	30.92	3.77	10.28	-22.05	5.01	0.40	92	876	159	124	5.2	2.8
652 - 653	31.64	3.86	9.65	-22.08	5.27	0.40	85	833	162	127	5.0	3.2
657 - 658	29.57	3.59	10.17	-22.27	5.05	0.39	83	859	155	123	2.4	0.9
662 - 663	35.15	3.91	9.67	-21.99	4.98	0.39	80	859	154	122	3.3	2.8
667 - 668	35.36	3.84	10.02	-21.83	4.87	0.38	79	852	152	123	3.4	3.7
672 - 673	34.27	3.65	9.79	-21.94	4.77	0.39	79	859	153	123	6.1	2.6
677 - 678	34.45	4.44	9.53	-22.12	4.92	0.39	80	872	152	118	6.0	1.4
682 - 683	35.12	3.69	10.07	-21.91	4.20	0.39	81	875	153	119	5.9	1.0
687 - 688	30.69	3.53	10.14	-21.88	4.95	0.39	81	872	154	125	2.9	2.2

Appendix 4.3 (continued)

	Isotopic and biogeochemical data			Sedimentary	Inorganic geochemical data							
Sample depth (cm bsf)	Opal (wt%)	TOC (wt%)	C/N ratio	$\delta^{13}C$ (‰ VPDB)	Al (wt%)	Ti (wt%)	Zr (ppm)	Mn (ppm)	V (ppm)	Cr (ppm)	Mo (ppm)	U (ppm)
692 - 693	38.20	3.84	10.09	-22.01	4.28	0.40	82	875	154	123	3.0	2.3
697 - 698	30.78	3.35	10.59	-22.13	4.99	0.39	80	859	153	125	2.8	1.6
702 - 703	25.53	3.67	10.20	-22.29	4.93	0.39	79	839	157	124	3.2	3.0
707 - 708	30.35	3.41	10.25	-22.58	4.93	0.39	81	833	153	119	2.9	2.9
712 - 713	27.44	3.39	10.54	-22.16	4.98	0.39	80	846	158	123	2.6	2.9
717 - 718	33.43	3.62	10.10	-22.03	4.98	0.39	81	846	155	123	3.4	2.8
722 - 723	26.20	3.95	10.51	-22.26	4.73	0.38	77	826	154	120	4.9	2.0
727 - 728	30.83	3.42	10.60	-22.18	4.97	0.39	78	833	155	121	6.1	2.4
732 - 733	27.53	3.97	10.61	-22.26	4.69	0.38	77	833	149	117	2.9	1.9
737 - 738	29.40	3.73	10.23	-22.14	4.76	0.38	77	846	154	119	3.6	2.3
742 - 743	31.72	3.44	10.81	-22.18	4.82	0.38	79	852	151	120	3.5	2.3
747 - 748	31.36	3.49	10.70	-22.04	4.85	0.38	79	846	151	116	3.2	1.6
752 - 753	26.00	3.98	10.21	-22.37	4.79	0.39	79	846	154	121	2.3	1.1
757 - 758	19.91	4.17	9.98	-22.21	4.83	0.38	78	833	153	119	2.9	1.1
762 - 763	26.56	4.03	9.99	-22.31	4.76	0.38	80	833	152	121	2.8	0.7
767 - 768	30.29	4.10	10.12	-22.28	4.87	0.39	81	860	159	123	5.6	3.1
772 - 773	27.17	4.17	9.69	-22.23	4.81	0.38	81	852	152	124	2.6	1.4
777 - 778	30.29	4.09	9.72	-22.06	4.75	0.38	80	836	150	117	1.9	1.6
782 - 783	29.23	4.06	9.90	-22.04	4.77	0.38	80	844	153	122	2.9	1.8
787 - 788	28.36	4.01	10.02	-22.05	4.60	0.37	77	821	145	121	2.8	0.9
792 - 793	30.99	4.10	9.77	-21.87	4.67	0.38	80	821	151	117	2.8	2.0
797 - 798	29.60	4.01	9.97	-21.98	4.66	0.38	77	852	151	118	2.8	3.6
802 - 803	28.19	4.02	10.16	-22.10	4.86	0.38	80	883	154	123	4.0	2.0
807 - 808	26.50	3.89	9.85	-21.98	4.62	0.37	77	852	146	115	3.1	2.0
812 - 813	30.01	4.05	9.90	-22.05	4.71	0.38	79	860	152	118	2.9	2.6
817 - 818	27.24	3.92	10.04	-22.02	4.68	0.38	80	856	153	123	3.4	2.4
822 - 823	28.76	3.96	9.95	-21.97	4.52	0.38	79	840	148	122	3.6	1.5
827 - 828	27.60	3.96	9.95	-21.93	4.45	0.36	75	813	144	115	3.7	2.9
832 - 833	30.65	3.95	9.83	-21.80	4.63	0.36	76	829	149	118	3.0	3.5
837 - 838	27.45	4.27	9.84	-21.89	4.61	0.36	76	813	150	115	3.5	1.2
842 - 843	28.04	3.92	9.98	-21.93	4.78	0.38	80	852	155	124	2.5	2.7
847 - 848	27.78	3.68	10.02	-21.90	3.96	0.38	78	829	150	122	2.9	1.3
852 - 853	26.75	3.80	10.69	-22.12	4.61	0.38	79	836	152	123	3.5	1.3
857 - 858	24.25	3.68	10.39	-22.11	4.83	0.38	80	867	156	124	3.6	1.2
862 - 863	24.71	3.75	10.15	-21.96	4.93	0.39	80	883	154	120	3.8	2.2
867 - 868	26.28	3.83	10.13	-21.86	4.77	0.38	81	860	156	123	3.7	2.7
872 - 873	29.53	3.74	10.31	-21.89	4.96	0.39	82	891	160	124	4.9	3.2
877 - 878	24.44	3.87	10.56	-22.13	4.16	0.39	83	883	156	116	3.7	1.9
882 - 883	25.93	3.98	10.37	-22.01	3.92	0.37	79	867	152	118	4.2	2.4
887 - 888	35.32	3.58	10.00	-21.91	4.54	0.37	77	852	152	113	3.3	3.0
892 - 893	26.96	3.74	10.72	-21.89	4.57	0.39	83	852	157	126	2.9	2.9
897 - 898	25.87	3.77	10.74	-21.98	4.68	0.39	82	867	156	119	4.8	2.9
902 - 903	27.94	4.21	10.94	-22.18	4.41	0.36	76	829	152	116	4.5	1.6
907 - 908	25.85	3.96	10.00	-21.72	4.53	0.37	78	836	150	119	4.2	3.8
912 - 913	24.49	4.18	9.82	-21.93	4.77	0.39	80	875	159	125	5.5	2.6
917 - 918	24.71	4.61	10.62	-22.01	4.56	0.39	82	852	157	123	4.7	2.7
922 - 923	26.26	4.41	10.06	-22.10	4.64	0.39	80	860	154	124	5.6	2.8
927 - 928	28.24	4.18	10.40	-22.14	4.78	0.38	79	875	159	124	7.4	3.1
932 - 933	24.91	4.18	9.62	-21.83	5.00	0.40	82	883	160	128	7.4	1.6
937 - 938	24.72				4.81	0.41	84	891	164	134	6.5	3.4
942 - 943	27.62	3.69	10.42	-22.08	4.71	0.39	83	883	157	127	6.0	2.4
947 - 948	23.67	3.61	10.23	-22.05	4.83	0.40	84	883	161	124	5.6	2.7
952 - 953	27.65	4.24	10.34	-21.92	4.87	0.40	83	929	158	124	7.2	1.8
957 - 958	30.29	3.86	9.93	-21.99	4.70	0.39	81	875	153	125	6.9	2.8
962 - 963	29.38	4.10	9.86	-21.76	4.75	0.39	82	898	157	121	7.3	2.9
967 - 968	25.78	4.03	9.91	-21.83	4.57	0.37	78	852	150	122	8.7	4.2
972 - 973	27.04	4.08	9.98	-21.77	4.45	0.35	75	821	145	111	7.4	1.7
977 - 978	30.45	3.68	9.55	-22.02	4.38	0.35	74	829	145	109	6.5	2.5
982 - 983	27.47	3.67	9.23	-21.90	4.49	0.36	76	829	148	115	5.2	2.2
987 - 988	27.93	3.39	9.59	-22.13	4.59	0.38	78	860	152	123	4.2	1.3
992 - 993	27.81	4.01	9.52	-23.54	4.29	0.34	73	821	140	111	4.3	2.6
997 - 998	25.55	3.98	9.70	-22.16	4.45	0.36	73	829	146	111	4.8	4.0
1002 - 1003	24.28	4.15	10.22	-22.57	4.62	0.37	78	852	151	118	4.7	2.8
1007 - 1008	23.33	4.26	10.20	-22.66	4.85	0.39	82	898	157	126	3.9	1.8
1012 - 1013	23.43	4.19	10.28	-22.71	4.78	0.38	80	898	154	122	4.9	2.5
1017 - 1018	25.44	4.30	10.03	-22.62	5.09	0.41	85	929	157	130	4.7	0.7
1022 - 1023	28.62	4.28	10.07	-22.65	4.93	0.40	84	922	159	125	3.7	3.0
1027 - 1028	29.39	4.30	9.92	-22.57	4.88	0.40	85	883	155	129	3.5	2.5
1032 - 1033	26.21	4.26	9.79	-22.33	4.78	0.39	82	867	155	125	3.6	3.2

Appendix 4.3 (continued)

	Isotopic and biogeochemical data			Sedimentary δ¹³C (‰ VPDB)	Inorganic geochemical data							
Sample depth (cm bsf)	Opal (wt%)	TOC (wt%)	C/N ratio	$\delta^{13}C$ (‰ VPDB)	Al (wt%)	Ti (wt%)	Zr (ppm)	Mn (ppm)	V (ppm)	Cr (ppm)	Mo (ppm)	U (ppm)
1037 - 1038	25.06	4.31	10.19	-21.97	4.65	0.38	81	852	148	123	3.1	2.8
1042 - 1043	29.69	4.35	9.82	-22.08	4.73	0.39	82	867	153	130	3.5	2.3
1047 - 1048	26.55	4.13	9.97	-22.31	4.77	0.39	81	875	154	124	3.7	3.2
1052 - 1053	29.81	4.29	9.78	-22.33	4.69	0.39	83	875	150	121	3.0	2.4
1057 - 1058	26.04	4.12	9.84	-21.87	4.59	0.38	81	893	152	124	3.0	2.9
1062 - 1053	24.41	4.19	9.87	-21.78	4.65	0.38	80	906	152	124	2.3	2.2
1067 - 1068	29.28	4.05	10.09	-21.88	4.68	0.39	83	883	154	127	4.1	1.5
1072 - 1073	23.27	3.89	10.09	-21.97	4.63	0.38	82	883	151	121	4.5	1.2
1077 - 1078	24.82	3.98	10.00	-21.91	4.77	0.39	80	860	151	118	4.9	1.7
1082 - 1083	23.74	3.97	10.09	-21.84	4.81	0.39	82	867	154	121	4.9	3.5
1087 - 1088	25.98	4.03	10.18	-22.04	5.06	0.40	84	898	157	128	4.5	4.2
1092 - 1093	24.19	4.06	9.81	-21.93	5.10	0.41	85	906	165	129	4.1	3.2
1097 - 1098	22.51	3.68	10.10	-21.97	5.02	0.40	84	898	158	129	3.8	2.6
1102 - 1103	27.44	3.74	10.10	-22.01	4.94	0.40	83	891	162	127	4.2	3.5
1107 - 1108	28.93	3.72	10.17	-22.10	4.95	0.40	83	906	158	124	3.5	2.5
1112 - 1113	27.80	3.64	10.24	-22.00	4.99	0.40	83	898	158	120	3.0	2.4
1117 - 1118	31.60	3.46	10.28	-22.04	4.93	0.39	83	898	156	124	3.5	2.6
1122 - 1123	26.59	3.62	10.23	-21.99	4.78	0.39	80	891	155	124	6.3	3.2
1127 - 1128	26.45	3.73	10.35	-21.92	4.72	0.39	80	906	151	119	5.0	2.2
1132 - 1133	28.56	3.84	10.30	-21.90	4.64	0.37	77	902	149	120	4.3	2.2
1137 - 1138	28.62	3.65	10.27	-22.01	4.62	0.37	77	906	152	120	6.4	1.8
1142 - 1143	26.83	3.98	9.93	-22.04	4.86	0.40	82	937	158	130	7.1	3.4
1147 - 1148	29.85	4.05	9.83	-22.11	4.70	0.38	78	891	150	129	6.1	3.0
1152 - 1153	24.54	3.88	10.08	-21.93	4.67	0.38	79	879	148	121	6.0	3.7
1157 - 1158	25.35	3.80	10.20	-22.08	4.85	0.39	80	914	156	124	6.0	3.4
1162 - 1163	25.51	3.84	10.02	-21.90	4.76	0.39	80	906	153	127	3.8	2.6
1167 - 1168	25.87	3.70	10.22	-22.03	4.68	0.38	80	883	147	115	3.5	2.7
1172 - 1173	27.51	3.81	9.96	-21.74	4.56	0.37	79	860	142	113	3.9	1.7
1177 - 1178	24.28	3.89	9.99	-21.76	4.89	0.39	82	922	153	121	4.3	1.7
1182 - 1183	27.12	3.86	9.90	-21.78	4.87	0.39	83	914	151	124	4.3	2.1
1187 - 1188	28.73	4.09	8.72	-21.12	4.87	0.40	82	937	153	128	3.2	2.1
1194 - 1195	27.18	3.86	10.21	-22.05	4.74	0.39	79	922	148	124	4.0	2.0
1197 - 1198	30.33	3.93	10.06	-21.84	4.71	0.38	78	898	151	121	4.2	1.4
1202 - 1203	29.85	4.05	10.05	-21.79	4.63	0.40	80	945	148	127	6.3	2.0
1207 - 1208	32.20	4.05	10.00	-21.91	4.56	0.38	79	898	149	118	6.0	2.7
1217 - 1218	27.66	3.85	9.75	-21.84	4.64	0.38	79	891	148	119	4.6	3.2
1222 - 1223	25.41	3.91	10.14	-22.15	4.60	0.38	78	891	147	120	5.8	2.2
1227 - 1228	23.36	3.91	10.21	-22.22	4.47	0.36	77	860	139	118	4.2	3.1
1232 - 1233	24.18	3.95	10.10	-22.16	4.73	0.39	81	906	147	118	5.1	4.4
1237 - 1238		3.92	10.25	-21.80	4.63	0.39	81	898	147	118	3.5	1.9
1242 - 1243	26.80	3.73	10.27	-21.88	4.74	0.40	81	914	150	120	4.7	1.7
1247 - 1248	26.64	3.83	10.22	-21.91	4.83	0.40	85	937	151	125	3.3	1.2
1252 - 1253	25.22	3.98	10.39	-21.96	4.87	0.40	85	968	155	127	3.4	1.9
1257 - 1258	22.64	4.17	10.17	-22.68	4.79	0.40	82	937	151	122	5.1	2.8
1262 - 1263	22.16	4.07	10.25	-22.41	4.84	0.40	84	1022	154	125	4.7	2.4
1267 - 1268	23.38	3.94	10.43	-22.21	4.73	0.40	81	937	153	124	4.4	2.7
1272 - 1273	28.63	4.23	9.71	-21.91	4.68	0.39	80	991	148	120	4.3	2.0
1277 - 1278	28.45	3.95	9.97	-21.88	4.88	0.41	87	922	156	128	4.1	1.9
1282 - 1283	27.02	4.12	9.57	-21.73	4.92	0.41	88	922	154	127	4.0	2.7
1287 - 1288	26.74	3.93	10.02	-22.07	4.59	0.38	80	898	143	119	2.7	3.3
1292 - 1293	24.22	3.96	9.88	-21.92	4.77	0.40	83	929	148	121	4.0	1.9
1297 - 1298	24.11	3.91	9.94	-21.92	4.90	0.40	84	922	155	121	3.8	1.3
1302 - 1303	23.94	3.77	10.10	-21.84	4.93	0.40	84	929	151	124	3.2	2.6
1307 - 1308	26.58	3.95	10.10	-22.09	4.72	0.39	83	898	150	121	3.6	1.6
1312 - 1313	25.59	3.88	10.04	-21.95	4.93	0.41	87	929	155	128	3.3	1.5
1317 - 1318	22.35	3.91	10.13	-22.13	4.87	0.41	85	945	154	128	3.5	1.6
1322 - 1323	22.42	4.11	9.91	-21.97	4.85	0.40	83	914	152	127	2.9	2.1
1327 - 1328	24.87	3.61	10.53	-22.11	4.89	0.41	86	914	152	126	3.2	1.4
1332 - 1333	24.05	3.61	10.44	-22.22	4.94	0.41	85	905	156	131	3.2	1.7
1337 - 1338	19.82	3.95	10.35	-22.21	4.97	0.41	86	937	155	124	3.9	1.9
1342 - 1343	20.38	3.74	10.68	-21.99	5.06	0.42	89	945	159	141	3.1	2.4
1347 - 1348	25.36	4.12	10.21	-22.16	5.16	0.43	91	953	159	134	3.6	2.1
1352 - 1353	24.81	4.00	10.00	-22.14	5.11	0.43	91	937	156	135	3.4	1.9
1357 - 1358	20.72	4.24	9.92	-22.11	5.29	0.43	91	953	160	131	4.2	1.1
1362 - 1363	24.38	3.99	9.78	-21.68	5.09	0.42	90	929	156	131	4.6	4.0
1367 - 1368	23.90	3.93	10.28	-22.10	5.20	0.42	88	960	163	131	4.8	1.7
1372 - 1373	25.36	4.02	9.86	-21.64	5.26	0.43	91	960	161	130	5.8	3.1
1377 - 1378	24.23	4.03	10.15	-22.18	5.00	0.42	90	922	156	131	3.8	2.3
1382 - 1383	25.72	4.05	9.75	-21.89	4.99	0.41	87	929	157	133	4.7	3.3

Appendix 4.3 (continued)

	Isotopic and biogeochemical data				Inorganic geochemical data							
Sample depth (cm bsf)	Opal (wt%)	TOC (wt%)	C/N ratio	δ13C (‰, VPDB)	Al (wt%)	Ti (wt%)	Zr (ppm)	Mn (ppm)	V (ppm)	Cr (ppm)	Mo (ppm)	U (ppm)
1387 - 1388	23.29	4.04	10.07	-21.99	5.11	0.41	87	937	153	132	4.3	1.7
1392 - 1393	22.51	4.10	10.31	-22.67	5.08	0.42	87	937	154	133	4.2	4.0
1397 - 1398	21.59	3.91	10 36	-22.78	4.81	0.40	83	891	148	127	6.2	2.8
1402 - 1403	27 06	3.75	10.33	-22.22	4.81	0.40	83	953	151	124	4.5	2.7
1407 - 1408	26.59	3.88	10.27	-22.25	5.03	0.41	85	968	157	125	6.3	2.0
1412 - 1413	24.62	3.80	10.20	-22.12	4.64	0.41	84	945	159	134	6.2	4.4
1417 - 1418	23.59	3.83	10.22	-22.05	4.74	0.39	80	914	143	127	5.9	3.4
1422 - 1423	27.19	3.95	9.87	-21.86	4.77	0.40	84	914	151	126	5.2	2.3
1427 - 1428	29.85	3.98	9.92	-21.90	4 95	0.41	84	929	153	123	3.7	3 0
1432 - 1433	24.40	4.16	9.89	-21.92	5.01	0.42	89	960	153	131	3.2	2.0
1437 - 1438	22.22	4.12	9.97	-21.93	4.78	0.40	85	914	150	131	3.2	1.6
1442 - 1443	24.58	3.89	10.01	-22.02	4.81	0.40	83	898	146	124	2.0	2.1
1447 - 1448	29.77	4 03	9 92	-21.80	4 88	0.41	84	914	148	129	3.4	1 6
1452 - 1453	35.82	3.95	9.67	-21.76	4.82	0.40	85	898	147	128	3.2	1.7
1457 - 1458	33.36	4 00	9 79	-21.91	4 33	0.40	86	906	154	136	2.4	2 2
1462 - 1463	28.87	3.96	9.75	-21.77	4.45	0.40	86	898	148	130	4.4	2.4
1467 - 1468	25.96	3.85	9.87	-22.07	3 87	0.34	74	798	129	112	2.7	1.9
1472 - 1473	26.22	3.85	10.06	-21.98	4.28	0.37	76	844	139	125	3.7	2.0
1477 - 1478	27.82	4.13	10 15	-22.19	4.43	0.38	80	844	144	127	5.0	2.5
1482 - 1483	25.65	3.67	10.13	-21.89	4 28	0.37	78	813	134	121	3.8	1.3
1487 - 1488	28.06	3.94	9.81	-21.85	4.58	0.39	83	883	146	125	3.4	1.3
1492 - 1493	24.41	4.13	10.00	-22.03	4.65	0.42	88	883	151	136	2.9	1.9
1497 - 1498	24.08	4.00	9.92	-21.88	4.84	0.41	85	960	149	131	3.2	2.3
1502 - 1503	24.86	3.96	9.95	-21.95	4.72	0.40	84	883	152	132	2.6	2 3
1507 - 1508	28.44	4.27	10.02	-22.12	4.77	0.41	87	906	153	135	3.3	2.7
1512 - 1513	28.13	4.07	9.77	-21.85	4.70	0.40	84	906	149	123	2.6	3.5
1517 - 1518	28.17	4.26	10.02	-22.67	4.71	0.41	86	906	149	134	2.8	1 2
1522 - 1523	28.61	3.82	10.14	-22.49	4.78	0.40	86	906	149	128	2.8	1.4
1527 - 1528	30.85	4.31	9.99	-22.34	4.70	0.40	85	898	145	129	3.0	2.1
1532 - 1533	28.19	4.16	10.12	-22.34	4.49	0.38	80	883	140	118	5.0	2.2
1537 - 1538	29.33	3.93	9.79	-21.34	4.39	0.37	80	852	138	116	4.7	3 9
1542 - 1543	27.65	4.18	10.17	-21.93	4 21	0.37	78	867	136	116	5.3	1 5
1547 - 1548	27.18	4.01	9.94	-21.54	4.27	0.36	79	867	138	113	5.3	1.1
1552 - 1553	26.79	4.13	10.25	-22.07	4.37	0.37	79	860	137	119	5.0	3.6
1557 - 1558	29.69	4.10	9.78	-21.35	4.51	0.39	85	883	143	123	4.0	2 0
1562 - 1563	28.45	4 26	9.90	-21.66	4.56	0.40	85	891	142	125	3.3	1.1
1567 - 1568	26.76	4.07	9.79	-21.40	4.57	0.40	85	906	145	130	3.2	1.3
1572 - 1573	24.46	4.19	10.20	-21.93	4.38	0.40	84	898	144	127	3.3	2.7
1577 - 1578	27.97	4.23	10.27	-21.66	4.43	0.39	84	883	144	121	3.3	2.0
1582 - 1583	22 93	4.04	9 92	-21.52	4.68	0.41	86	914	151	125	4.0	2 2
1587 - 1588	28.71	4.15	10.11	-21.99	4.65	0.40	85	875	144	124	4.8	2.6
1592 - 1593	26.10	3.83	10.10	-22.06	4.63	0.40	85	898	144	129	4.4	2.8
1597 - 1598	25.64	3.76	10.27	-22.25	4.64	0.41	86	883	146	133	4.6	2.1
1602 - 1603	21.53	3.75	10 17	-22.27	4 44	0.39	83	860	144	119	4.1	1.9
1607 - 1608	22.03	3.61	10.27	-22.20	4.67	0.40	87	898	148	134	4.3	2.8
1612 - 1613	17.29	3.44	10.61	-22 57	4 89	0.42	90	937	157	139	3.5	3.4
1617 - 1618	17.98	3.29	10.84	-22.70	4.94	0.43	91	945	156	140	2.9	3.0
1622 - 1623	22.10	3.63	10 46	-22.31	5.09	0.44	93	953	167	141	3.1	1.4
1627 - 1628	30.10	5.04	12.87	-23.94	5.34	0.47	98	1022	171	155	2.8	0.9
1632 - 1633	27.76	3.99	10.06	-21.80	5.38	0.48	99	1038	175	158	2.9	3.2
1637 - 1638	29.79	3.84	10.05	-21.87	4.93	0.44	95	953	158	140	3.6	2.1
1642 - 1643	27.49	3.99	10.06	-21.81	4.39	0.38	80	883	143	127	4.0	
1647 - 1648	27.18	4.09	10.27	-22.49	4.35	0.38	81	883	137	125	3.8	2.1
1652 - 1653	32.61	4.03	9.82	-21.59	4 43	0.37	79	883	135	126	3.3	2.0
1657 - 1658	29.07	4 04	9.94	-21.53	4.42	0.38	79	898	142	123	3 8	
1662 - 1663	25.57	3.85	9 86	-21.44	4.45	0.38	81	883	137	120	3.4	2.3
1667 - 1668	26.96	3.98	9.93	-21.35	4.57	0.39	83	883	140	128	3.9	2.4
1672 - 1673	32.04	3.91	9.92	-21.67	4.58	0.39	83	898	140	129	4.7	2 2
1677 - 1678	25.44	3.58	9 88	-22.10	4.64	0.39	83	875	139	125	3.2	1 1
1682 - 1683	32.70	3.81	9.67	-21.89	4.72	0.40	86	891	144	129	3.6	1 7
1687 - 1688	35 59	4.06	10 00	-22 12	4.63	0.39	83	860	141	127	3.7	1 9
1692 - 1693	27.76	3.97	9 91	-22.13	4.59	0.39	87	844	135	121	3 2	1.7
1697 - 1698	31.85	3.70	9.70	-21.93	4.60	0.39	83	891	138	126	4.3	1.5
1702 - 1703	29 87	3.85	9.68	-21.79	4.59	0.40	86	898	148	129	3.6	1.8
1707 - 1708	27.75	3.60	9.70	-22.07	4.12	0.39	83	875	145	128	2 6	3.1
1712 - 1713	32.29	3.68	9.66	-21.92	4 27	0.40	87	875	143	126	4.0	2 6
1717 - 1718	33.93	3.91	9.87	-22.50	4.22	0.39	86	883	144	129	3.9	3.7
1722 - 1723	35.53	4.05	10.23	-22.83	4.59	0.38	83	860	138	122	4.1	2.9
1727 - 1728	31.32	3.91	9.65	-21.96	4.48	0.38	81	875	136	120	3 4	1.7

Appendix 4.3 (continued)

| | Isotopic and biogeochemical data | | | Sedimentary | Inorganic geochemical data | | | | | | | |
Sample depth (cm bsf)	Opal (wt%)	TOC (wt%)	C/N ratio	δ¹³C (‰ VPDB)	Al (wt%)	Ti (wt%)	Zr (ppm)	Mn (ppm)	V (ppm)	Cr (ppm)	Mo (ppm)	U (ppm)
1732 - 1733	29.68	3.98	9.64	-21.83	4.35	0.37	80	844	136	115	3.4	3 1
1737 - 1738	31.06	4.05	9.87	-22.26	3.95	0.38	82	875	142	119	3.6	1.7
1742 - 1743	30.52	3.98	9.95	-22.31	3.92	0.38	82	852	135	118	3.6	2.6
1747 - 1748	37.45	4.02	9.76	-22.14	4.12	0.39	84	891	144	117	4.1	1.9
1752 - 1753	27.89	3.72	9.77	-22.10	4.13	0.39	85	898	145	119	5.5	1.8
1757 - 1758	28.35	3.97	11.13	-23.03	4.14	0.40	87	914	147	122	4.6	1.0
1762 - 1763	32.54	3.95	10.08	-21.49	4.22	0.39	84	883	145	118	4.0	1 6
1767 - 1768	34.36	3.79	9.65	-21.31	4.25	0.39	86	922	142	124	3.8	0.8
1772 - 1773	30.73	4.09	9.83	-21.38	4.20	0.38	85	898	144	120	3.8	2.9
1777 - 1778	30.06	4.09	9.99	-22.00	4.18	0.39	84	898	144	129	3.1	2 4
1782 - 1783	29.30	4.10	9.96	-22.01	4.08	0.39	84	898	138	119	3 2	
1787 - 1788	29.90	4.08	10.07	-21.93	4.26	0.40	87	922	148	122	3.5	1.1
1792 - 1793	24.89	3.84	10.12	-21.97	4.14	0.40	87	891	144	125	3.7	1.3
1797 - 1798	30.64	3.94	9.94	-21.98	4.31	0.40	88	898	149	126	3.0	1 9
1802 - 1803	25.90	3.96	9.99	-22.37	4.25	0.40	88	891	147	126	4.0	1.8
1807 - 1808	30.59	3.84	10.12	-22.32	4.14	0.38	87	852	143	124	3.4	0.9
1812 - 1813	30.78	3.86	9.92	-22.31	4.04	0.38	81	852	138	115	4.6	1.7
1817 - 1818	29.53	4.00	9.90	-22.40	4.07	0.37	81	891	139	113	5.5	2.6

Appendix 4.4 EW0408-44JC biogeochemical data. Sample depths corrected for gas expansion and overlap with EW0408-43MC as described in the text.

Corrected sample depth (cm bsf)	Opal (wt%)	TOC (wt%)	C/N ratio	Sedimentary $\delta^{13}C$ (‰, VPDB)	Corrected sample depth (cm bsf)	Opal (wt%)	TOC (wt%)	C/N ratio	Sedimentary $\delta^{13}C$ (‰, VPDB)
25 - 26	68.75	8.27	9.15	-21.21	575 - 576	62.59	8.84	8.45	-20.66
27 - 28	60.77	8.54	5.95	-22.12	593 - 594	51.74	9.38	9.80	-21.88
33 - 34	60.42	8.89	9.17	-21.28	600 - 601	70.15	8.91	9.00	-20.95
37 - 38	63.68	9.52	8.71	-20.62	608 - 609	70.14	9.00	9.24	-21.09
42 - 43	64.02	8.30	8.30	-20.25	626 - 627	60.87	9.82	10.62	-22.10
43 - 44	64.65	8.90	8.97	-21.31	645 - 646	68.75	9.17	8.60	-20.74
46 - 47	60.41	9.40	9.54	-21.57	663 - 664	57.92	9.13	9.09	-21.34
51 - 52	54.83	10.09	9.07	-20.77	679 - 680	64.74	9.07	8.94	-20.86
52 - 53	52.88	9.78	9.82	-22.15	695 - 696	67.08	8.75	8.67	-20.80
55 - 56	53.70	9.19	9.54	-21.19	705 - 706	71.13	8.10	9.38	-21.32
58 - 59	54.86	9.99	9.19	-20.61	720 - 721	34.69	12.02	18.55	-24.67
62 - 63	57.11	9.29	9.33	-21.88	729 - 730	74.78	7.57	8.84	-20.97
63 - 64	58.74	8.88	9.05	-20.72	749 - 750	64.67	8.20	9.31	-21.40
67 - 68	61.82	9.63	8.93	-20.60	769 - 770	84.57	6.72	7.82	-19.91
72 - 73	71.68	7.71	8.21	-19.79	789 - 790	21.20	16.44	28.80	-26.05
75 - 76	65.73	8.78	8.96	-20.69	809 - 810	64.87	8.18	9.78	-21.57
79 - 80	60.28	9.60	8.90	-21.41	829 - 830	63.46	9.42	9.72	-21.32
80 - 81	61.41	8.74	8.73	-20.54	849 - 850	76.54	8.53	9.23	-21.12
84 - 85	66.14	7.98	8.80	-20.56	859 - 860	73.39	7.32	8.56	-21.03
89 - 90	73.72	7.73	8.50	-20.07	869 - 870	65.42	7.56	8.92	-21.36
92 - 93	64.73	8.89	8.71	-20.27	889 - 890	65.17	8.42	9.07	-21.19
96 - 97	69.21	7.98	8.71	-20.49	909 - 910	61.58	8.87	9.59	-21.53
97 - 98	63.98	9.02	8.86	-20.89	929 - 930	64.88	8.07	9.21	-21.35
101 - 102	62.13	9.05	9.02	-20.62	949 - 950	67.85	8.19	9.27	-21.46
105 - 106	66.04	8.52	8.63	-20.27	969 - 970	74.56	8.18	8.97	-20.94
110 - 111	58.72	8.19	9.14	-20.85	986 - 987	66.39	8.34	9.24	-21.53
114 - 115	68.21	7.82	9.10	-21.56	992 - 993	68.72	8.31	8.89	-21.22
115 - 116	57.89	7.98	9.03	-20.78	1002 - 1003	70.83	8.82	9.38	-21.72
120 - 121	70.35	7.31	8.65	-20.44	1022 - 1023	60.76	9.58	9.90	-22.19
125 - 126	63.19	8.15	9.20	-21.05	1042 - 1043	63.87	8.89	9.37	-21.58
130 - 131	63.25	8.48	9.02	-20.65	1062 - 1063	69.38	8.34	9.08	-21.80
134 - 135	67.19	7.97	9.09	-21.47	1077 - 1078	59.25	8.72	9.65	-21.83
135 - 136	70.72	7.55	8.71	-20.77	1097 - 1098	67.30	8.99	9.57	-21.73
140 - 141	72.27	7.55	8.61	-20.41	1117 - 1118	64.27	8.26	9.42	-21.62
141 - 142	62.20	8.94	8.77	-21.49	1124 - 1125	70.92	7.49	8.80	-21.10
148 - 149	55.34	9.75	9.42	-21.94	1130 - 1131	71.28	7.83	9.11	-21.33
157 - 158	55.42	9.69	9.05	-21.46	1148 - 1149	56.59	8.35	9.79	-22.07
169 - 170	68.18	9.17	8.84	-21.23	1168 - 1169	48.70	8.22	10.38	-22.32
185 - 186	68.59	8.61	9.25	-21.49	1188 - 1189	62.68	8.04	9.94	-22.01
202 - 203	73.99	8.40	8.87	-21.09	1206 - 1207	59.54	9.41	9.52	-21.39
211 - 212	58.24	9.82	9.26	-21.81	1227 - 1228	83.96	5.94	8.77	-20.83
217 - 218	62.94	8.67	9.12	-21.73	1246 - 1247	60.94	8.07	9.15	-21.44
229 - 230	63.85	8.97	9.01	-21.66	1266 - 1267	69.53	7.77	8.96	-20.81
239 - 240	57.12	8.40	8.82	-21.30	1270 - 1271	60.35	7.55	9.25	-21.09
257 - 258	62.01	9.02	9.03	-21.66	1280 - 1281	61.74	7.77	8.53	-20.86
275 - 276	56.28	9.64	9.32	-21.64	1300 - 1301	78.05	6.65	9.34	-20.91
280 - 281	61.72	9.12	9.09	-21.49	1320 - 1321	59.03	7.75	9.05	-20.92
300 - 301	59.96	9.30	9.11	-21.87	1339 - 1340	58.19	6.92	9.87	-21.61
320 - 321	58.43	9.95	8.95	-21.66	1358 - 1359	62.22	6.35	8.95	-20.63
340 - 341	60.80	9.33	9.80	-21.58	1378 - 1379	61.64	7.32	9.20	-20.70
360 - 361	58.74	9.87	9.95	-22.19	1398 - 1399	58.84	8.55	10.34	-21.83
371 - 372	45.58	11.55	11.35	-23.28	1401 - 1402	38.47	11.24	14.70	-23.99
378 - 379	62.79	9.56	8.64	-21.38	1413 - 1414	60.25	6.76	9.24	-20.97
398 - 399	54.04	8.42	8.84	-21.25	1419 - 1420	69.24	7.19	8.95	-20.64
418 - 419	68.71	8.46	8.33	-20.61	1439 - 1440	74.89	6.50	9.03	-20.48
438 - 439	55.50	8.72	9.72	-21.87	1459 - 1460	71.77	7.32	9.03	-20.72
458 - 459	72.99	7.40	8.50	-20.47	1478 - 1479	59.42	6.63	9.42	-21.34
473 - 474	78.22	7.36	8.35	-20.40	1494 - 1495	63.65	7.36	9.89	-21.27
476 - 477	77.51	7.16	8.56	-20.48	1507 - 1508	60.22	7.76	9.81	-21.62
485 - 486	67.14	7.83	8.50	-20.70	1526 - 1527	68.63	7.14	10.35	-21.37
495 - 496	60.90	8.62	8.64	-21.07	1546 - 1547	82.32	6.29	8.78	-20.33
515 - 516	76.44	6.94	8.52	-20.80	1550 - 1551	69.25	6.66	9.54	-20.76
535 - 536	64.48	8.87	9.26	-21.46	1554 - 1555	73.97	6.76	9.35	-20.50
555 - 556	70.00	8.82	9.24	-21.12	1557 - 1558	69.07	7.33	8.53	-20.76

Appendix 4.5: EW0408-11JC downcore productivity proxies.

EW0408-11JC
(Gulf of
Esquibel)

Bulk MAR (g/cm²/yr)

Opal (wt%)

TOC (wt%)

C/N ratio

Sedimentary δ¹³C$_{V-PDB}$ (‰)

Calibrated yrs BP

Olive gray
silty clay
with faint
laminations

Bioturbated
massive
dark gray
silty clay

Color
stratified
silty clay
with
dropstones

• AMS ¹⁴C
dates

····· bulk MAR

— bulk MAR
(linear
sed rate)

Core depth (cm bsf)
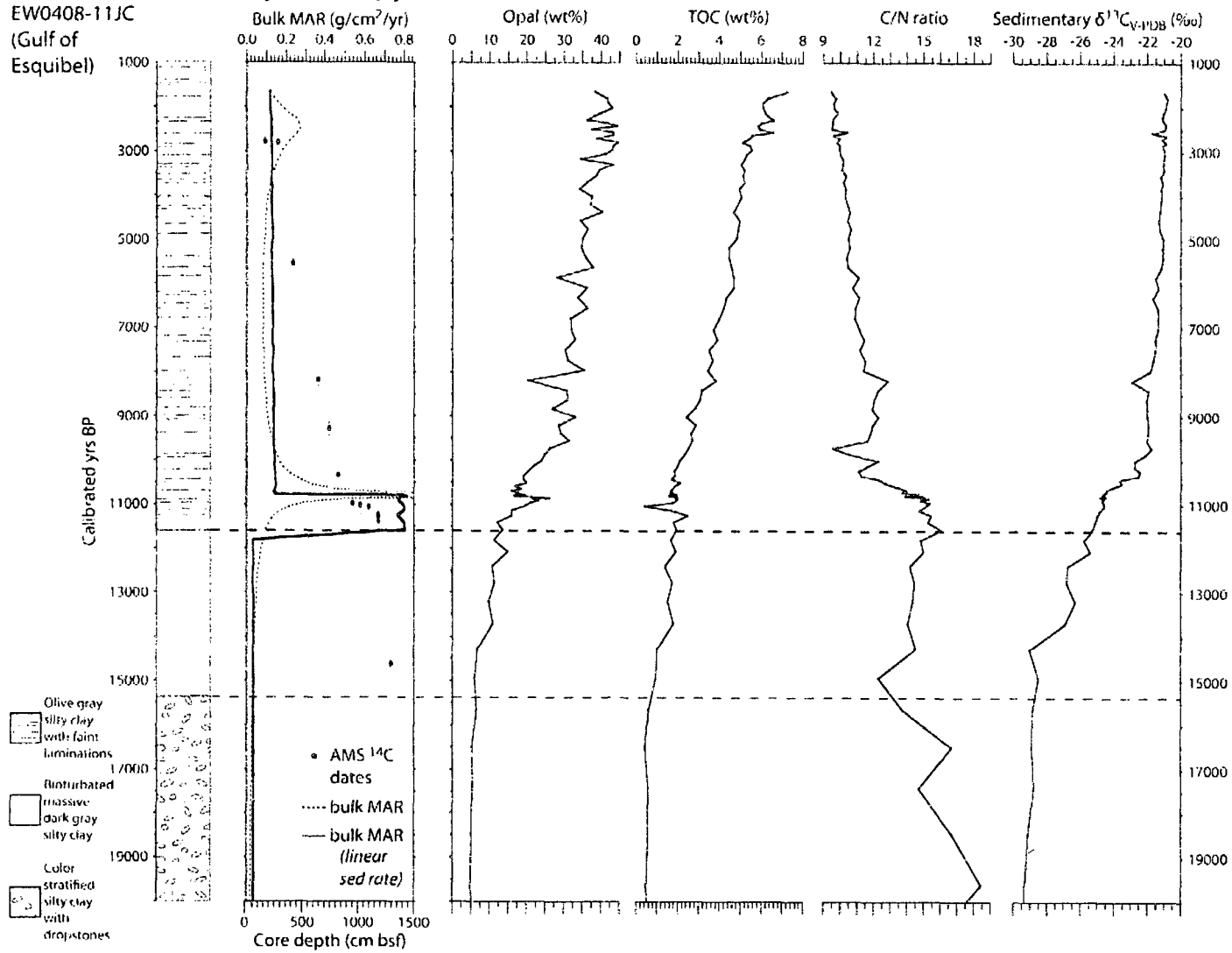
Appendix 4.6: EW0408-22JC downcore productivity proxies.

EW0408-22JC
(West Crawfish Inlet)

Note: Core is single lithology, composed of massive olive gray silty clay

Bulk MAR (g/cm²/yr)

Opal (wt%)

Calibrated yrs BP

Core depth (cm bsf)

- AMS ¹⁴C dates
— Quadratic age model
— bulk MAR

TOC (wt%) C/N ratio Sedimentary δ¹³C_V-PDB (‰)

160
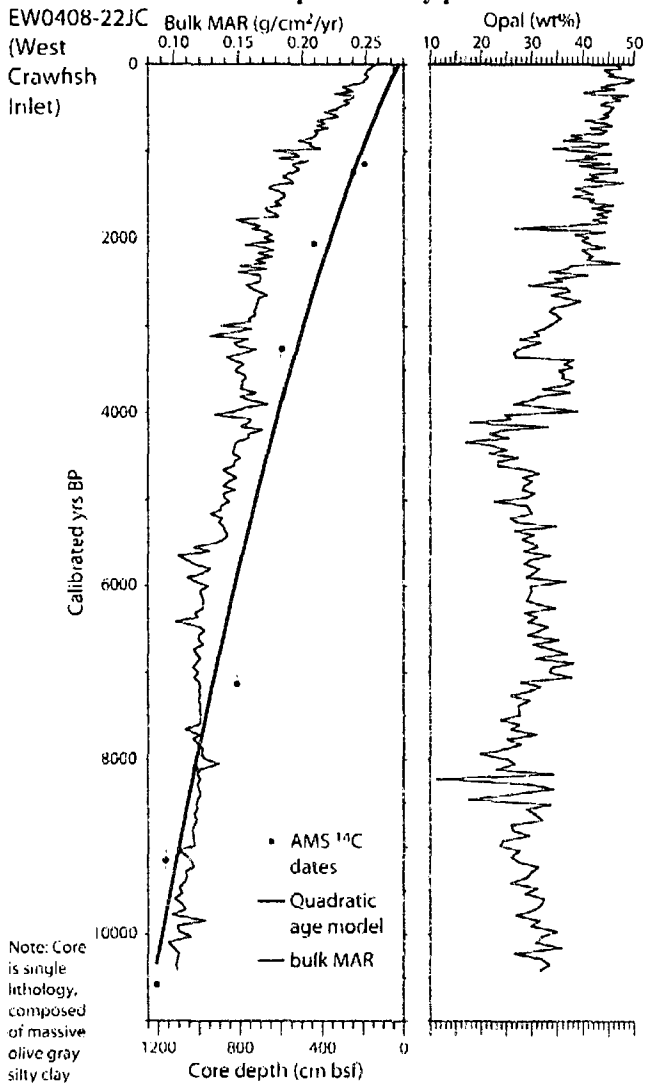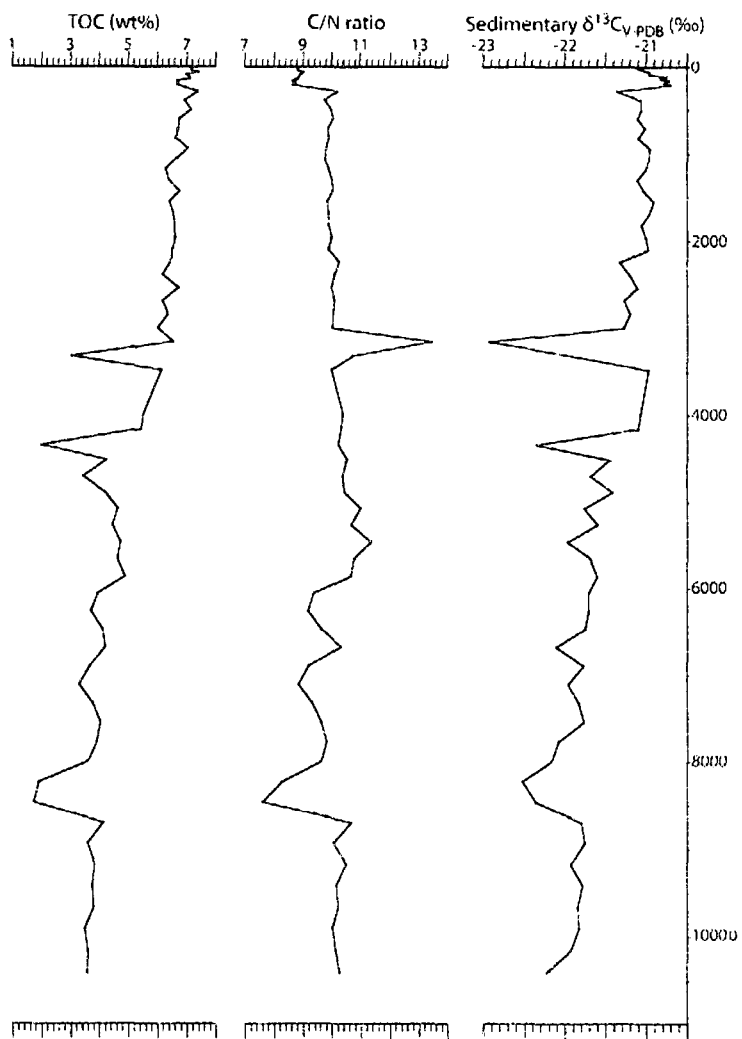
Appendix 4.7: EW0408-33JC downcore productivity proxies.

EW0408-33JC
(Katlian Bay)

Bulk MAR (g/cm²/yr)

Opal (wt%)

Calibrated yrs BP

Core depth (cm bsf)

- AMS ¹⁴C dates
— Linear age model
— bulk MAR

Note: Core is single lithology, a massive olive gray silty clay

161
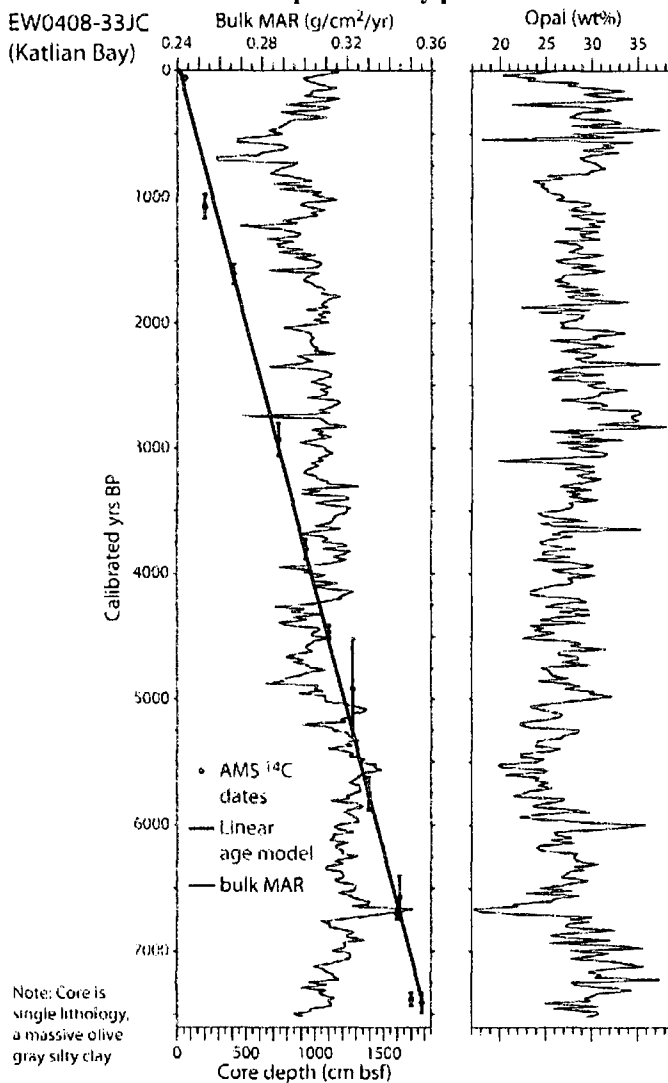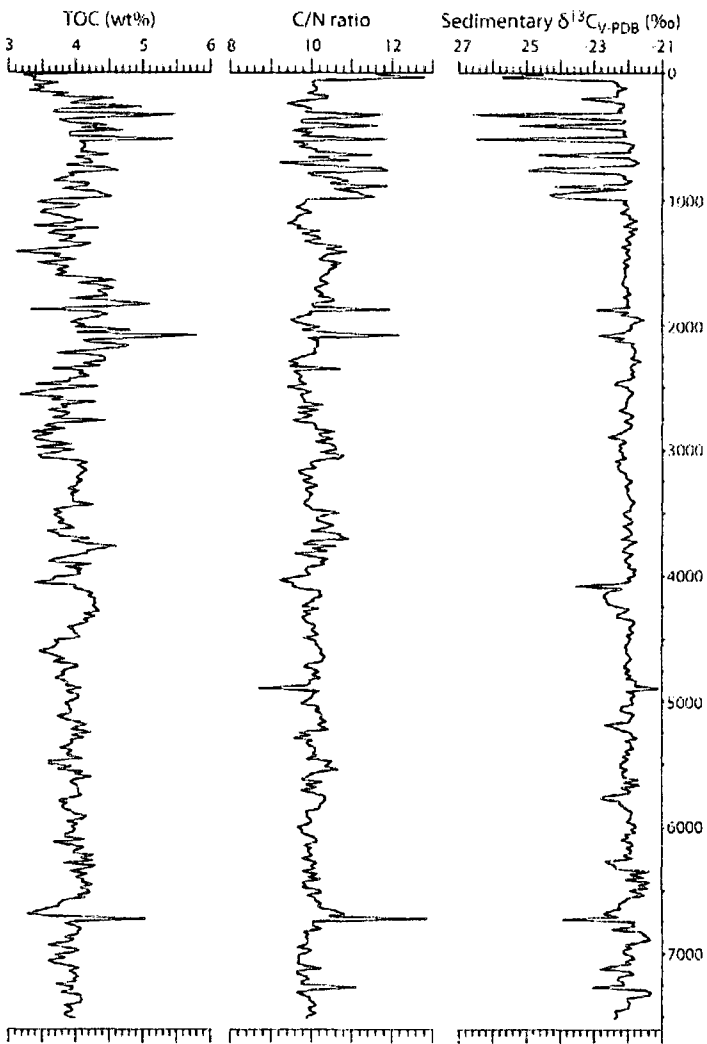
Appendix 4.8: EW0408-44JC downcore productivity proxies.
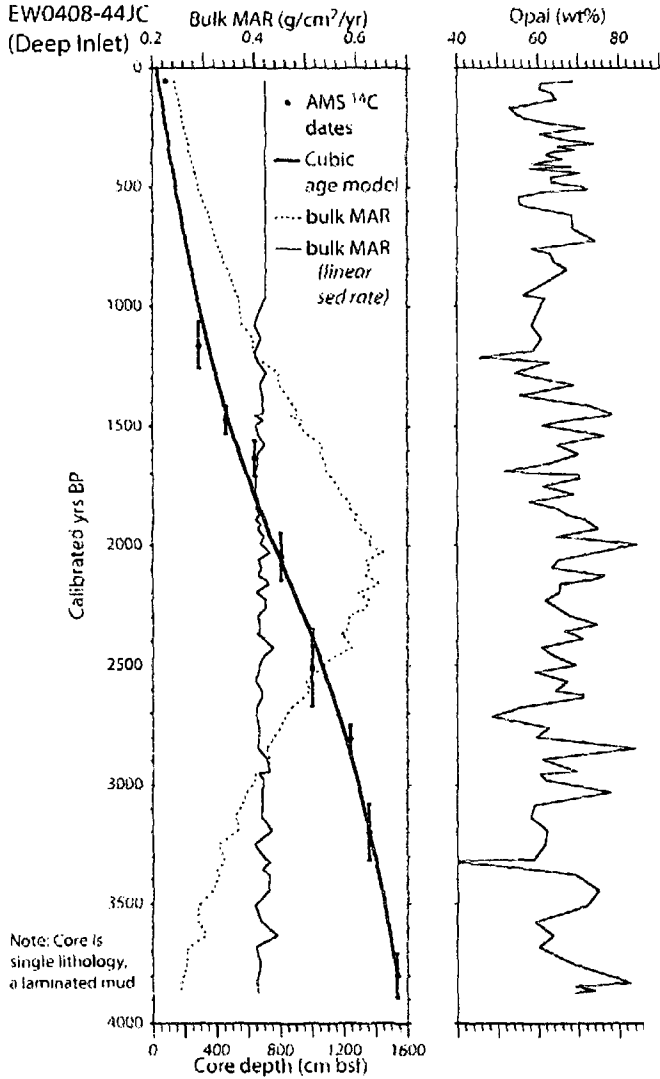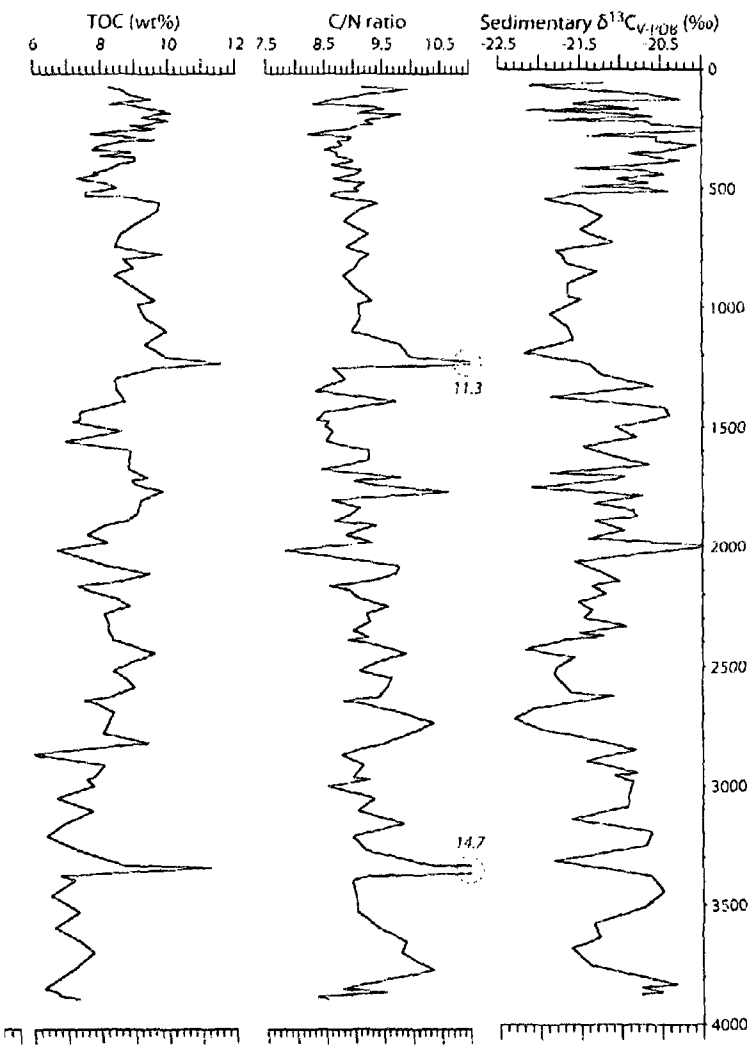
TOC (wt%)

C/N ratio

Sedimentary δ¹³C_V-PDB (‰)

11.3

14.7

162

Chapter 5 Decoupling of the coastal marine ecosystem and glaciomarine Cordilleran Ice Sheet dynamics in the Gulf of Alaska during the Last Glacial Maximum/Holocene transition[1]

5.1 Abstract

Environmental conditions in the Subarctic Northeast Pacific Ocean (SNPO) are an important component of North American climate patterns, as well as a potential driver of Northern Hemisphere climate variability. The SNPO is also the terminus of modern global thermohaline circulation. Paleoceanographic records from the SNPO thus have the potential to preserve detailed evidence of both climate forcing and response on regional and global scales. Paleoproductivity, biogeochemical, and mineralogical data are presented from a well-dated, high-resolution jumbo piston core (EW0408-85JC) recovered from the northern Gulf of Alaska continental slope at 682 m water depth. Holocene productivity proxies are consistently higher than those of the Last Glacial Maximum (LGM) and the Younger Dryas, with maxima associated with the deglacial Bølling-Allerød (B-A) and the early Holocene Preboreal Oscillation. The B-A interval is laminated, and enrichments of redox-sensitive elements are present, suggesting productivity-driven dysoxic-to-anoxic conditions in the water column. These laminations are also associated with an increase in total iron concentrations and enriched sedimentary $\delta^{15}N$ ratios, suggesting a link between productivity, N cycle dynamics and micronutrient availability. Similar laminations and/or abruptly elevated B-A productivity trends have been observed during the deglacial transition in other continental margin settings of North America, as well as in the Cariaco Basin in the Atlantic, indicative of a systematic marine response to a large-scale atmospheric forcing. However, refractory element provenance analysis in EW0408-85JC indicates that terrestrial sediment sources

were similar during both the LGM and B-A. This temporal decoupling between biogenic and terrigenous sedimentation during the Holocene/LGM transition is likely associated with a slow Cordilleran Icesheet response to rapid changes in the North Pacific thermal regime.

5.2 Introduction

Strong evidence exists for modulation of past climate by atmospheric CO_2 concentrations (pCO_2) at glacial and interglacial timescales [Petit et al., 1999]. The biosphere is thought to be a major control on pCO_2 levels, with the marine ecosystem component of this biological C pump appearing to exert the dominant influence on these timescales. Data linking primary productivity fluctuations with paleoenvironmental forcing mechanisms remain inconclusive however. Changes in delivery of iron bound in aeolian sediment to micronutrient limited regions of the world ocean is a favored hypothesis to induce large marine productivity changes [Martin, 1990]. Several studies of artificial iron seeding in the Southern [Coale et al., 2004] and North Pacific Oceans [Boyd et al., 2004] support the Fe-limitation hypothesis. Indirect evidence is also provided by terrestrial paleoclimate studies [e.g. Begét, 2001] and GCM results [Kutzbach et al., 1998] that show large continental areas were both more arid and susceptible to enhanced aeolian erosion during glacial stades relative to present. Several recent studies indicate that Fe delivered to the ocean via aeolian deposition is less soluble than Fe associated with other transport modes [Schroth et al., 2009], and thus less bioavailable for primary producers. These observations therefore suggest additional sources of Fe beyond aeolian dust input may be necessary to initiate large basin-scale increases in primary productivity to adequately reconcile proposed changes in the marine biological C pump and atmospheric pCO_2.

The North Pacific Ocean (Fig. 5.1a) is the largest high-nutrient-low-chlorophyll (HNLC) region in the Northern Hemisphere, and the productivity in this area is largely iron-limited [Harrison et al., 1999]. In contrast, the coastal regions of both the Northeast and Northwest Pacific are macronutrient-limited (e.g. nitrate, silicic acid) [Whitney et al., 2005]. Cross-shelf exchange of water masses between the shallow and deep basinal

waters is the chief mechanism underlying the high seasonal productivity observed in the North Pacific [*Ladd et al.*, 2005]. Hydrographic time-series data in the northern Gulf of Alaska show an onshore nutrient flux below a prominent halocline forced by increased freshwater discharge during the spring and summer [*Weingartner et al.*, 2005], and that subsequent intense vertical mixing by winter storms bring these nutrients into the euphotic zone, where they are then completely utilized during the spring phytoplankton bloom [*Childers et al.*, 2005]. Water column iron concentrations along a transect from the Northeast Pacific shelf to the deep basin show orders of magnitude greater iron concentrations in shelf waters derived from fluvial sources [*Nishioka et al.*, 2001]. Additionally, seasonal measurements of water column iron concentrations offshore from river mouths along the Northeast Pacific margin indicate shelf accumulation of iron-bearing flocculants during the high-flow season, with subsequent release of this bound iron to the euphotic zone during periods of relaxed stratification [*Chase et al.*, 2007]. Finally, mesoscale eddies that form in the coastal areas and spin out into the open Northeast Pacific lead to large-scale increases in productivity due to transport of this continentally-derived iron into the HNLC zone [*Johnson et al.*, 2005].

These observations suggest strong linkages between hydrography, nutrient availability, and productivity exist in the North Pacific Ocean. In this report, a high-resolution proxy record of paleoproductivity that spans the last 18 calibrated kiloyears before present (cal kyr BP) is examined, in conjunction with a suite of geochemical and mineralogical assays from the continental slope of the northern Gulf of Alaska (Fig. 5.1b). In particular, the relationship between primary productivity, iron availability, and nutrient cycling during the LGM/Holocene transition is highlighted.

5.2.1 Modern environment and paleoceanographic setting

The Gulf of Alaska is bordered along its eastern and northern margins by the St. Elias, Wrangell, and Chugach Mountain Ranges; these high-relief features contribute to making this margin a location of extreme precipitation, exceeding 2 – 4 m/yr [*Weingartner*, 2005]. In turn, this precipitation drives a highly effective glacial erosion system with denudation rates exceeding 10 mm/yr with minimal terrestrial sediment

storage [*Hallet et al.*, 1996]. Correspondingly, the Copper, Susitna, and Stikine Rivers along the Gulf of Alaska margin collectively drain <4% of the area of the Mississippi River valley, yet discharge nearly a third as much sediment [*Milliman and Syvitski*, 1992]. Terrestrial-derived marine sediment accumulation rates are thus relatively high, ranging from 0.02 - 20 cm/yr [*Jaeger et al.*, 1998; *Ullrich et al.*, 2009].

Ocean circulation in the Gulf of Alaska is dominated by a dynamic atmosphere-ocean linkage between the Aleutian Low (AL) pressure cell and the Alaska Gyre (Fig. 5.1). During the winter months (e.g. November to March), the statistical center of the AL is located over the central Gulf of Alaska, where it favors: (i) enhanced upwelling in the HNLC Alaska Gyre; and (ii) vigorous vertical mixing by winter storms [*Rodionov et al.*, 2005; *Rodionov et al.*, 2007]. The spring and summer seasons (e.g. April – September) see a relaxation in the AL and the resumption of a strongly stratified water column forced by the spring freshet and enhanced thermal warming of the upper water column [*Mundy and Olsson*, 2005].

Seasonal atmospheric dynamics in the Gulf of Alaska are controlled by the position and intensity of the AL [*Mundy and Olsson*, 2005]. During the winter, when the AL is located over the Gulf of Alaska, it reduces sea surface temperature (SST) and sea level pressure (SLP), increases precipitation, and intensifies the northeastern Pacific storm track [*Trenberth and Hurrell*, 1994; *Rodionov et al.*, 2007]. The AL-driven SLP reduction leads to enhanced upwelling in the Alaska Gyre [*Harrison et al.*, 1999]. Cyclonic Alaska Gyre circulation leads to horizontal advection of shallow nutrient-rich water towards the continental shelf of the Gulf of Alaska where it contributes to large phytoplankton blooms in the spring and summer [*Childers et al.*, 2005]. Concurrent with the spring bloom is the seasonal freshet along the margin when freshwater discharge into the Gulf of Alaska is high, and is entrained in the Alaska Coastal Current [*Royer*, 2005]. The summer runoff maxima thus reflects atmospheric conditions driven by the preceding wintertime AL [*Royer et al.*, 2001].

The Gulf of Alaska is an integral component of the global ocean-atmosphere system. Environmental conditions within this region have been linked with decadal-scale

atmospheric variability patterns that affect Northern Hemisphere temperature and precipitation regimes as distant as the Atlantic coast of the southeastern United States [*Wallace and Gutzler*, 1981; *Trenberth and Hurrell*, 1994; *Royer et al.*, 2001], and the Sonoran Desert in northern Mexico [*Carleton et al.*, 1990; *Higgins and Shi*, 2000]. The Subarctic North Pacific Ocean is also viewed as the terminus of the global thermohaline circulation [*Stommel*, 1958; *Broecker*, 1991], thus linking it to circulation changes in the world ocean. Collectively, these observations serve to indicate that paleoceanographic records from the Gulf of Alaska have the potential to preserve evidence of both climate forcing and response on regional and global scales. However, there are relatively few high-resolution records of the paleoceanographic development of the Gulf of Alaska since the Last Glacial Maximum (LGM). This lack of data is compounded by a complex LGM environment that has no modern analogue that incorporates (i) more than 3,500 kilometers of coastline engulfed by the Cordilleran Ice Sheet (CIS) [*Kaufman and Manley*, 2004], (ii) complex relative and eustatic sea level changes associated with a tectonically-active margin [*Gulick and Jaeger*, 2003], and (iii) a re-organization of North Pacific Ocean circulation due to the LGM closure of the Bering Strait and the emergence of central Beringia [*Hopkins*, 1959].

The limited paleoceanographic data available from the Gulf of Alaska is primarily associated with DSDP Leg 18 [*Kulm et al.*, 1973], activities connected with ODP Site 887 [*Rea et al.*, 1995], and investigations of the Outer Continental Shelf Environmental Assessment Program [e.g. *Molnia*, 1982]. The ODP Site 887 has provided a well-resolved millennial-scale record of pelagic sedimentation [*Rea and Snoeckx*, 1995], productivity [*McDonald et al.*, 1999], and nutrient cycling [*Galbraith et al.*, 2007; *Galbraith et al.*, 2008a] for the last 750 kyr. In addition, cores collected during cruise PAR87A from the Patton-Murray Seamounts (ODP Site 887) preserve detailed sub-millenial patterns of Gulf of Alaska paleoceanographic change from the LGM and Holocene [*De Vernal and Pedersen*, 1997]. Collectively, these studies indicate the LGM Gulf of Alaska was cooler, experienced a high ice-rafting sediment flux, and had relatively low primary productivity.

Key paleoceanographic reconstructions from the Bering Sea [*Sancetta et al.*, 1985; *Cook et al.*, 2005; *Okazaki et al.*, 2005] and the Sea of Okhotsk [*Morley et al.*, 1991; *Gorbarenko*, 1996; *Keigwin*, 1998; *Gorbarenko et al.*, 2004] give additional insight into the state of the marginal seas of the Subarctic North Pacific Ocean during the LGM and subsequent deglaciation. While the Bering Sea shelf was subaerially exposed due to the low LGM eustatic sea level stand [*Hopkins*, 1959; *Fairbanks*, 1989], the deeper Bering Sea basin was exposed to continuous marine sedimentation throughout both the LGM and Holocene [*Sancetta et al.*, 1985]. High LGM concentrations of the diatom species *Thalassiosira antarctica* and the genus *Nitzschia*, combined with depleted diatom $\delta^{18}O$ values, are consistent with the presence of LGM sea ice and an enhanced freshwater flux, both of which would have facilitated the formation of strongly stratified, cold, and low-saline surface waters that restricted primary productivity [*Sancetta et al.*, 1985]. This observation of low LGM productivity is seen in other proxies from the deep Bering Sea, including reduced concentrations of sedimentary biogenic silica and total organic carbon (TOC) [*Okazaki et al.*, 2005], and reduced concentrations of the high-TOC-flux-associated diatom *Rhizosolenia hebetata* [*Cook et al.*, 2005]. Clay mineral and detrital provenance analyses of these LGM sediments are indicative of high fluvially-derived sediment input to the basin, consistent with increased terrestrial drainage from the subaerial Bering shelf [*Sancetta et al.*, 1985; *VanLaningham et al.*, 2009]. Several aspects of the Holocene sedimentary record contrast with many of these LGM proxy trends, including: (i) much higher siliceous primary productivity; (ii) sharp reduction in fluvially-derived terrigenous sediment; (iii) a reduction or absence of sea ice; and (iv) increasing salinity of surface waters. All of the authors above ascribe these changes to a combination of a warming Northern Hemisphere and rising eustatic sea level, permitting the inundation of most of the shallow Bering Sea shelf between 11.3 – 12.4 cal kyr BP [*Keigwin et al.*, 2006], as well as the onset of modern Bering Sea circulation that favors high levels of productivity along the shallow Bering shelf and "Green Belt" of *Springer et al.* [1996].

Proxy evidence from the Sea of Okhotsk indicate similar productivity minima during the LGM [*Gorbarenko*, 1996], as well as higher occurrences of coarse lithic iceberg-rafted debris (IRD), both of which are likely associated with increases in sea ice cover [*Gorbarenko et al.*, 2004]. However, the glacial ocean conditions in the Sea of Okhotsk have broader implications for North Pacific circulation. This marginal basin is the dominant source of North Pacific Intermediate Water (NPIW) via cabelling of low-saline coastal waters derived from freshwater influx along the margin, and North Pacific waters that enter through the Kurile Island Straits [*Talley*, 1993; *You et al.*, 2000]. During the LGM, foraminiferal isotope evidence [*Keigwin*, 1987; *Keigwin et al.*, 1992; *Gorbarenko*, 1996; *Keigwin*, 1998], diatom assemblages and sediment characteristics [*Gorbarenko et al.*, 2004] indicate that the extensive sea ice cover present in the Sea of Okhotsk strengthened NPIW formation via lower regional sea surface temperatures [*COHMAP*, 1988; *Kutzbach et al.*, 1998] and increased salinity from brine rejection during sea ice formation. Changes in NPIW circulation have been linked with paleoenvironmental shifts as distant as the Mexican margin in the subtropical Northeast Pacific Ocean [*van Geen et al., 2003; Crusius et al., 2004*].

The preceding observations of the Bering Sea and the Sea of Okhotsk indicate the marginal seas of the Subarctic Northeast Pacific Ocean have experienced large variations in oceanographic conditions since the LGM, and that this variability has had basin-wide effects throughout the North Pacific Ocean. By comparison, the Gulf of Alaska has not received similar levels of scrutiny despite its clear importance in modern Northern Hemisphere climate dynamics. This lack of paleoceanographic data highlights the importance of developing such high-resolution records from the Gulf of Alaska. Furthermore, the dynamic atmosphere-ocean-ecosystem feedback system in the Gulf of Alaska is a natural laboratory for studying past environmental variability and its effects on marine primary productivity.

5.3   Methods

5.3.1   Core description

Jumbo piston core EW0408-85JC (59° 33.3'N, 144° 9.21'W, depth 682 m) was recovered by the *R/V Maurice Ewing* from the continental slope along the Gulf of Alaska margin in 2004 (Fig. 5.1). Following retrieval, the core was sectioned and analyzed shipboard using a GEOTEK Multi-Sensor Core Logger (MSCL) to measure high spatial resolution geophysical properties at 1-cm intervals [*Blum*, 1997]. Each core section was subsequently split, lithologies described and high-resolution linescan imagery was collected. All EW0408 sediment cores are stored at the Oregon State University core repository in Corvallis, Oregon.

5.3.2   Geochronological approach

The chronological approach presented here builds on that presented by *Barron et al.* [2009]. These authors used accelerator mass spectrometry (AMS) ^{14}C dates derived from three marine bivalve shells to constrain the geochronology of EW0408-85JC, and further refined this chronology by using stratigraphic correlations to similar lithologies from the temperate North Pacific margin. In this work, these bivalve dates are supplemented with 33 AMS ^{14}C dates on planktonic foraminifera. This dating approach, as well as a high-resolution foraminiferal δ^{18}O and δ^{13}C record, will be the subject of a forthcoming paper by *Davies et al.* [in prep.].

5.3.3   Biogeochemical approach

Bulk 1-cm-thick sediment samples were collected from EW0408-85JC at 5 cm intervals. Samples were then freeze-dried, homogenized and powdered by hand with mortar and pestle, and further subsampled. The first split was treated in 2 N HCl overnight, rinsed with Millipore distilled water three times, and freeze-dried. An aliquot powder was then measured for biogenic silica (opal) following a wet-alkali extraction method and using a Spectronic 20D+ spectrophotometer set at a wavelength of 812 nm [*Mortlock and Froelich*, 1989]. An estimated error of 4.6% (calculated as the coefficient

of variation, e.g. the standard deviation divided by the mean) based on replicate measurements of two internal opal-rich sediment standards was determined for this method, and is broadly equivalent to the results of an interlaboratory comparison for this technique [*Conley*, 1998]. A second carbonate-free subsample was combusted in a Costech 4010 HCNS elemental analyzer to determine TOC and total nitrogen (TN) concentrations. The analyzer was coupled to a Finnigan Delta^{plus}XP isotope ratio mass spectrometer for $\delta^{13}C$ and $\delta^{15}N$ measurements. All isotope values are reported in permil units (‰) according to the relationship

$$\delta X = \frac{R_{sample} - R_{standard}}{R_{standard}} \times 1000$$

[Eqn. 1]

where X is the element of interest and R is the measured stable isotopic ratio. All carbon isotope measurements are relative to the V-PDB standard ($\delta^{13}C$ = 0‰) and all nitrogen measurements are relative to atmospheric nitrogen ($\delta^{15}N$ = 0‰). Molar ratios of TOC:TN (hereafter referred to as C/N ratios) were calculated for use in describing sedimentary organic matter provenance and nutrient cycling. While *Muller* [1977] noted sorption of ammonium ions to clays in the deep sea manifested as C/N values <6, the assumption that sedimentary TN values are representative of total organic nitrogen seems plausible due to (i) water depths of 680 m that favor reduced remineralization relative to abyssal depths and (ii) minimal clay fractions present within the full mineral assemblage (Table 5.1). To fully address this issue requires additional analyses beyond the scope of this present work. Replicate measurements of internal standards run alongside TOC, TN, sedimentary $\delta^{13}C$ and sedimentary $\delta^{15}N$ samples yielded coefficients of variation of 4.4%, 6.9%, 1.2%, and 2.8%, respectively.

A second non-acid-treated split was used for geochemical and mineralogical assays. Total inorganic carbonate concentrations were measured by standard coulometric methods, and then multiplied by 8.333 (the molar stochiometric ratio of $CaCO_3/C$) to convert to $CaCO_3$ concentrations. The bulk inorganic geochemistry of core EW0408-85JC was analyzed by a combination of inductively coupled plasma optical emission spectrometry (ICP-OES) and inductively coupled plasma mass spectrometry (ICP-MS)

by SGS Minerals Services. Samples were digested in a sequential acid leaching method using HNO_3, HCl, HF, and $HClO_4$. Following the acid digestion, the bulk geochemistry sample was divided into 2 aliquots for analysis by ICP-OES and ICP-MS, and yielded a suite of 40 element concentrations. This data is presented in *Barron et al.* [2009]. Replicate samples and international standards (SGR-1, NBS-SRM1646, and PBD-1) were analyzed within the analytical runs to monitor accuracy and precision. The mean percent difference between analyzed concentrations and literature values for the standards for all elements was 11%, and most elements are within the reported 1σ range. A mean coefficient of variation for all elements calculated from all replicate samples was 4.1%. For the purposes of reconstructing CIS-derived glaciomarine sediment, elements derived from the accumulation of detrital mineral phases (Al, Ti, Zr, K, Nb, Y, and others) are of primary interest. These refractory elements are generally associated with aluminosilicate and oxide minerals that are highly insoluble in natural waters [*Marshall and Fairbridge*, 1999], and thus their presence in core EW0408-85JC can be used to infer terrigenous sediment input [*Haug et al.*, 2001] and sedimentary provenance [*McLennan et al.*, 1993]. As an aside, this approach implicitly assumes these mineral phases were dissolved completely during the ICP-OES and ICP-MS analyses [*Wray*, 2005]. Several redox-sensitive elements (U, Mo, Fe, and Mn) are also of interest, and while these were discussed at length by *Barron et al.* [2009] as proxies of bottom-water oxygen concentration, the coupling between biogeochemical cycling and the independent productivity datasets of opal and TOC are of primary interest in this paper [*Morel and Price*, 2003]. Briefly, the redox-sensitive elements are predominantly derived from two sources, either associated with terrestrially-derived detrital mineral phases and organic particles via substitution or adsorption processes, or direct precipitation from seawater as reduced sulphide phases sensitive to prevailing Eh conditions within the water column [e.g. *Calvert and Pedersen*, 1993; *Tribovillard et al.*, 2006; *Piper and Calvert*, 2009]. To estimate the precipitated authigenic fraction, the excess fraction was calculated based on normalization to a global average sediment composition, assuming a constant aluminosilicate-hosted terrigenous flux according to

$$\text{excess } X = X_{measured} - \left(Al_{measured} \times \left[\frac{X}{Al} \right]_{avg\,sed} \right)$$

[Eqn. 2]

where $X_{measured}$ is the measured ICP-MS sample concentration of the element of interest, and $(X/Al)_{avg\,sed}$ is the global mean sediment Al-normalized ratio for element X [*McLennan*, 1995]. In other cases presented in this paper (opal and Nb), the unnormalized concentration divided by the total aluminum concentration [e.g. *Van der Weijden*, 2002] is used as a method to correct for dilution by the large contributions of detrital aluminosilicates delivered to the nearshore environment along the Gulf of Alaska continental slope.

X-ray diffraction (XRD) analyses were performed on 16 sediment samples that span the full compositional (both lithological and geochemical) range of EW0408-85JC. Samples for quantitative mineralogical analysis were prepared by combining 2 g sample with 0.222 g of zincite (ZnO) and 8 mL of methanol, pulverizing the resultant mixture for 5 min in a SPEX 8000D sediment mixer using hardened stainless steel vials, and then heating at 85°C for 30 minutes for methanol evaporation. The XRD samples were then re-homogenized by hand using a mortar and pestle, and gently packed into a glass sample mount to ensure random grain orientation. XRD patterns were obtained on a PANalytical MRD instrument with a Cu X-ray tube (Kα radiation = 1.5916Å). The following optical package was used, arranged in order of beam path: X-ray generator, Ni attenuator, 0.02° soller slit, 10-mm Ni mask, 0.5° divergence slit, 1° aperture slit, sidemount sample holder, 6.6-mm aperture slit, 0.02° soller slit and an X'Celerator solid state multi-strip detector. A minimum of ten XRD patterns per sample were scanned from 5 to 65° 2θ at a step-size of 0.012 °/s; the resulting patterns were then averaged and the results interpolated to a step-size of 0.02 °/s for semi-quantitative estimation of major phases using the RockJock 7.0 software package [*Eberl*, 2003]. This analysis uses a Microsoft Excel macro routine with previously measured mineral intensity factors, and combined with the inclusion of a known ZnO:sample ratio of 10 wt%, permits a semi-quantitative estimation of bulk mineralogy of randomly oriented samples. The RockJock program utilizes the embedded SOLVER macro within Excel to fit a composite pattern of user-

selected minerals to the measured sample pattern, and then evaluates the model using a calculated "degree of fit" parameter. The ability of RockJock to quantify mineral phases was evaluated independently using several prepared simple mixtures of quartz, kaolinite, smectite, iron-rich smectite, and illite.

The mineral assemblage selected for this study (Table 5.1) met several qualifications for inclusion, including (i) previously recorded mineral presence along the Gulf of Alaska continental shelf [*Slatt and Piper*, 1974; *Naidu et al.*, 1976; *Molnia and Hein*, 1982; *Naidu and Mowatt*, 1983; *Eberl*, 2004]; (ii) specific interest from a biogeochemical cycling perspective [*Cole and Shaw*, 1983; *Dean and Arthur*, 1989; *Dymond*, 1992]; and (iii) RockJock outputs from test patterns. In all samples, the degree-of-fit parameter was <0.065, indicating good agreement between experimental and modeled XRD patterns. A second check of RockJock accuracy is that the individual sample mineral concentration totals do not exceed 100 wt%. The complicated multi-phase nature of the EW0408-85JC sediment samples however exceeded an unnormalized 100 wt% total. Common reasons for analyses exceeding 100 wt% include insufficient sample homogeneity, preferred orientations induced during XRD sample mounting, or zincite peak shape changes induced during grinding [*Eberl*, 2003; D. Eberl, personal communication]. As an additional check of RockJock concentrations, correlation coefficents between selected element concentrations measured by ICP-MS and the associated mineral phases calculated by RockJock were also calculated.

The stoichiometries of Fe-bearing mineral phases were used to estimate the total concentration of solid-phase ferrous and ferric iron as a proxy for bioavailable iron in the sedimentary record. Because Fe^{2+}-bearing silicates and sulphides tend to be more soluble than Fe^{3+} phases under oxidizing water conditions [*Langmuir*, 1997; *Moffett*, 2001], it follows that higher dissolution fluxes of Fe^{2+} into the oxygenated portions of the water column would be associated with higher sedimentary accumulation of these solid-phase ferrous minerals. Using the semi-quantitative concentrations of amphibole (treated as hornblende for calculation purposes), pyrite, goethite, ilmenite, and biotite, these values were multiplied by the stoichiometric percentage of atomic Fe^{2+} or Fe^{3+} contained within

each mineral phase. For chlorite, RockJock was unable to differentiate between Fe-rich chlorite and other chlorite phases successfully. To correct this problem, the relative peak height difference between the 14Å:7Å chlorite peaks were used to estimate the percentage of Fe-rich chlorite. The stoichiometry of a mixed chamosite composition $(Fe^{2+}{}_2Mg)_{1.5}(Fe^{3+}{}_{0.5}Al)Si_3AlO_{12}(OH)_6$ was then used to calculate the relative Fe^{2+} and Fe^{3+} contributions from chlorite.

Time-series analysis was performed on the mid- and late Holocene organic matter data using the REDFIT analysis software package [*Schulz and Mudelsee*, 2002]. Briefly, this program utilizes a bias-corrected Lomb-Scargle Fourier transform appropriate for unevenly-spaced data with no need for interpolation to equal time steps. To asses the significance of resulting spectral peaks, REDFIT calculates a first-order autoregressive (AR1) process representing stochastic variability in the dataset, and then tests the data time-series against the AR1 time-series using a Monte Carlo ensemble. The REDFIT approach inherently assumes that the AR1 process approximates the background noise in the respective datasets, and that the distribution of data along the time axis is not too clustered [*Schulz and Mudelsee*, 2002].

5.4   Results

5.4.1   Core lithology and geochronology

Sediment core EW0408-85JC is composed of four major lithologic units (Fig. 5.2). The uppermost unit, a dark gray silty clay [Unit 1] that extends from 0 – 610 cm below the seafloor (bsf), conformably overlies a gray coarser silty clay with dispersed sand grains [Unit 2] from 610 – 645 cm bsf. A highly-organic, gray silty clay with olive brown laminations [Unit 3] extends from 645 – 680 cm bsf, which in turn grades downcore into a dark gray massive diamicton with scattered pebbles and large angular clasts [Unit 4] that continues to the bottom of EW0408-85JC at 1124 cm bsf. In general, the ultrahigh-resolution gamma-ray attenuated wet bulk density scan corresponds to these lithologic units (Fig. 5.2).

The high-resolution age-depth model of *Davies et al. [in prep.]* reveals that EW0408-85JC contains a continuous record of sedimentation since the Late Pleistocene (Fig. 5.2). The mean sedimentation rate for the Holocene portion [Unit 1] is 0.05 cm/yr, whereas the LGM section [Unit 4] older than ~16.7 cal kyr BP accumulated at a much higher rate of 0.53 cm/yr. The intervening Units 2 and 3 correspond to the Younger Dryas (YD) and Bølling-Alleröd (B-A) periods, respectively, and together with the uppermost ~70 cm of Unit 4 were deposited at a linear accumulation rate of 0.03 cm/yr. A low-density sediment layer is present immediately following the YD/Holocene transition, and appears chronologically analogous with the Preboreal Oscillation (PBO) identified in the North Atlantic region [*Rasmussen et al.*, 2007].

5.4.2 Paleoproductivity and redox-sensitive elements

Biogenic sediment concentrations suggest a high degree of variability in marine ecosystem paleoproductivity since the LGM. Both opal and TOC proxies show consistently higher Holocene concentrations relative to lower LGM concentrations (Fig. 5.3a, c). Natural-log-transformed opal and TOC concentrations are significantly correlated (n = 165, r = 0.718, p < 0.01; Fig. 5.4a), indicating excellent preservation of these export productivity proxies given the different conditions under which these sedimentary components are preserved [*Hedges et al.*, 1999; *Ragueneau et al.*, 2000]. The $CaCO_3$ record displays only limited correspondence to either the opal or TOC trends (Fig. 5.3b), suggesting alternative processes controlling carbonate accumulation such as differential $CaCO_3$ preservation or detrital carbonate contributions from the erosion of adjacent terrestrial carbonate outcrops. An issue arises when attempting to use mass accumulation rates (MARs) to infer paleoproductivity from biogenic fluxes in core EW0408-85JC; this problem will be fully addressed in the following discussion section.

The Holocene/LGM transition preserves striking evidence for abrupt ecosystem shifts. For example, the transition from minimal LGM opal concentrations to maximal B-A concentrations indicate a three-fold increase in siliceous concentrations. This increase is short-lived, and ends abruptly during the YD/B-A transition about 1500 years later, when opal concentrations drop by 40% relative to B-A values. A second abrupt

increase is observed during the PBO; the transition from this period of heightened productivity into the early Holocene is associated with a decrease of opal concentrations from 9.5 to 6.5 wt%.

The sedimentary $\delta^{13}C$, $\delta^{15}N$, and molar C/N ratios show a large range of variability, with values between -26.3 to -22.1‰, 2.2 to 6.7‰, and 8.8 to 28.0, respectively (Fig. 5.4). These elemental and isotopic ranges suggest differing contributions of autochthonous organic matter sourced from the marine environment, and allochthonous organic matter derived from the adjacent terrestrial margin. To estimate the relative proportions of marine- versus terrestrial organic matter, a linear mixing model was employed following the guidelines of *Walinsky et al.* [2009] that was used to evaluate the organic matter provenance of surface sediment samples from different depocenters along the Gulf of Alaska margin. These authors calibrated their model using three end-member compositional ranges for marine phytoplankton, vascular plant detritus, and soil based on literature values [*Meyers*, 1994; *McQuoid et al.*, 2001; *Geider and LaRoche*, 2002; *Gaye-Haake et al.*, 2005; *Walsh et al.*, 2008]. The application of this mixing model yields mean terrestrial contributions of 50, 48, 37, 43, and 77% for Holocene, PBO, YD, B-A, and LGM intervals, respectively. When these values are viewed in terms of modern Gulf of Alaska surface sediment provenance values [*Walinsky et al.*, 2009], the LGM samples have characteristics similar to sediments derived from modern Bering Glacier outwash, while the remainder of the Holocene EW0408-85JC samples are broadly analogous with the ranges measured for offshore locations along the northern Gulf of Alaska shelf (Fig. 5.5). When viewed in relation to the biogenic opal data, the LGM opal minima is clearly associated with isotopically light $\delta^{13}C$ and $\delta^{15}N$, consistent with the predominant source of organic matter being terrestrially-derived (Fig. 5.4). The elevated Holocene opal concentrations are linked with relatively more enriched isotopic values though there is a large degree of variability, indicative of fluctuations in the proportions of marine- versus terrestrially derived organic matter. Deviations from the general pattern of terrestrial- versus marine-derived organic matter mixing are seen during the Holocene/LGM deglaciation, in that the YD and early Holocene are somewhat

[13]C-enriched (Fig. 5.4b), while the PBO and B-A display anomalously enriched $\delta^{15}N$ values (Fig. 5.4c).

Because of the high proportions of terrestrially-derived TOC present within the total TOC measurements in the EW0408-85JC samples, the mixing model approach was again used to estimate the marine TOC contributions as an independent measure of productivity using the equation

$$TOC_{marine} = \frac{\delta^{13}C_{sample} - \delta^{13}C_{terrestrial}}{\delta^{13}C_{marine} - \delta^{13}C_{terrestrial}} \times TOC_{sample} \qquad \text{[Eqn. 3]}$$

where TOC_{marine} is the calculated marine-derived TOC (in wt%), $\delta^{13}C_{sample}$ is the measured $\delta^{13}C$, $\delta^{13}C_{marine}$ is the fully marine endmember $\delta^{13}C$, $\delta^{13}C_{terrestrial}$ is the fully terrestrial endmember $\delta^{13}C$, and TOC_{sample} is the measured total TOC for a sample. Values of -21‰ (modern marine phytoplankton) and -26‰ (vascular plant detritus) were used as the marine and terrestrial $\delta^{13}C$ endmember values, respectively, following the similar approach of *Walinsky et al.* [2009]. Given the anomalous sedimentary $\delta^{13}C$ values observed during the YD (Fig. 5.4b), this calculation is not appropriate for estimating marine TOC during this time interval. It is also unlikely to accurately depict a similar anomaly during the early Holocene that is marked with moderate opal concentrations but enriched $\delta^{13}C$ values (Fig. 5.4b). Therefore, these intervals are indicated on the downcore plot of marine-derived TOC (Fig. 5.3d). The results of Eqn. 3 are broadly consistent with both total TOC and opal measurements.

A comparison of the downcore trends in opal, molar C/N ratio, and sedimentary $\delta^{13}C$ and $\delta^{15}N$ data show several coherent patterns (Fig. 5.6). LGM sediments are composed of low opal concentrations (<4.8%), high molar C/N ratios, and depleted $\delta^{13}C$ and $\delta^{15}N$ values, all of which are consistent with low export siliceous productivity and predominantly terrestrial-derived organic matter. This contrasts with the opal maxima seen during the B-A and PBO, both of which are associated with moderate C/N ratios (12.1 – 13.8), and enriched $\delta^{13}C$ and $\delta^{15}N$ (mean values of -23.2‰ and 5.9‰, respectively). The Younger Dryas is marked with opal values similar to Holocene concentrations (mean 6.1%), a slightly lower mean C/N ratio of 11.15, a mean

sedimentary $\delta^{13}C$ value of -22.8‰, and a mean $\delta^{15}N$ value of 5.3‰. Holocene sediments preserve moderate opal concentrations (mean 8.8%) with little variability, but in-phase shifts during the mid- and late Holocene are observed in the molar C/N ratio, and sedimentary $\delta^{13}C$ and $\delta^{15}N$. The organic matter provenance model described above indicates changes from a maximum of 62.8% terrestrial-derived organic matter at ~3700 cal yr BP to a minimum value of 29.6% at ~2600 cal yr BP.

Sedimentary concentrations of the redox-sensitive elements Mn, Mo, and U also show distinctive intervals of authigenic enrichment associated with changing lithologies in core EW0408-85JC (Fig. 5.6). In particular, high excess concentrations of Mo and U are indicative of bottom-water anoxia during both the laminated B-A and massive PBO deglacial intervals, which are also contemporaneous with high TOC and opal concentrations. Conversely, high excess Mn and minimal excess Mo and U during the Younger Dryas interval argue for suboxic bottom waters, while Holocene excess Mn concentrations are likely indicative of fully oxic water conditions.

5.4.3   Detrital accumulation and mineralogy

The ICP-MS and XRD analyses indicate several distinctive geochemical and mineralogical associations in core EW0408-85JC. Considering the concentrations of several refractory or highly refractory elements [*McLennan*, 1999] in ternary space as indicative of detrital sediment provenance (Fig. 5.7), two distinctive patterns are apparent when samples are grouped by time of deposition. There is relatively little compositional variability during the LGM and the B-A, suggesting only one source of detrital sediment. The much greater compositional variability in the Holocene data, and to some extent during the YD and the PBO, indicates multiple sediment sources. This Holocene variability likely reflects mixing between two distinctive geochemical signatures, with one source (high Nb – low Y) containing the same refractory elemental composition as during the LGM, and the second source (low Nb – high Y) unique to the Holocene, YD, and PBO. These fluctuations are illustrated in the downcore Nb record (Fig. 5.8). Prior to YD time, Nb concentrations are 7.4 ± 0.6 ppm. Beginning around 13.0 cal kyr BP, these Nb values change to 6.5 ± 2.0 ppm. The application of Levene's test for equality of

variance [*Levene*, 1960] indicates the difference in variance between the two time groups (e.g. pre-YD and YD/post-YD) is statistically significant at the 95% confidence level. The results of this test reflect the change from a single sediment source with a consistent Nb concentration during the LGM and B-A, to a YD/post-YD environment that receives sediment from alternating between two different sources with different Nb concentrations. However it is also important to note that the same high Nb detrital signature seen during the LGM dominates during the late Holocene from ~3000 cal yr BP to recent time (Fig. 5.8).

The measured XRD patterns from the EW0408-85JC samples point to a dominantly detrital mineral character with only minor contributions of clay minerals (Fig. 5.9). Comparison between patterns derived from prepared samples and EW0408-85JC samples indicate little smectite of any variety. RockJock quantification of major components (Table 5.1) are dominated by plagioclase (20.5±1.2 wt%), quartz (16.1±3.6 wt%), and illite (13.9±1.9 wt%). An independent samples t-test performed on the Holocene and LGM estimated quartz concentrations show that the Holocene values are significantly lower (exceed the 95% rejection level) relative to the LGM. The combined XRD analyses also indicate a mean kaolinite concentration of 5.0±1.2%, an anomalous finding given all previous XRD work has measured ≤1% kaolinite within the clay-size fraction from this region of the Gulf of Alaska continental shelf, if any [e.g. *Naidu et al.*, 1976; *Molnia and Hein*, 1982; *Naidu and Mowatt*, 1983]. This result may reflect differences in sample preparation technique, and requires further analysis for confirmation.

Nonparametric coefficients of correlation show significant positive relationships between several groups of minerals and key elements (Table 5.3). Several refractory elements (e.g. Al and K) and some redox-sensitive elements (Fe, Co, Ni, Cu, and Zn) have high correlations with the minerals amphibole, chlorite, and goethite. Both pyrite and barite are correlated with S, which is reasonable given these two minerals are major inorganic solid-phase S carriers in marine sediments [*Kastner*, 1999]. The high correlation between the XRD-derived estimation of calcite content and the coulometric

$CaCO_3$ values also provide an independent check of the RockJock quantification results (Fig. 5.10a). While RockJock appears to consistently overestimate coulometric analyses by approximately 1 wt%, the correlation between the two different techniques is highly significant (n = 12, r = 0.834, p < 0.01). Therefore, it seems most appropriate to consider the RockJock mineral concentration data as semi-quantitative under these circumstances.

The estimated concentrations of amphibole, chlorite, and goethite (Table 5.1), as well as the high correlation coefficients with total Fe concentration measured by ICP-MS (Table 5.3), indicate these minerals are the dominant sources of iron to the EW0408-85JC sedimentary record. This is confirmed through the stoichiometric calculations of Fe concentrations partitioned between all iron-bearing mineral phases contained within the XRD dataset (Fig. 5.11). Together, both amphibole and goethite account for >60% of the solid-phase iron present within both the Holocene and LGM sediments. Accounting of the Fe^{2+} and Fe^{3+} atomic concentrations contained within these iron-bearing minerals shows that the ratio of $Fe^{2+}:Fe^{3+}$ has remained fairly constant through time (Holocene 67:33% and LGM 68:32%, respectively) over the period of deposition of EW0408-85JC, while a single B-A sample shows a minor increase in this ratio (70%:30%).

The solid-phase iron partitioning estimates seem robust, given the high correlation between the measured ICP-MS total Fe concentration and the derived Fe concentration data from the XRD mineralogy (Fig. 5.10b; n = 15, r = 0.853, p <0.01). However, the difference in absolute values suggest a key phase is not included in the stoichiometric calculations. This systematic error may be due to the presence of Fe contained within non-crystalline phases not measurable with standard XRD methods, such as amorphous Fe oxyhydroxides or ligand-complexed Fe associated with organic matter [*Moffett*, 2001]. Therefore, these results should serve only as a first-order estimation of Fe geochemical dynamics within this limited dataset. An improved methodology to measure the concentration of various solid-phase Fe carriers using a sequential chemical extraction technique [*Chester and Hughes*, 1967; *Tessier et al.*, 1979; *Filgueiras et al.*, 2002] is currently underway.

5.5   Discussion

5.5.1   Relationships between productivity and environmental proxies during the Last Glacial Maximum and the Holocene

The biogenic sediment preserved in EW0408-85JC presents the first high-resolution productivity record spanning the LGM to present for the northeastern Gulf of Alaska continental slope. This unique location captures coastal primary productivity changes, but also is influenced by Cordilleran Ice Sheet dynamics during the LGM and subsequent deglaciation. The order-of-magnitude difference in sedimentation rates between the Holocene and older LGM portions of EW0408-85JC bias calculations of biogenic mass accumulation rates (MARs) for use as primary productivity proxies. This discrepancy is illustrated by comparing the mean Holocene opal MAR of 1.34 $g \cdot cm^{-2} \cdot yr^{-1}$ with the mean LGM value of 9.62 $g \cdot cm^{-2} \cdot yr^{-1}$. The higher LGM opal MAR seems unlikely to reflect higher productivity given the probable growing conditions experienced by primary producers within the LGM Gulf of Alaska. For instance, the paraglacial environment at the EW0408-85JC site saw extensive light limitation from suspended glacial flour (Fig. 5.1b) from extensive meltwater discharge, as well as very cold surface water temperatures with ample sea ice [De Vernal and Pedersen, 1997], all of which would have likely limited primary productivity. Micropaleontology results from EW0408-85JC also support lower productivity, indicating a microfossil-barren zone extending from 14,800 cal yrs BP to the bottom of the core [Barron et al., 2009]. Collectively, these observations suggest biogenic MAR calculations for this core are not proportional to export productivity, and thus likely reflect preservation, sediment focusing, or other redistribution processes on the seafloor [Francois et al., 2004].

The multi-proxy methodology can assist in circumventing the sedimentation rate problem to address paleoproductivity changes. By combining the records of opal and marine-derived TOC concentrations with the sedimentary $\delta^{15}N$ and redox-sensitive element evidence, marine ecosystem dynamics along the Gulf of Alaska slope for the last 18,000 years can be documented. As stated above, the LGM sediments in EW0408-85JC preserve low concentrations of autochthonous marine organic matter, as evidenced by

low opal and marine TOC concentrations (Fig. 3a, d), but contains high concentrations of terrestrially-derived organic matter, exceeding 70% of the total organic matter in this portion of the core based on the relatively low isotopic ratios in both sedimentary $\delta^{13}C$ and $\delta^{15}N$ (Figs. 5.3, 5.5). Given the lack of terrestrial vegetation present along the Gulf of Alaska margin during this cold period, it seems likely that the allochthonous organic matter is derived primarily from eroding sedimentary bedrock. This same conclusion is consistent with that of *Walinsky et al.* [2009] for similar trends in isotopic and molar C/N ratios associated with sediments from modern Bering Glacier outwash. When viewed alongside the excess Mn, U, and Mo records (Fig. 5.6), the lack of appreciable authigenic precipitation of any of these elements suggests a dominantly detrital source for these normally redox-sensitive elements, consistent with the extremely high sedimentation rates (>0.5 cm/yr) experienced at the EW0408-85JC site during the LGM. Collectively, these observations imply the LGM Gulf of Alaska continental slope was functionally similar to one of the many glaciated fjords along the modern coast, with a cold and strongly stratified euphotic zone [*De Vernal and Pedersen*, 1997], ample terrestrially-derived suspended sediment and glacial flour, extremely low primary productivity, icebergs, and seasonal sea ice [*Barron et al.*, 2009]. The absence of sedimentary structures, and the absence of authigenic precipitation of Mo and U, also imply the bottom-waters were likely oxygenated enough to maintain a benthic biota capable of surviving in this rapidly-accumulating environment.

The Holocene portion of EW0408-85JC by comparison represents a completely different environment relative to the LGM Gulf of Alaska. The regional Cordilleran Ice Sheet likely became grounded sometime around 14.0 – 13.7 cal kyr BP [*Molnia and Post*, 1995; *D. Peteet*, personal communication, 2009]; the majority of sea-ice and sea-ice-related diatom taxa and subarctic silicoflagellate taxa disappear from EW0408-85JC at the end of the Younger Dryas around 11.4 cal kyr BP [*Barron et al.*, 2009]; and dinocyst-based transfer functions indicate the onset of modern regional surface salinities (>32 psu) by at least 10.2 cal kyr BP [*De Vernal and Pedersen*, 1997]. These results indicate the onset of Holocene conditions favored enhanced primary productivity relative to LGM

levels (Fig. 5.3a, d). During the early Holocene (11.0 – 8.5 cal kyr BP), relatively low molar C/N ratios are indicative of algal-derived organic matter, and combined with moderate opal and sedimentary $\delta^{13}C$ values, suggest that primary production may have been nutrient-limited. The dissolved anion HCO_3^- is the dominant C substrate for marine phytoplankton during photosynthesis, and thus fluctuations in HCO_3^- (aq) concentrations can be driven by changes in productivity [*Sarmiento and Gruber*, 2006]. These nutrient dynamics are recorded in $^{13}C/^{12}C$ fractionation associated with biological uptake following Rayleigh closed-system dynamics [*Rau et al.*, 1989; *Laws et al.*, 1995].

The early Holocene sedimentary $\delta^{15}N$ record (Fig. 5.6) exhibits some of the same behavior as the sedimentary $\delta^{13}C$, in that LGM sediments tend to have more depleted values (mean 3.09±0.37‰) relative to an early Holocene mean $\delta^{15}N$ of 4.64±0.51‰; an independent-samples t-test indicates the differences between the Holocene and LGM $\delta^{15}N$ data are significant at the 95% confidence level. This difference reflects the relatively greater contributions of terrigenous OM contained within the LGM sediments (Fig. 5.5), thus the LGM data appear to be more diagnostic of N-fixation of atmospheric N_2 ($\delta^{15}N$ = 0‰) by terrestrial plants. In contrast, the early Holocene $\delta^{15}N$ data are virtually indistinguishable from modern marine nitrate $\delta^{15}N$ (4.1±0.9‰) measured at 400 m water depth at Ocean Station Papa near Vancouver Island [*Wu et al.*, 1997], or world oceanic mean nitrate $\delta^{15}N$ of approximately 5‰ [*Galbraith et al.*, 2008b]. Because observations from multiple high-export-productivity margins indicate bulk sedimentary $\delta^{15}N$ has an excellent correlation with local sub-euphotic zone nitrate $\delta^{15}N$ [*Altabet and Francois*, 1994; *Thunell et al.*, 2004], the early Holocene values present within EW0408-85JC appear to record N-cycle variations driven by nitrate utilization by primary producers, such that complete nitrate utilization (and hence high productivity) is suggested by sedimentary $\delta^{15}N$ values approximately equal to mean oceanic nitrate $\delta^{15}N$.

The synchronicity of the sedimentary $\delta^{13}C$, $\delta^{15}N$, and molar C/N ratio data after 7500 cal yr BP suggest a linked process independent of marine productivity contributions, as evident in the approximately constant opal values during this same time span (Fig. 5.6). The highly depleted mid-Holocene $\delta^{15}N$ values can be explained by two

mechanisms: (i) increased contributions of terrigenous OM, which is consistent with the sedimentary $\delta^{13}C$ and C/N ratio trends (Fig. 5.6); or (ii) incomplete nitrate utilization that limits export productivity. Increased N-fixation can also result in lightening of $\delta^{15}N$ values [Carpenter et al., 1997], but modern circulation patterns in the North Pacific Ocean argue against increased N-fixation as evidenced by (i) negative N* values throughout the entire water column of the Subarctic Northeast Pacific Ocean [Gruber and Sarmiento, 1997; Sarmiento and Gruber, 2006] and (ii) high nitrate concentrations measured directly in the Alaska Gyre and along the adjacent Gulf of Alaska shelf [Childers et al., 2005]. Given these N-cycle constraints, and the synchronicity of the mid- and late Holocene fluctuations in sedimentary $\delta^{13}C$, $\delta^{15}N$, and molar C/N ratio data, the most straightforward interpretation is that these cycles represent discrete periods of enhanced terrigenous sediment delivery along the Gulf of Alaska slope.

The proximity of the EW0408-85JC site to both the Copper River delta and the terminus of Bering Glacier suggests both fluvial and glaciomarine processes likely contribute terrigenous sediment. However, the constant refractory elemental pattern preserved during the late Holocene (Figs. 5.7 and 5.8) remains unchanged throughout both millennial- and centennial-scale advances of the Bering Lobe during the late Holocene [Wiles et al., 1999; Calkin et al., 2001], implying the organic matter sedimentation oscillations are unrelated to Bering Glacier dynamics. Contributions of terrigenous organic material from longshore transport sourced in the heavily forested region of southeast Alaska can also be ruled out because modern sediments in both the nearshore and outer shelf regions in the northern Gulf of Alaska indicate accumulation of dominantly marine organic matter, and thus limited export of terrestrial material beyond the southeast Alaskan fjords in which these terrigenous sediments accumulate [Walinsky et al., 2009].

Modern satellite imagery shows distinctive sediment plumes transported westward by the Alaska Coastal Current along the northern Gulf of Alaska shelf (Fig. 5.1b). These plumes are driven primarily by summer meltwater discharge, and surface sediments from this area are characteristically rich in terrigenous organic matter

[*Walinsky et al.*, 2009]. Changes in this coastal meltwater discharge thus appear to be the most likely source of the low-frequency shifts in terrigenous organic matter preserved in EW0408-85JC. REDFIT time-series analysis of the Holocene portion of the sedimentary $\delta^{13}C$ dataset indicates a 600-yr frequency that exceeds a Monte Carlo test at the 80% significance level. This centennial-scale frequency pattern has not been recognized previously in Alaskan coastal records, probably because most paleoclimate datasets from this area capable of resolving such oscillations are either too short [*Wiles et al.*, 2004; *MacDonald and Case*, 2005] or too low-resolution [*Peteet and Mann*, 1994]. In other long paleoceanographic records where such resolution is possible from the southeast Alaskan fjords [*Addison*, 2009], there is also no such frequency, suggesting this phenomena may be limited only to the northern Gulf of Alaska shelf. While the presence of similar frequencies in independent records do not necessarily indicate related processes, a 700-800 yr frequency range in proxies of Kuroshio Current SST was recently identified [*Jian et al.*, 2000] and attributed to the second harmonic of a Holocene 1500-yr cyclicity in North Atlantic ice rafting events [*Bond et al.*, 1997]. At this time, the Holocene relationship between northern Gulf of Alaska meltwater discharge, western Pacific SST and North Atlantic ice discharge is tenuous and requires continued analysis for verification.

The Holocene record of redox-sensitive elements shows a distinctively different behavior than that associated with the LGM (Fig. 5.6). Starting around 11.0 cal kyr BP, there is a monotonic increase in excess Mn concentrations, while there is almost zero accumulation of excess U or Mo. These respective patterns are only disrupted during (i) the PBO/Holocene transition, when minimal excess Mn and maxima in both excess U and Mo suggest productivity-induced bottom water anoxia; (ii) a single data point at 10.5 cal kyr BP, high in excess U and Mo unrelated to productivity changes that may be an anomaly in the dataset; and (iii) a maxima in excess Mn around 3,000 cal yr BP. Interpreted purely in qualitative terms of bottom-water oxygenation, it appears that the Holocene Gulf of Alaska continental slope has become progressively more oxygen-rich despite the higher Holocene export productivity. This increasingly oxic bottom water

may be related to a number of factors, including enhanced vertical mixing, better ventilation of deep waters, or reduced remineralization rates of sinking particles. Because none of these conditions seem likely given the Gulf of Alaska is in the modern North Pacific Oxygen Minimum Zone [*Paulmier and Ruiz-Pino*, 2009], an alternative explanation is that the Mn/Al ratio of *McLennen* [1995] does not adequately describe the bulk detrital sediment composition along the Gulf of Alaska margin for excess element calculations. Nonetheless, it is clear the lack of Holocene enrichments in Mo and U, and at least some precipitation of authigenic Mn, are likely due to at least suboxic dissolved O_2 concentrations [*Calvert and Pedersen*, 1993; *Tribovillard et al.*, 2006].

5.5.2 The Bølling-Alleröd in the northern Gulf of Alaska: decoupling between glaciomarine sedimentation and the North Pacific marine ecosystem

The Bølling-Alleröd period occurs between 14.7 – 12.9 cal kyr BP in the North Atlantic region [*Steffensen et al.*, 2008]. This time range corresponds to an interval of radical change in all biogenic proxies in core EW0408-85JC. Sedimentation rates rapidly decrease by an order-of-magnitude to 0.03 cm·yr^{-1}, while biogenic siliceous and marine TOC concentrations double relative to prior LGM values (Fig. 5.3a, d). Sedimentary $\delta^{13}C$ and $\delta^{15}N$ ratios become relatively enriched (-23.15 ±0.24‰ and 5.65±0.31‰, respectively). In addition, the combined presence of excess Mo, U, and Mn concentrations, as well as 1- to 2-cm-thick laminations (Fig. 5.6), are all suggestive of dysoxic-to-anoxic bottom water oxygen concentrations.

This data collectively suggests enhanced primary productivity, though as described above, the biogenic export flux calculations do not show an increase likely due to the sedimentation rate changes. However, micropaleontology results from EW0408-85JC [*Barron et al.*, 2009] show that the B-A is associated with increased percentages of the diatoms *Thalassiosira pacifica* and *Neodenticula seminae* and the silicoflagellate *Distephanus speculum speculum*, all of which are considered to be diagnostic of high primary productivity conditions. Considered alongside the biogenic sediment concentrations, both lines of evidence argue for enhanced marine ecosystem productivity during the B-A. The enriched $\delta^{15}N$ values are thus consistent with enhanced nitrate

assimilation to the point of either almost complete consumption of the residual nitrate pool [*Altabet*, 2006; *Knies et al.*, 2007], or mild denitrification [*Altabet et al.*, 1995; *Ganeshram et al.*, 1995]. This intense productivity then seems likely responsible for the generation of the low bottom-water oxygen concentrations, probably facilitated by enhanced export of organic matter to the benthos and remineralization of sinking particulates within the water column.

While it appears that abrupt deglacial shifts in ecosystem parameters in the Gulf of Alaska correspond to the timing of similar paleoceanographic changes throughout the Pacific and Atlantic Oceans [*Zheng et al.*, 2000; *Dean*, 2007], the detrital element record of EW0408-85JC does not correspond to such abrupt changes. Given its small degree of variability, the most straightforward interpretation of the LGM detrital element signature (Figs. 5.7 and 5.8) is that it represents CIS sediment delivery, given that glacial sediment transport processes tend to homogenize entrained sediment from multiple sources [*Klassen*, 2001]. Therefore, despite the diverse lithologies of southern Alaska [*Beikman*, 1994], the large extent of the CIS would likely homogenize these distinctive geochemical signatures and produce the low variability refractory signature preserved in EW0408-85JC. The massive diamicton lithology, dominantly terrestrial organic matter provenance, and sedimentation rates associated with the LGM section (Unit 4; Fig. 5.2) are also consistent with glacial delivery, though these rates are too low to represent a full proximal glaciomarine sedimentation regime [*Jaeger et al.*, 1998; *Ullrich et al.*, 2009] suggesting instead the CIS margin is tens of kilometers away from the EW0408-85JC site.

The lack of a discernable trend in the detrital sediment provenance during the LGM/B-A transition despite the high peak in primary productivity suggests a temporal decoupling between CIS glaciomarine dynamics and the North Pacific marine ecosystem. The correspondence between the productivity dataset in EW0408-85JC and other Northern Hemisphere paleoenvironmental datasets during this time interval is indicative of a rapid environmental perturbation of global extent, possibly transmitted from the North Atlantic Ocean to the Pacific via shifts in atmospheric circulation [*Dean*, 2007].

Unlike those other sites, however, EW0408-85JC contains an exclusively subarctic climatic signature that is controlled to some degree by local CIS dynamics during the LGM and the subsequent B-A. *Barron et al.* [2009] present diatom and silicoflagellate population data from EW0408-85JC, and while their assemblages are barren during the LGM, the B-A populations show evidence of relatively high concentrations of sea-ice and sea-ice related diatom groups and the subarctic silicoflagellate *Distephanus octangulatus*. Combined with the detrital element data, these multiple lines of evidence indicate proximity to the CIS still exerted some control over local water conditions, in that while the B-A is classically considered a global period of warming, the micropaleontology data clearly show the northern Gulf of Alaska remained cold and contained at least seasonal sea ice. A terrestrial ice advance along the Kenai Peninsula during the Elmendorf stade that peaked at 14,400 calibrated yrs BP agrees with this interpretation [*Reger et al.*, 2008], as does an increase in CIS-derived IRD observed along the Vancouver Island continental shelf between 14,600 – 14,800 cal yrs BP [*Hendy and Cosma*, 2008]. A millennial-scale sea surface environmental reconstruction using dinocyst transfer functions from core PAR87A-10 in the central Gulf of Alaska indicate warming winter and summer SST conditions, but decreasing salinity and a concomitant increase in sea ice during the deglacial transition [*De Vernal and Pedersen*, 1997]. This sea ice expansion dropped from approximately 8 mths·yr^{-1} at 15.3 cal kyr BP to 0 by 10.2 cal kyr BP, encompassing both the B-A and YD chronozones identified in EW0408-85JC.

Why does this B-A disconnect between northern Gulf of Alaska CIS dynamics and the productivity status of North Pacific marine ecosystems occur? One explanation is that the increased thermal "inertia" of the extensive CIS dampens response to abrupt environmental shifts, relative to the marine system which may be more sensitive to perturbations. The transgressive pattern of onset of the Holocene Thermal Maximum across arctic and temperate North America is a good example of this damping behavior related to the position of the Laurentide Ice Sheet [*Kaufman et al.*, 2004]. The decreased surface salinities identified by *De Vernal and Pedersen* [1997], presumably derived from

meltwater from the receding CIS, would also have strengthened stratification along the continental shelf of the Gulf of Alaska, as well as enhanced the Alaska Coastal Current. The positive feedback cycle between modern freshwater discharge, Alaska Coastal Current transport, and primary productivity [*Mundy and Olsson*, 2005] suggests that the coastal B-A productivity maxima was intimately related to the adjacent CIS margin and its associated meltwater discharge. Therefore, the modern feedback paradigm appears sufficient as a first-order approximation to describe the anomalous B-A conditions that occurred along the Gulf of Alaska margin 15,000 years ago.

5.5.3 Evidence for modulation of the N cycle and productivity by micronutrient availability?

Enhanced stratification from CIS meltwater during the B-A alone seems insufficient to explain the heightened productivity shifts preserved along the Gulf of Alaska slope relative to modern Holocene productivity. While the freshwater-stratification-productivity positive feedback mechanism agrees with modern observations [*Gargett*, 1997], stratification by itself does not enhance primary productivity. Sustained phytoplankton blooms also require macro- and micronutrients, and it is well established that the downwelling margin of the Subarctic Northeast Pacific Ocean is an HNLC region (Fig. 1a), and that productivity within the Alaska Gyre is dominantly iron limited [*Martin*, 1990; *Harrison et al.*, 1999]. Given the changing environmental conditions associated with the B-A, perhaps indirect effects of regional climate change are responsible for this large productivity peak?

One potential climate-induced environmental shift may be a relaxation of iron limitation in the nearshore Gulf of Alaska. Iron is an important component of the marine food web and the N cycle. The nitrogen-fixation pathway utilized by diazotrophic cyanobacteria requires dissolved Fe [*Falkowski et al.*, 1998], while nitrate assimilation by large celled phytoplankton is inhibited by low ambient Fe concentrations [*Price et al.*, 1994]. Several well-documented iron enrichment experiments in the North Pacific have initiated substantial phytoplankton blooms, particularly among large-celled diatoms, and resulted in significant reductions in nitrate [e.g. *Coale et al.*, 1996; *Boyd et al.*, 2004].

While aeolian dust has been the favored mechanism for alleviating iron limitation in HNLC regions, two recent papers have considered iron fluxes related to continental shelf sedimentation as equally important. *Lam and Bishop* [2008] examined the concentration and speciation of dissolved iron along both the Northwest and Northeast Pacific Ocean margins, and found a subsurface particulate Fe maxima. Lam and Bishop also discovered that the particulate Fe maxima in the Northwest Pacific contained a relatively large contribution of Fe^{2+} (up to 25% of the total Fe) diagnostic of iron derived from the dissolution of primary minerals along the Kuril/Kamchatka margin. A series of leaching experiments by *Schroth et al.* [2009] on samples of Alaskan glacial flour, and dust from the Chinese Loess Plateau and Saharan Africa, showed that iron derived from glacial flour was an order of magnitude more soluble than iron from either dust sample. *Schroth et al.* [2009] also examined the iron speciation of these samples, as well as the Fe-bearing mineral phases, and found that Alaskan glacial flour was overwhelmingly dominated by Fe^{2+} phases: 44% hornblende, 40% biotite, 9% ferrihydrite, and 7% magnetite. This assemblage is equivalent to an $Fe^{2+}:Fe^{3+}$ ratio of 79% : 21%. The relatively high concentration of Fe^{2+} is significant because Fe^{2+}-dominated primary mineral phases tend to be more soluble under oxidizing water conditions [*Moffett*, 2001], implying higher dissolution of iron into the water column where it would become more bioavailable. Indeed, the addition of ferrous sulphate ($Fe^{2+}SO_4$) was the basis by which large phytoplankton blooms were induced during the SERIES iron addition experiment in the Gulf of Alaska [*Boyd et al.*, 2004].

The calculated $Fe^{2+}:Fe^{3+}$ ratio of all Fe-bearing phases in the XRD samples from EW0408-85JC (Fig. 5.11) agree broadly with the iron speciation results of *Schroth et al.* [2009] on modern Alaskan glacial flour from Matanuska Glacier outwash, with minor differences in the Fe-bearing mineral assemblage. In the case of the amphibole and chlorite concentrations, both phases are likely due to detrital sediment influx to the EW0408-85JC site, as has been observed in other mineralogy studies of the northern Gulf of Alaska shelf [*Slatt and Piper*, 1974; *Feder et al.*, 1976; *Naidu et al.*, 1976; *Naidu and Mowatt*, 1983]. Goethite is a weathering product derived from the oxidation of primary

ferrosilicates and other oxyhydroxides, particularly ferrihydrite, and is the most thermodynamically stable oxyhydroxide in cold natural waters [*Langmuir*, 1997]. While goethite was not found in the study of *Schroth et al.* [2009], ferrihydrite accounted for approximately 10-20% of the Fe-bearing species in different samples of Alaskan glacial flour, suggesting the goethite results may be due to geochemical reactions during transport from terrestrial outcrop sources to the marine continental shelf sediment sink. This explanation also accounts for the relatively smaller percentages of biotite and amphibole. Therefore, the results of the iron speciation calculations based on the XRD results appear analogous with those of modern Alaskan glacial flour [*Schroth et al.*, 2009]. While there are some minor differences between the calculated $Fe^{2+}:Fe^{3+}$ ratios between the Holocene, LGM, and B-A intervals (Fig. 5.11), it seems unlikely that the 2-3% increase in Fe^{2+} concentrations during the B-A is significant. Further statistical testing of this relationship is hampered by the small B-A sample population size.

Because there appears to be little covariation between the productivity and mineral-hosted Fe^{2+} concentrations, the hypothesis of a relaxation of iron limitation during the B-A as an explanation for the enhanced nitrate utilization leading to the pronounced productivity maxima requires further testing. The total Fe concentration measured by ICP-MS shows an abrupt increase at the LGM/B-A boundary, as do both opal concentrations and sedimentary $\delta^{15}N$ (Fig. 5.12). The synchronous increase of these three different measurements at this boundary argue for a related process. Further investigations of alternative Fe phases that could account for this large shift in total Fe concentrations is required. The difference between the total XRD-estimated and ICP-MS iron concentrations (Fig. 5.10b) suggests a phase invisible to XRD analysis is important. Therefore, the application of a sequential chemical leaching method to distinguish between exchangeable, carbonate-bound, reducible, oxidizable, and detrital Fe phases is underway [*Chester and Hughes*, 1967; *Tessier et al.*, 1979; *Filgueiras et al.*, 2002].

The Fe-$\delta^{15}N$-opal pattern seen along the Gulf of Alaska slope during the B-A is likely insufficient to explain similar increases in productivity seen along other regions of the coastal North Pacific Ocean. The Gulf of Alaska is unique in this case due to the

proximity of the CIS to this location. A recent compilation of Northeast Pacific Ocean continental shelf sedimentary $\delta^{15}N$ records from northern Mexico to ODP Site 887 in the central Gulf of Alaska show remarkable correspondence in enriched $\delta^{15}N$ during the B-A, with values exceeding 9‰ in the south, and 7.5 – 8‰ in the far north [*Chang et al.*, 2008]. While these authors attribute this latitudinal gradient to transport of ^{15}N-enriched nitrate northwards by the California Undercurrent as suggested by *Galbraith et al.* [2008a], increased iron availability and associated increased nitrate utilization for both the Gulf of Alaska and the Vancouver Island continental shelves could be an alternative explanation. Further studies of past iron accumulation and speciation patterns from the Northeast Pacific margin are required to fully evaluate this alternate hypothesis.

5.5.4 Carbon cycle perturbations during the Younger Dryas and 8000 yr BP?

Two sections of the EW0408-85JC sedimentary $\delta^{13}C$ record are difficult to explain in either productivity or organic matter provenance terms. The Younger Dryas period is marked with reduced opal, TOC, and a low molar C/N ratio (Fig. 5.6), which indicate low plankton-derived export productivity and relatively low contributions (37%) of terrestrial-derived organic matter (Fig. 5.5). Under the assumption that sedimentary $\delta^{13}C$ can be used as a qualitative estimator of nutrient availability under dominantly authochtonous marine organic matter accumulation conditions [*Rau et al.*, 1989; *Laws et al.*, 1995], then low productivity would favor nutrient-replete conditions and hence more depleted $\delta^{13}C$ values. Instead, the opposite is true in that the YD data indicates enriched $\delta^{13}C$ values (Fig. 5.6). While sedimentary $\delta^{13}C$ ratios are not the ideal proxy for discussing marine C cycle dynamics, the EW0408-85JC data warrant explanation nonetheless.

Elevated excess Mn values in EW0408-85JC indicate an oxic water column, consistent with increased vertical mixing of YD surface waters observed as far south as the Santa Barbara Basin [*Kennett and Ingram*, 1995]. Several coastal Alaskan sites indicate abrupt environmental shifts during the YD, generally trending towards more cryophilic and/or xerophilic vegetation [*Engstrom et al.*, 1990; *Mathewes*, 1993;

Mathewes et al., 1993; *Peteet and Mann,* 1994; *Bigelow and Edwards,* 2001], though some coastal areas lack similarly persuasive evidence [*Ager,* 1998]. A recent review of terrestrial YD records from Beringia coupled with synoptic-scale atmospheric modeling results point to coastal Alaskan records being forced by enhancements of both the wintertime Aleutian Low and the summertime Pacific Subtropical High pressure cells, coupled with complex local topographic effects [*Kokorowski et al.,* 2008], ultimately responding to cooling of North Pacific sea surface temperatures [*Kiefer and Kienast,* 2005].

Carbon cycle modeling efforts based on data from the Cariaco Basin and GISP2 ice core show maxima in atmospheric $\Delta^{14}C$ during the YD can be accounted for by carbon cycle perturbations forced by changes in global ocean circulation during this abrupt climate event [*Hughen et al.,* 2004]. Given the multiple proxy datasets from EW0408-85JC, the YD sedimentary $\delta^{13}C$ data seems best explained by an ocean circulation perturbation manifested by enriched $\delta^{13}C$ values. These relatively high $\delta^{13}C$ samples likely reflect a change in isotopic source caused by an increase in ventilation rates of the deep Pacific carbon pool. An enhanced YD Aleutian Low cell would increase the rate of upwelling in the Alaska Gyre thus enhancing transport of deep North Pacific waters to the Gulf of Alaska slope. As a result, any geochemical signal present within this deep water mass could be expressed at the relatively shallow EW0408085JC site. However, *McManus et al.* [2004] show convincing evidence for a reduction in North Atlantic Deep Water (NADW) formation during the YD using excess $^{231}Pa/^{230}Th$ ratios as a proxy for particle flux rate. Linking the Santa Barbara Basin bioturbation index [*Kennett and Ingram,* 1995] with benthic foraminiferal isotope data from the Northeast Pacific abyssal plain [*Lund and Mix,* 1998] and planktic foraminferal isotope data from the northern California shelf [*Mix et al.,* 1999], Lund and Mix suggest the spatial and depth patterns of enriched North Pacific $\delta^{13}C$ values during periods of reduced NADW formation are due to the "Antarctic flywheel" mechanism, in which increased southward transport of North Pacific Deep Water occurs as a necessity for compensating flow to the Southern Ocean due to the reduction in southward NADW

flow. This mechanism thus decreases the residence time of North Pacific Deep Water during the YD and enriches the $\delta^{13}C$ pool, and could account for increased Alaska Gyre upwelling and the preservation of enriched sedimentary $\delta^{13}C$ values along the Gulf of Alaska slope.

A second period of enriched sedimentary $\delta^{13}C$ in EW0408-85JC occurs between 7800-8400 cal yrs BP (Fig. 5.6). This early Holocene period coincides with a short-lived switch from Holocene Thermal Maximum conditions [*Kaufman et al.*, 2004] to relatively cooler and/or drier conditions based on several terrestrial Alaskan records [*Denton and Karlen*, 1973; *Andreev and Peteet*, 1997; *Mason et al.*, 2001]. It also corresponds to a very rapid decrease in the Mt. Logan ice core $\delta^{18}O$ record [*Fisher et al.*, 2008], followed by a 500-yr-long interval of nearly constant composition that is coeval with the sedimentary $\delta^{13}C$ perturbation in EW0408-85JC. This anomalous interval in EW0408-85JC encompasses the time range of the "8200 yr event," an early Holocene abrupt cooling interval recognized in the Greenland ice core $\delta^{18}O$ datasets and lasting approximately 200-300 years [*Alley and Agustsdottir*, 2005]. This climate event is not globally recognized, and thus is interpreted to represent a somewhat weaker manifestation of YD-like perturbations, yet this time interval contains the most enriched $\delta^{13}C$ values in the entire EW0408-85JC core. The longer time span in EW0408-85JC associated with the "8200 yr event" may be an artifact of bioturbation. Furthermore, unlike the YD sedimentary $\delta^{13}C$ signal preserved in EW0408-85JC, this period is also marked with less enriched $\delta^{15}N$ values indicative of normal levels of nitrate utilization for the Gulf of Alaska [*Wu et al.*, 1997]. Because most North Pacific marine records either have resolution too low to recognize sub-millenial events, or poor Holocene recovery, it is difficult to assess Pacific-wide forcing mechanisms for this biogeochemical signal. Nevertheless, an increase in North Pacific ventilation rates would also be consistent with these enriched sedimentary $\delta^{13}C$ values.

5.6 Conclusions

The productivity, sedimentary isotope and detrital mineral accumulation patterns preserved in core EW0408-85JC from the northern Gulf of Alaska slope provides a detailed reconstruction of many environmental parameters at this site since the LGM. The low concentrations of siliceous primary producers during the LGM relative to Holocene levels suggests this shelf region experienced reduced productivity despite increased iron availability inferred from increased LGM aeolian dust fluxes [*Kienast et al.*, 2004]. An increase in productivity during the B-A is associated with an increase in nitrate utilization efficiency and total iron concentrations, suggesting an ecosystem feedback potentially driven by an interplay between the N cycle and micronutrient availability within the context of Cordilleran Ice Sheet glaciomarine dynamics. This period of increased productivity is observed throughout the marginal North Pacific Ocean, and while these other locations are certainly not proximal to icesheets, perhaps increased fluvial discharge and/or upwelling of dissolved iron was related to hypothesized changes in B-A atmospheric dynamics that lead to these productivity maxima [*Dean*, 2007].

The strong indication of abrupt environmental changes along the northern Gulf of Alaska continental slope reinforces the idea that high-latitude regions are sensitive to both global and regional climate forcing processes. The distinctive indication of productivity and isotopic perturbations preserved during the YD, the B-A, and the PBO highlight the sensitivity of marine ecosystems to abrupt change. However, it is also clear that the retreat of the CIS lagged the shifts in the marine ecosystem by over a thousand years. When considered in this context, it is apparent that the marine ecosystem is a much more sensitive system than glacial icesheets for highlighting the effects of rapid climate shifts. However, the marine ecosystem also has a level of inherent resiliency, in that it can reach a new equilibrium relatively quickly under radically different environmental conditions as observed in the equivalent levels of siliceous productivity seen during the YD and the early Holocene, two periods with radically different climatic configurations. These productivity fluctuations have broad implications for the marine

environment, as well as coastal terrestrial environments that depend on marine-derived nutrient supplies.

5.7   Acknowledgements

5.8   Figures

Figure 5.1: (a) Location of EW0408-85JC and generalized surface circulation of the North Pacific Ocean. Shading and contours indicate dissolved nitrate concentrations (μmoles·L^{-1}; data from 2005 World Ocean Atlas and plotted with Ocean Data View). AC = Alaska Current, ACC = Alaska Coastal Current (white line), AG = Alaska Gyre, AS = Alaska Stream, CC = California Current, KaC = Kamchatka Current, KuC = Kuroshio Current. (b) Northern Gulf of Alaska shelf. Solid white lines are 1000-m-interval bathymetry contours. Dashed white line indicates LGM ice margin [Kaufman and Manley, 2004]. Base MODIS satellite image taken 22 August 2003 [http://visibleearth.nasa.gov, catalogue number 5723]. Note extensive light-colored sediment plumes traveling west along shelf.

Lithostratigraphy

Gamma-ray attenuated wet bulk density (g·cm⁻³)

Calibrated years BP

Homogenous
dark gray silty clay

Massive dark gray silty
clay with dispersed sand

Gray silty clay with
olive-brown laminations

Massive dark gray diamicton
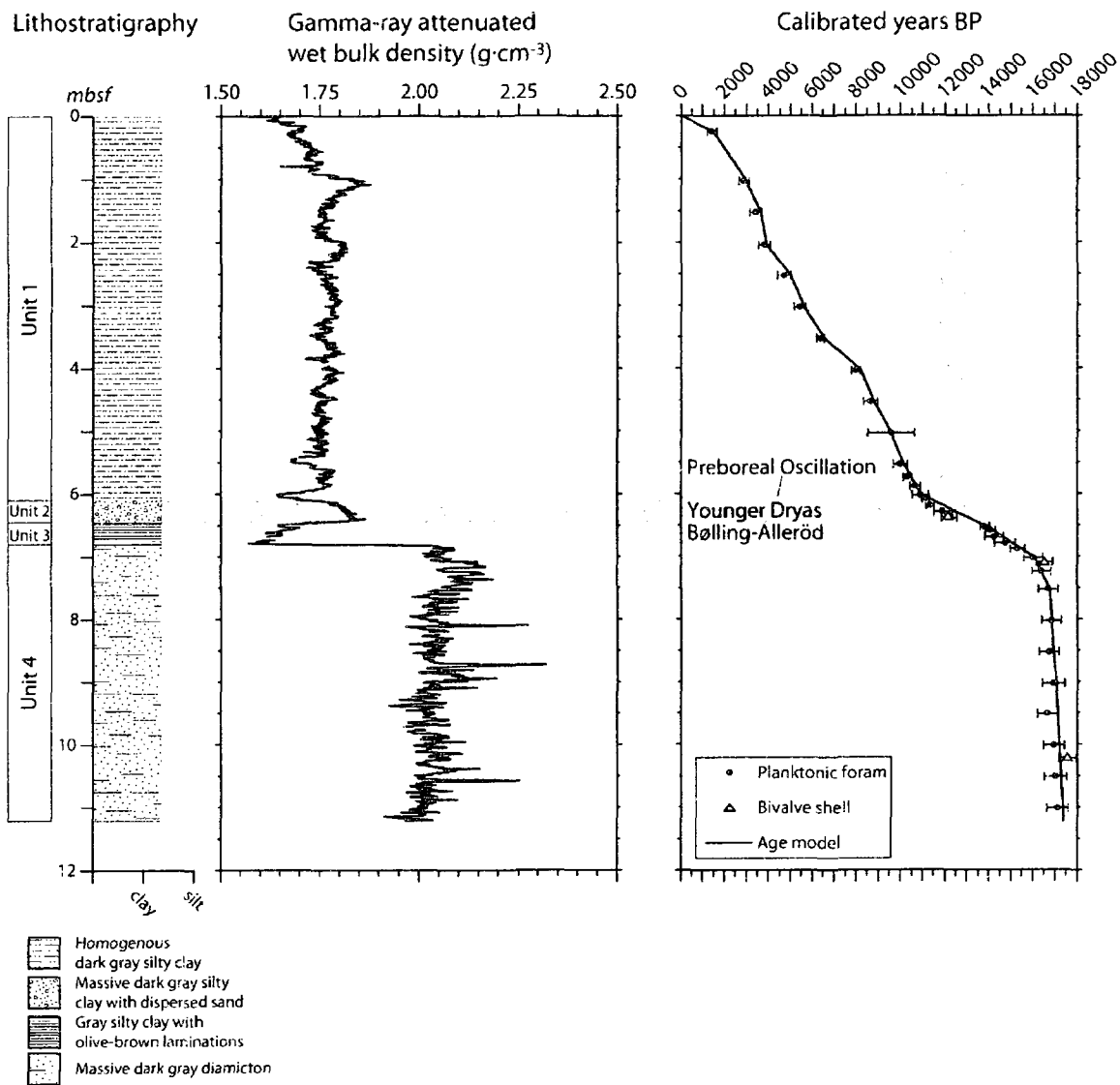
Figure 5.2: Lithological characteristics of EW0408-85JC and age-depth model of *Davies et al.* [in prep.].
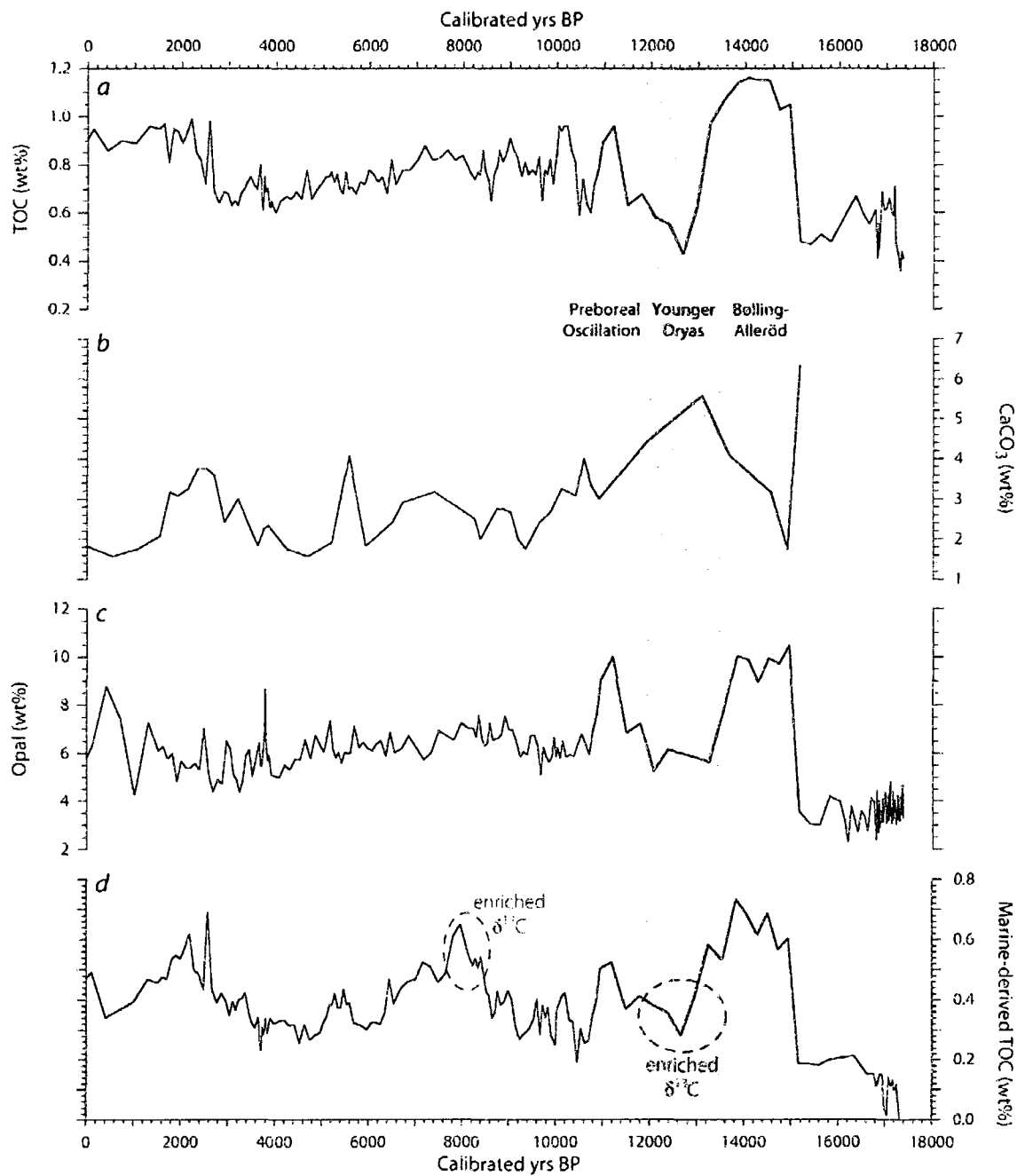
Figure 5.3: EW0408-85JC biogenic sediment concentrations for (a) total organic carbon (TOC), (b) CaCO₃, (c) opal, and (d) marine-derived TOC, estimated by use of Eq. 3.
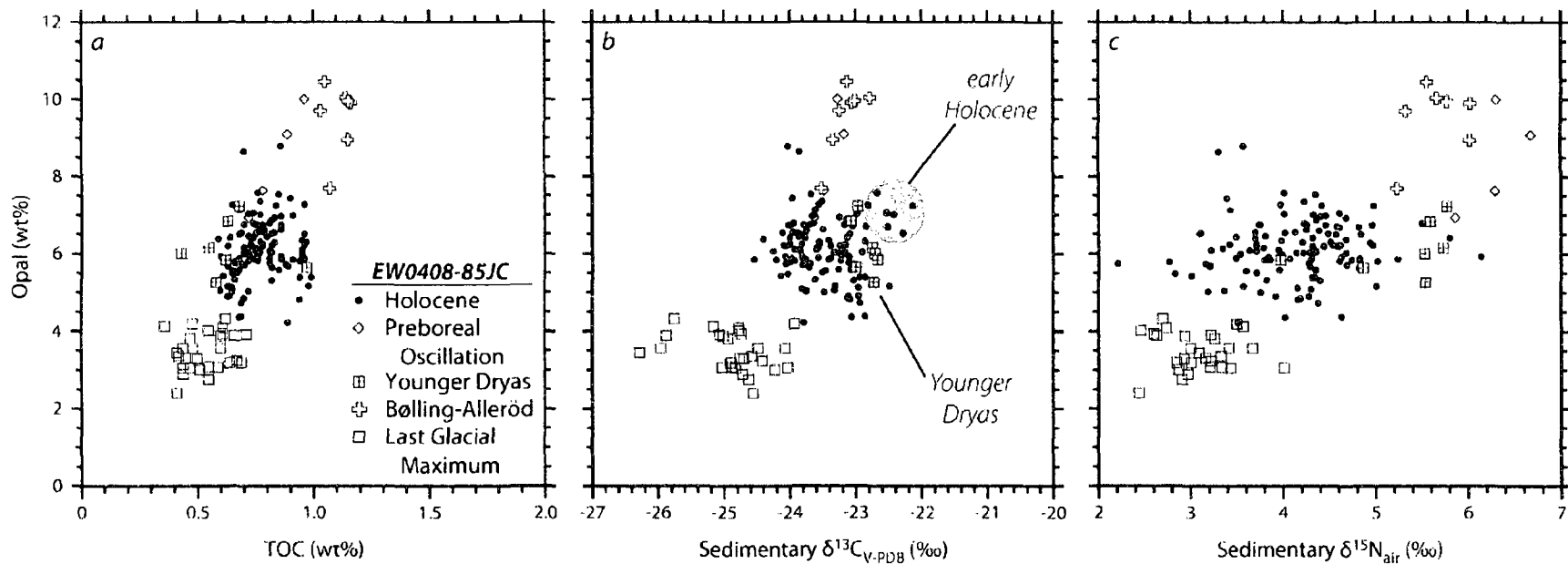
Figure 5.4: Bivariate relationships between opal and (a) TOC, (b) sedimentary $\delta^{13}C$, and (c) sedimentary $\delta^{15}N$. Natural-log-transformed correlation coefficient between TOC and opal is significant at the 99% confidence level ($n = 165$, $r = 0.718$, $p < 0.01$). During both the Younger Dryas and early Holocene, $\delta^{13}C$ values are ~+1‰ enriched relative to mid- and late Holocene samples with similar opal concentrations (see text for further discussion).

EW0408-85JC

- ● Holocene
- ○ Preboreal Oscillation
- ⊡ Younger Dryas
- ⊹ Bølling-Alleröd
- ☐ Last Glacial Maximum

modern Gulf of Alaska

- ◇ Inlets north of 58°N
- ○ Ocean north of 58°N
- ⊞ Ocean south of 58°N
- ○ Northern Gulf of Alaska rivers
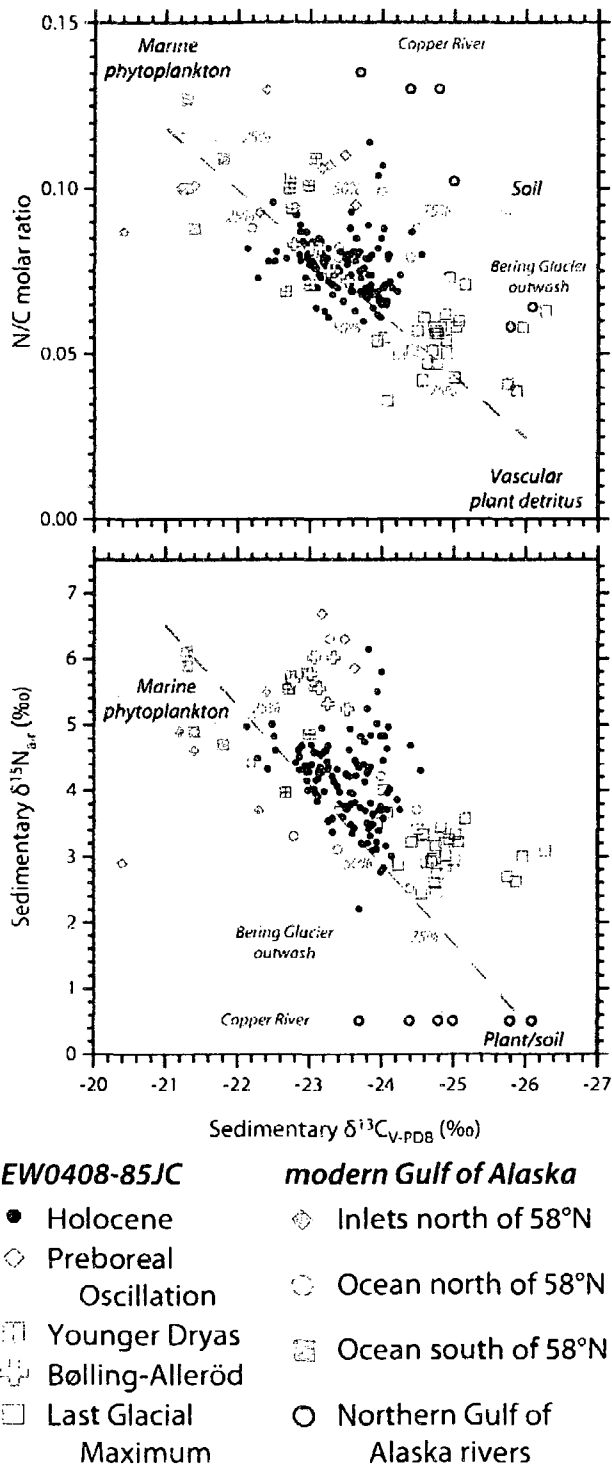
Figure 5.5: Organic matter provenance diagrams. Modern Gulf of Alaska surface sediment data from *Walinsky et al.* [2009]. Calibrated lines indicate percentage of terrestrial-derived organic matter, using a linear endmember mixing model as described in the text. Also note that no δ^{15}N data was available for the modern river samples, so a default value of +0.5‰ was used for plotting purposes.
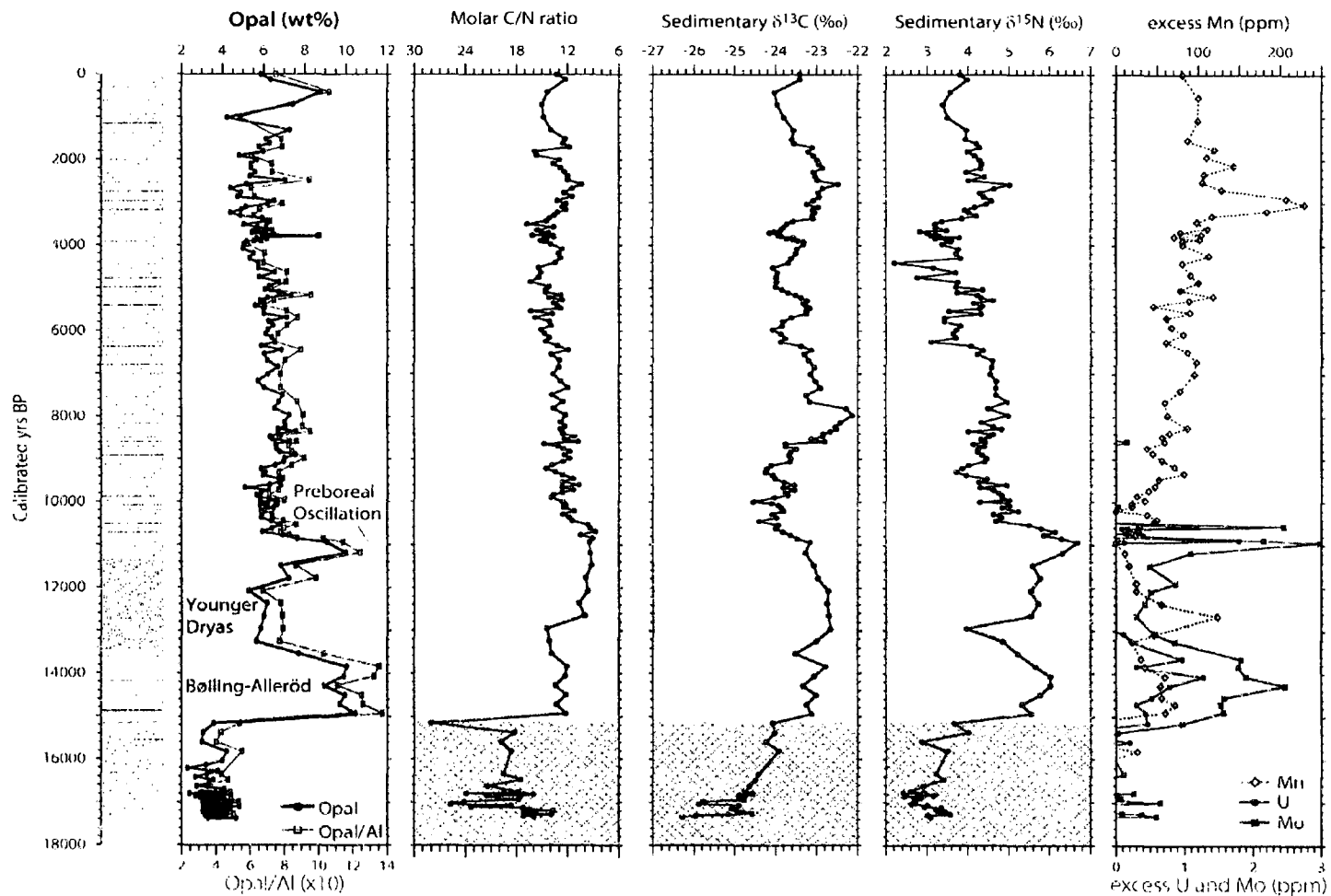
Figure 5.6: EW0408-85JC downcore results for opal, molar C/N ratios, carbonate-free sedimentary isotope data, and redox-sensitive element concentrations. Lithology patterns same as in Figure 5.3. Diamond pattern at bottom of molar C/N, $\delta^{13}C$, and $\delta^{15}N$ data indicate periods exceeding 70% terrestrial-derived organic matter as calculated from Figure 5.5.
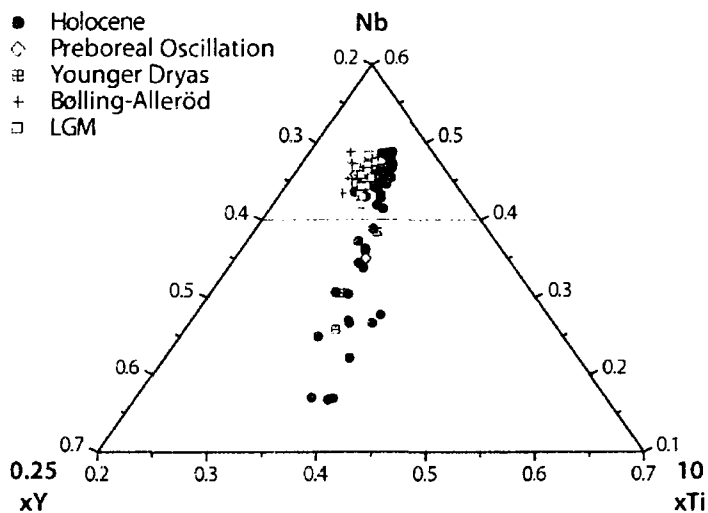
Figure 5.7: Refractory element ternary diagram. Titanium and ytterium coefficients used for scaling purposes to maximize dispersion of data points. Values along axes indicate normalized concentrations for this three-component system.
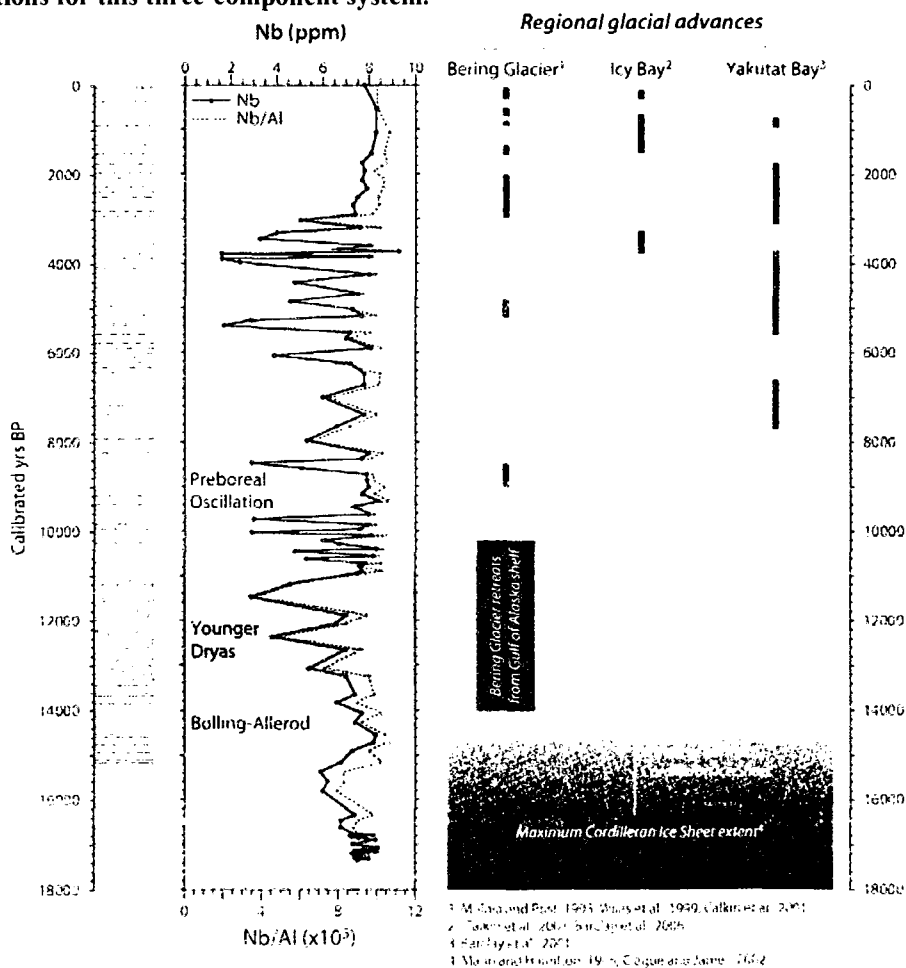
Figure 5.8: EW0408-85JC downcore refractory element accumulation trends for niobium relative to local glacial advance phases during the LGM and Holocene.

Prepared compositions

a

Kaolinite (33 wt%)
Quartz (33 wt%)
Na-rich smectite (33 wt%)
ZnO

Kaolinite (33.7 wt%)
Quartz (34.4 wt%)
Na-rich smectite (31.8 wt%)

degree-of-fit: 0.0809

Kaolinite (5 wt%)
Quartz (45 wt%)
Na-rich smectite (20 wt%)
Fe-rich smectite (30 wt%)
ZnO

Kaolinite (11.3 wt%)
Quartz (36.7 wt%)
Na-rich smectite (22.7 wt%)
Fe-rich smectite(29.3 wt%)

degree-of-fit: 0.0897

Kaolinite (30 wt%)
Quartz (30 wt%)
Na-rich smectite (20 wt%)
Illite (20 wt%)
ZnO

Kaolinite (35.8 wt%)
Quartz (29.2 wt%)
Na-rich smectite (26.4 wt%)
Illite (8.6 wt%)

degree-of-fit: 0.1011

Legend

a	amphibole
ap	apatite
b	biotite
ba	barite
c	chlorite
ca	calcite
f	K-feldspar
g	goethite
i	illite
il	ilmenite
k	kaolinite
m	muscovite
ma	magnetite
p	plagioclase
py	pyrite
q	quartz
s	smectite
se	serpentine
z	zincite (standard)

b

Representative
Holocene pattern
EW0408-85JC, 3.57 mbsf

Representative
LGM pattern
EW0408-85JC, 11.02 mbsf

5   15   25   35   45   55   65   °2θ

c   i,m   a   se   k   g   il   ba   b   q   f   p   ca   py   ma   z

Figure 5.9: X-ray diffraction patterns and RockJock calculated compositions for (a) prepared sample mixtures and (b) representative EW0408-85JC samples from Holocene and LGM intervals. Quartz and ZnO peaks have been truncated for scaling purposes. Diagnostic mineral XRD peaks indicated in black; secondary XRD peaks in gray. Smectite and apatite primary peak variability indicated by boxes.
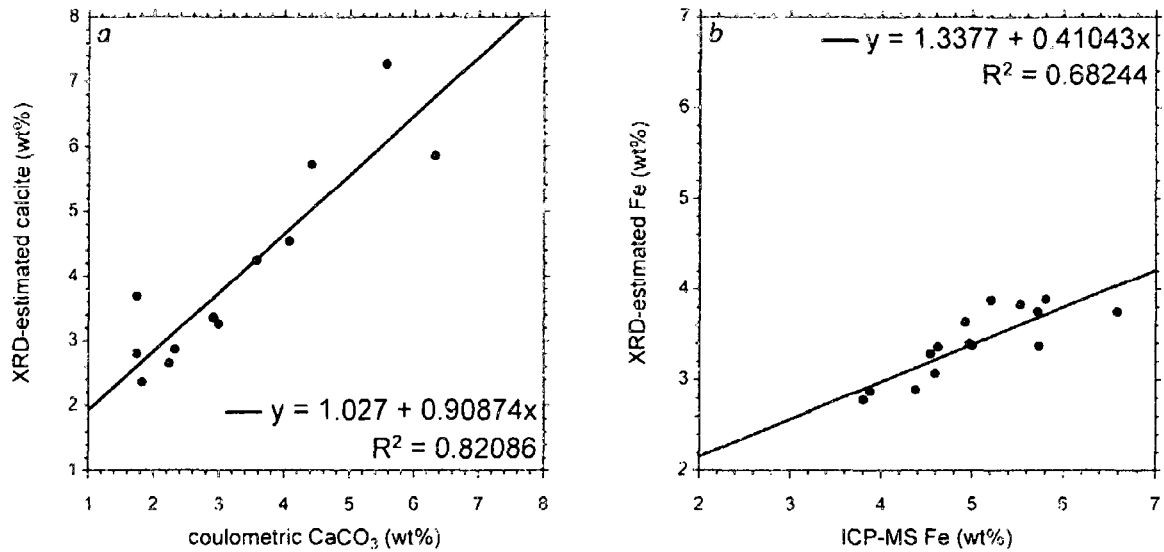
Figure 5.10: Bivariate diagrams of ICP-MS geochemical analyses and selected XRD results. (a) calcite vs $CaCO_3$ and (b) total Fe measured by ICP-MS vs total iron estimated by stoichiometric calculations of Fe-bearing minerals quantified by RockJock XRD analysis.
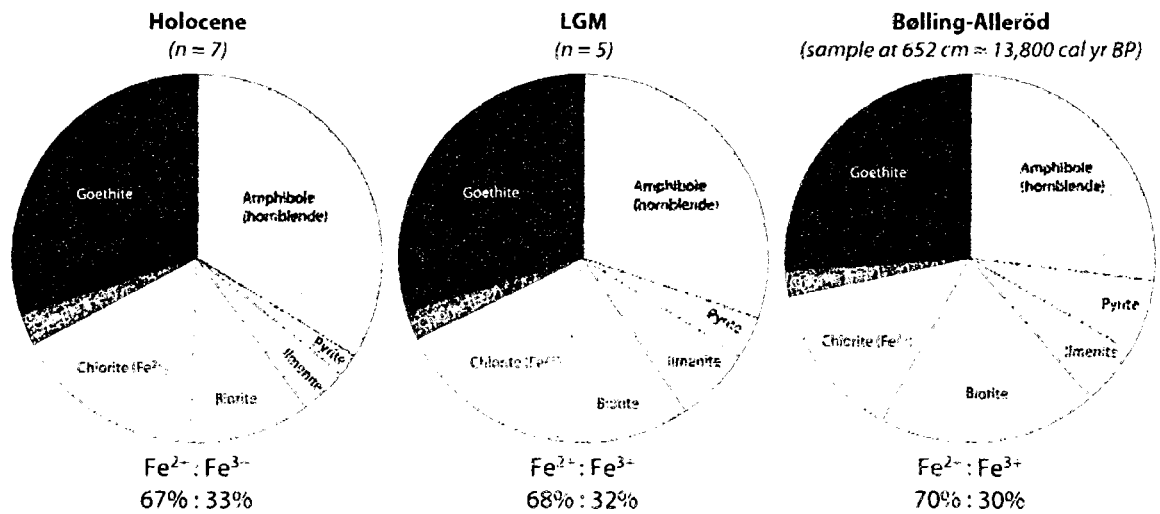
Figure 5.11: Holocene, LGM, and B-A Fe concentrations partitioned by mineral phase. Black lettering indicates Fe^{2+}-bearing phases and Fe^{3+} phases are indicated by the white lettering. Chlorite contributions of both Fe species are also depicted. The ratio of $Fe^{2+}:Fe^{3+}$ has remained fairly constant through time.
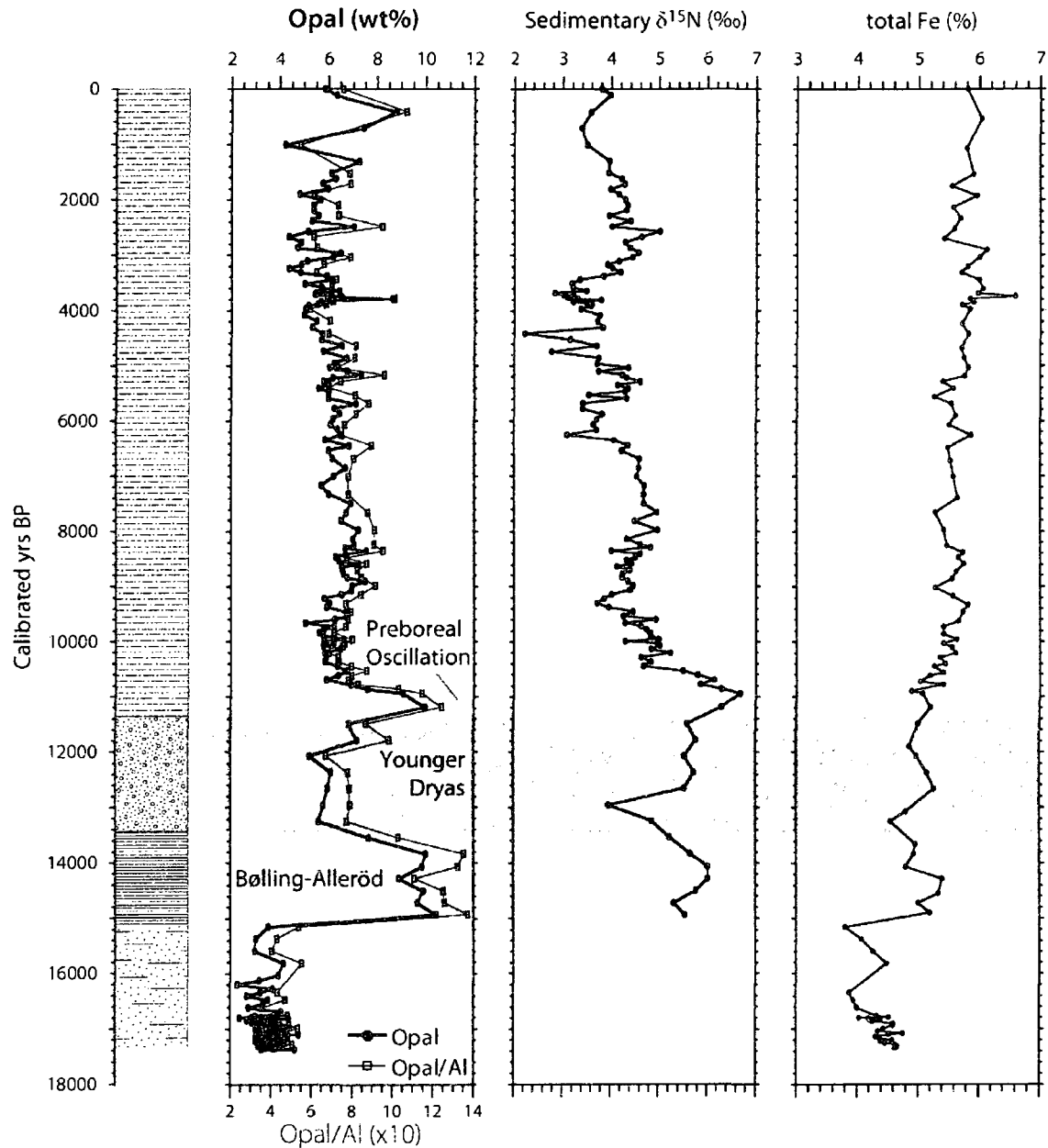
Figure 5.12: Productivity, N-cycle dynamics, and total iron availability in EW0408-85JC since the LGM. High terrigenous organic matter-dominated portions of the sedimentary $\delta^{15}N$ dataset have been excluded due to scaling considerations. The onset of the Bolling-Allerod period sees contemporaneous onset of laminated sedimentary structures, enhanced opal concentrations, enriched $\delta^{15}N$, and an increase in total Fe concentration.

5.9   Tables

Table 5.1 Mineralogical analysis calculated from composite RockJock model fit of measured XRD pattern. Values are normalized to 100 wt%.

	Holocene n = 7	Younger Dryas n = 2	Bolling-Allerod n = 2	Last Glacial Max. n = 5	all samples n = 16
calculated degree of fit	0.057 ± 0.004	0.061 ± 0.000	0.063 ± 0.001	0.060 ± 0.001	0.059 ± 0.003
K-feldspar*	5.4 ± 0.5	6.0 ± 0.5	6.5 ± 0.2	5.6 ± 0.3	5.7 ± 0.5
Plagioclase†	20.0 ± 0.9	20.6 ± 0.8	19.8 ± 1.7	21.4 ± 1.2	20.5 ± 1.2
Calcite	3.1 ± 0.6	6.5 ± 1.1	4.1 ± 0.6	3.3 ± 1.5	3.7 ± 1.5
Amphibole‡	5.6 ± 0.8	4.6 ± 0.7	4.1 ± 0.1	3.8 ± 0.6	4.7 ± 1.0
Pyrite	0.2 ± 0.1	0.3 ± 0.2	0.3 ± 0.2	0.2 ± 0.1	0.2 ± 0.2
Barite	0.7 ± 0.1	0.9 ± 0.0	0.7 ± 0.1	0.7 ± 0.1	0.7 ± 0.1
Magnetite	0.0 ± 0.0	0.0 ± 0.0	0.0 ± 0.0	0.0 ± 0.0	0.0 ± 0.0
Goethite	1.9 ± 0.4	1.5 ± 0.1	1.6 ± 0.1	1.4 ± 0.2	1.6 ± 0.4
Apatite	1.5 ± 0.3	1.7 ± 0.2	1.9 ± 0.2	1.6 ± 0.2	1.6 ± 0.3
Ilmenite	0.4 ± 0.1	0.6 ± 0.1	0.6 ± 0.1	0.5 ± 0.1	0.5 ± 0.1
Quartz	14.2 ± 0.8	16.7 ± 0.4	12.6 ± 0.5	20.0 ± 3.8	16.1 ± 3.6
Kaolinite	4.4 ± 1.1	5.5 ± 0.7	6.4 ± 0.9	5.3 ± 1.1	5.0 ± 1.2
Illite	14.2 ± 2.7	12.6 ± 1.1	15.6 ± 1.0	13.4 ± 0.6	13.9 ± 1.9
Biotite	2.3 ± 0.7	2.2 ± 0.2	3.7 ± 0.2	1.9 ± 0.6	2.3 ± 0.8
Chlorite	10.8 ± 2.5	7.3 ± 0.1	7.7 ± 0.6	7.3 ± 1.6	8.9 ± 2.5
Serpentine	7.4 ± 2.0	8.4 ± 1.0	8.1 ± 0.9	8.5 ± 1.2	8.0 ± 1.6
Muscovite	8.2 ± 0.9	4.8 ± 1.1	6.2 ± 2.7	4.9 ± 2.3	6.5 ± 2.2
Non-clay subtotal	52.9 ± 2.6	59.3 ± 2.0	52.2 ± 2.7	58.6 ± 5.3	55.4 ± 4.6
Clay subtotal	47.1 ± 2.6	40.7 ± 2.0	47.8 ± 2.7	41.4 ± 5.3	44.6 ± 4.6

* as microcline
† as albite
‡ as ferrotschermakite (hornblende)

Table 5.2 EW0408-85JC biogeochemical dataset. All units are wt% unless otherwise indicated. For calculated excess elemental concentrations less than zero, values have been replaced with zeros, indicating no authigenic precipitation.

Sample depth (cm bsf)	Opal	CaCO₃	TOC	C/N ratio	Sedimentary δ¹³C (‰ V-PDB)	δ¹⁵N (‰ air)	Al	Fe	Ti	Nb (ppm)	Y (ppm)	Calculated excess Mn (ppm)	Mo (ppm)	U (ppm)
0 - 1	5.85	1.83	0.91	11.19	-23.41	3.80	7.80	5.81	0.47	7.8	18.2	81.0	0.00	0.00
2 - 3	6.34		0.95	10.58	-23.41	3.98								
7 - 8	8.79		0.36	11.76	-24.02	3.58								
9 - 10		1.58					8.25	6.04	0.50	8.3	17.2	100.9	0.00	0.00
12 - 13	7.44		0.90	12.12	-23.96	3.39								
17 - 18	4.23		0.89	11.96	-23.79	3.51								
18 - 19		1.75					7.77	5.80	0.48	8.3	17.6	99.8	0.00	0.00
22 - 23	7.28		0.96	11.28	-23.56	3.97								
27 - 28	6.11		0.95	10.65	-23.60	3.95								
28 - 29		2.08					7.79	5.91	0.48	8.1	17.7	87.9	0.00	0.00
32 - 33	6.30		0.97	10.85	-23.55	4.21								
37 - 38	5.77		0.81	10.55	-23.11	4.28								
39 - 40		3.17					7.32	5.55	0.45	7.7	17.6	119.9	0.00	0.00
42 - 43	5.99		0.95	12.84	-23.20	3.99								
47 - 48	4.82		0.94	13.03	-23.08	4.16								
48 - 49		3.08					7.92	5.97	0.49	7.8	17.9	110.5	0.00	0.00
52 - 53	5.67		0.89	11.77	-22.99	4.29								
57 - 58	5.39		0.94	11.24	-22.94	4.34								
59 - 60		3.25					7.41	5.57	0.47	7.7	18.0	143.3	0.00	0.00
62 - 63	5.39		0.99	10.99	-22.86	4.31								
67 - 68	5.59		0.85	11.18	-23.08	3.96								
69 - 70		3.75					7.66	5.70	0.48	7.9	18.3	107.4	0.00	0.00
72 - 73	5.31		0.82	10.14	-23.03	4.40								
77 - 78	7.04		0.72	10.59	-22.98	4.01								
79 - 80		3.75					7.43	5.59	0.47	7.5	18.3	105.4	0.00	0.00
82 - 83	5.16		0.98	9.30	-22.48	5.01								
87 - 88	4.38		0.69	9.62	-22.86	4.63								
88 - 89		3.58					7.21	5.42	0.45	7.3	18.7	128.5	0.00	0.00
92 - 93	4.90		0.64	10.75	-22.96	4.28								
97 - 98	4.73		0.69	10.20	-22.94	4.38								
99 - 100		2.42					7.57	6.13	0.50	7.4	18.8	207.0	0.00	0.00
102 - 103	6.51		0.68	10.55	-23.09	4.57								
107 - 108	6.19		0.63	10.90	-23.24	4.44	7.85	6.01	0.46	5.0	19.7	229.2	0.00	0.00
112 - 113	5.12		0.65	10.06	-22.96	4.16								
117 - 118	4.90		0.63	10.87	-23.11	3.92								
119 - 120		3.00					7.47	5.81	0.49	7.6	18.7	183.6	0.00	0.00
122 - 123	4.36		0.68	10.51	-23.06	4.02								
127 - 128	4.85		0.70	11.29	-23.12	4.19	7.82	5.71	0.43	4.0	19.4	117.0	0.00	0.00
132 - 133	5.92		0.73	12.03	-23.10	3.84								
137 - 138	6.14		0.75	13.37	-23.59	3.35	8.57	6.00	0.44	3.3	16.8	98.2	0.00	0.00
142 - 143	5.03		0.72	13.13	-23.74	3.19								
147 - 148	5.71		0.70	12.54	-23.81	3.21								
149 - 150		1.83					8.20	6.06	0.49	8.0	17.0	111.6	0.00	0.00
152 - 153	6.44		0.80	12.50	-23.87	3.49								
157 - 158	5.48		0.65	13.34	-24.03	2.83	8.71	5.98	0.46	6.7	17.3	78.8	0.00	0.00
162 - 163	5.44		0.61	13.37	-24.14	3.01								
167 - 168	6.10		0.75	12.52	-23.93	3.22								
169 - 170		2.25					9.08	6.59	0.54	9.3	19.6	104.4	0.00	0.00
172 - 173	6.54		0.69	12.95	-23.93	3.11								
177 - 178	8.64		0.70	12.50	-23.85	3.31	8.58	5.85	0.36	1.6	17.0	71.3	0.00	0.00
182 - 183	6.15		0.70	11.50	-23.57	3.79								
187 - 188	5.68		0.63	12.31	-23.72	3.21								
189 - 190		2.33					8.10	5.91	0.48	8.0	17.2	102.2	0.00	0.00
192 - 193	5.89		0.62	12.31	-23.57	3.49								
197 - 198	5.56		0.65	12.43	-23.46	3.60	8.32	5.72	0.36	1.6	17.4	81.2	0.00	0.00
202 - 203	5.16		0.63	11.74	-23.31	3.58								
207 - 208	5.05		0.60	11.76	-23.32	3.37	8.60	5.85	0.40	2.4	17.7	81.3	0.00	0.00
212 - 213	5.00		0.65	11.56	-23.48	3.76								
217 - 218	5.52		0.67	11.05	-23.51	3.71								
219 - 220		1.75					8.04	5.72	0.47	8.0	18.4	113.0	0.00	0.00
222 - 223	5.33		0.66	11.15	-23.62	3.82								
227 - 228	5.75		0.69	11.96	-23.69	2.21	8.46	5.82	0.44	4.8	18.2	80.7	0.00	0.00
232 - 233	5.74		0.66	12.26	-24.06	3.15								
237 - 238	6.56		0.78	12.33	-23.96	3.70								
239 - 240		1.58					8.02	5.72	0.48	7.5	16.8	90.9	0.00	0.00
242 - 243	5.79		0.66	14.08	-23.99	2.77								

Table 5.2 (continued)

Sample depth (cm bsf)	Opal	CaCO₃	TOC	C/N ratio	δ¹³C (‰, V-PDB)	δ¹⁵N (‰, air)	Al	Fe	Ti	Nb (ppm)	Y (ppm)	Mn (ppm)	Mo (ppm)	U (ppm)
247 - 248	6.76		0.70	12.76	-23.98	3.75	8.34	5.75	0.44	4.6	18.4	100.2	0.00	0.00
252 - 253	6.25		0.73	12.81	-24.00	3.71								
257 - 258	6.06		0.75	11.74	-23.84	4.36	8.36	5.83	0.45	7.3	17.3	78.3	0.00	0.00
262 - 263	6.76		0.75	11.85	-23.70	3.74								
267 - 268	7.35		0.77	11.41	-23.51	4.23								
269 - 270		1.92					7.67	5.77	0.46	7.7	16.6	118.4	0.00	0.00
272 - 273	6.20		0.73	11.67	-23.38	4.32								
277 - 278	5.82		0.76	11.34	-23.23	4.61	7.87	5.40	0.38	2.9	19.7	89.3	0.00	0.00
282 - 283	6.03		0.70	11.24	-23.33	4.14								
287 - 288	5.59		0.68	11.70	-23.26	4.35	8.20	5.57	0.36	1.7	18.7	45.6	0.00	0.00
292 - 293	6.04		0.77	11.27	-23.17	4.29								
297 - 298	6.00		0.70	12.94	-23.25	3.54								
299 - 300		4.08					7.38	5.26	0.45	7.2	17.3	90.2	0.00	0.00
302 - 303	6.01		0.71	11.41	-23.25	4.32								
307 - 308	7.13		0.68	12.62	-23.62	3.43	8.12	5.54	0.43	7.0	19.1	61.3	0.00	0.00
312 - 313	6.24		0.73	13.15	-23.82	3.42								
317 - 318	6.46		0.72	12.93	-23.84	3.81								
319 - 320		1.83					7.90	5.61	0.47	8.1	16.6	67.4	0.00	0.00
322 - 323	6.21		0.78	13.15	-24.07	3.71								
327 - 328	6.10		0.76	12.30	-23.87	3.64	8.01	5.51	0.40	3.9	19.3	81.8	0.00	0.00
332 - 333	6.40		0.73	12.85	-23.77	3.70								
337 - 338	6.53		0.75	13.27	-23.88	3.10	8.75	5.88	0.47	7.2	17.0	61.0	0.00	0.00
342 - 343	5.88		0.68	11.60	-23.38	4.07								
349 - 350		2.42					7.67	5.49	0.46	7.8	16.4	86.4	0.00	0.00
352 - 353	6.03		0.72	11.80	-23.31	4.22								
357 - 358	6.19		0.78	10.98	-23.20	4.59								
358 - 359		2.92					7.67	5.53	0.48	7.8	17.5	97.4	0.00	0.00
362 - 363	6.71		0.78	10.80	-23.05	4.58								
367 - 368	6.23		0.82	11.62	-23.15	4.54	7.99	5.58	0.44	6.0	16.3	95.8	0.00	0.00
372 - 373	5.73		0.88	11.36	-23.02	4.69								
377 - 378	6.04		0.82	10.61	-22.90	4.68								
379 - 380		3.17					7.75	5.65	0.49	7.8	18.3	77.7	0.00	0.00
382 - 383	6.93		0.83	11.18	-23.25	4.68								
387 - 388	6.74		0.86	10.86	-23.17	4.96	7.69	5.28	0.43	6.6	17.8	59.5	0.00	0.00
392 - 393	6.53		0.82	11.14	-22.28	4.49								
397 - 398	7.25		0.84	11.13	-22.13	4.98	7.97	5.42	0.43	5.3	18.5	62.7	0.00	0.00
402 - 403	7.02		0.77	10.98	-22.42	4.33								
407 - 408	7.06		0.74	10.49	-22.53	4.61								
409 - 410		2.50					7.79	5.47	0.46	8.0	17.1	86.9	0.00	0.00
412 - 413	6.69		0.77	10.40	-22.51	4.82								
417 - 418	7.58		0.76	10.80	-22.67	4.01								
419 - 420		2.00					7.96	5.74	0.46	7.7	16.5	64.6	0.00	0.00
422 - 423	6.70		0.86	10.23	-22.85	4.61								
427 - 428	6.31		0.77	10.21	-22.86	4.51	8.17	5.66	0.40	2.9	15.9	56.5	0.00	0.00
432 - 433	6.41		0.74	10.43	-23.13	4.32								
437 - 438	7.26		0.65	9.10	-22.81	4.42	8.33	5.75	0.44	5.1	18.2	59.2	0.16	0.00
442 - 443	6.56		0.76	12.53	-23.76	4.13								
447 - 448	6.60		0.79	11.77	-23.75	4.39								
449 - 450		2.75					8.01	5.63	0.46	7.9	16.4	37.8	0.00	0.00
452 - 453	6.62		0.86	11.02	-23.50	4.25								
457 - 458	6.79		0.81	10.38	-23.64	4.23								
459 - 460		2.75					8.05	5.56	0.46	7.9	16.0	45.0	0.00	0.00
462 - 463	7.54		0.85	10.79	-23.68	4.35								
467 - 468	6.99		0.91	10.40	-23.63	4.46								
469 - 470		2.67					7.65	5.28	0.45	8.0	15.7	56.3	0.00	0.00
472 - 473	6.97		0.86	10.38	-23.66	4.40								
477 - 478	6.55		0.83	11.93	-24.11	4.02								
479 - 480		2.00					7.78	5.57	0.46	7.7	15.9	70.9	0.00	0.00
482 - 483	5.85		0.75	11.63	-24.21	3.86								
487 - 488	6.07		0.81	12.15	-24.25	3.71								
489 - 490		1.75					7.90	5.82	0.48	8.4	17.0	82.4	0.00	0.00
492 - 493	5.94		0.76	11.19	-24.07	3.96								
497 - 498	6.74		0.78	10.37	-24.02	4.46	8.52	5.74	0.45	7.4	16.7	52.0	0.00	0.00
502 - 503	6.75		0.76	10.74	-23.79	4.26								
507 - 508	6.29		0.83	9.59	-23.56	4.94								
509 - 510		2.42					8.09	5.67	0.47	8.0	16.4	47.2	0.00	0.00
512 - 513	5.09		0.65	10.91	-23.81	4.30								

Table 5.2 (continued)

Sample depth (cm bsf)	Opal	CaCO₃	TOC	C/N ratio	Sedimentary δ¹³C (‰ V-PDB)	δ¹⁵N (‰ air)	Al	Fe	Ti	Nb (ppm)	Y (ppm)	Calculated excess Mn (ppm)	Mo (ppm)	U (ppm)
517 - 518	6.25		0.78	10.31	-23.55	4.62	8.15	5.42	0.39	3.0	17.4	39.4	0.00	0.00
522 - 523	5.85		0.76	10.51	-23.76	4.74								
527 - 528	5.64		0.82	10.99	-23.71	4.82								
529 - 530		2.67					7.94	5.42	0.46	7.9	16.2	25.5	0.00	0.00
532 - 533	5.82		0.72	11.19	-24.04	4.83								
537 - 538	6.66						8.32	5.64	0.43	7.6	18.0	35.2	0.00	0.00
540 - 541	5.86		0.86	11.20	-24.54	4.30								
543 - 544	6.23		0.96	10.60	-24.09	4.97	8.19	5.42	0.37	2.9	16.6	19.6	0.00	0.00
547 - 548	5.81		0.94	10.26	-23.93	5.02								
549 - 550		3.25					7.71	5.56	0.45	8.1	16.2	19.6	0.04	0.00
552 - 553	6.50		0.96	10.38	-23.85	4.84								
557 - 558	5.87		0.96	9.92	-23.80	5.24	8.56	5.62	0.43	6.1	16.6	0.2	0.00	0.00
562 - 563	5.93		0.86	10.20	-24.07	4.63	8.14	5.36	0.43	6.7	16.7	38.4	0.00	0.00
567 - 568	5.88		0.81	9.49	-23.98	4.83								
569 - 570		3.08					8.01	5.45	0.47	8.3	16.1	49.8	0.00	0.00
572 - 573	6.38		0.59	9.11	-24.40	4.68	8.03	5.27	0.42	4.8	17.4	46.9	0.00	0.00
577 - 578	6.79		0.74	8.69	-23.94	5.50								
579 - 580		4.00					7.79	5.41	0.45	8.2	16.7	28.9	2.45	1.18
582 - 583	6.42		0.64	8.38	-24.00	5.80	8.05	5.20	0.42	5.3	16.6	27.0	0.17	0.09
587 - 588	5.93		0.60	7.98	-23.82	6.14								
589 - 590		3.33					7.62	5.04	0.46	7.8	16.3	14.2	0.34	0.13
592 - 593	6.93		0.72	8.80	-23.63	5.86	8.37	5.41	0.46	7.6	18.0	23.4	0.40	0.00
597 - 598	7.63		0.78	7.84	-23.48	6.29								
599 - 600		3.00					7.42	4.89	0.44	7.7	16.4	2.4	2.16	1.80
602 - 603	9.09		0.89	7.88	-23.17	6.68	7.95	5.07	0.42	7.5	18.7	0.6	2.98	0.12
607 - 608	10.01		0.96	8.15	-23.27	6.30	8.06	5.21	0.42	4.6	17.3	11.1	1.09	0.00
612 - 613	6.84		0.63	8.18	-23.07	5.59	7.89	5.00	0.38	2.9	18.1	16.3	0.49	0.00
617 - 618	7.23		0.68	8.65	-22.97	5.77								
619 - 620		4.42					7.34	4.86	0.44	7.0	15.8	25.0	0.87	0.00
622 - 623	5.27		0.58	8.52	-22.72	5.54	7.83	4.98	0.41	6.6	17.7	25.1	0.51	0.00
627 - 628	6.15		0.55	8.57	-22.75	5.73	7.90	5.15	0.40	3.8	18.5	55.4	0.42	0.00
632 - 633	6.01		0.43	8.31	-22.71	5.53	7.62	5.27	0.41	7.0	17.7	123.2	0.30	0.00
637 - 638	5.84		0.62	11.97	-22.67	3.97								
639 - 640		5.58					7.38	4.80	0.44	5.4	17.0	46.2	0.57	0.11
642 - 643	5.64		0.97	11.61	-23.00	4.86	7.29	4.55	0.39	7.0	18.2	19.8	0.86	0.24
647 - 648	7.70		1.07	11.84	-23.52	5.23								
649 - 650		4.09					7.49	4.96	0.44	7.4	15.7	30.6	1.83	0.97
652 - 653	10.04		1.14	10.03	-22.78	5.66	7.42	4.93	0.39	6.6	18.8	35.4	1.79	0.30
657 - 658	9.90		1.16	10.92	-23.06	6.02	7.47	4.80	0.40	7.7	18.3	59.6	1.90	1.28
662 - 663	8.95		1.15	11.43	-23.33	6.02	8.06	5.40	0.42	7.4	18.3	54.1	2.47	0.79
667 - 668	9.95		1.15	10.53	-23.01	5.77								
668 - 669		3.17					7.95	5.34	0.46	8.3	17.2	55.6	1.58	0.52
672 - 673	9.71		1.03	11.04	-23.25	5.32	7.71	5.01	0.40	8.2	18.5	71.6	1.53	0.30
676 - 677		1.75					7.62	5.20	0.45	7.3	17.6	60.2	1.57	0.43
677 - 678	10.46		1.05	10.01	-23.13	5.55								
682 - 683	3.57	6.33	0.48	19.88	-24.07	3.67	6.61	3.81	0.38	6.8	15.4	0.0	0.97	0.46
687 - 688	3.06		0.47	15.79	-24.03	4.01	7.12	4.08	0.37	5.9	15.9	0.0	0.02	0.00
692 - 693	3.00		0.51	20.04	-24.23	2.87	7.41	4.27	0.40	6.2	16.9	0.0	0.00	0.20
697 - 698	4.19		0.48	15.76	-23.93	3.50	7.56	4.49	0.40	5.0	17.1	25.9	0.00	0.00
702 - 703	3.99													
707 - 708	3.20													
712 - 713	2.30													
717 - 718	3.76													
722 - 723	3.25		0.67	17.17	-24.42	3.22	7.49	3.88	0.40	7.4	17.7	0.0	0.11	0.00
727 - 728	2.69													
732 - 733	3.57		0.60	15.09	-24.49	3.41	7.54	3.94	0.40	6.8	17.7	0.0	0.00	0.00
737 - 738	3.37													
742 - 743	2.76		0.55	16.89	-24.63	2.91	7.71	4.01	0.41	6.8	17.4	0.0	0.00	0.00
747 - 748	4.10													
752 - 753	3.93		0.61	17.07	-24.74	2.60	8.11	4.33	0.44	7.3	17.4	0.0	0.00	0.00
757 - 758	3.03													
762 - 763	3.30		0.50	14.76	-24.70	2.93	8.28	4.53	0.46	8.2	18.5	0.0	0.26	0.00
767 - 768	3.32													
772 - 773	2.40		0.41	17.06	-24.56	2.44	7.63	4.04	0.42	7.2	17.6	0.0	0.00	0.00
777 - 778	3.18													
782 - 783	2.89		0.44	15.92	-24.72	2.97	7.81	4.20	0.43	7.3	17.9	0.0	0.00	0.00
787 - 788	4.41													

Table 5.2 (continued)

Sample depth (cm bsf)	Opal	CaCO₃	TOC	C/N ratio	δ¹³C (‰, V-PDB)	δ¹⁵N (‰, air)	Al	Fe	Ti	Nb (ppm)	Y (ppm)	Mn (ppm)	Mo (ppm)	U (ppm)
792 - 793	3.09	0.55	15.44	-24.88	3.21	7.95	4.21	0.43	7.6	18.1	0.0	0.03	0.00
797 - 798	3.76													
802 - 803	3.31	0.45	15.26	-24.76	3.16	7.94	4.39	0.44	7.3	17.5	0.0	0.02	0.00
807 - 808	2.73													
812 - 813	3.21													
817 - 818	2.69													
821 - 822	4.02	0.55	17.78	-24.76	2.46	8.01	4.26	0.43	7.6	17.8	0.0	0.00	0.00
823 - 824	3.42													
827 - 828	3.60													
832 - 833	2.91													
837 - 838	3.20													
842 - 843	3.19	0.69	17.13	-24.90	2.85	8.33	4.60	0.47	8.3	17.8	0.0	0.07	0.00
847 - 848	3.14													
852 - 853	3.56													
857 - 858	3.29													
862 - 863	4.09	0.61	15.78	-24.78	2.74	8.32	4.59	0.45	7.9	17.8	0.0	0.00	0.00
867 - 868	3.11													
872 - 873	3.52													
877 - 878	3.81													
882 - 883	4.32	0.62	18.56	-25.75	2.70	8.07	4.44	0.44	7.3	17.9	0.0	0.65	0.00
887 - 888	4.13													
892 - 893	3.06													
897 - 898	3.26													
902 - 903	3.89	0.66	23.67	-25.87	2.63	8.00	4.35	0.45	7.8	18.3	0.0	0.00	0.00
907 - 908	3.67													
912 - 913	4.15													
917 - 918	4.26													
922 - 923	3.20	0.64	17.77	-24.89	3.01	8.45	4.76	0.47	8.4	18.4	0.0	0.00	0.00
927 - 928	3.98													
932 - 933	4.29													
937 - 938	4.83													
942 - 943	3.88	0.60	17.77	-25.01	2.94	8.50	4.53	0.45	8.1	18.4	0.0	0.00	0.00
947 - 948	3.38													
952 - 953	3.63													
957 - 958	3.66													
962 - 963	3.07	0.59	16.25	-25.03	3.34	8.10	4.31	0.44	7.4	18.0	0.0	0.00	0.00
967 - 968	3.52													
972 - 973	4.01													
973 - 974	3.21													
977 - 978	4.39													
982 - 983	3.92	0.71	15.23	-25.07	3.22	8.19	4.38	0.44	8.3	17.9	0.0	0.00	0.00
987 - 988	3.63													
992 - 993	3.28													
997 - 998	3.94													
1002 - 1003	3.82	0.47	12.38	-24.94	3.26	8.37	4.58	0.45	7.3	18.6	0.0	0.00	0.00
1007 - 1008	4.04													
1012 - 1013	4.02													
1017 - 1018	3.68													
1022 - 1023	3.05	0.44	12.81	-24.82	3.44	7.98	4.39	0.44	7.7	18.8	0.0	0.00	0.00
1027 - 1028	3.32													
1032 - 1033	3.25													
1037 - 1038	3.60													
1042 - 1043	3.36	0.42	12.68	-24.58	3.33	8.01	4.47	0.45	7.6	18.1	0.0	0.09	0.00
1047 - 1048	4.22													
1052 - 1053	3.52													
1057 - 1058	3.24													
1062 - 1063	4.13	0.36	10.47	-25.18	3.57	6.16	4.64	0.45	7.4	19.2	0.0	0.38	0.00
1067 - 1068	3.34													
1072 - 1073	3.58													
1077 - 1078	3.16													
1082 - 1083	3.57	0.44	14.07	-25.96	3.00	8.23	4.67	0.46	8.0	18.8	0.0	0.59	0.00
1087 - 1088	3.66													
1092 - 1093	3.73													
1097 - 1098	4.16													
1102 - 1103	3.46	0.41	13.99	-26.28	3.09	8.19	4.63	0.45	7.5	18.0	0.0	0.00	0.00
1107 - 1108	3.87													
1112 - 1113	3.74													
1117 - 1118	4.66													
1120 - 1121	3.29													

Table 5.3 XRD and ICP-MS nonparametric correlations that exceed 95% significance level.

Mineral(s)	Associated elements
Amphibole, chlorite, goethite	Li, Mg, Al (chlorite only), K, V, Cr, Mn, Fe, Co, Ni, Cu, Zn (goethite only)
Biotite, muscovite	Mn, Cd, Sb, U
Calcite	S, Ca, Sr, U
Pyrite, barite	S, Sr, Mo, Ag, Cd

5.10 References

Addison, J. A. (2009), High-resolution paleoceanography from the Gulf of Alaska, Subarctic Northeast Pacific Ocean, since the Last Glacial Maximum: insights into a dynamic atmosphere-ocean-ecosystem linkage at decadal timescales, PhD dissertation, 250 pp, University of Alaska Fairbanks, Fairbanks, AK.

Ager, T. A. (1998), Postglacial vegetation history of the Kachemak Bay area, Cook Inlet, South-Central Alaska, in *Geologic Studies in Alaska by the U.S. Geological Survey, 1998*, edited by K. D. Kelley and L. P. Gough, pp. 147-165, U.S. Geological Survey.

Alley, R. B., and A. M. Agustsdottir (2005), The 8k event: cause and consequences of a major Holocene abrupt climate change, *Quaternary Science Reviews*, *24*, 1123-1149.

Altabet, M. A., and R. Francois (1994), Sedimentary nitrogen isotopic ratio as a recorder for surface ocean nitrate utilization, *Global Biogeochemical Cycles*, *8*(1), 103-116.

Altabet, M. A., et al. (1995), Climate-related variations in denitrification in the Arabian Sea from sediment $^{15}N/^{14}N^{14}$ ratios, *Nature*, *373*(6514), 506-509.

Altabet, M. A. (2006), Isotopic tracers of the marine nitrogen cycle: present and past, in *Marine organic matter: biomarkers, isotopes and DNA*, edited by O. Hutzinger, pp. 251-293, Springer-Verlag, Berlin Heidelberg.

Andreev, A. A., and D. M. Peteet (1997), An 8100 year record of vegetation changes from a site near Fairbanks, Alaska, paper presented at Beringian Paleoenvironments Workshop, Florissant, CO.

Barron, J. A., et al. (2009), Paleoceanography of the Gulf of Alaska during the past 15,000 years: results from diatoms, silicoflagellates, and geochemistry, *Marine Micropaleontology*.

Begét, J. E. (2001), Continuous Late Quaternary proxy climate records from loess in Beringia, *Quaternary Science Reviews*, *20*(1-3), 499-507.

Beikman, H. M. (1994), Geologic map of Alaska, in *The geology of Alaska*, edited by G. Plafker and H. C. Berg, Geological Society of Alaska, Boulder, CO.

Bigelow, N. H., and M. E. Edwards (2001), A 14,000 yr paleoenvironmental record from Windmill Lake, Central Alaska: Lateglacial and Holocene vegetation in the Alaska range, *Quaternary Science Reviews*, *20*(1-3), 203-215.

Blum, P. (1997), Physical properties handbook: a guide to the shipboard measurement of physical properties of deep-sea cores, edited, p. doi:10.2973/odp.tn.2926.1997, Ocean Drilling Program.

Bond, G., et al. (1997), A pervasive millennial-scale cycle in North Atlantic Holocene and glacial climates, *Science*, *278*(5341), 1257-1266.

Boyd, P. W., et al. (2004), The decline and fate of an iron-induced subarctic phytoplankton bloom, *Nature*, *428*(6982), 549-553.

Broecker, W. S. (1991), The great ocean conveyor, *Oceanography*, *4*, 79-90.

Calkin, P. E., et al. (2001), Holocene coastal glaciation of Alaska, *Quaternary Science Reviews*, *20*(1-3), 449-461.

Calvert, S. E., and T. F. Pedersen (1993), Geochemistry of recent oxic and anoxic marine-sediments - implications for the geological record, *Marine Geology*, *113*(1-2), 67-88.

Carleton, A. M., et al. (1990), Mechanisms of interannual variability of the Southwest United States summer rainfall maximum, *Journal of Climate*, *3*(9), 999-1015.

Carpenter, E. J., et al. (1997), Biogeochemical tracers of the marine cyanobacterium Trichodesmium, *Deep-Sea Research I*, *44*(1), 27-38.

Chang, A. S., et al. (2008), Late Quaternary paleoproductivity history on the Vancouver Island margin, western Canada: a multiproxy geochemical study, *Canadian Journal of Earth Sciences*, *45*, 1283-1297.

Chase, Z., et al. (2007), Iron links river runoff and shelf width to phytoplankton biomass along the U.S. West Coast, *Geophysical Research Letters*, *34*(L04607), doi:10.1029/2006GL028069.

Chester, R., and M. J. Hughes (1967), A chemical technique for the separation of ferro-manganese minerals, carbonate minerals and adsorbed trace elements from pelagic sediments, *Chemical Geology*, *2*, 249-262.

Childers, A. R., et al. (2005), Seasonal and interannual variability in the distribution of nutrients and chlorophyll a across the Gulf of Alaska shelf: 1998-2000, *Deep-Sea Research Part II-Topical Studies in Oceanography*, *52*(1-2), 193-216.

Coale, K. H., et al. (1996), A massive phytoplankton bloom induced by an ecosystem-scale iron fertilization experiment in the equatorial Pacific Ocean, *Nature*, *383*, 495-501.

Coale, K. H., et al. (2004), Southern ocean iron enrichment experiment: Carbon cycling in high- and low-Si waters, *Science*, *304*(5669), 408-414.

COHMAP (1988), Climatic changes of the last 18,000 years: observations and model simulations, *Science*, *241*(4869), 1043-1052.

Cole, T. G., and H. F. Shaw (1983), The nature and origin of authigenic smectites in some recent marine sediments, *Clay Minerals, 18*, 239-252.

Conley, D. J. (1998), An interlaboratory comparison for the measurement of biogenic silica in sediments, *Marine Chemistry, 63*, 39-48.

Cook, M. S., et al. (2005), The deglacial history of surface and intermediate water of the Bering Sea, *Deep-Sea Research Part II-Topical Studies in Oceanography, 52*(16-18), 2163-2173.

Crusius, J., et al. (2004), Influence of northwest Pacific productivity on North Pacific Intermediate Water oxygen concentrations during the Bølling-Alleröd interval (14.7-12.9 ka), *Geology, 32*(7), 633-636.

Davies, M., et al., Regional deglaciation of the Gulf of Alaska, to be submitted to *Paleoceanography*.

De Vernal, A., and T. F. Pedersen (1997), Micropaleontology and palynology of core PAR87A-10: a 23,000 year record of paleoenvironmental changes in the Gulf of Alaska, northeast North Pacific, *Paleoceanography, 12*(6), 821-830.

Dean, W. E., and M. A. Arthur (1989), Iron-sulfur-carbon relationships in organic-carbon-rich sequences I: Cretaceous Western Interior Seaway, *American Journal of Science, 289*(6), 708-743.

Dean, W. E. (2007), Sediment geochemical records of productivity and oxygen depletion along the margin of western North America during the past 60,000 years: teleconnections with Greenland Ice and the Cariaco Basin, *Quaternary Science Reviews, 26*(1-2), 98-114.

Denton, G. H., and W. Karlen (1973), Holocene climatic variations - their pattern and possible cause, *Quaternary Research, 3*, 155-205.

Dymond, J. (1992), Barium in deep-sea sediments: a geochemical proxy for paleoproductivity, *Paleoceanography, 7*(2), 163-181.

Eberl, D. D. (2003), User's guide to RockJock - a program for determining quantitative mineralogy from powder X-ray diffraction data, edited by U. S. G. Survey, p. 47, US Geological Survey, Boulder, CO.

Eberl, D. D. (2004), Quantitative mineralogy of the Yukon River system: changes with reach and season, and determining sediment provenance, *American Mineralogist, 89*, 1784-1794.

Engstrom, D. R., et al. (1990), A possible Younger Dryas record in southeastern Alaska, *Science, 250*(4986), 1383-1385.

Fairbanks, R. G. (1989), A 17,000-year glacio-eustatic sea-level record - influence of glacial melting rates on the Younger Dryas event and deep-ocean circulation, *Nature*, *342*(6250), 637-642.

Falkowski, P. G., et al. (1998), Biogeochemical controls and feedbacks on ocean primary production, *Science*, *281*, 200-206.

Feder, H. M., et al. (1976), The sediment environment of Port Valdez, Alaska: the effect of oil on this ecosystem, edited, p. 322, Environmental Research Laboratory, Office of Research and Development, US Environmental Protection Agency.

Filgueiras, A. V., et al. (2002), Chemical sequential extraction for metal partitioning in environmental solid samples, *Journal of Environmental Monitoring*, *4*(6), 823-857.

Finney, B. P., et al. (2000), Impacts of climatic change and fishing on Pacific salmon abundance over the past 300 years, *Science*, *290*(5492), 795-799.

Fisher, D., et al. (2008), The Mt Logan Holocene-late Wisconsinan isotope record: Tropical Pacific-Yukon connections, *Holocene*, *18*(5), 667-677.

Francois, R., et al. (2004), Th-230 normalization: An essential tool for interpreting sedimentary fluxes during the late Quaternary, *Paleoceanography*, *19*(1), 16.

Galbraith, E. D., et al. (2007), Carbon dioxide release from the North Pacific abyss during the last deglaciation, *Nature*, *449*, 890-894.

Galbraith, E. D., et al. (2008a), Consistent relationship between global climate and surface nitrate utilization in western Subarctic Pacific throughout the last 500 ky, *Paleoceanography*, *23*, doi:10.1029/2007PA001518.

Galbraith, E. D., et al. (2008b), Nitrogen in past marine environments, in *Nitrogen in the marine environment*, edited by D. G. Capone, et al., pp. 1497-1535, Academic Press, San Diego, CA.

Ganeshram, R. S., et al. (1995), Large changes in oceanic nutrient inventories from glacial to interglacial periods, *Nature*, *376*(6543), 755-758.

Gargett, A. E. (1997), The optimal stability 'window': a mechanism underlying decadal fluctuations in North Pacific salmon stocks?, *Fisheries Oceanography*, *6*(2), 109-117.

Gaye-Haake, B., et al. (2005), Biogeochemical processes in the northern Indian Ocean, *Deep-Sea Research Part II-Topical Studies in Oceanography*, *52*(14-15), 1845-1847.

Geider, R. J., and J. La Roche (2002), Redfield revisited: variability of C:N:P in marine microalgae and its biochemical basis, *European Journal of Phycology*, *37*(1), 1-17.

Gorbarenko, S. A. (1996), Stable isotope and lithologic evidence of late-glacial and Holocene oceanography of the northwestern Pacific and its marginal seas, *Quaternary Research*, *46*(3), 230-250.

Gorbarenko, S. A., et al. (2004), Late Pleistocene-Holocene oceanographic variability in the Okhotsk Sea: geochemical, lithological and paleontological evidence, *Palaeogeography Palaeoclimatology Palaeoecology*, *209*(1-4), 281-301.

Gruber, N., and J. L. Sarmiento (1997), Global patterns of marine nitrogen fixation and denitrification, *Global Biogeochemical Cycles*, *11*(2), 235-266.

Gulick, S., and J. Jaeger (2003), The interplay of collisional tectonics and Late Cenozoic glacial climate in Alaska and the Northeastern Pacific Ocean, Continental Dynamics Program, Earth Sciences Division, National Science Foundation and Joint Oceanographic Institutions/U.S. Science Support Program, Austin, Texas.

Hallet, B., et al. (1996), Rates of erosion and sediment evacuation by glaciers: A review of field data and their implications, *Global and Planetary Change*, *12*(1-4), 213-235.

Hameed, S., and A. Conversi (1995), Signals in the interannual variations of zooplankton biomass in the Gulf of Alaska, *Journal of Coastal Research*(17), 21-27.

Harrison, P. J., et al. (1999), Comparison of factors controlling phytoplankton productivity in the NE and NW subarctic Pacific gyres, *Progress in Oceanography*, *43*(2-4), 205-234.

Haug, G. H., et al. (2001), Southward migration of the intertropical convergence zone through the Holocene, *Science*, *293*(5533), 1304-1308.

Hedges, J. I., et al. (1999), Sedimentary organic matter preservation: A test for selective degradation under oxic conditions, *American Journal of Science*, *299*(7-9), 529-555.

Hendy, I. L., and T. N. Cosma (2008), Vulnerability of the Cordilleran Ice Sheet to iceberg calving during late Quaternary rapid climate change events, *Paleoceanography*, *23*, PA2101, doi:2110.1029/2008PA001606.

Higgins, R. W., and W. Shi (2000), Dominant factors responsible for interannual variability of the summer monsoon in the southwestern United States, *Journal of Climate*, *13*(4), 759-776.

Hopkins, D. M. (1959), Cenozoic history of the Bering Land Bridge, *Science*, *129*(3362), 1519-1528.

Hughen, K., et al. (2004), C-14 activity and global carbon cycle changes over the past 50,000 years, *Science*, *303*(5655), 202-207.

Jaeger, J. M., et al. (1998), Sediment accumulation along a glacially impacted mountainous coastline: north-east Gulf of Alaska, *Basin Research, 10,* 155-173.

Jian, Z. M., et al. (2000), Holocene variability of the Kuroshio Current in the Okinawa Trough, northwestern Pacific Ocean, *Earth and Planetary Science Letters, 184*(1), 305-319.

Johnson, W. K., et al. (2005), Iron transport by mesoscale Haida eddies in the Gulf of Alaska, *Deep-Sea Research Part II-Topical Studies in Oceanography, 52,* 933-953.

Kastner, M. (1999), Oceanic minerals: Their origin, nature of their environment and significance, *Proceedings of the National Academy of Sciences of the United States of America, 96*(7), 3380-3387.

Kaufman, D., and W. F. Manley (2004), Pleistocene Maximum and Late Wisconsinan glacier extents across Alaska, U.S.A., in *Quaternary Glaciations - Extent and chronology, Part II: North America,* edited by J. Ehlers and P. L. Gibbard, pp. 9-27, Elsevier, Amsterdam.

Kaufman, D. S., et al. (2004), Holocene thermal maximum in the western Arctic (0-180 degrees W), *Quaternary Science Reviews, 23*(5-6), 529-560.

Keigwin, L. D. (1987), North Pacific deep water formation during the latest glaciation, *Nature, 330*(6146), 362-364.

Keigwin, L. D., et al. (1992), A 15,000 year paleoenvironmental record from Meiji Seamount, Far Northwestern Pacific, *Earth and Planetary Science Letters, 111*(2-4), 425-440.

Keigwin, L. D. (1998), Glacial-age hydrography of the far northwest Pacific Ocean, *Paleoceanography, 13*(4), 323-339.

Keigwin, L. D., et al. (2006), Rapid sea-level rise and Holocene climate in the Chukchi Sea, *Geology, 34*(10), 861-864.

Kennett, J. P., and B. L. Ingram (1995), A 20,000 year record of ocean circulation and climate change from the Santa Barbara Basin, *Nature, 377*(6549), 510-514.

Kiefer, T., and M. Kienast (2005), Patterns of deglacial warming in the Pacific Ocean: a review with emphasis on the time interval of Heinrich event 1, *Quaternary Science Reviews, 24*(7-9), 1063-1081.

Kienast, S. S., et al. (2004), Export production in the subarctic North Pacific over the last 800 kyrs: No evidence for iron fertilization?, *Journal of Oceanography, 60*(1), 189-203.

Klassen, R. A. (2001), A Quaternary geological perspective on geochemical exploration in glaciated terrain, in *Drift exploration in glaciated terrain*, edited by M. B. McClenaghan, et al., pp. 1-17, The Geological Society of London, London.

Knies, J., et al. (2007), Re-assessing the nitrogen signal in continental margin sediments: new insights from the high northern latitudes, *Earth and Planetary Science Letters*, *253*, 471-484.

Kokorowski, H. D., et al. (2008), A re-evaluation and spatial analysis of evidence for a Younger Dryas climatic reversal in Beringia, *Quaternary Science Reviews*, *27*, 1710-1722.

Kulm, L. D., et al. (1973), Introduction, in *Initial reports of the Deep Sea Drilling Project, Leg 18*, edited by L. F. Musich and O. E. Weser, pp. 5-8, US Government Printing Office, Washington D.C.

Kutzbach, J., et al. (1998), Climate and biome simulations for the past 21,000 years, *Quaternary Science Reviews*, *17*(6-7), 473-506.

Ladd, C., et al. (2005), A note on cross-shelf exchange in the northern Gulf of Alaska, *Deep-Sea Research Part II-Topical Studies in Oceanography*, *52*(5-6), 667-679.

Lam, P. J., and J. K. B. Bishop (2008), The continental margin is a key source of iron to the HNLC North Pacific Ocean, *Geophysical Research Letters*, *35*(7), 5.

Lamb, A. L., et al. (2006), A review of coastal palaeoclimate and relative sea-level reconstructions using delta C-13 and C/N ratios in organic material, *Earth-Science Reviews*, *75*, 29-57.

Langmuir, D. (1997), *Aqueous environmental geochemistry*, 600 pp., Prentice Hall, Upper Saddle River, New Jersey.

Laws, E. A., et al. (1995), Dependence of phytoplankton carbon isotopic composition on growth rate and $[CO_2]_{aq}$: theoretical considerations and experimental results, *Geochimica Et Cosmochimica Acta*, *59*, 1131-1138.

Levene, H. (1960), Robust tests for equality of variance, in *Contributions to probability and statistics: essays in honor of Harold Hotelling*, edited by I. Olkin et al., pp. 278-292, Stanford University Press, Stanford, CA.

Lund, D. C., and A. C. Mix (1998), Millenial-scale deep water oscillations: reflections of the North Atlantic in the deep Pacific from 10 to 60 ka, *Paleoceanography*, *13*(1), 10-19.

MacDonald, G. M., and R. A. Case (2005), Variations in the Pacific Decadal Oscillation over the past millennium, *Geophysical Research Letters*, *32*(8).

Mann, D. H., and T. D. Hamilton (1995), Late Pleistocene and Holocene paleoenvironments of the North Pacific Coast, *Quaternary Science Reviews, 14*(5), 449-471.

Mann, D. H., et al. (1998), Holocene geologic and climatic history around the Gulf of Alaska, *Arctic Anthropology, 35*(1), 112-131.

Marshall, C. P., and R. W. Fairbridge (Eds.) (1999), *Encyclopedia of geochemistry*, 712 pp., Kluwer Academic Publishers, Dordrecht, The Netherlands.

Martin, J. H. (1990), Glacial-interglacial CO_2 change: the iron hypothesis, *Paleoceanography, 5*, 1-13.

Mason, O. K., et al. (2001), The early Holocene Milankovitch thermal maximum and humans: adverse conditions for the Denali complex of eastern Beringia, *Quaternary Science Reviews, 20*, 525-548.

Mathewes, R. W. (1993), Evidence for Younger Dryas age cooling on the North Pacific Coast of America, *Quaternary Science Reviews, 12*(5), 321-331.

Mathewes, R. W., et al. (1993), Evidence for a Younger Dryas like cooling event on the British Columbia coast, *Geology, 21*(2), 101-104.

McDonald, D., et al. (1999), Multiple late Quaternary episodes of exceptional diatom production in the Gulf of Alaska, *Deep-Sea Research Part II-Topical Studies in Oceanography, 46*(11-12), 2993-3017.

McFarlane, G. A., and R. J. Beamish (1992), Climatic influence linking copepod production with strong year-classes in sablefish, Anoplopoma-Fimbria, *Canadian Journal of Fisheries and Aquatic Sciences, 49*(4), 743-753.

McLennan, S. M., et al. (1993), Geochemical approaches to sedimentation, provenance, and tectonics, in *Processes controlling the composition of clastic sediments*, edited by M. J. Johnsson and A. Basu, pp. 21-40, Geological Society of America, Boulder, CO.

McLennan, S. M. (1995), Sediments and soils: chemistry and abundances, in *Rock physics & phase relations - a handbook of physical constants*, edited by T. J. Ahrens, pp. 8-19, American Geophysical Union, Washington D.C.

McLennan, S. M. (1999), Geochemical classification of the elements, in *Encyclopedia of geochemistry*, edited by C. P. Marshall and R. W. Fairbridge, pp. 263-266, Kluwer Academic Publishers, Dordrecht, The Netherlands.

McManus, J. F., et al. (2004), Collapse and rapid resumption of Atlantic meridional circulation linked to deglacial climate change, *Nature, 428*, 834-837.

McQuoid, M. R., et al. (2001), A post-glacial isotope record of primary production and accumulation in the organic sediments of Saanich Inlet, ODP Leg 169S, *Marine Geology*, *174*(1-4), 273-286.

Meyers, P. A. (1994), Preservation of elemental and isotopic source identification of sedimentary organic matter, *Chemical Geology*, *114*(3-4), 289-302.

Milliman, J. D., and J. P. M. Syvitski (1992), Geomorphic Tectonic Control of Sediment Discharge to the Ocean - the Importance of Small Mountainous Rivers, *Journal of Geology*, *100*(5), 525-544.

Mix, A. C., et al. (1999), Rapid climate oscillations in the Northeast Pacific during the last deglaciation reflect Northern and Southern Hemisphere sources, in *Mechanisms of global climate change at millenial time scales*, edited by P. U. Clark, et al., pp. 127-148, American Geophysical Union, Washington D.C.

Moffett, J. W. (2001), Transformations among different forms of iron in the ocean, in *The biogeochemistry of iron in seawater*, edited by D. R. Turner and K. A. Hunter, pp. 343-372, John Wiley and Sons, Ltd., West Sussex, England.

Molnia, B. F. (1982), Erosion, deposition, faulting, and instability of shelf sediments: Eastern Gulf of Alaska, in *Outer Continental Shelf Environmental Assessment Program, Final Reports of Principal Investigators*, pp. 1-638.

Molnia, B. F., and J. R. Hein (1982), Clay mineralogy of a glacially dominated, subarctic continental shelf: northeastern Gulf of Alaska, *Journal of Sedimentary Petrology*, *52*(2), 515-527.

Molnia, B. F., and A. Post (1995), Holocene history of Bering Glacier, Alaska: a prelude to the 1993-1994 surge, *Physical Geography*, *16*(2), 87-117.

Morel, F. M. M., and N. M. Price (2003), The biogeochemical cycles of trace metals in the oceans, *Science*, *300*(5621), 944-947.

Morley, J. J., et al. (1991), Late Pleistocene/Holocene radiolarian and pollen records from sediments in the Sea of Okhotsk, *Paleoceanography*, *6*(1), 121-131.

Mortlock, R. A., and P. N. Froelich (1989), A simple method for the rapid determination of biogenic opal in pelagic marine sediments, *Deep-Sea Research*, *36*(9), 1415-1426.

Muller, P. J. (1977), C/N ratios in Pacific deep-sea sediments: effect of inorganic ammonium and organic nitrogen compounds sorbed by clays, *Geochimica Et Cosmochimica Acta*, *41*, 765-776.

Mundy, P. R., and P. Olsson (2005), Climate and weather, in *The Gulf of Alaska: biology and oceanography*, edited by P. R. Mundy, pp. 25-34, Alaska Sea Grant College Program, University of Alaska Fairbanks.

Naidu, A. S., et al. (1976), Clay minerals in recent sediments of the continental shelf, northern and western Gulf of Alaska, in *Proceedings of the 27th Alaska Science Conference*, edited, pp. 202-212, Alaska Division, American Association for the Advancement of Science, Fairbanks, Alaska.

Naidu, A. S., and T. C. Mowatt (1983), Sources and dispersal patterns of clay minerals in surface sediments from the continental-shelf areas off Alaska, *Geological Society of America Bulletin, 94*, 841-854.

Nishioka, J., et al. (2001), Size-fractionated iron concentrations in the Northeast Pacific Ocean: distribution of soluble and small colloidal iron, *Marine Chemistry, 74*, 157-179.

Okazaki, Y., et al. (2005), Productivity changes in the Bering Sea during the late Quaternary, *Deep-Sea Research Part II-Topical Studies in Oceanography, 52*(16-18), 2150-2162.

Paulmier, A. and Ruiz-Pino, D., 2009. Oxygen minimum zones (OMZs) in the modern ocean. *Progress in Oceanography* 80(3-4): 113-128.

Peteet, D. M., and D. H. Mann (1994), Late-glacial vegetational, tephra, and climatic history of southwestern Kodiak Island, Alaska, *Ecoscience, 1*(3), 255-267.

Petit, J. R., et al. (1999), Climate and atmospheric history of the past 420,000 years from the Vostok ice core, Antarctica, *Nature, 399*(6735), 429-436.

Piper, D. Z., and S. E. Calvert (2009), A marine biogeochemical perspective on black shale deposition, *Earth-Science Reviews, 95*, 63-96.

Price, N. M., et al. (1994), The equatorial Pacific Ocean: grazer-controlled phytoplankton populations in an iron-limited ecosystem, *Limnology and Oceanography, 39*(3), 520-534.

Ragueneau, O., et al. (2000), A review of the Si cycle in the modern ocean: recent progress and missing gaps in the application of biogenic opal as a paleoproductivity proxy, *Global and Planetary Change, 26*(4), 317-365.

Rasmussen, S. O., et al. (2007), Early Holocene climate oscillations recorded in three Greenland ice cores, *Quaternary Science Reviews, 26*(15-16), 1907-1914.

Rau, G. H., et al. (1989), Latitudinal variations in plankton $\delta^{13}C$ - implications for CO_2 and productivity in past oceans, *Nature, 341*(6242), 516-518.

Rea, D. K., et al. (1995), Scientific results of drilling the North Pacific Transect, in *Proceedings of the Ocean Drilling Program, Scientific Results, Vol. 145*, edited by D. K. Rea, et al., pp. 577-596.

Rea, D. K., and H. Snoeckx (1995), Sediment fluxes in the Gulf of Alaska; paleoceanographic record from Site 887 on the Patton-Murray Seamount Platform, in *Proceedings of the Ocean Drilling Program, Scientific Results*, edited by D. K. Rea, et al., pp. 247-256, Ocean Drilling Program, College Station, Texas.

Redfield, A. C., et al. (1963), The influence of organisms on the composition of sea-water, in *The Sea: ideas and observations on progress in the study of the seas*, edited by M. N. Hill, pp. 26-77, John Wiley and Sons.

Reger, R. D., et al. (2008), A guide to the late Quaternary history of northern and western Kenai Peninsula, Alaska, edited, p. 112, Alaska Division of Geological and Geophysical Surveys.

Rodionov, S. N., et al. (2005), Spatial and temporal variability of the Aleutian climate, *Fisheries Oceanography, 14*, 3-21.

Rodionov, S. N., et al. (2007), The Aleutian Low, storm tracks, and winter climate variability in the Bering Sea, *Deep-Sea Research Part II-Topical Studies in Oceanography, 54*, 2560-2577.

Royer, T. C., et al. (2001), Interdecadal variability of Northeast Pacific coastal freshwater and its implications on biological productivity, *Progress in Oceanography, 49*(1-4), 95-111.

Royer, T. C. (2005), Hydrographic responses at a coastal site in the northern Gulf of Alaska to seasonal and interannual forcing, *Deep-Sea Research Part II-Topical Studies in Oceanography, 52*(1-2), 267-288.

Sancetta, C. A., et al. (1985), Wisconson-Holocene paleoenvironment of the Bering Sea: evidence from diatoms, pollen, oxygen isotopes and clay minerals, *Marine Geology, 62*, 55-68.

Sarmiento, J. L., and N. Gruber (2006), *Ocean biogeochemical dynamics*, 503 pp., Princeton University Press, Princeton, New Jersey.

Schroth, A. W., et al. (2009), Iron solubility driven by speciation in dust sources to the ocean, *Nature Geoscience, 2*, 337-340.

Schulz, M., and M. Mudelsee (2002), REDFIT: estimating red-noise spectra directly from unevenly spaced paleoclimatic time series, *Computers & Geosciences, 28*, 421-426.

Slatt, R. M., and D. J. W. Piper (1974), Sand-silt petrology and sediment dispersal in the Gulf of Alaska, *Journal of Sedimentary Petrology*, *44*(4), 1061-1071.

Springer, A. M., et al. (1996), The Bering Sea Green Belt: Shelf-edge processes and ecosystem production, *Fisheries Oceanography*, *5*(3-4), 205-223.

Steffensen, J.P. et al., 2008. High-resolution Greenland ice core data show abrupt climate change happens in few years. Science 321(5889): 680-684.

Stommel, H. (1958), The abyssal circulation, *Deep-Sea Research*, *5*, 80-82.

Talley, L. D. (1993), Distribution and formation of North Pacific Intermediate Water, *Journal of Physical Oceanography*, *23*, 517-537.

Tessier, A., et al. (1979), Sequential extraction procedure for the speciation of particulate trace metals, *Analytical Chemistry*, *51*(7), 844-851.

Thunell, R. C., et al. (2004), Nitrogen isotope dynamics of the Cariaco Basin, Venezuela, *Global Biogeochemical Cycles*, *18*(3), doi:10.1029/2003GB002185.

Trenberth, K. E., and J. W. Hurrell (1994), Decadal atmosphere-ocean variations in the Pacific, *Climate Dynamics*, *9*(6), 303-319.

Tribovillard, N., et al. (2006), Trace metals as paleoredox and paleoproductivity proxies: An update, *Chemical Geology*, *232*(1-2), 12-32.

Ullrich, A. D., et al. (2009), Intra-annual variability in benthic foraminiferal abundance in sediments of Disenchantment Bay, an Alaskan glacial fjord, *Arctic, Antarctic, and Alpine Research*, *41*(2), 257-271.

Van der Weijden, C. H. (2002), Pitfalls of normalization of marine geochemical data using a common divisor, *Marine Geology*, *184*(3-4), 167-187.

van Geen, A., et al. (2003), On the preservation of laminated sediments along the western margin of North America, *Paleoceanography*, *18*, doi:10.1029/2003PA000911.

VanLaningham, S., et al. (2009), Glacial-interglacial sediment transport to the Meiji Drift, northwest Pacific Ocean: evidence for timing of Beringian outwashing, *Earth and Planetary Science Letters*, *277*, 64-72.

Walinsky, S. E., et al. (2009), Distribution and composition of organic matter in surface sediments of coastal southeast Alaska, *Continental Shelf Research*.

Wallace, J. M., and D. S. Gutzler (1981), Teleconnections in the geopotenital height field during the Northern Hemisphere winter, *Monthly Weather Review*, *109*(4), 784-812.

Walsh, E. M., et al. (2008), Sources and transport of terrestrial organic matter in Vancouver Island fjords and the Vancouver-Washington Margin: A multiproxy approach using $\delta^{13}C_{org}$, lignin phenols, and the ether lipid BIT index, *Limnology and Oceanography, 53*(3), 1054-1063.

Weingartner, T. J. (2005), Physical and geological oceanography: coastal boundaries and coastal and ocean circulation, in *The Gulf of Alaska: biology and oceaongraphy*, edited by P. R. Mundy, pp. 35-48, Alaska Sea Grant College Program, University of Alaska Fairbanks.

Weingartner, T. J., et al. (2005), Freshwater variability and predictability in the Alaska Coastal Current, *Deep-Sea Research Part II-Topical Studies in Oceanography, 52*(1-2), 169-191.

Whitney, F. A., et al. (2005), Physical processes that enhance nutrient transport and primary productivity in the coastal and open ocean of the subarctic NE Pacific, *Deep-Sea Research Part II-Topical Studies in Oceanography, 52*(5-6), 681-706.

Wiles, G. C., et al. (1999), Dendrochronology and late Holocene history of Bering Piedmont Glacier, Alaska, *Quaternary Research, 52*(2), 185-195.

Wiles, G. C., et al. (2004), Century-scale solar variability and Alaskan temperature change over the past millennium, *Geophysical Research Letters, 31*(15).

Wray, D. (2005), Geological analysis, in *ICP mass spectrometry handbook*, edited by S. M. Nelms, pp. 432-451, Blackwell Publishing Ltd., Oxford, UK.

Wu, J. P., et al. (1997), Nitrogen isotope variations in the subarctic northeast Pacific: Relationships to nitrate utilization and trophic structure, *Deep-Sea Research Part I-Oceanographic Research Papers, 44*(2), 287-314.

You, Y., et al. (2000), Roles of the Okhotsk Sea and Gulf of Alaska in forming the North Pacific Intermediate Water, *Journal of Geophysical Research, 105*(C2), 3253-3280.

Zheng, Y., et al. (2000), Intensification of the northeast Pacific oxygen minimum zone during the Bolling-Allerod warm period, *Paleoceanography, 15*(5), 528-536.

Chapter 6 Conclusions

The work presented in this volume describes several aspects of the climatic and oceanographic evolution of the Gulf of Alaska region since the Last Glacial Maximum (LGM). Perhaps the single most important observation from this work is that the North Pacific marine ecosystem is a sensitive high-fidelity recorder of past environmental conditions, both in a direct manner as forced by oceanographic conditions, and indirectly via atmosphere-climate-ocean linkages. Paleoenvironmental reconstructions that depend heavily on marine productivity parameters can potentially yield incredibly detailed records of past changes. However, the major limitation of using records of marine productivity as a basis for paleoenvironmental work is also its greatest benefit – marine ecosystems by their very nature are complex and complicated systems. Only through the utilization of multi-proxy approaches can these complications be addressed. Other key findings presented in this volume, divided by chapter, are as follows:

Chapter 2: *Marine tephrochronology of the Mt. Edgecumbe Volcanic Field, Southeast Alaska, USA*

- While few terrestrial deposits of tephra exist along the terrestrial margin of the Gulf of Alaska, there is an extensive record of Late Quaternary volcanism preserved in the adjacent marine environment. These marine macroscopic tephra and cryptotephra deposits are useful marker horizons for establishing stratigraphic correlations between marine sediment cores, as well as linking offshore deposits with terrestrial outcrops and ice cores. Combined with AMS ^{14}C dating of macrofossils, complementary geochronologies can be established with high fidelity, yielding paleoenvironmental records of sub-decadal temporal resolution.

- The tephra deposits of the Mt. Edgecumbe Volcanic Field provide a series of useful LGM and Holocene horizons. In particular, the MEd dacite tephra is important due to its association with the Pleistocene/Holocene boundary.

- The regionally significant White River Ash, dated at 1147 cal yr BP, is found in southeast Alaska over 1,000 km from its postulated source in the Wrangell Volcanic Field.

Chapter 3: *Holocene evolution of the Pacific Decadal Oscillation in the Gulf of Alaska*

- The coupled atmosphere-ocean-ecosystem structure in the Gulf of Alaska has experienced multiple modes of variability throughout the Holocene, ranging from seasonal to millennial time scales. The sediment records described in this volume exhibit patterns of decadal- and centennial-scale variability.

- Models of North Pacific climate variability based on modern human observations can be inadequate for describing the full range of potential environmental conditions, particularly for systems that operate at periods exceeding 100 years. The Pacific Decadal Oscillation appears to be such a system, based on a synthesis of high-quality spatially diverse Northern Hemisphere paleoclimate records, including data from the fjords of southeastern Alaska.

- The onset of mid-Holocene Aleutian Low intensification in the Gulf of Alaska at 4000 cal yr BP is due to a linkage with the Intertropical Convergence Zone, more than 5000 km distant. This linkage was facilitated by an increase of the meridional temperature gradient between equatorial and high-latitude regions that enhanced heat transport to the poles via Hadley cell circulation.

Chapter 4: *High-resolution paleoproductivity evidence for Holocene evolution of the Aleutian Low Pressure System from coastal fjords in the Subarctic Northeast Pacific Ocean*

- Multiple fjords throughout the Gulf of Alaska region preserve a complementary regional record of Holocene marine productivity and terrestrial run-off intensity. Together, these records indicate a millennial-scale mid-Holocene intensification of the Aleutian Low pressure cell responsible for enhancing primary productivity and precipitation. However, between 8000 – 6500 cal yr BP, these same sites

indicate a decoupling between Aleutian Low atmospheric dynamics and marine ecosystem variability.

- The onset of fjord-style reverse estuarine circulation in the Southeast Alaska region is complicated by changes in both eustatic and relative sea level due to the high levels of tectonism and isostasy present along this margin. Nevertheless, using a combined approach consisting of biogeochemical, isotopic, and inorganic geochemistry, as well as diatom and silicoflagellate population data, fjord-style circulation appears to have initiated around 12,000 years ago following the retreat of the regional Cordilleran Ice Sheet.

Chapter 5: *Decoupling of the coastal marine ecosystem and glaciomarine Cordilleran Ice Sheet dynamics in the Gulf of Alaska during the Last Glacial Maximum/Holocene transition*

- The continental shelf of the northern Gulf of Alaska preserves evidence linking paleoceanographic conditions in the Subarctic Northeast Pacific Ocean to abrupt changes occurring in the North Atlantic Ocean during the LGM/Holocene transition. In particular, the presence of laminated intervals along the Gulf of Alaska continental slope associated with the Bølling-Ålleröd (B-A) chronozone, as identified in the Greenland GISP2 ice core and other continental margin settings of North America, demonstrate this connection.

- The response of the LGM glaciomarine Cordilleran Ice Sheet complex (present along the continental shelf of the Gulf of Alaska) during the deglacial transition lags contemporaneous changes in the record of marine primary production. This apparent decoupling suggests the marine ecosystem is much more sensitive to global environmental change, yet the marine ecosystem also displays a high degree of resiliency as indicated by rapid shifts to steady-state conditions under radically different environmental parameters.

- The laminated B-A interval contains evidence for high primary productivity, facilitated by enhanced nitrate utilization and a possible reduction in

micronutrient limitation. This data suggests a link between active tectonism,
climate and the marine ecosystem, but requires further testing.

6.1   Future directions

There is still much scientific work to be done along the Gulf of Alaska margin.
Data from seven EW0408 sediment cores were presented in this dissertation (Tables 6.1
and 6.2); an additional 23 cores await detailed analysis. One of the major strengths of the
EW0408 sediment core collection is that most are long enough to resolve millennial
timescales without requiring painstakingly precise spatial sampling strategies. Future
work this author has planned for the EW0408 collection capitalizes on these high
accumulation rates to conduct ultra-high-resolution analyses of biogeochemical
parameters using advanced X-ray fluorometry core scanning instrumentation, as well as
refining new isotopic proxies focused on the use of diatom frustules for paleosalinity
reconstructions. This first technique will potentially yield seasonal records of authigenic
element precipitation patterns relevant to reconstructing the occurrence of bottom-water
renewal events in the fjords of southeast Alaska, and by inference regional scale
circulation patterns in the Gulf of Alaska. Combined with a $\delta^{18}O_{diatom}$ paleosalinity
record of the Alaska Coastal Current, I hope to achieve some of the most detailed records
ever developed from the Northeast Pacific Ocean margin. Better measurements of past
iron availability are also necessary; the estimation technique presented in Chapter 5 can
be improved using synchrotron-based iron speciation measurements. Additionally, I also
hope to participate in future IODP cruises to the Gulf of Alaska for which the EW0408
cores were originally collected. The work presented in this volume has evidently only
whetted my appetite for future Gulf of Alaska investigations.

Table 6.1: Significant paleoclimate datasets generated by the author for this work. Following journal publication, these datasets will be available for public use from the NOAA Paleoclimatology website (http://www.ncdc.noaa.gov/paleo/data.html).

EW0408-11JC (55.63°N, 133.51°W, 183 m water depth)

Composite age model based on AMS ^{14}C macrofossils and 1 tephra correlation

Biogenic silica (opal)

Total organic carbon (TOC) and total nitrogen (TN)

Carbonate-free sedimentary δ^{13}C and δ^{15}N

EW0408-22JC (56.80°N, 135.21°W, 188 m water depth)

Composite age model based on AMS ^{14}C macrofossils and 1 tephra correlation

Biogenic silica (opal)

Total organic carbon (TOC) and total nitrogen (TN)

Carbonate-free sedimentary δ^{13}C and δ^{15}N

Inorganic geochemistry (28 elements)

EW0408-33JC (57.16°N, 135.36°W, 144 m water depth)

Composite age model based on AMS ^{14}C macrofossils and 2 tephra correlations

Biogenic silica (opal)

Total organic carbon (TOC) and total nitrogen (TN)

Carbonate-free sedimentary δ^{13}C and δ^{15}N

Inorganic geochemistry (28 elements)

EW0408-44JC (56.97°N, 135.27°W, 90 m water depth)

Composite age model based on AMS ^{14}C macrofossils

Biogenic silica (opal)

Total organic carbon (TOC) and total nitrogen (TN)

Carbonate-free sedimentary δ^{13}C and δ^{15}N

Inorganic geochemistry (28 elements)

EW0408-85JC (59.56°N, 144.15°W, 680 m water depth)

Biogenic silica (opal)

Total organic carbon (TOC) and total nitrogen (TN)

Carbonate-free sedimentary δ^{13}C and δ^{15}N

XRD quantitative mineralogy

Table 6.2: The analytical contributions of the author for the work presented in this volume.

EW0408-11JC

Collected all macrofossil samples for AMS 14C analysis
Collected and analyzed tephra samples at 1295-1299 cm bsf
for major oxide geochemistry
Derived age model calculations
Collected all ICP-MS samples
Performed all univariate and multivariate statistical analyses
Extracted NOAA bathymetry data and generated a digital
elevation model (DEM; see Fig. 4.1c)

EW0408-22JC

Collected all macrofossil samples for AMS 14C analysis
Collected and analyzed cryptotephra sample at 163 cm bsf
for major oxide geochemistry
Derived age model calculations
Collected all biogenic silica (opal) samples
Collected all TOC, TN, and stable isotope samples
Collected all XRF geochemistry samples
Performed all XRF geochemistry analyses
Performed all univariate and multivariate statistical analyses
Performed all time-series statistical analyses

EW0408-33JC

Collected all macrofossil samples for AMS 14C analysis
Collected and analyzed cryptotephra samples at 1278 and
1618 cm bsf for major oxide geochemistry
Derived age model calculations
Collected all biogenic silica (opal) samples
Collected all TOC, TN, and stable isotope samples
Collected all XRF geochemistry samples
Performed all XRF geochemistry analyses
Performed all univariate and multivariate statistical analyses
Performed all time-series statistical analyses
Performed spatial and temporal analyses for North Pacific
teleconnection dataset

EW0408-40JC

Analyzed 10 tephra samples for major oxide geochemistry
Derived age model calculations
Performed all univariate and multivariate statistical analyses
Extracted NOAA bathymetry and generated a DEM (see Fig. 2.9)

EW0408-44JC

Collected all macrofossil samples for AMS 14C analysis
Derived age model calculations
Collected biogenic silica (opal) samples
Collected TOC, TN, and stable isotope samples
Performed all univariate and multivariate statistical analyses
Performed all time-series statistical analyses

EW0408-66JC

Derived age model calculations
Collected all biogenic silica (opal) samples
Collected all TOC, TN, and stable isotope samples
Collected all XRF geochemistry samples
Performed all XRF geochemistry analyses
Performed all univariate and multivariate statistical analyses

EW0408-79JC

Collected biogenic silica (opal) samples
Collected TOC, TN, and stable isotope samples
Collected all XRF geochemistry samples

EW0408-85JC

Collected all biogenic silica (opal) samples
Collected all TOC, TN, and stable isotope samples
Collected ICP-MS geochemistry samples
Collected and analyzed all XRD samples
Performed all univariate and multivariate statistical analyses
Performed all time-series statistical analyses